Epigenetic alterations at γ-H2AX-decorated chromatin regions after ionizing radiation

Dissertation der Fakultät für Biologie der Ludwigs-Maximilians-Universität

München

durchgeführt an der Klinik und Poliklinik für Strahlentherapie und

Radioonkologie in der Arbeitsgruppe Molekulare Strahlenbiologie

vorgelegt von Doris Mirjam Seiler

im September 2011

Table of Contents

Summary

Ionizing radiation (IR) induces DNA double-strand breaks (DSB) which are among the most severe lesions that can occur in a cell. Inefficient repair of DSB can cause cell death or lead to tumor progression. Recently, alterations of epigenetic information, such as histone modifications, were observed following DNA damage induced by ionizing radiation. Because epigenetic alterations are a common hallmark of cancer cells, radiation-induced epigenetic alterations might contribute to the carcinogenic process.

A well-known histone modification induced by DNA damage is the phosphorylation of the histone variant H2AX into γ-H2AX in a Mbp large region around DSB. γ-H2AX is a common marker for chromatin regions around DSB. In the present work I investigated whether histone modifications associated either with active or inactive genes, are altered in the vicinity of DSB. For this, I analyzed the distribution of the histone modification in question at chromatin decorated with γ-H2AX using microscopic approaches. Since common 3D confocal microscopy is limited in axial resolution to approx. 600 nm, I introduced a new technique by imaging of cells after ultra-microtome slicing. Here, fixed and stained cells were cut into ultra-thin sections of ~150nm thickness and imaged by using confocal 2D microscopy. I used ultrathin sectioning to improve image analysis in addition to conventional microscopy.

The first challenge of my work was to find a reliable method to qualitatively and quantitatively analyze microscopic images. I evaluated various programs frequently used for co-localization measurement. However, none of these methods was suitable to verify exclusion of two fluorochromes. Thus, in cooperation with the Institute of Statistics, I combined Intensity Correlation Analysis (ICA) of pixel pairs of two images and statistical evaluation for quantitative analysis of 3D image stacks. By this, I was able to show that inhibition of transcription, as indicated by loss of active RNA polymerase II, went along with the loss of active histone marks, such as H3K4me3. Statistical evaluation revealed that loss of H3K4me3 was more pronounced at later times following IR suggesting an active removal process of H3K4me3 from damaged sites. Furthermore, I observed the accumulation of several marks and proteins associated with silencing at DSB in a time-dependent manner. The pattern obtained suggested that silencing at DSB resembles polycomb-mediated silencing rather than heterochromatic silencing.

Subsequently, I investigated potential mechanisms which might be responsible for the loss of active marks at damaged sites, such as histone deposition or active removal processes by demethylases. I identified the H3K4 demethylase Jarid1A/RBP2 as a potential candidate for the removal of H3K4 at damaged sites. Since histone H3 variants were not significantly altered in

the vicinity of DSB and Jarid1A was recruited to laser-induced damage, my results suggest that histone demethylation is a mechanism to prevent transcription in the vicinity of damaged sites.

1 Introduction

1.1 Chromatin

The genetic information is 'stored' in the DNA. DNA is packaged into chromatin, which is further organized, until it reaches the final confirmation, the chromosomes (Felsenfeld and Groudine, 2003) (Figure 1.1 A). The first level of DNA packaging is the formation of nuclesomes which consist of approximately 147 base pairs (bp) of DNA wrapped around an octamer of histones (Luger et al., 1997) (Figure 1.1 B). The four main histone proteins H2A, H2B, H3 and H4 build an octamer which forms the nucleosomal core unit. Two copies of each histone form either a $(H3-H4)_2$ tetramer or a H2A-H2B heterodimer (Figure 1.1 B). For higher compaction levels, each nucleosome is linked to its adjacent nucleosome by the linker histone H1 which is thought to organize the nucleosomes into a 30-nm fibre (Figure 1.1 A). It is traditionally thought that the 30-nm fibres then build the higher order chromatin structure (Figure 1.1 A). However, experimental evidence for some of these packaging levels is rather questionable. Maeshima and colleagues argue that the 30-nm chromatin fibres are only present at in vitro conditions (Maeshima et al., 2010). In contrast, in vivo, the nucleosome fibres form a so-called 'polymer-melt' which consists of dynamic nucleosome chains which are interdigitated and able to interact (Maeshima et al., 2010). Recent investigations show that the localization of chromatin within perichromatin regions (Cremer et al., 2006; Cremer and Cremer, 2010) determines its transcriptional activity (Markaki et al., 2010).

Regions of transcription activity or inactivity can be separated into euchromatin (EC) and heterochromatin (HC) (Misteli, 2007). Euchromatin is characterized by a decondensed chromatin structure during interphase. Here, most genes are in a so-called permissive state for transcription. Heterochromatin is highly condensed and either consists of non-coding and repetitive DNA sequences (constitutive HC) or of locally silenced genes (facultative HC). Facultative HC can develop by transformation of EC via epigenetic alterations and can be reversed into EC when needed. By contrast, constitutive HC includes centromeric, pericentric and telomeric regions of the genome that remain condensed throughout the cell cycle (Probst et al., 2009). EC and HC chromatin regions can be distinguished by a specific modification pattern of the DNA itself or of histones. Histone post-translational modifications (PTMs) along with DNA methylation are the key components of epigenetic information (Bernstein et al., 2007).
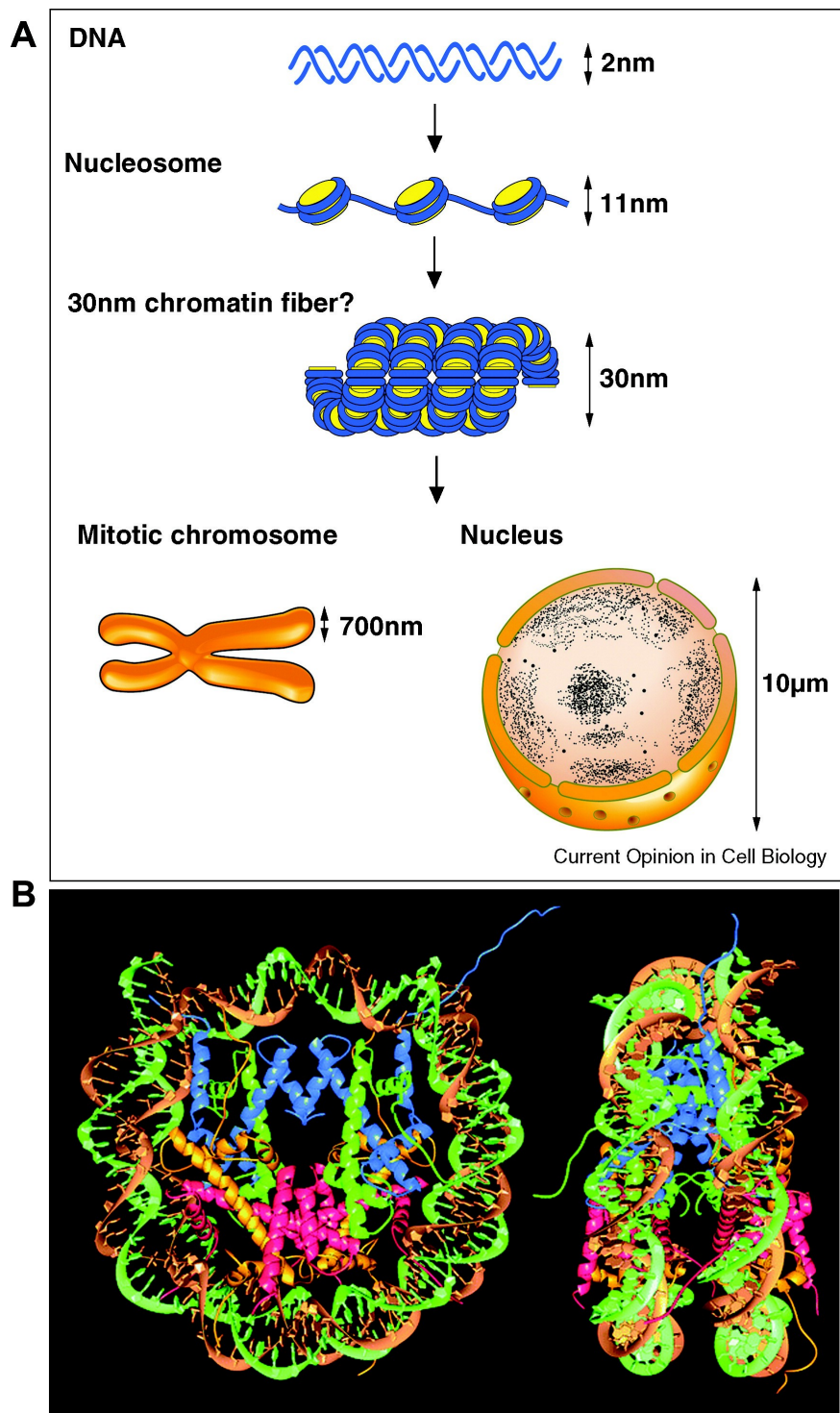
Figure 1.1: A) Different levels of DNA packaging. The first level of DNA packaging is the organization of DNA (blue) and histone proteins (yellow) into nucleosomes. The nucleosomes are then linked by linker DNA and further by the linker histone H1 and organized into higher-order chromatin structures. The existence of the 30-nm fibre in vivo was recently called into question. The final conformation, the chromosomes, are further organized in non-random global genome organization (not shown) (taken from Maeshima et al. 2010). B) Crystal structure of the nucleosome. Front view (left) and side view (right) of the nucleosome is shown. The four main histones H2A (yellow), H2B (red), H3 (blue) and H4 (green) build an octamer and form the core unit of the nucleosome. Approximately ~147 bp of the DNA double helix (light green and orange) are wrapped around the histone core. N-terminal histone tails are protruding from the core of the nucleosome (Luger et al. 1997, modified).

1.2 Epigenetic information

Epigenetic information is 'on top' of the genetic information. Epigenetic information plays a key role in gene regulation and thus regulates the inheritance of functional chromatin states. The word epigenetics refers to heritable changes of gene expression without alterations of the DNA sequence (Berger et al., 2009). Once established, the epigenetic pattern of cells, which is preserved during cell division, is inherited to daughter cells and thus influences gene expression patterns of the progeny as well (Bernstein et al., 2007). However, epigenetic information can be altered with regard to cell differentiation or due to environmental conditions.

The epigenetic information is composed of the chemical modification of cytosine on the DNA and of post-translational modifications (PTMs) of histones. Non-coding RNAs also contribute to the epigenetic information. Methylation of DNA impairs the binding of transcription factors to DNA and thus represses transcription (Robertson, 2005). Moreover, DNA methylation together with non-coding RNAs and histone modifications leads to the formation of heterochromatin (Zaratiegui et al., 2007; Lopez-Serra and Esteller, 2011). In normal cells, the so-called CpG islands, genomic regions which are rich in CpG dinucleotides mostly located proximally to a transcriptional start site, are usually not methylated and thus transcription is maintained. In contrast, transcription of repetitive genomic regions including satellite repeats is repressed by the hypermethylation of DNA (Robertson, 2005). Thus, DNA methylation is an important tool for maintaining genomic stability and proper gene expression. Histone PTMs are a more complex type of epigenetic information than DNA methylation because histones can be modified with different chemical modifications (see 1.2.1). Hence, various modifications are either involved in transcriptional activation or inactivation and heterochromatin formation (see 1.2.4).

1.2.1 Post-translational histone modifications

The N-terminal tails of the core histones H2A, H2B, H3 and H4, together with the C-terminal tail of H2A, are protruding from the nucleosome (Figure 1.1 B). The tails are subject to various post-translational modifications that are established on the respective amino acids of the histone tails, such as methylations, acetylations, ubiquitylations and phosphorylations (Gardner et al., 2011). For example, lysine residues (K) can be methylated or ubiquitylated, arginines (R) can be methylated as well, and serines (S) and threonines (T) can be phosphorylated. Figure 1.2 shows examples of how the N-terminal tails of the histones can be modified.
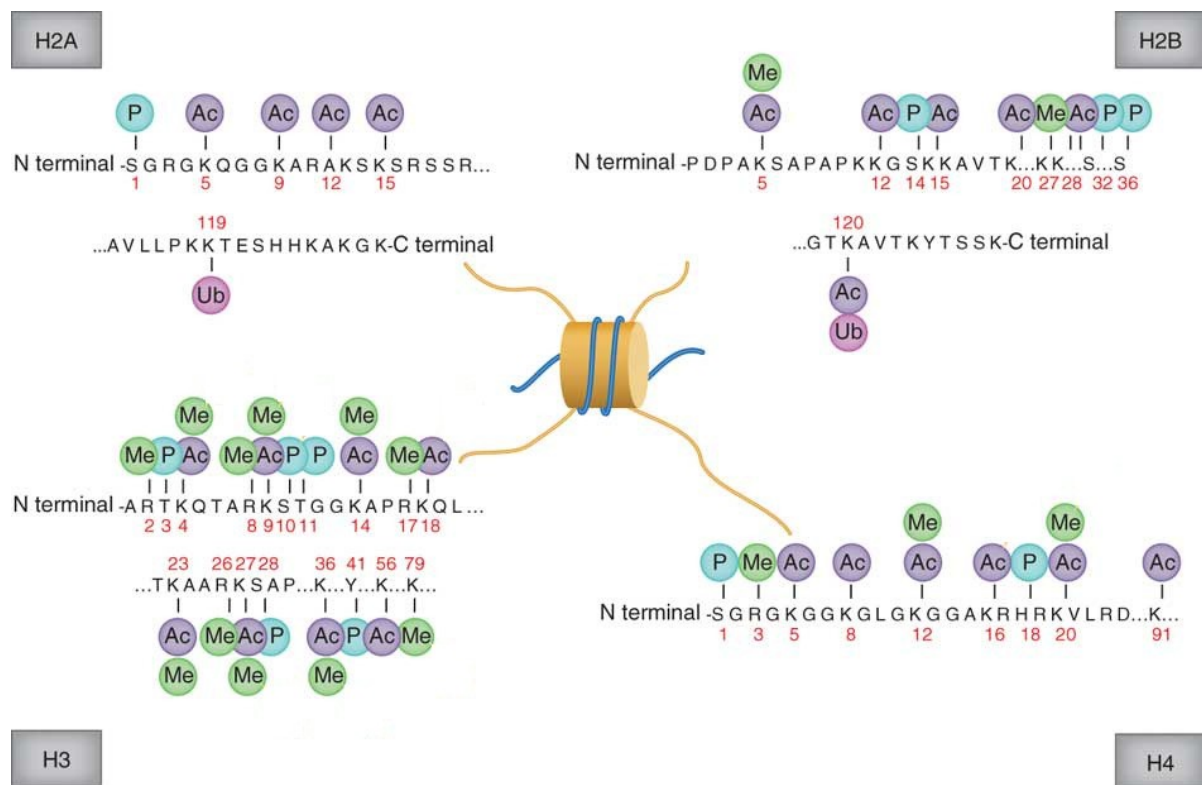
Figure 1.2: Post-translational modifications of the core histones. N-terminal histone tails of the four core histones together with the C-terminal tails of histone H2A and H2B are subject to various post-translational modifications. Shown are the amino acids of the tails of the four core histone (type and position of the amino acid sequence) and the respective modifications. Serines (S) can be phosphorylated (P), lysines (K) and arginines (R) can be either acetylated (Ac), methylated (Me) or ubiquitylated (Ub) (Rodriguez-Paredes and Esteller, 2011, modified).

Histone lysine residues are often subject to acetylation which is associated with an open chromatin status correlating with transcription, whereas deacetylation is associated with a compacted chromatin status correlating with repression (Luebben et al., 2010; Allahverdi et al., 2011). Histone acetylation disturbs the formation of higher order chromatin structures thereby regulating chromatin accessibility and transcription (Tse et al., 1998; Shogren-Knaak et al., 2006). Acetylations are established or removed by specific enzymes which either add acetyl groups (histone acetyltransferases - HATs) or which remove the acetyl groups from the histone tails (Histone deactelyases – HDACs) (Roth et al., 2001; de Ruijter et al., 2003). Thus, these enzymes are parts of transcription regulating complexes.

Compared to histone acetylation, methylation of histone residues is more complex. At first, arginines can be also methylated in addition to lysines. Lysines can be either mono (me1), di (me2)- or trimethylated (me3) and arginines can be either mono or dimethylated (Gardner et al.,

2011). Second, the methylation has diverse outcomes with either activating or repressive functions, depending on its localization on the histone tail. Their influence on chromatin structure and function is mainly dependent on the chromatin-associated proteins which specifically bind the various methylation sites of the histones (Figure 1.3).

Methylation of histones is established by histone methyltransferases (HMTs) (Hublitz et al., 2009). Quite recently, also specific demethylases (HDMs) have been identified, which remove the methyl groups from either arginine or lysine (Shi et al., 2004; Iwase et al., 2007; Klose et al., 2007; Yamane et al., 2007). Table 1.1 gives examples of various histone modifications and their role in the regulation of transcription.

1.2.2 Histone variants

In addition to the four main histones a number of histone variants exist in mammalian cells. These are the H2A-variants H2AX, macroH2A, H2AZ, the H3 variants H3.1, H3.2, H3.3, a testis specific H3(t), and CENP-A, a centromere-specific H3 variant (Yuan and Zhu, 2011). Recently, two new primate-specific H3 variants, H3.X and H3.Y, have been identified (Wiedemann et al., 2010). Histone variants can be deposited or incorporated to regulate the inheritance of chromatin functionality, e.g. during replication or dependent on cell cycle (Dunleavy et al., 2011).

Histone H3 variants are also subject to PTMs (Loyola et al., 2006) and can either carry activating marks, repressive marks or both (Hake et al., 2006). Histone chaperones make use of modified histones and histone variants and are responsible for their proper deposition or incorporation where needed (Elsaesser and Allis, 2010). The distribution and functions of histone H3 variants are still a matter of debate. Recently, the establishment and distribution of H3.3 was investigated in more detail (Goldberg et al., 2010). In this study they show that the H3.3 pattern is dynamic with regard to cell differentiation. Consistent with earlier findings (Hake et al., 2006), they showed that H3.3 overlaps with active histone modifications, such as H3K4me1/me3.

1.2.3 The histone code hypothesis

The observation of a specific histone modification pattern in a biological context led to the so-called 'histone code hypothesis' (Strahl and Allis, 2000; Jenuwein and Allis, 2001). The histone code hypothesis proposes that combinatorial histone marks lead to unique downstream events in a sequential manner or in combination (Strahl and Allis, 2000).

Indeed, many proteins were discovered in the last years that bind specific histone modifications. This includes chromatin binding proteins which recognize a specific modification or proteins which regulate the modification itself. This led to the model of writers, readers and erasers of the histone code (recent review by Gardner et al., 2011). It distinguishes between writers that establish the marks, readers that bind the marks by specific structural domains, and erasers that remove the marks. A misreading of the histone code is linked to oncogenic transformations (Matthews et al., 2007; Wang et al., 2009) or human disorders (Iwase et al., 2011).

The function of a specific histone mark is determined by its reader, whose recognition and binding results in specific downstream events. For example, the transcription-associated factor CHD1 binds H3K4me3, the heterochromatin protein 1 (HP1) binds H3K9me2/me3 and the polycomb group (silencing-) proteins bind H3K27me3 via specific protein binding domains (Taverna et al., 2007) (Figure 1.3). Consequently, these modifications are associated with transcription activation or silencing, respectively (see below). In addition to this, PTMs are not only established on nucleosomal histones, but also mark soluble histones for the nuclear translocation and incorporation (Alvarez et al., 2011).

Histone modification	Regulation of transcription or other functions
H3S10ph	ON, cell-cycle dependent
H2AXS139ph	DNA repair
H3K9Ac	ON
H3K14Ac	ON
H4K16Ac	ON
H3K4me1*/me2/me3	ON
H3K36me3*	ON
H3K56Ac	ON?, DNA repair?
H2BK120ub	ON
H2AK119ub	OFF
H2AK123ub	OFF[1]
H3K79me3	ON?, DNA repair
H3K9me1	ON
H3K9me2/me3	OFF
H4K20me1	ON
H4K20me2	DNA repair
H4K20me3	OFF
H3K27me1	ON
H3K27me3	OFF
H3.1 variant	ON/OFF[2]
H3.2 variant	OFF[2]
H3.3 variant*	ON[2], differentiation*
MacroH2A1.1	DNA repair†
CenpA	Mitosis, DNA repair‡

Table 1.1: Histone modifications and their role in regulation of transcription and other functions as indicated. Information is summarized from (Allis et al., 2007; Barski et al., 2007; Heintzman et al., 2007; Kouzarides, 2007; Rodríguez-Paredes and Esteller, 2011) and references therein, or as indicated; *(Goldberg et al., 2010); †(Timinszky et al., 2009); ‡(Zeitlin et al., 2009). (ph = phosphorylation, Ac = Acetylation; Me = methylation; me1 = mono-, me2 = di-, me3 = trimethylation; ub = ubiquitylation; [1]*S. cerevisiae;* [2]mostly dependent on its decoration with activating or inactivating modifications, respectively).
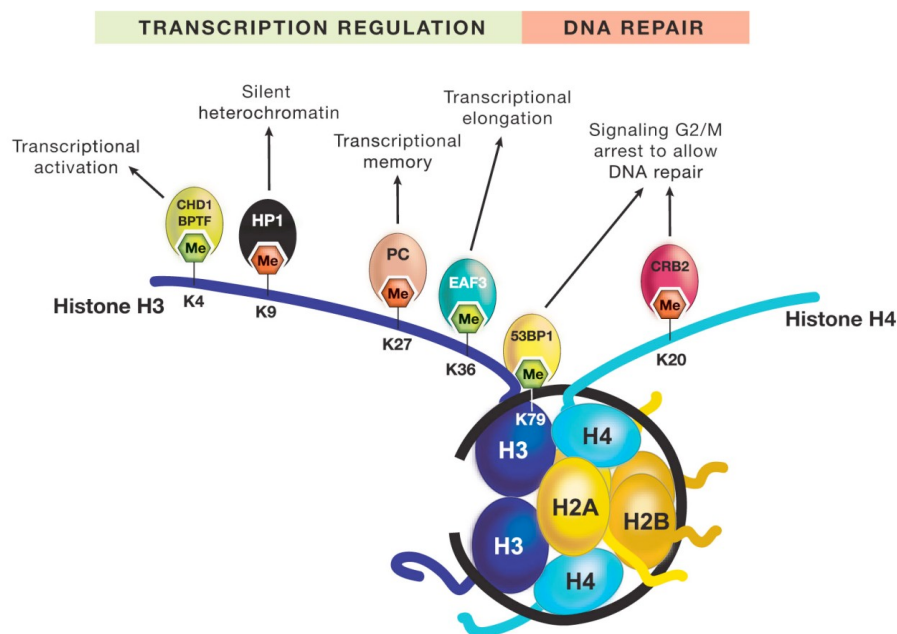
Figure 1.3: Specific recognition of histone methylation on histone H3 and H4 by specific binding proteins. Various methylation marks of the H3 and H4 tails are shown. Green hexagons represent active methylation marks, whereas red hexagons represent repressive histone marks. These marks are recognized by either transcription factors, e.g. CHD1 or BPTF, or by silencing proteins such as HP1 and Polycomb (PC) proteins. Additionally, methylation of H3K79 and H4K20 is bound by 53BP1 and Crb2 (yeast homologue of 53BP1) in the context of DNA repair (Allis et al., 2007).

1.2.4 Role of histone PTMs in transcriptional regulation and silencing

As mentioned above, histone acetylations are associated with transcription, such as the acetylation of H3K14 and H3K9. In addition, several histone methylations are involved in active transcription (see Table 1.1). For example, H3K4me3/me2 is found at transcriptional start sites (TSS) of active promoters and coincides with active RNA Polymerase II (Barski et al., 2007; Heintzman et al., 2007). An additional active histone mark is H3K36me3 (Barski et al., 2007). It was shown that subunits of transcription factors directly bind to acetylated or one of the above mentioned methylated histones (Gardner et al., 2011). For example, H3K4me3 is bound by the TAF3-subunit of TFIID (Vermeulen et al., 2007) and an abrogation of these modification patterns lead to decreased transcription of the respective promoters.

Besides histone marks which are associated with transcription, other marks are involved in gene silencing. Gene silencing involves three major steps, (i) the initial recruitment of the respective silencing factors to the target sites, (ii) the inhibition of transcription, and (iii) the establishment of an epigenetic information that passes the silenced status to the progeny (Beisel and Paro,

2011). The importance of histone modifications in theses processes is supported by the fact that histone modifying enzymes such as HATs, HDACs, HMTs and HDMs are components of these silencing 'machineries'. Gene silencing is mediated through two major silencing pathways, the Polycomb-mediated silencing and the heterochromatin (HC) pathway (Campos and Reinberg, 2009; Beisel and Paro, 2011).

The two pathways are associated with different histone modification patterns. Formation of constitutive heterochromatin is associated with the methylation of H3K9 and the binding of heterochromatin protein 1 (HP1) (Probst and Almouzni, 2011). For the formation of constitutive pericentric HC, HP1 binds H3K9me2/me3 with its chromodomain (Bannister et al., 2001; Lachner et al., 2001). After this, the chromoshadow domain of HP1 is involved in its dimerization which probably mediates higher-order chromatin compaction (Thiru et al., 2004). In addition to this, trimethylation of H4K20 contributes to pericentric heterochromatin formation (Schotta et al., 2004).

In contrast, facultative heterochromatin is marked by heterochromatin proteins which repress a certain target gene in an euchromatic environment (Beisel and Paro, 2011). Polycomb-group proteins (PcG) repress specific target genes which are marked with H3K27me3 (Kirmizis et al., 2004).

1.2.5 Epigenetic alterations and tumor development

As described above, epigenetic information regulates gene expression by its main tools, DNA methylation and histone modifications. Since gene expression patterns are aberrantly altered in cancer cells, a link to epigenetic alterations is given. Indeed, in many cancer cell types, checkpoint activation and growth inhibition is aberrant due to the activation of oncogenes or the repression of tumor suppressor genes, most probably dependent on epigenetic alterations (Berdasco and Esteller, 2010).

For example, at DNA level, local and global hypomethylation is observed in cancer cells. Local hypomethylation of promoter regions may lead to activation of oncogenes which are usually silenced. Likewise, global hypomethylation of CpG islands or repetitive sequences results in genomic instability (Baylin and Ohm, 2006). On the other hand, local hypermethylation of promoters of active genes may cause silencing of tumor suppressors, such as p53 or the G1 inhibitor p16 (CDKN2A) (Baylin and Ohm, 2006). This aberrant gene regulation at the first step followed by further mutations resulting in genetic and epigenetic instability, led to the model of

the epigenetic progenitor cell of cancer (Feinberg et al., 2006). This model suggests that initial epigenetic alterations are paving the way for further mutations leading to malignant tumors.

Similarly, histone modification patterns are altered in cancer cells. For example, global hypoacetylation of H4K16 and global hypermethylation of H4K20 were observed (Fraga et al., 2005). Other combinatorial alterations of PTMs together with DNA hypermethylation occur at promoter regions of tumor suppressor genes, such as the deacetylation of histone H3 and H4, loss of H3K4me3, and, in contrast, gain of H3K9 and H3K27 methylation (Jones and Baylin, 2007; Berdasco and Esteller, 2010). Additionally, a number of enzymes involved in regulating histone modifications are overexpressed or mutated in various tumor types (see Berdasco and Esteller, 2010, for review).

On the one hand, irradiation of tumors in radiotherapy is used to eliminate malignant cells from healthy tissues utilizing the lethal effect of radiation on cells (see 1.3). On the other hand, enhanced tumor incidence in humans after radiation exposure during the second world war or due to accidents of nuclear plants show the carcinogenic risk of radiation exposure (Kovalchuk and Baulch, 2008). Carcinogenesis is also a severe side-effect of radiotherapy. Beside direct effects of radiation on the DNA, such as double-strand breaks which may cause mutations if misrepaired, epigenetic alterations induced by radiation might contribute to such oncogenic transformations and disregulations. Moreover, this fact is supported by radiation effects observed in bystander cells and tissues (Kovalchuk and Baulch, 2008). Indeed, radiation induces global DNA hypomethylation (Mothersill and Seymour, 2003; Streffer, 2010). Additionally, a number of global and local alterations of the epigenetic information have been reported as a consequence of radiation exposure (Pogribny et al., 2005; Koturbash et al., 2006). This links radiation-induced epigenetic alterations to carcinogenesis (Koturbash et al., 2005; Loree et al., 2006). However, exactly how radiation leads to cancer, and to what extent epigenetic alterations contribute to it, is not fully understood (Barcellos-Hoff and Nguyen, 2009).

1.3 Cellular response to radiation damage

Each day human cells encounter a large number of DNA lesions which have to be repaired effectively (Jackson and Bartek, 2009). DNA lesions can develop from physiological processes, such as DNA mismatches, hydrolytic reactions and attack by reactive oxygen species. These lesions result in impaired base pairing, impaired DNA replication and transcription, and in base damage or DNA single strand breaks (SSBs). These lesions can mostly be repaired in an error-

free manner when the complementary DNA strand is available. An additional DNA-damaging agent is ultraviolet (UV) light, which induces bulky lesions and UV photo-products. UV-induced damage is repaired by nucleotide excision repair (NER) (Jackson and Bartek, 2009).

DNA double-strand breaks (DSBs), however, are most severe lesions because, first, they are difficult to repair because the complementary strand is also damaged, and second, because inefficient repair can lead to cell death or genomic instability (Mothersill and Seymour, 2003). DSBs can be induced by physical agents, such as ionizing radiation (IR), oxidative stress, and aberrant DNA replication, or by V(D) recombination or chemical agents, such as topoisomerase I inhibitors (Kinner et al., 2008). IR is a major factor in DSB induction to which humans are exposed due to medical applications such as x-ray and radiotherapy, or due to environmental conditions (Kovalchuk and Baulch, 2008). Thus, the cells have evolved basic mechanisms to efficiently recognize and repair those DNA lesions in the DNA damage response (DDR) (Jackson and Bartek, 2009).

The induction of DSBs initiates various signaling cascades which lead to the main actions of the DDR, namely repair, cell cycle arrest or apoptosis. Three major initiators of DSB repair that are involved in the early recognition of the breaks are the protein kinases ATM (Ataxia telangiectasia mutated), ATR (Ataxia telangiectasia and Rad-related) and the MRN protein complex (see below). ATM/ATR target the protein kinases CHK1 and CHK2 involved in cell-cycle checkpoints, and reduce the levels of cyclin-dependent kinases (CDK) by mechanisms which include the activation of the tumor suppressor p53 (Kastan and Bartek, 2004; Riley et al., 2008).

1.3.1 DSB repair mechanisms

DSBs are repaired by two major pathways, the non-homologous end-joining (NHEJ) pathway, and the homologous recombination (HR) pathway (reviewed in Lieber, 2008; San Filippo et al., 2008). NHEJ can occur in all phases of the cell cycle, whereas HR is restricted to S and G2 phase because it uses the sister chromatid as a template. The major protein components of the NHEJ pathway are the Ku proteins (Ku70/Ku80) that bind and activate the catalytic subunit of DNA-dependent protein kinases and then recruit end-processing enzymes, polymerases and ligase (DNA ligase IV). In contrast, within HR, DSBs are recognized by the MRN (Mre11-Rad50-NBS1) complex which generates single-strands that are then bound by RPA (replication protein A), Rad51 and Rad52. After this, they invade the homologous template, build D-loops and a Holliday junction and finally restore the DNA (Misteli and Soutoglou, 2009).

An important event in the initiation of DSB repair is the phosphorylation of the histone variant H2AX at serine 139 by the ATM/ATR/DNA-PK protein kinases (Rogakou et al., 1998). The initial steps of the DDR have been an open question for a long time. Recently, the involvement of chromatin structure and histone modifications in the early recognition of DSBs was shown (Kim et al., 2009b; Sun et al., 2009). In this model, ATM is targeted to DSB sites via the MRN complex (Williams et al., 2007; Sun et al., 2010), which also targets the acetyltransferase Tip60 to DSBs via histone H3 interactions (Sun et al., 2009). Tip60 then acetylates ATM and thus induces its kinase activity (Sun et al., 2005). At the same time, autophosphorylation of ATM leads to the dissociation of its inactive dimers (Bakkenist and Kastan, 2003) and to the subsequent phosphorylation of H2AXS139 by ATM. The phosphorylated form of H2AXS139 is called γ-H2AX and is a commonly used marker for DSBs. The initiation and recruitment of the repair machinery and other chromatin-modifying proteins by γ-H2AX promotes DSB repair and amplifies the signaling (Figure 1.4).

An additional major component of DSB repair initiation is MDC1 (mediator of DNA damage checkpoint 1) (Stewart et al., 2003), a protein which is quickly recruited to DSBs and binds γ-H2AX (Stucki et al., 2005). MDC1 promotes further recruitment of ATM and MRN complexes which leads to the spreading of γ-H2AX over approx. 2 Mbp around the break (Kinner et al., 2008) (Figure 1.4). In addition to this, the checkpoint protein 53BP1 (p53-binding protein 1) is recruited to damaged sites in a MDC1-dependent manner (Bekker-Jensen et al., 2005).

Additionally, the methylation of histone H3 at lysine 79 is probably responsible for the binding of 53BP1 at DNA damage (Huyen et al., 2004), although the involvement of the histone modification is still under debate (FitzGerald et al., 2011; Tatum and Li, 2011). Further ubiquitinating proteins are involved in recruitment and tethering of damage response proteins, such as the ubiquitin ligase RNF8, the E2 conjugating enzyme Ubc13, which ubiquitylates H2A at lysine 63 (Huen et al., 2007; Mailand et al., 2007), and RNF168 (Pinato et al., 2009). Ubiquitylations were shown to stimulate the recruitment of additional 53BP1, as well as the BRCA1-BARD1 complex (Figure 1.4). Most of the mentioned proteins that are recruited to DSB sites to a larger extent, such as ATM, MDC1, NBS1, and 53BP1, are so-called foci forming proteins. Thus they can be visualized as irradiation-induced foci (IRIF) at DSB sites by simple immunodetection or live-cell imaging.
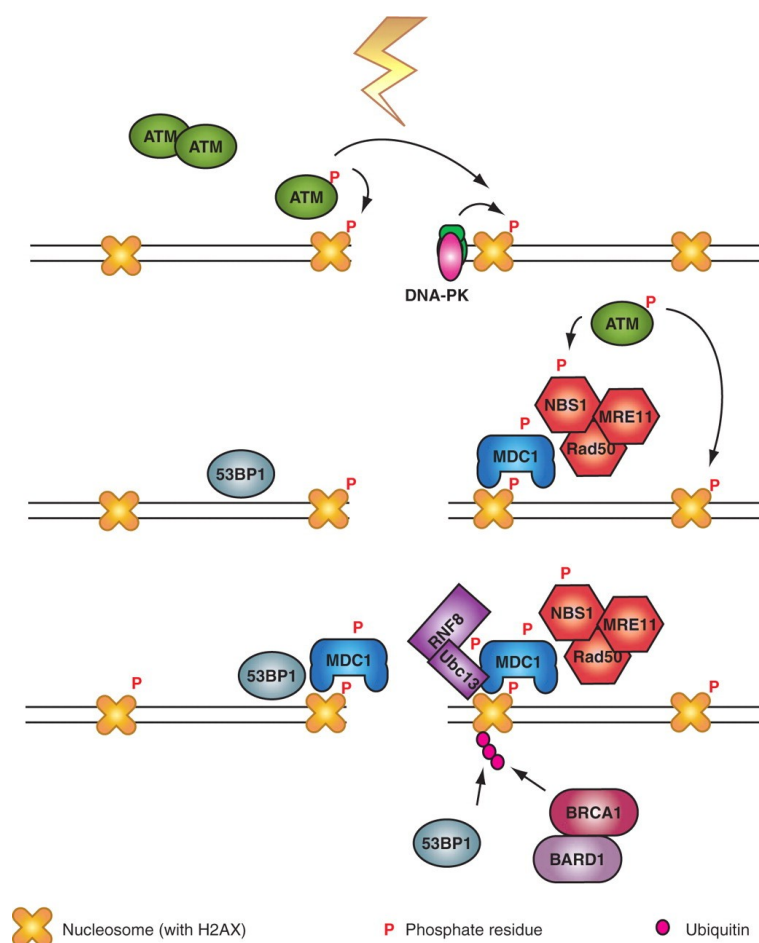
Figure 1.4: Initiating steps after DNA double-strand break induction. The histone variant H2AX is phosphorylated (γ-H2AX) by the protein kinase ATM or DNA-PK in an early onset of the DNA damage response. By this, MDC1 is recruited and further activates ATM which leads to a wide-spread phosphorylation of H2AX around the DSB. 53BP1 and the MRN (Mre11-Rad50-NBS1) complex and additional downstream mediators, such as RNF8 and BRCA1, are recruited. RNF8 mediates the polyubiquitylation of H2A (taken from Kinner et al. 2008).

1.3.2 Access – repair – restore model

The access – repair – restore model (ARR) (Green and Almouzni, 2002) is based on earlier findings that showed global hyperacetylation of nuclear proteins including histone proteins following UV-induced DNA damage (Ramanathan and Smerdon, 1986). The ARR model suggests that chromatin itself is inhibitory to repair due to its compaction and hence, chromatin-opening is necessary to allow the DNA repair machinery to find and repair the lesions. However, following repair, the previous chromatin status has to be re-established (Green and Almouzni, 2002). In this context, chromatin remodelers were shown to be involved in chromatin assembly and disassembly during NER in UV-damaged mammalian cells and in yeast (Green and

Almouzni, 2003; Linger and Tyler, 2005). Moreover, p53-mediated global chromatin decondensation, as well as histone H3 acetylation by the HAT p300 indicated the necessity of chromatin relaxation for efficient repair (Rubbi and Milner, 2003). More recently, evidence for hyperacetylation of histone H4 (Murr et al., 2006) and local chromatin decondensation after damage induction in mammalian cells has been reported (Kruhlak et al., 2006; Ziv et al., 2006). (Murr et al., 2006) showed that the hyperacteylation of histone H4 by the HATs Trrap and Tip60 is necessary for chromatin relaxation and the accumulation of repair factors, such as 53BP1, Rad51 and BRCA1. These findings raised the question if a histone code exists for the DNA damage response (van Attikum and Gasser, 2005).

1.3.3 A histone code for the DNA damage response?

A well-known histone modification involved in the DDR is the phosphorylation of H2AX, as mentioned above. However, this modifications seems to be quite unique for the DDR with no further known functions in transcription or repression. The hyperacetylations observed after damage induction were primarily attributed to their function in chromatin opening, rather than to their role in transcription factor binding (Campos and Reinberg, 2009). In contrast, methylated H3K79, which is associated with active genes (Kouzarides, 2007), was implicated in the DDR by recruiting the checkpoint protein 53BP1 (Huyen et al., 2004). On the other hand, histone modifications associated with heterochromatin, such as H4K20 methylation (Botuyan et al., 2006) and H2A ubiquitylation (Huen et al., 2007; Mailand et al., 2007), are also involved in DSB repair. Interestingly, 53BP1 interacts with dimethylated H4K20, but not with the trimethylated form (Botuyan et al., 2006). Other damage responsive histone modifications, such as ubiquitylation of H3 and H4 have been reported, but the function of these modifications is still unknown (Wang et al., 2006).

In the meantime, global alterations of PTMs and DNA methylation were reported (Pogribny et al., 2005; Koturbash et al., 2006). Here, global loss of H4K20me3 was observed in the murine thymus after irradiation of mice (Pogribny et al., 2005), and loss of DNA methylation and enzymes mediating DNA methylation (Koturbash et al., 2005; Koturbash et al., 2006). In addition to this, the distribution of repair foci in respect to chromatin compaction was extensively analyzed (Costes et al., 2007; Karagiannis et al., 2007) while PTMs were used to distinguish HC from EC regions (Cowell et al., 2007; Goodarzi et al., 2008). Only a few studies analyzed local alterations of PTMs at DSB sites with regard to their function in transcription or

repression (Falk et al., 2007; Solovjeva et al., 2007). Interestingly, (Solovjeva et al., 2007) observed mutual exclusion of nascent RNA and γ-H2AX foci which suggests that transcription is inhibited at DSB sites. However, they were not able to detect alterations in the H3K9me3 pattern at DSB sites, suggesting that inhibition of transcription was not associated with HC formation (Solovjeva et al., 2007).

From the results of (Solovjeva et al., 2007) it can be hypothesized that marks associated with transcription are altered in the vicinity of DSBs. Indeed, preliminary experiments conducted before the onset of this thesis did hint at an under-representation of the histone mark H3K4me3 at ion microirradiation-induced DSB sites (C. Ottmann and H. Strickfaden, personal communication). Consequently, the question arose if a general repressive pattern is established at DSB sites which goes along with the loss of active marks. Although (Solovjeva et al., 2007) relied on a measure of correlation of intensities, the lack of robust quantification methods to determine enrichment or, particularly, losses of respective PTMs from DSB sites, limited the possibility to study such alterations in fluorescence images. This prompted the need for a robust quantification method for fluorescence images that not only quantifies co-localization, but also alterations such as losses of respective marks from specific sites in the cell nucleus.

1.4 Fluorescence microscopy

1.4.1 The Abbe limit in conventional microscopy

The most common fluorescence imaging methods are wide-field and confocal microscopy (Fernández-Suárez and Ting, 2008). By this, fluorescence-labeled cellular and nuclear structures are visualized and proteins or other molecules can be tracked. However, the resolution of these conventional microscopes is limited. The limitation results from optical features first described by Ernst Abbe (Abbe limit) in 1873. The Abbe limit describes how the optical resolution depends on the wavelength (λ) and the numerical aperature (NA) of the optical lens of a microscope (Fernández-Suárez and Ting, 2008). This is why focused light always appears as a blurred spot. The size of the spot is equal to the limit to which a single spot can be dissolved. The point spread function (PSF) is a measure to define the size of the spot (Fernández-Suárez and Ting, 2008).

The resolution of conventional confocal microscopes is thus limited to about 200 nm in x,y- and 600 nm in z-direction (Rouquette et al., 2010 and references therein). To circumvent the resolution limit, super-resolution microscopes are being built (Schermelleh et al., 2010). Still,

conventional optical sectioning in fluorescence microscopy offers the opportunity to gain a 3D view of the analyzed object (Conchello and Lichtman, 2005).

1.4.2 Overview of tools to analyze fluorescence microscopy images

One possibility to analyze changes of epigenetic information located at damaged chromatin is the analysis of images obtained by fluorescence microscopy. For this, DSB are visualized by detection of γ-H2AX in the one channel and the protein or modification of interest is detected with a specific antibody in the other channel. To address the question whether a signal is lost or enriched at γ-H2AX foci, pixel pairs, which means pixels of the two channels sharing the same x- and y-coordinate, had to be analyzed for their correlation. The terms co-localization, contra-localization or anti-correlation and random distribution can be used to describe the relation of pixel pairs in two corresponding channels.

In (Ronneberger et al., 2008), co-localization is defined as "if the centers of two objects labeled by different fluorochromes tend to be situated at a distance notably smaller than the characteristic size of these objects [...] then these objects co-localize". Visually, an overlay of two objects in the red and the green channel will result in a yellow dye and will indicate co-localization (Bolte and Cordelières, 2006). However, this method simply shows co-localization of one object to the other and does not give any information about the degree of co-localization or the 3D situation (Bolte and Cordelières, 2006). Besides co-localization, two other situations are possible. These are exclusion (contra-localization or anti-correlation) and random distribution. Among these, other mixed relations occur such as partial correlations which can be dependent on or independent of each other (Bolte and Cordelières, 2006). Visual observation of co-localization by the researcher might not be precise and objective enough, which is why a list of automated programs exist. To estimate co-localization in a qualitative and quantitative way, different coefficients can be used:

Pearson´s correlation coefficient

Pearson´s correlation coefficient Rr (Rodgers and Nicewander, 1988) is often used to determine the degree of correlation between two objects and was adapted for microscopic analysis by (Manders et al., 1992). Rr adopts values between +1 and -1, which indicate perfect correlation and perfect anti-correlation, respectively. Perfect correlation means that the highest value in channel 1 is correlated with the highest value in channel 2, the second highest value in channel 1

is correlated with the second highest value in channel 2 and so on. In objects obtained from biological systems, this cannot be assumed because, first, in assumption of a perfect situation, two physical objects cannot occupy exactly the same space (French et al., 2008) and second, a biological meaning of such perfect correlations is questionable (Costes et al., 2004). Additionally, a linear relation of signal intensity, which would be expected to increase linearly with the number of macromolecules, cannot be guaranteed in optical images (French et al., 2008). A large number of pixels have low intensities, which strongly influences Pearson´s Rr. In the case of histone modifications, their distribution within the nucleus varies depending on chromatin structure (Ronneberger et al., 2008; Shilatifard, 2008). Signals of low intensity can reflect true signals where the concentration of the respective object is low and thus need to be distinguished from background signals leading to a threshold-dependency of Pearson´s coefficient. Further a large number of low signals has strong influence on Pearson´s correlation coefficient and disturbs the generation of highly negative values (Ronneberger et al., 2008). By and large, Pearson´s correlation coefficient helps to give an impression about the correlation of two objects.

Manders´ coefficients

Another coefficient suggested for co-localization measurement is the Manders´ overlap coefficient R (Manders et al., 1993). The coefficient is based on Pearson and adopts values between 0 (perfect anti-correlation) and +1 (perfect correlation). A disadvantage of Manders´ R is the dependency on a more or less equal amount of pixels that contribute to the analysis. For example, if the number of pixels in channel 1 is significantly lower than in channel 2 but all pixels in channel 1 are completely overlapping, the coefficient would result in a value smaller than 1, because pixels in channel 2 would not have enough counterparts in channel 1. The Manders´ Colocalization Coefficients (M1 and M2) additionally describe the percentage of overlap for two objects (Manders et al. 1993). Manders´ coefficient R, and as well M1 and M2, suffer from the fact that signal intensities are not considered and the overlap of a strong red signal with a low green signal is equalized with the overlap of two strong red and green signals. Depending on the question to be analyzed, this might, however, also be assumed as an advantage, in case one wants to perform co-localization measurement regardless of intensity distribution (Bolte and Cordelières, 2006).

Intensity Correlation Analysis and Quotient

To take the influence of intensities into account, (Li et al., 2004) proposed the Intensity Correlation Analysis (ICA), where the *Product of the Differences from the Mean* (PDM) for each pixel is calculated. PDM is defined as PDM = (A-a)*(B-b) with A being the intensity of a pixel in channel A and a being the mean of all intensities in channel A (for a detailed description see chapter 4.10). It is assumed that if two fluorochromes co-localize, they both will be either above or below the mean level at a given position. For quantitative measure, the Intensity Correlation Quotient (ICQ) calculates the relation of pixels with positive PDM values to the total number of pixels. With this analysis, correlation can be determined in a quantitative and qualitative manner also for image stacks. However, ICA is also threshold-dependent (Ronneberger et al., 2008).

Spearman´s rank correlation coefficient

An alternative statistical measure for pixel correlations in fluorescence images is the Spearman´s rank correlation coefficient ρ (proposed by French et al., 2008). Here, the data are ranked and sorted in an ascending order. A rank is attributed to each data point, which indicates its position in the sorted list. This means that each pixel intensity is given a rank, by which, for example, higher intensities can be attributed to a higher rank. This makes the Spearman´s coefficient ρ less sensitive to outliers and independent of linear relation between the data, in contrast, for example, to Pearson´s coefficient. The plug-in JACoP (Just Another Colocalization Plug-in) used by (French et al., 2008) lists both Pearson´s and Spearman´s correlation coefficients. However, it was implemented primarily to determine co-localization rather than anti-correlation (Bolte and Cordelières, 2006).

The described methods offer the possibility to analyze pixels in fluorescent images for their correlation. It should carefully be determined which method is best suited for the situation in question. For statistical significance of the obtained data different methods where established to test coefficients for their reliability by comparison with randomly generated images (van Steensel et al., 1996; Costes et al., 2004). Additionally, commercially available programs were generated for automated analysis. Those programs are primarily designed for co-localization analysis rather than other situations such as anti-correlation (e.g. the software Imaris provided by Bitplane). As reviewed by (Ronneberger et al., 2008) and others, problems and pitfalls during image acquisition and processing such as chromatic shift, cross-talk of fluorochromes,

deconvolution and threshold-setting have strong influence on this kind of analysis and should be treated with care.

1.5 Aims of the present work

Recent findings report a role for histone modifications in DNA repair (Murr et al., 2006). Furthermore, the efficiency of repair is also dependent on DNA architecture (Kruhlak et al., 2006; Ziv et al., 2006). One important histone modification involved in DNA repair is the histone variant H2AX which is rapidly phosphorylated at serine 139 (called γ-H2AX). γ-H2AX can be visualized by immunofluorescence staining of cells and DNA double-strand breaks are thereby visualized as so-called irradiation-induced foci (IRIF).

The aim of the present work was to investigate whether alterations of histone modifications occur at chromatin regions decorated with γ-H2AX. Damage was induced by targeted ion microirradiation of human cells. With fluorescence microscopy techniques, DNA damage (γ-H2AX foci) and the histone modification in question were visualized and images were analyzed for local changes occurring at the damaged site.

The first challenge of the present work was to find a reliable analysis method that could evaluate alterations qualitatively and quantitatively, including cases which are rarely discussed, such as random distribution or anti-correlation. An additional requirement to the analysis was to consider the evaluation of image stacks of the cell nucleus.

Second, to improve the analysis of fluorescence images in the present work, I established a new method, namely ultrathin sectioning of fixed and stained cells into 150-nm ultrathin sections for subsequent confocal microscopy.

With help of the established approaches, major questions with regard to alterations of histone modifications at damaged DNA were investigated:

Do alterations of histone modification patterns occur in the vicinity of DSB sites that hint at an establishment of transcriptional silencing ? If so, which players are involved? In addition, are active marks lost from these sites?

Does the DSB-induced silencing resemble one of the known silencing pathways?

Which potential mechanisms might contribute to DSB-induced silencing at damaged chromatin?

2 Results

2.1 Evaluation of Intensity Correlation Analysis for image stacks

As described in 1.4.2, a variety of simple or more advanced methods exist to determine correlations of pixels in two fluorescence images. In the present work, histone modifications and other candidate proteins were analyzed for alterations at radiation-induced DSB sites, which are marked by γ-H2AX. For this, it was necessary not only to use methods which can identify co-localization, but also to evaluate methods which can identify a decrease or a loss of a marker from the DSB sites. For this, I thoroughly tested various freely available plug-ins (*Colocalization Finder, Colocalization Test, Mander´s Coefficient*, and *JACoP,* all by ImageJ) and also the commercially available software Imaris (Bitplane Scientific Software). These plug-ins either use a simple overlay technique to highlight co-localized pixels or determine Manders´ and Pearson´s coefficients. Among these approaches, the Intensity Correlation Analysis (ICA) proposed by (Li et al., 2004) turned out to be most suitable to determine also negative correlations in addition to positive correlations. Using ICA, these correlations can be visualized and quantified, although quantification faces some difficulties. In the following, I will describe the evaluation by ICA for various applications and I will describe why other approaches and coefficients, such as Pearson´s and Manders´ coefficients, were not suitable for the questions investigated.

2.1.1 Measuring co-localization and anti-correlation

Detection of histone modifications by immunofluorescence results in an inhomogeneous, pan-nuclear staining pattern. This pattern is an outcome of the specificity of the histone modification dependent on chromatin function, for example heterochromatin and euchromatin. These regions of the nucleus are characterized by different chromatin density and are marked with different histone modifications (Zinner et al., 2006). Figure 2.1 shows ICA for two histone modifications in correlation with chromatin density, as determined by DAPI staining, performed for five optical mid-sections of the nucleus (five optical slices which are each 250 nm apart). The two well-described histone modifications H3K9me2 and H3K4me3 correlate with chromatin architecture and function in an opposite way. H3K9me2 is found in silent regions situated predominantly in heterochromatin, where chromatin density is high, whereas H3K4me3 marks transcriptionally

active chromatin where chromatin density is low (reviewed in Shilatifard, 2008). Thus H3K9me2 staining pattern and DNA counter staining with DAPI were expected to strongly co-localize. This is demonstrated in Figure 2.1 A. Here, ICA was performed for the green (histone modification) and the blue (chromatin) channel. In the PDM map, the PDM values are color-coded (Figure 2.1 A,B mid rows). Green staining represents positive correlation (co-localization) and pink staining represents negative correlation (contra-localization). In the PDM image in Figure 2.1 A, bright green staining represents areas which are enriched in H3K9me2 and also enriched in DAPI. PDM values are positive indicating co-localization of the two staining patterns. This is also demonstrated in the PDM plots, where each PDM value is plotted against the intensity of the corresponding pixel and values of high intensity are skewing to the positive range. The waistline in the PDM plots represents the mean value of intensities. The scatter plot further indicates positive correlation for pixel intensities of both channels. In Figure 2.1 B, ICA was performed for H3K4me3 and DAPI, the staining patterns of which were expected to be strongly anti-correlated. In the PDM image, negative PDM values represented by pink color are predominant. Despite some areas marked by green color where some pixel pairs are co-localized, for example the area close to the nucleoli where both staining intensities are low, the PDM image in Figure 2.1 B shows strong anti-correlation. However, PDM plots show that PDM values are only slightly negative or even close to zero. This results from a large number of pixels with low intensities which are close to the background. They decrease the mean value and thus influence the PDM value. Additionally, a pixel pair with comparable low intensities in both channels still results in a positive PDM value, which makes it even more difficult to gain negative values. The scatter plot in Figure 2.1 B represents anti-correlation of most pixel intensities with a few positively correlated pixels.

The above described examples show that ICA is suitable to visually represent correlations between histone modification and chromatin (Figure 2.1 A,B). PDM maps color-code the correlation between pixels and thereby enable a fast and simple way to detect correlations of pixels in different regions of the nucleus. However, the source code implemented by the plug-in normalizes the PDM values to the maximum gray value obtained in the respective channel. Thus, same color in different images might represent a different degree of correlation. PDM- and scatter plots demonstrate the distribution of intensities and PDM values and thus correlations for pixels with high intensities, which are of highest interest, can be assessed quickly. The ICA plug-in calculates additional coefficients, as shown in the following chapter.
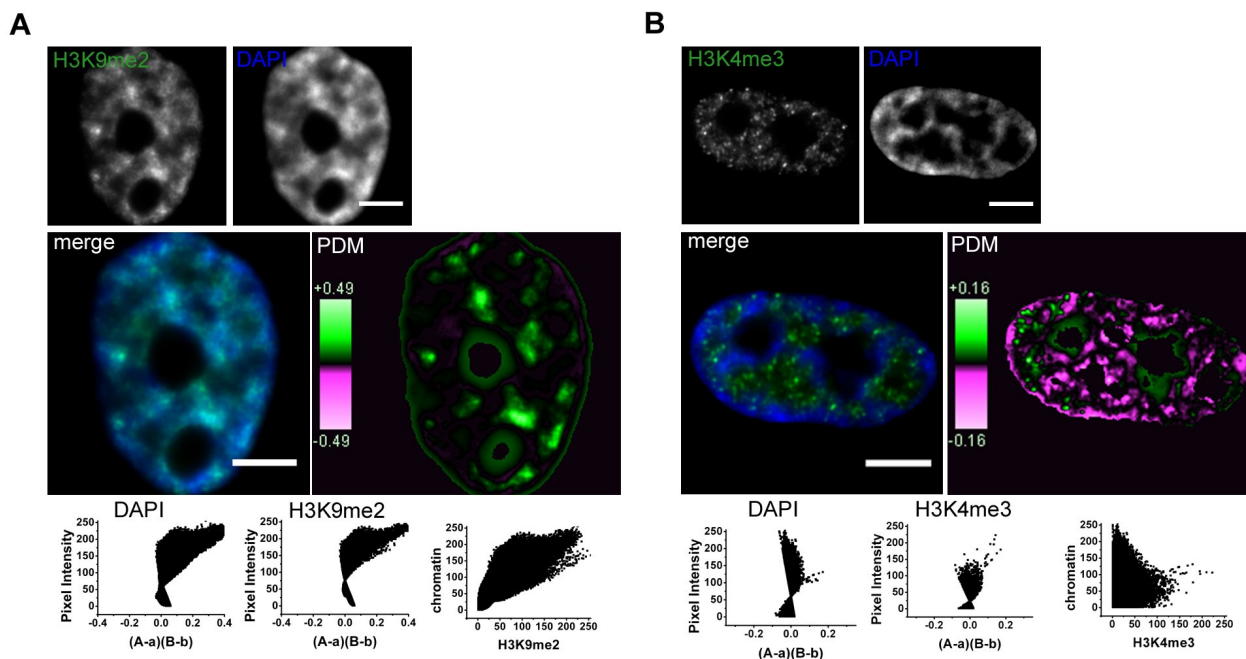
Figure 2.1: Intensity correlation analysis of histone modifications and chromatin. A) Positive correlation between H3K9me2 and chromatin and B), negative correlation of H3K4me3 and chromatin. Upper rows in A) and B) show single slices of green and blue channel after 3D epifluorescence microscopy. Mid rows show green-blue merge image and the PDM color-coded map, where positively correlated pixel pairs are represented in green and negatively correlated pixel pairs are represented in pink. Bottom rows show the PDM plots where PDM values were plotted against their corresponding pixel intensity for channel 1 and channel 2 (left and middle plot). The scatter plot on the right indicates the distribution of intensities of the two channels. PDM values were calculated from five mid-sections with clear staining. In A), bright green staining in the PDM image marks regions where H3K9me2 and DAPI are enriched and thus are highly correlated. In both PDM plots, PDM values of high intensities are skewing to the positive range indicating co-localization. B) Bright pink staining in the PDM image marks areas where either H3K4me3 or DAPI is enriched and intensities of the adverse channel are low, showing that they are anti-correlated. This is also represented by the PDM plots, where PDM values of high intensities are negative in the DAPI channel and close to zero in the green channel, despite a few overlapping pixels. Scale is 5 μm.

2.1.2 Correlation coefficients for quantitative analysis

For quantification and statistical analysis, Intensity Correlation Quotient (ICQ) was proposed by (Li et al., 2004), for which the relation of pixels with a positive PDM value to the total number of pixels is calculated. From this value 0.5 is subtracted to obtain the ICQ, which is thus distributed between +0.5 to -0.5 (Li et al., 2004). Additional coefficients calculated by the ICA plug-in for the above described situations are listed in Table 2.1. In chapter 1.4.2 an overview of different coefficients is given. These are Pearson´s correlation coefficient Rr with +1 for perfect correlation and -1 for perfect anti-correlation, Manders´ overlap coefficient R with +1 for perfect correlation and 0 for perfect anti-correlation, and Manders´ colocalization coefficients M1 and M2 which indicate the percentage of overlap of one channel to the other. The positive correlation

of H3K9me2 and DAPI (chromatin) shown in Figure 2.1 A is represented by a strong positive Pearson´s correlation coefficient with Rr = 0.858 and a strong positive Manders´ overlap coefficient with R = 0.96. Manders´ colocalization coefficients M1 and M2 are M1 = 1 and M2 = 0.99. By contrast, ICQ is only slightly positive with ICQ = 0.34. The maximum value for perfect correlation would be 0.5 and for perfect anti-correlation -0.5. In the lower panel of Table 2.1, the results for the negative correlation of H3K4me3 and chromatin demonstrated in Figure 2.1 B are shown. Here, Pearson´s and Manders´ coefficients show lack of positive correlation by more negative values. However, they are still close to zero for Pearson´s Rr = -0.04 and closer to 0.5 for Manders´ R = 0.67, respectively, representing random distribution. Manders´ M1 and M2 both yield a high value close to 1, which would indicate 100% overlap. This shows that M1 and M2 are not suited for that kind of analysis, because low intensities of one channel overlap with high intensities in the other channel and thus result in high overlap, although, when considering their intensities, they are anti-correlated. Also Pearson´s and Manders´ coefficients do not represent the negative correlation expected from the images (Figure 2.1 B). The ICQ calculated for the negative correlation of H3K4me3 and DAPI (chromatin) was also close to zero, with a value of ICQ = -0.02 suggesting random distribution.

Sample	Rr Pearson [-1, 1]	R Manders [0, 1]	ch1:ch2	Manders´ M1 [0, 1]	Manders´ M2 [0, 1]	ICQ [-0.5, 0.5]
H3K9me2 and DAPI	0.858	0.96	0.99	1	0.99	0.34
H3K4me3 and DAPI	-0.04	0.67	0.93	0.97	0.93	-0.02

Table 2.1: Correlation and overlap coefficients calculated by ICA ImageJ plug-in for the nuclei shown in Figure 2.1. Upper row shows results for positive correlation, lower row for negative correlation. Pearson´s correlation coefficient Rr adopts values between [+1] for perfect correlation and [-1] for perfect anti-correlation. Manders´ overlap coefficient R adopts values between [+1] for perfect correlation and [0] representing perfect anti-correlation. Manders´ colocalization coefficients M1 and M2 indicate the percentage of overlap of channel 1 and channel 2 and vice-versa. Ch1:Ch1 shows the pixel ratio of the two images. ICQ is calculated by the number of pixels with positive PDM to the total number of pixels. This value is subtracted by 0.5 and thus the ICQ ranges from 0.5 to -0.5.

The above described results suggest that all these coefficients or quotients are not suitable to robustly describe anti-correlations. One reason is the sensitivity of the coefficients to the large proportion of pixels with low intensity, which make it difficult or almost impossible to obtain strong negative values. For calculation of the ICQ, the number of pixels with positive PDMs is used. The ICQ is thus also affected by the large proportion of pixels with small intensity, for which a positive PDM value is obtained, albeit these intensities might be an outcome of background noise. These problems also were frequently discussed in the literature (Bolte and

Cordelières, 2006; French et al., 2008; Ronneberger et al., 2008; Barlow et al., 2010). To circumvent such sensitivities and false-positive values of these coefficients, (French et al., 2008) proposed Spearman´s rank correlation coefficient ρ to calculate pixel correlations. In this study they use a plug-in called JACoP (Just Another Colocalization Plug-in), which was introduced earlier by (Bolte and Cordelières, 2006). JACoP is also used with the public domain software ImageJ. I tested this plug-in to determine co-localization and anti-correlation, but it showed lack of estimation of anti-correlation, because it focuses on the estimation of co-localization (Bolte and Cordelières, 2006; French et al., 2008). By testing anti-correlated images with this plug-in, the simple information "no positive correlation found" for these images was reported and no coefficients were obtained. With the help of Prof. Volker Schmid, head of the BioImaging Group of the Statistics Department at LMU, calculation of Spearman´s rank correlation coefficients was performed and compared to ICQ and a corrected ICQ*, as described in the following chapter.

2.1.3 Spearman´s rank correlation coefficient ρ

The following paragraph was written and evaluated in cooperation with Volker J. Schmid from the Statistics Department, LMU Munich, and will also be published in (Seiler et al., 2011).

PDM values and the Intensity Correlation Quotient (ICQ) proposed by (Li et al., 2004) assume a symmetric distribution for both channels, which is unrealistic for most images. In order to quantify the bias introduced by ICQ, we used a bootstrap technique to compute the value of ICQ under independence for given distributions of intensities for both channels (Efron and Tibshirani, 1993). For this, we paired each pixel intensity of one channel with a randomly sampled pixel intensity of the other channel and computed the ICQ. This was reiterated 1000 times and the mean value ICQ_0 was computed as value of ICQ under assumption of no correlation. The ICQ_0 value is typically not equal to zero. From this one can calculate a corrected ICQ value ICQ* = ICQ - ICQ_0. Figure 2.2 a) depicts a scatter plot of corrected and uncorrected ICQ values for a number of images analyzed (images which are shown in chapters 2.2.4 and 2.2.7) and shows that for a high proportion of images the ICQ is positive, i.e., suggests correlation, where the corrected ICQ* is negative, i.e., suggests anti-correlation. As an alternative to statistically evaluate correlation of intensities over an image, Spearman's rank correlation coefficient ρ was proposed by (French et al., 2008). For this, the intensities of each channel are ranked. Spearman's coefficient is defined as $\rho = 1 - 6\ \Sigma d_i^2/(n(n^2-1))$, where d_i is the difference of the ranks of both channels in voxel i and n is the number of pixel pairs. Spearman´s ρ can adopt values between [-

1,1]. Figure 2.2 b) compares ICQ and ρ, where in many cases both values disagree on the direction of correlation. Figure 2.2 c) compares the corrected ICQ* and ρ and both coefficients agree on the direction of correlation in nearly all cases. Since Spearman's correlation coefficient is easier to compute, we rely on Spearman's rank correlation coefficient for quantification of correlation between channels and use PDM maps to visualize regions with positive or negative correlations of both channels only. To test for correlation, p values for a test on the null hypothesis ρ = 0 were computed. To compare images at different time points after radiation, we used a Mann-Whitney U test on the rank correlation coefficients to test differences in co-localization between groups. All statistical computations were performed in the statistical language R, version 2.11.1 (R Development Core Team, 2010).
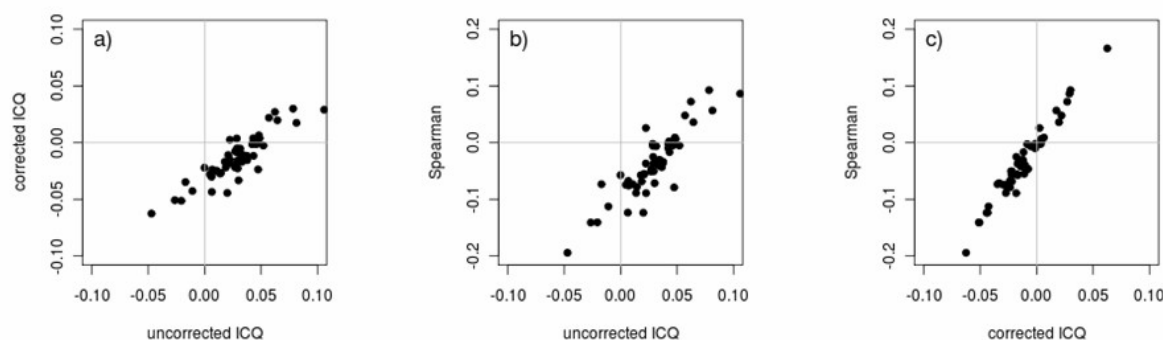
Figure 2.2: Comparison of different coefficients for evaluation of the correlation of intensities for all images used in the analysis. a) Scatter plot of ICQ values versus corrected ICQ* values (ICQ*=ICQ-ICQ$_0$). The uncorrected ICQ is clearly biased towards positive correlation. b) Scatter plot of ICQ value versus Spearman's coefficient ρ. Both coefficients disagree in many cases. c) Scatter plot of corrected ICQ* values versus Spearman's coefficient. There is a nearly linear relationship between both coefficients, i.e., both coefficients give a consistent quantification of correlation.

2.1.4 Evaluation of ICA to determine correlation of histone modifications and γ-H2AX foci

γ-H2AX foci are induced in a line pattern of 5 μm x 5 μm or 1 μm x 5 μm to the cell nucleus with the ion microbeam. This yields a sharp and confined staining pattern in the red channel which reflects the irradiation pattern in contrast to the flake-like staining pattern of histone modifications in the green channel, as described above. It is obvious that, because the two staining patterns show a completely different distribution across the nucleus, this situation is not exactly conferrable to the situations tested above (2.1.1). High intensities of the red channel are limited to the area of γ-H2AX foci and areas outside of foci might have weak background

intensities. By contrast, the area captured by staining of histone modifications is usually much larger and consequently, correlation analysis would indicate anti-correlation wrongfully. Thus, it was necessary to limit the area which should be analyzed for correlation to the area marked with γ-H2AX foci. These areas were not manually segmented, but instead a threshold was applied to ICA settings of usually 1 (see also methods section 4.10.2). Before performing ICA, background was subtracted from images and thus areas devoid of radiation-induced foci should not contain any or at least no high signal intensities. By this it was achieved that analyzed areas are limited to radiation-induced foci. Additionally, I tested the influence of higher thresholds on ICA. As expected, with increase of threshold also the mean value of intensities increases and the number of analyzed pixels is reduced.

2.1.5 Summary

Determination of correlation of pixels pairs in two fluorescence images is not trivial. The simple red-and-green-gives-yellow technique can be used for a first impression of relations, but can neither be used for objective correlation analysis nor for quantification. ICA represents correlations of pixel pairs in a simple manner and it is also suitable to determine anti-correlation and random distributions in several slices of an image stack. PDM plots and scatter plots can be used to quickly asses the correlations of intensities and the user can distinguish between high and low intensities. However, they represent correlations in a simple manner, and coefficients calculated such as Pearson´s, Manders´ and ICQ, are strongly influenced by the large number of small intensities that still exist inspite of a suitable threshold. Spearman´s rank correlation coefficient is less sensitive to small intensities and is also not influenced by the distribution of signals in an image (V.J. Schmid, personal communication, and French et al., 2008; for detailed discussion see chapter 3.1.) Therefore, ICA, PDM maps and plots in the present work were used for visualization of correlations. For quantitative analysis, however, Spearman´s rank correlation coefficient ρ was calculated by V.J. Schmid. Calculation of Spearman´s ρ was performed with a special program and for large data sets of pixels intensities which were obtained with the ICA plug-in. For this reason, Spearman´s ρ was only calculated in combination with detailed analysis of a modification and if a more sensitive measure was needed, for example to determine time-dependent alterations. In the following, ICA was used, with respective settings and keeping potential dangers in mind, to analyze correlation of various proteins and histone modifications at γ-H2AX foci.

2.2 Inhibition of transcription at DNA double-strand breaks

2.2.1 Induction of DSBs with the ion microbeam – experimental conditions

Limitations of experiments using the microbeam

Ion microirradiation was performed at the ion microbeam SNAKE as described in chapter 4.4.1. The advantage of ion microirradiation over laser microirradiation is the well characterized damage thus induced (Hauptner et al., 2004; Greubel et al., 2008b; Nagy and Soutoglou, 2009). Moreover, the medical relevance of ion irradiation is important due to radiotherapy and environmental radiation to which humans are exposed. In contrast to broad beam irradiation, the microbeam offers the opportunity to induce the damage in a predefined pattern to the cell. Cells are grown on a 6 µm mylar foil because of the limited range of accelerated ions in matter (Hauptner et al., 2004). With ion microirradiation, damage-induced foci can be distinguished from spontaneously formed foci. A limitation of ion microirradiation is the limited time for experiments and the large logistical effort, because the microbeam is located at the Munich tandem accelerator facility at the Maier-Leibnitz-Laboratory in Garching, in the North of Munich. The microbeam is used by a broad range of scientists and thus access to the facility is limited to so-called beam times. They were conducted within approx. five weeks per year. Accordingly, the number of experiments was limited and duplicates or replicates could not be performed for all experiments. For this reason, additional experiments were performed with α-particle irradiation or x-irradiation, which were much easier to conduct and the access to these facilities was not limited. α-irradiation was favored over x-irradiation, because α-particles in the applied dose of ~0.4 Gy induce on average four IRIF in a cell nucleus which are easier to analyze than the large number of IRIF induced by X-rays. An additional advantage of α-irradiation is that it is high LET (linear energy transfer) radiation, as are ions (Pouget and Mather, 2001). During my thesis, I tried to perform all important experiments using ion microirradiation, but in some cases I was forced to extend the experiments to α- or x-irradiation. Furthermore, in some cases it was desirable to verify results after different types of ionizing radiation. In addition to ionizing radiation, also laser microirradiation using a 405 nm laser was used to analyze the recruitment to damaged sites of proteins, which where not detectable after ion-irradiation.

Variations of fixation times due to experimental conditions

In some experiments, samples need to be analyzed as quickly as possible after irradiation. Ion microirradiation, which takes about seven minutes, was performed at the accelerator in the tandem hall. For immediate fixation after irradiation, samples were placed on ice and carried to the laboratory, which takes about two minutes. These samples are denoted '5 min' after IR, which is the earliest time amenable to that kind of experiment. In contrast, alpha-irradiated samples could be fixed immediately after irradiation, where the irradiation itself takes takes four minutes. These samples are denoted '2 min' after IR. These variations might lead to small difference in the behavior of some proteins or modifications when tested shortly after IR.

Image acquisition – epifluorescence vs. confocal microscopy

Image acquisition was mainly performed with an epifluorescence wide-field microscope (Zeiss AxioObserver Z1) located at the Maier-Leibnitz-Laboratory in Garching. With this microscope, images can be acquired quickly and easily, but the resolution of epifluorescence microscopy is limited. For this reason, access to a confocal microscope (SP5 DMI 6000 CS, Leica) was kindly provided by Prof. T. Cremer. With a confocal microscope, resolution in x,y- and also in the z-dimension is increased and thus image analysis is improved (Conchello and Lichtman, 2005). Nonetheless, this method is more time-consuming and only one cell nucleus is acquired at a time, which takes about seven minutes, compared to epifluorescence microscopy, where about 20 cell nuclei are acquired in one image in two to three minutes. Additionally, access to the confocal microscope was limited due to a high number of users. For this reason, the epifluorescence microscope was used to acquire larger numbers of cell nuclei for quantification, whereas high quality images for detailed image analysis were acquired with the confocal microscope. Confocal and epifluorescence images were both deconvolved for further analysis.

2.2.2 Initiating and elongating RNA Polymerase II and DSB-induced γ-H2AX are mutually exclusive

Transcription inhibition at γ-H2AX foci induced by ionizing radiation was first suggested by (Solovjeva et al., 2007). They analyzed the distribution of nascent RNA, labeled by the incorporation of 5-bromouridine (BrUTP), and γ-H2AX foci after x-irradiation of HeLa and MCF7 cells in fluorescence images. Almost no overlap was observed between γ-H2AX foci and

nascent RNA. These results suggest an inhibition of transcription at DSB sites (Solovjeva et al., 2007). However, they did also not observe an increase of heterochromatin marks at these sites.

In the present work, initiating (Ser5-P) RNA Polymerase II and its correlation with γ-H2AX foci was tested after ion microirradiation and α-particle irradiation (Figure 2.3 and Figure 2.4 A). Image evaluation with ICA showed mutual exclusion of γ-H2AX and initiating RNA Pol II Ser5-P. Pixels highlighted in pink in PDM maps in Figure 2.3 and Figure 2.4 A indicate areas where pixels have a negative PDM value and thus are anti-correlated, whereas pixels in green show positive correlation which were almost not observed in the PDM maps. PDM plots show that PDM values at high intensities are skewing to the left (negative values) and scatter plots show anti-correlated intensity distribution. Thus, initiating Pol II Ser5-P was clearly under-represented at γ-H2AX foci 2 h following ion irradiation (Figure 2.3) and 2 h after α-irradiation (Figure 2.4 A). Shortly (approximately 5 min) after ion-irradiation exclusion of γ-H2AX and initiating RNA Pol II Ser5-P was already evident (Figure 2.3 left), but at approximately 2 min after α-irradiation, exclusion was not yet clearly detectable, as indicated by positive and negative PDM values (Figure 2.4 A). Similar observations were made for elongating RNA Pol II Ser2-P, which showed anti-correlation with γ-H2AX 2 h after α-irradiation (Figure 2.4 B).

By loss of the two activated forms of RNA Polymerase II from regions decorated with γ-H2AX, it can be concluded that inhibition of transcription is taking place at these sites. In the meantime, an under-representation of elongating RNA Pol II Ser2-P was also reported by others after laser microirradiation (Chou et al., 2010). This rises the question if the loss of transcription goes along with an establishment of a repressive chromatin pattern at sites of damage. Such a pattern could be indicated by an accumulation of repressive proteins or histone modifications associated with heterochromatin, such as HP1β, H3K9me3, H4K20me3, and H3K27me3. In the following, analysis of various heterochromatin marks and proteins associated with repression were analyzed at DSB sites.
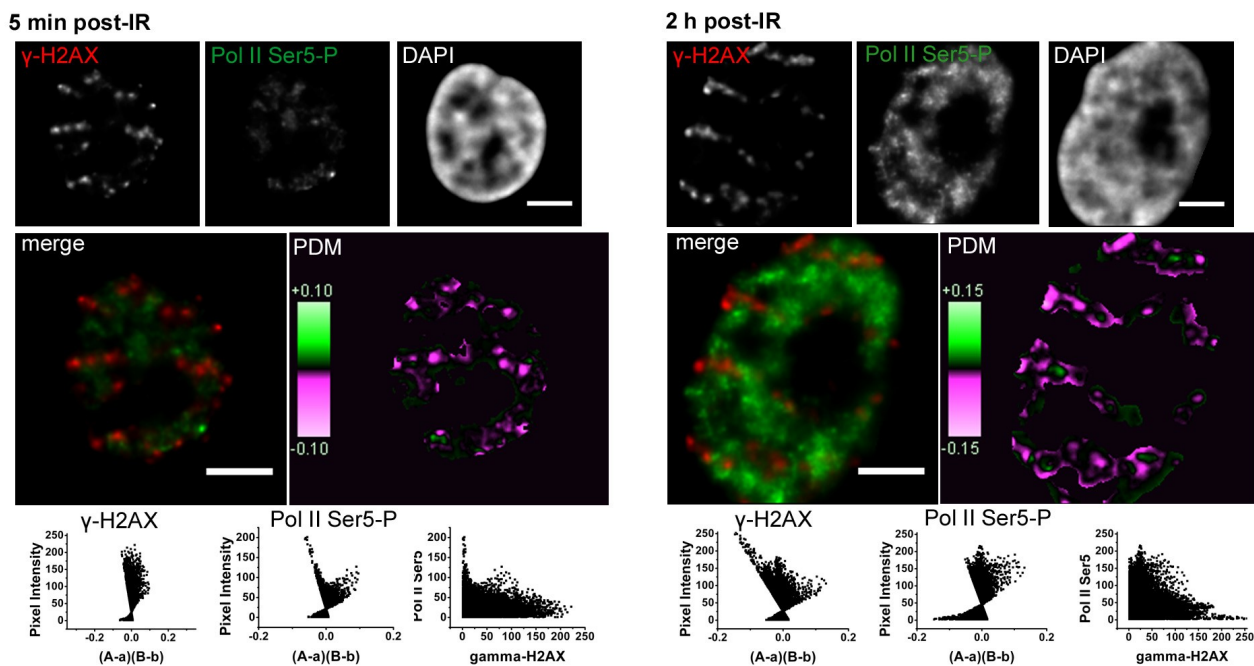
Figure 2.3: Distribution of initiating RNA Polymerase II (Ser5-P) and γ-H2AX foci after ion microirradiation of HeLa cells. Microscopic images show single slices of epifluorescence microscopy of HeLa cell nuclei with γ-H2AX in the red channel, RNA Pol II phosphorylated at Ser5 in the green channel and chromatin stain with DAPI (blue). Mid row shows red-green merges and PDM color-coded images. Anti-correlated pixels are highlighted in pink, co-localized pixels are highlighted in green. Already at 5 min after IR, anti-correlation was evident. At 2 h after IR, anti-correlation was more pronounced, which is demonstrated by strong negative PDM values shown in the PDM plots skewing to the negative range (bottom row). Scale bar is 5 μm.
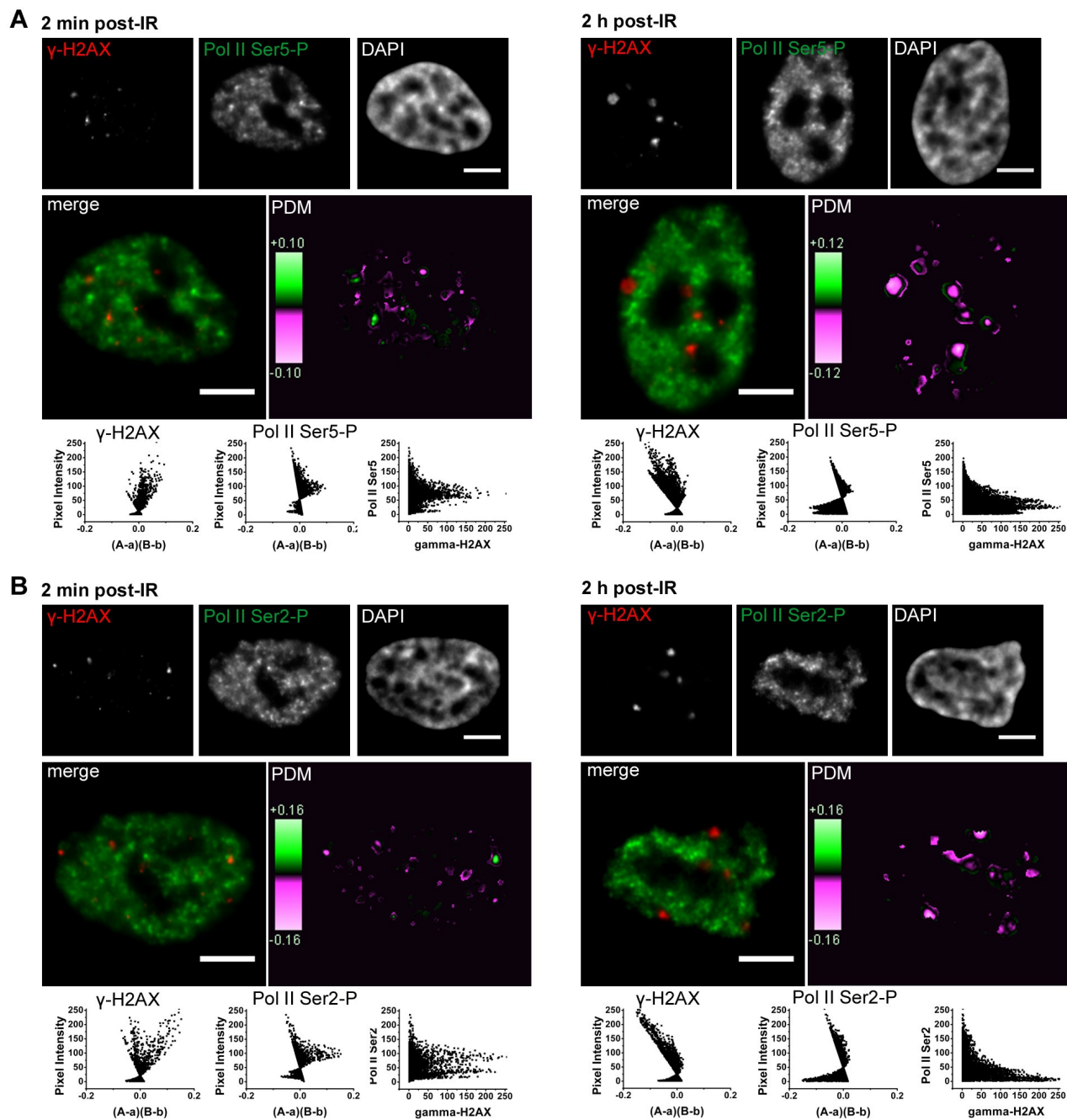
Figure 2.4: Distribution of initiating (Ser5-P) and elongating (Ser2-P) RNA Polymerase II and γ-H2AX foci induced by alpha-particle radiation of HeLa cells. Microscopic images show single epifluorescence images of γ-H2AX (red), RNA Pol II either phosphorylated at Ser5 (A) or Ser2 (B) (green), and DAPI stain. Mid rows show red-green merges and PDM color-coded images. PDM and scatter plots in the bottom line show distribution of PDM values and intensities. 2 h after IR, for both forms of RNA Polymerase strong anti-correlation with γ-H2AX foci was evident, represented by pink color in the PDM images and strong negative PDM values skewing to the left in the PDM plots. At earlier times (~ 2 min) after IR anti-correlated and some overlapping pixels which are highlighted in green in the PDM images and skew to the positive values in the plots were observed. Scale bar is 5 µm.

2.2.3 HP1β is accumulating at DSB in a time-dependent manner

Heterochromatin protein 1 (HP1) mediates heterochromatin silencing (reviewed in Billur et al., 2009). Three different isoforms of HP1 exist, which are HP1α, HP1β, and HP1γ. HP1 binds to DNA via an interaction of its chromodomain with the histone modification H3K9me3/me2 (Bannister et al., 2001; Lachner et al., 2001). Recent data in the literature describe a role for HP1β (Ayoub et al., 2008) and different HP1 isoforms (α, β and γ) (Luijsterburg et al., 2009) in DNA repair, although findings were somewhat controversial. On the one hand, a fast dispersal of HP1β from damaged chromatin and a later re-establishment of HP1β following targeted laser microirradiation of heterochromatic foci (chromocenters) in mouse cells (Ayoub et al., 2008) was reported. On the other hand, (Luijsterburg et al., 2009) did not observe a dispersal at early times after irradiation, but instead a later accumulation to damage sites was shown in human cells following irradiation with γ-rays or laser microirradiation.

To investigate this matter further, HeLa cells were ion-irradiated in a matrix pattern of 5 µm x 5 µm at SNAKE and fixed either as soon as possible after irradiation (~ 5 min) or 1 and 2 h following irradiation. In Figure 2.5 microscopic images of irradiated HeLa cells and image evaluation with ICA are shown. At later times post-irradiation incubation (1 and 2 h), accumulation of HP1β to γ-H2AX foci was observed. Evaluation of images with ICA verified positive correlation for both proteins. In the PDM images, areas where intensities in both channels co-localize are highlighted in green (Figure 2.5 B,C mid rows). By contrast, at 5 min after irradiation, γ-H2AX foci appear predominantly in areas where HP1β intensities are low, which is also represented by the pink color in the PDM image (Figure 2.5 A). The distribution of HP1β at short times was difficult to determine due to the small size of the foci and the small number of pixels analyzed (Figure 2.5 A). PDM plots indicate a random distribution with high intensity values being close to zero. Scatter plots show a mixed staining with a number of pixels being positively correlated and a number of pixels being negatively correlated.

From the evaluated images, it can be concluded that HP1β accumulates at γ-H2AX foci at later times after IR, whereas at short times after IR, no accumulation was evident.
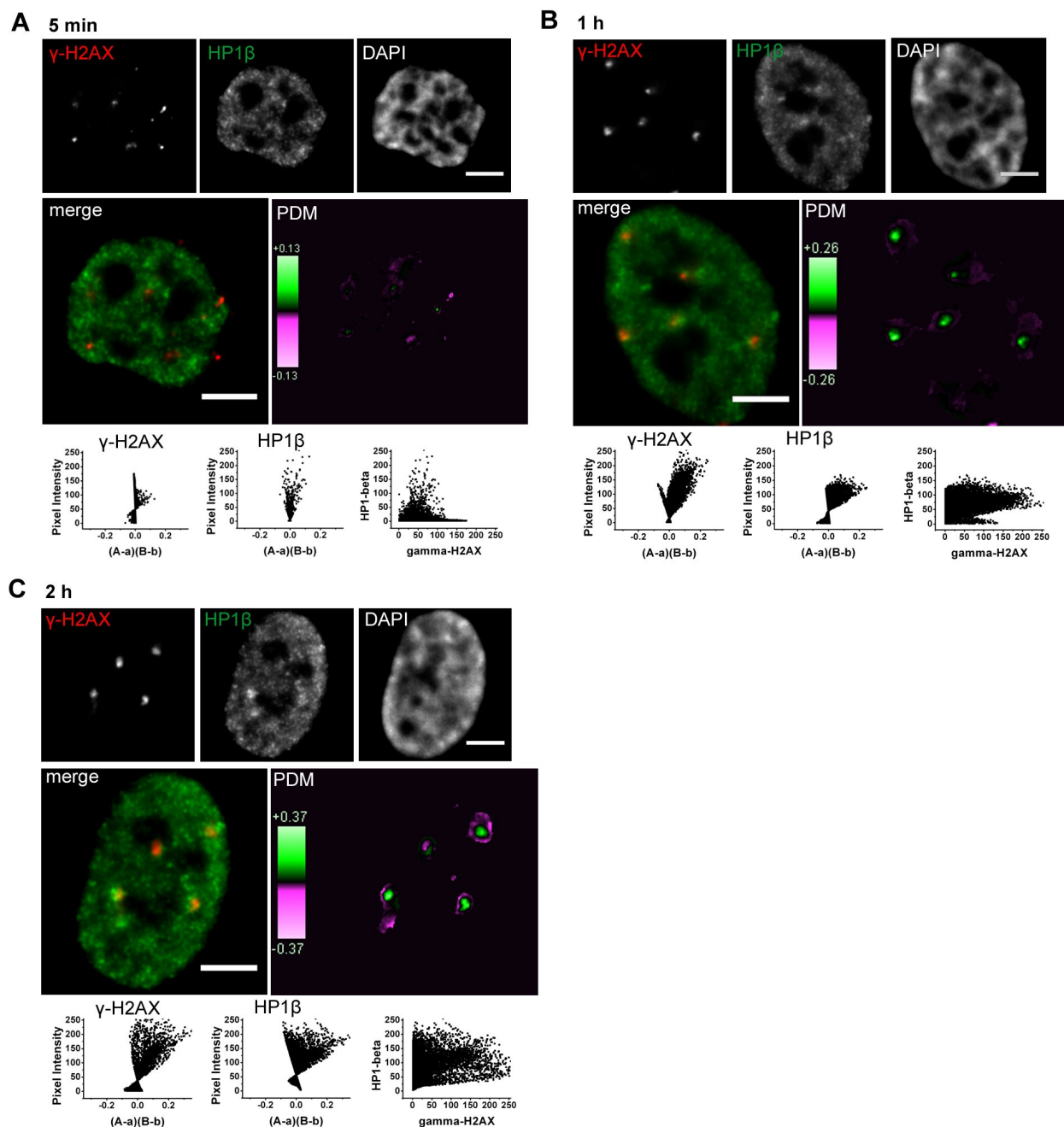
Figure 2.5: Distribution of HP1β and γ-H2AX following ion microirradiation of HeLa cells in a matrix pattern of 5 μm X 5 μm. Cells were irradiated and fixed either immediately after IR (A, indicated as 5 min), or after 1 (B) or 2 h (C) post-IR. Fluorescence images show mid-sections of epifluorescence image stacks. In the red channel, staining for γ-H2AX, in the green channel for HP1β, and in the blue channel DNA counter stain with DAPI is shown (upper rows in A-C). Mid rows in A)-C) show red-green merges and the PDM color-coded images. Co-localization is highlighted in green, anti-correlation is highlighted in pink. In the bottom rows (A-C), PDM plots (left and mid plot) show the PDM values for each channel and their corresponding intensities. Scatter plots (right plot) show the distribution of intensities of red and green channel. Shortly after IR (A), γ-H2AX foci were small and predominantly found in regions of low HP1β intensities, but also overlapping areas were observed. At later times (1 & 2 h post-IR, B and C), γ-H2AX foci were predominantly overlapping with high intensities of HP1β. Scale is 5 μm.

Similar results were obtained using the Spearman´s rank correlation coefficient ρ, which was determined for the different points of time for 5-6 cell nuclei (n) each (Figure 2.6). At 1 and 2 h after IR, ρ was strongly positive with $\rho_{1h} = 0.33 \pm 0.04$ (SD) and $\rho_{2h} = 0.34 \pm 0.08$ (SD). The mean coefficients were significantly different from zero ($P_0 = 5.85*10^{-5}$ at 1 h and $P_0 = 1.4*10^{-3}$ at 2 h) but not significantly different from each other (P = 0.79). The mean coefficient at 5 min after IR was close to zero with $\rho_{5min} = 0.09 \pm 0.15$ (SD) and was not significantly different from zero ($P_0 = 0.24$). However, coefficients for the later times (1 h & 2 h) were significantly different from the coefficient at 5 min (P = 0.009 for ρ_{2h} and ρ_{5min}; P = 0.02 for ρ_{1h} and ρ_{5min}).

A phenomenon observed in these and other images can be easily explained. At the borders of γ-H2AX foci, PDM values seem to indicate anti-correlation, as shown by pink staining surrounding the foci in the PDM images of Figure 2.5 B,C. At these borders of γ-H2AX foci, the intensities of the red channel are rather small and due to a high general mean intensity in the red channel, intensities at the borders of foci are below the mean level. In contrast, HP1β (green channel) is distributed more homogeneously across the nucleus and at the borders of γ-H2AX foci, its intensity is still above the mean level. This results in an apparent anti-correlation of γ-H2AX and HP1β at the borders of γ-H2AX foci and thus in a pink "corona" in the PDM image surrounding γ-H2AX foci. Another interpretation, which is that accumulation of HP1β is not directly restricted to γ-H2AX foci, cannot, however, be excluded.

Taken together, statistical evaluation with Spearman´s coefficient showed positive correlation of HP1β and γ-H2AX at 1 and 2 h after IR. However, the coefficients did not significantly differ from each other which implies that no detectable alteration occurred between 1 h and 2 h post-IR. At 5 min post-IR, the mean coefficient was close to zero which can be either interpreted as random distribution or as a mixed staining pattern with some γ-H2AX foci being devoid of HP1β and some γ-H2AX foci overlapping with HP1β. No exclusion of γ-H2AX and HP1β could be verified by this kind of analysis. However, also no strong positive correlation was observed at this point of time. Nonetheless, results show that HP1β is recruited to DSB in a time-dependent manner. Because HP1β binds to chromatin via interaction of its chromodomain with H3K9me2/me3, it can be hypothesized that H3K9me2/me3 staining pattern might be altered at DSB sites. However, (Luijsterburg et al., 2009) reported that the recruitment of HP1β is independent from its chromodomain and rather depends on its chromoshadow domain. Moreover, they did not find indications for alterations of H3K9me3 staining pattern. In contrast, (Falk et al., 2007) reported an early decrease of H3K9me2 following γ-irradiation. However, the

methods used in these studies might not be sensitive enough to reliably detect slight alterations of H3K9me pattern. Thus, I investigated the H3K9me2/me3 staining pattern after ion microirradiation.
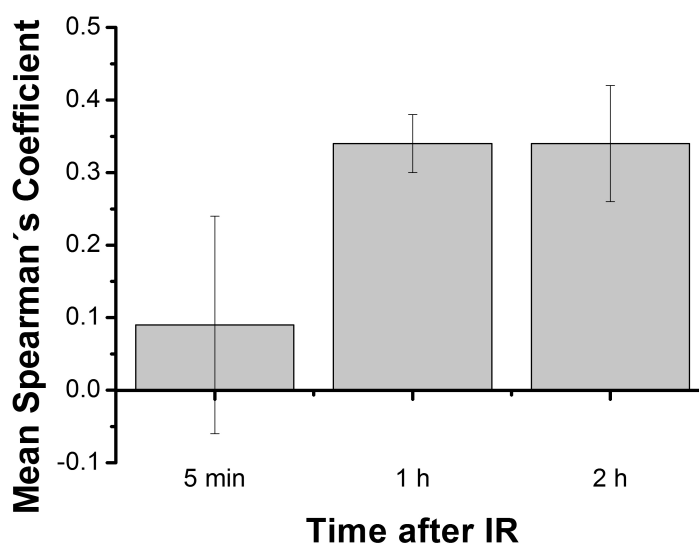
Figure 2.6: Mean Spearman´s rank correlation coefficient for HP1β and γ-H2AX in HeLa cells following ion microirradiation. Indicated are mean and standard deviation of Spearman rank correlation coefficients at 5 min (n = 6), 1 and 2 h after IR for n = 5 cell nuclei. Coefficient at 5 min was not significantly different from zero ($P_0 = 0.24$). Coefficients at 1 and 2 h were significantly different from zero ($P_0 = 5.85*10^{-5}$ at 1 h and $P_0 = 1.4*10^{-3}$ at 2 h) and significantly different from 5 min (Mann-Whitney U test). This indicates, that HP1β is accumulating at γ-H2AX foci in a time-dependent manner.

2.2.4 H3K9me2 and H3K9me3 are randomly distributed at DSB sites

My own results described above and recent literature (Ayoub et al., 2009; Luijsterburg et al., 2009; Zarebski et al., 2009) showed accumulation of HP1β to DSB, which rises the question if alterations of histone modifications might be responsible for HP1β recruitment. However, neither global nor local changes of H3K9me3 were observed following different types of radiation (Solovjeva et al., 2007; Ayoub et al., 2008; Luijsterburg et al., 2009). In contrast to H3K9me3, H3K9me2 is not predominantly enriched in centromeres (Schotta et al., 2004; Zinner et al., 2006). In immunofluorescence images, staining of H3K9me2 results in a more homogeneous pattern distributed across the nucleus (Schotta et al. 2008) but it still correlates predominantly with heterochromatic regions (reviewed in Shilatifard, 2008 and shown in Figure 2.1 A). Specificity of the H3K9me2 antibody used was confirmed by peptide competition assay (Appendix A).

Analysis of local distribution of H3K9me2 at γ-H2AX foci

The local distribution of H3K9me2 with respect to DSB was investigated following ion microirradiation (Figure 2.7 A,B). H3K9me2 signals were partially overlapping with foci and were also found at the borders of foci. ICA revealed a random or mixed distribution pattern. This is also demonstrated by the distribution of intensities in the scatter plots and the PDM values, which are distributed around the zero axis (Figure 2.7, diagrams in bottom rows). Spearman´s rank correlation coefficient was determined for 4-5 cell nuclei of confocal 3D image stacks for both points of time (Figure 2.8). Mean values of Spearman´s coefficients were $\rho_{15min} = 0.075 \pm 0.069$ (SD) and $\rho_{2h} = 0.034 \pm 0.031$ (SD). Both values were not significantly different from each other (Mann-Whitney U test; $P = 0.093$) and also not significantly different from zero ($P_0 = 0.13$ for 15 min and $P_0 = 0.88$ for 2 h) (statistical evaluation using Pearson´s coefficient see Appendix D).
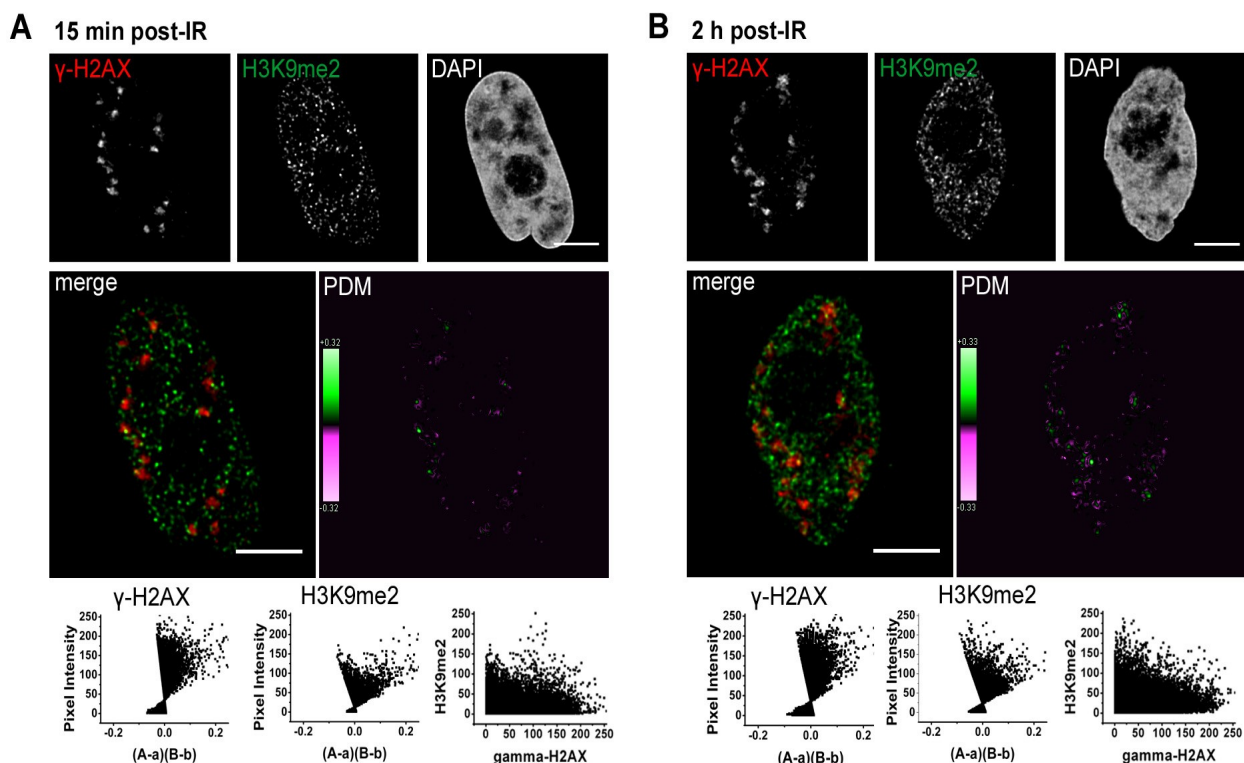
Figure 2.7: H3K9me2 in HeLa cells following ion microirradiation. Shown in the upper rows are mid-sections of confocal image stacks stained with γ-H2AX in the red channel, H3K9me2 in the green channel and DAPI in the blue channel. The middle rows show the respective red-green merges and the PDM color-coded images, with green pixels representing positive PDM values and pink pixels representing negative PDM values. Plots of γ-H2AX or H3K9me2 signal intensity vs PDM and the respective intensity scatter plots are shown in the bottom rows. At (A) 15 min and (B, C) 2 h after ion microirradiation in a line pattern (1 μm x 5 μm), both positive and negative PDM values are assigned to pixels with high γ-H2AX intensity. Scale bars are 5 μm
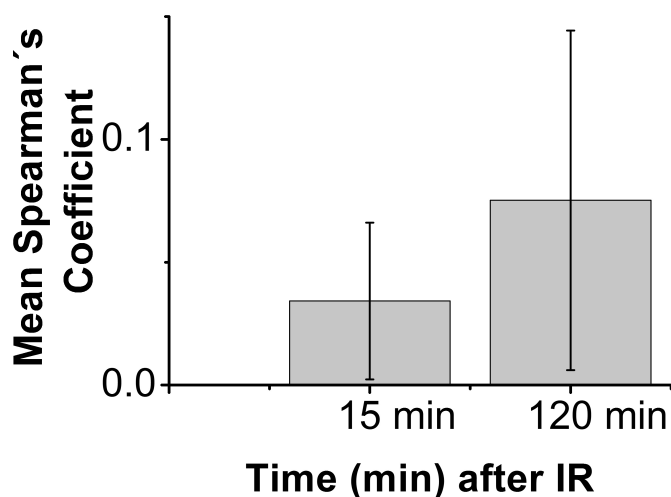
Figure 2.8: Mean Spearman´s rank correlation coefficient calculated for H3K9me2 and γ-H2AX in ion irradiated HeLa cells. Coefficient was determined for n = 4-5 cell nuclei for 15 min and 2 h after IR, respectively. Both values were not significantly different from each other (Mann-Whitney U test; P = 0.093) and also not significantly different from zero (P_0 = 0.13 for 15 min and P_0 = 0.88 for 2 h).

By visual inspection of images, it was apparent that a large proportion of H3K9me2 signals were located at borders of γ-H2AX foci. This raised the question if H3K9me2 is 'attached' to γ-H2AX foci in a manner that cannot be distinguished by ICA. It has to be considered that the resolution of conventional microscopes is limited to approx. 200 nm in x,y and 600 nm in z (see chapter 1.4.1). By analysis of 3D image stacks it cannot be excluded that two signals seem to co-localize but in reality they are < 600 nm apart from each other in the z-direction. Out-of focus light from other focal plains might contribute to this bias. To overcome these limits, super-resolution microscopes are being developed (reviewed in Rouquette et al., 2010; Schermelleh et al., 2010), but were not available for the present work. Instead, another option was offered in the laboratory of Prof. T. Cremer, where ultrathin sectioning was introduced. In this new method, fluorescent-labeled cells were cut into physical ultrathin sections of approx. 150 nm thickness. Thus, the quality of image analysis could be greatly improved.

Distribution of H3K9me2 and γ-H2AX in 150-nm ultrathin sections

Ultrathin sectioning of cells is a method commonly used for electron microscopy (Rouquette et al., 2009; Solimando et al., 2009). Here, the method was applied to fixed and stained cells that

were grown on a 6 μm Mylar foil for irradiation. Two challenges were faced during implementation of this method. At first, for ultrathin slicing, the cells are embedded in liquid resin, which is polymerized and than sliced. For this, cells are usually grown on glass cover slips. Here, the embedding had to be adapted for cells which were grown on a very thin foil which was tricky to handle. Second, irradiation with the microbeam is limited to a square of 300 μm x 300 μm and thus only a small number of cells from the total cell layer had been irradiated. This irradiated field had to be re-located and the thin foil had to exactly be placed in the middle of the resin-filled capsule in a way that, after polymerization, the pyramid, which had to be cut out from the polymerized surface, contains the field with irradiated cells ideally in the center of the surface (see also methods section 4.7 for details). This was realized by marking the coordinates at the edges of the irradiated field with a small needle. Before embedding, a small area containing the marked field was cut out from the whole foil and placed with the cell monolayer upside-down on the resin-filled capsule. After polymerization, the foil was removed and the irradiated cells could be re-located because the small holes introduced with the needle left a mark on the resin surface (in the best case).

In Figure 2.9, serial sections of an ion-irradiated cell nucleus 2 h after IR are shown. These images do not need deconvolution processes and thus give an original and unchanged view on signal distribution, except for some background correction. After immunodetection of γ-H2AX and H3K9me2 the nucleus was sectioned into slices of approximately 150 nm with an ultra microtome. Subsequently, sections were placed on a cover slip and embedded for microscopy. During image acquisition, subsequent sections could be retrieved and a serial of these sections was acquired. γ-H2AX ion tracks reflect the irradiated line pattern of 1 μm x 5 μm (Figure 2.9). The ion tracks could be identified in each section. In the third image taken from the left side, an artifact caused by a fold in the section is shown.

In ultrathin sections, the H3K9me2 staining pattern appears sharper and more defined because out-of-focus light is diminished and the signal obtained is axially limited to 150 nm. H3K9me2 signals directly overlapping with γ-H2AX and signals at the borders of γ-H2AX foci were observed, as well as signals which were devoid of γ-H2AX (Figure 2.9). 20 cell nuclei of ultrathin sections were analyzed with ICA. In Figure 2.10, distribution and evaluation of γ-H2AX and H3K9me2 with ICA of a representative ultrathin section is shown. Evaluation with ICA confirmed previous results obtained from conventional 3D microscopy, which showed that H3K9me2 and γ-H2AX are partially overlapping and H3K9me2 is also located at the borders of

foci. Additionally, ultrathin sections revealed that a number of γ-H2AX foci were devoid of any H3K9me2 signal (for statistical evaluation of H3K9me2 and γ-H2AX foci in ultrathin sections using Pearson´s Coefficient see Appendix D).

In conclusion, no indications for alterations of H3K9me2 staining patterns at DSB were observed at the points of time investigated. Statistical evaluation of conventional microscopic images using Spearman´s rank correlation coefficient demonstrated a random distribution of H3K9me2 at γ-H2AX foci. In addition, a new method of ultrathin slicing of fixed cells was established. By this, the quality of image analysis could be improved. Ultrathin sections helped to conclude that H3K9me2 is randomly distributed at DSB sites and is not necessarily attached to γ-H2AX foci.
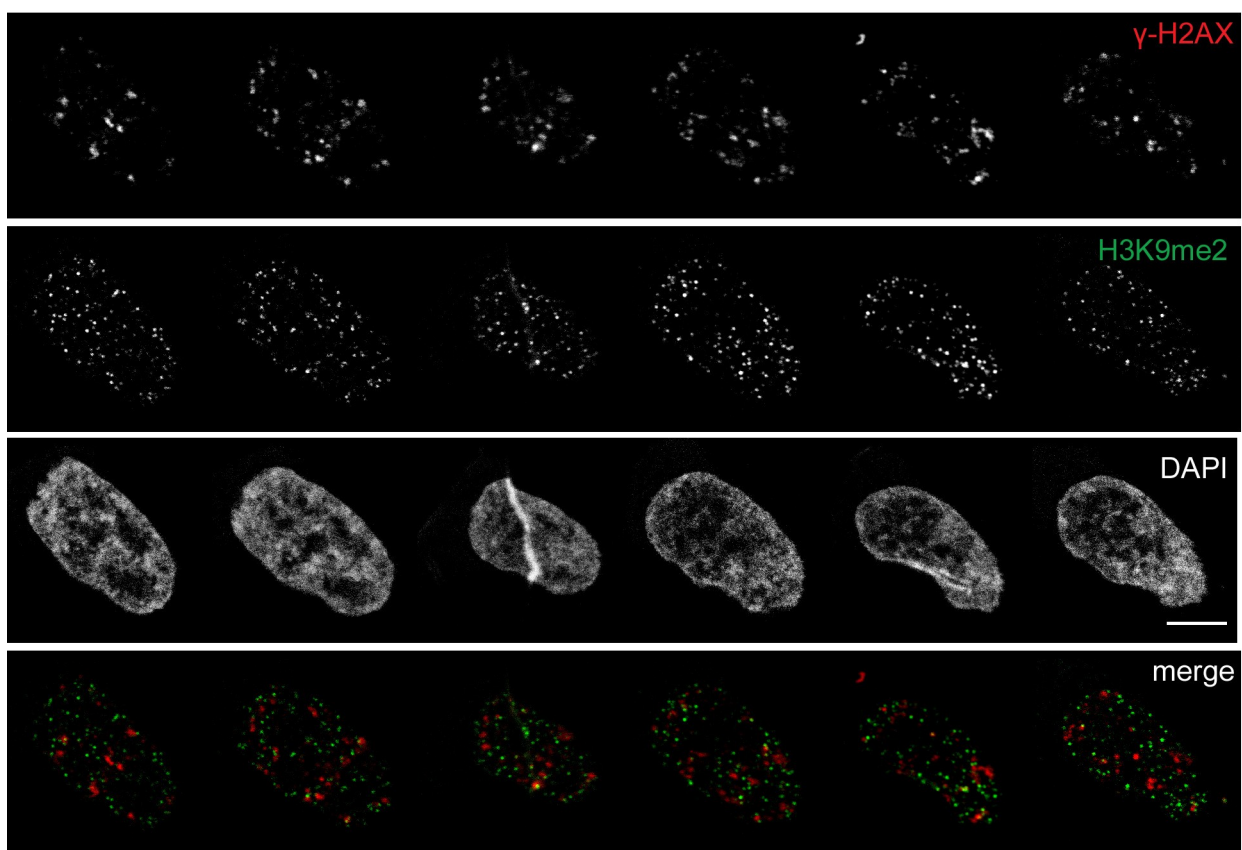
Figure 2.9: Serial 150-nm ultrathin sections of an ion-irradiated HeLa cell nucleus 2 h after IR. Shown are montages of six confocal serial images of one cell nucleus stained with γ-H2AX (red channel), H3K9me2 (green channel), DAPI (blue channel) and red-green merged images. Cells were cut into ultrathin slices of 150 nm with an ultra microtome and embedded for microscopy. Six serial sections of one cell nucleus were reproduced and a montage of serial images was arranged for each channel. Images show distribution of γ-H2AX and H3K9me2 after ion microirradiation with some H3K9me2 signal directly overlapping with foci and some signal located at the borders of foci. Additional γ-H2AX foci were observed which were devoid of any H3K9me2 signal. In the third image from the left side and, most probably, also in the fifth image from the left side, artifacts caused by folds in the section are shown. Scale is 5 μm.
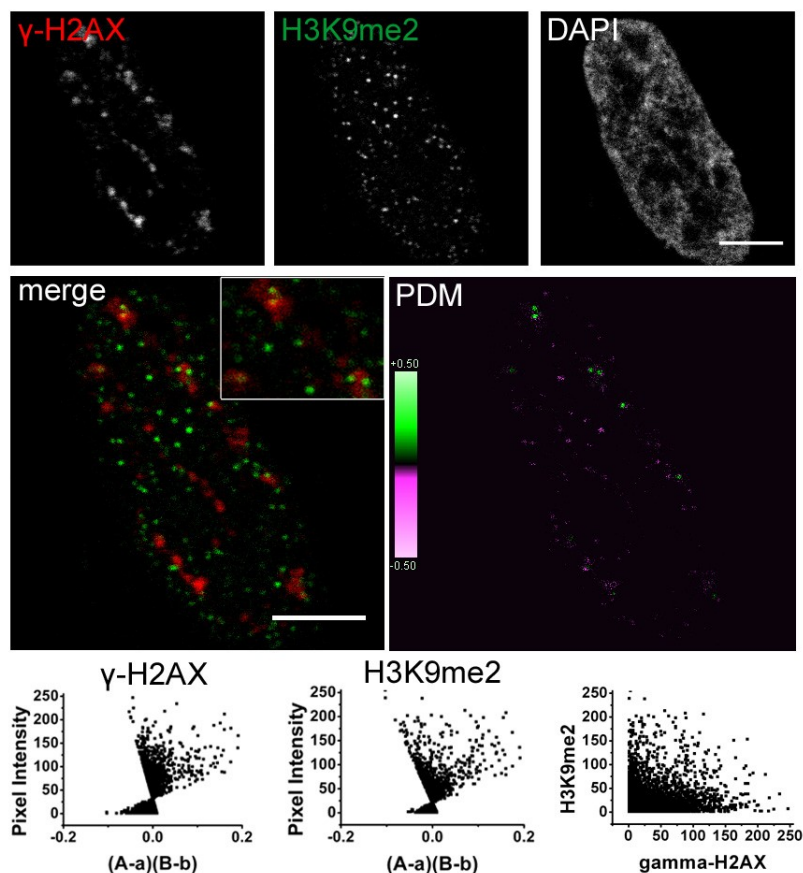
Figure 2.10: Distribution of H3K9me2 and γ-H2AX in 150nm- ultrathin section of an irradiated HeLa cell nucleus. Confocal single slices show γ-H2AX (red channel), H3K9me2 (green channel), DAPI (blue channel) in the upper row. Mid row shows red-green merge and a PDM color-coded image. Green dye represents overlapping areas, pink dye represents anti-correlated areas. PDM plots in the bottom row show the pixel intensities and their respective PDM value. Scatter plots (bottom right) shows distribution of intensities of red and green channel. H3K9me3 signal was found to be directly overlapping with γ-H2AX (magnified image, upper left focus) or was found at the borders of foci (see magnified image, lower right focus). Some γ-H2AX foci were devoid of any H3K9me2 signal. Scale bar is 5 μm, insert is 4 μm x 6 μm.

Analysis of local distribution of H3K9me3 at DSB

To analyze local alterations of H3K9me3 at DSB sites, damage was induced to HeLa cells with the ion microbeam (Figure 2.11). At both incubation times (~ 5 min and 2 h) after ion microirradiation, H3K9me3 signals were partially overlapping with γ-H2AX foci or found at the borders of foci. Some γ-H2AX foci were devoid of any H3K9me3 signal (Figure 2.11 A,B). Evaluation of images with ICA confirmed this observation with positive and negative PDM

values spreading around the zero axis (Figure 2.11 A,B diagrams and PDM images). Specificity of the H3K9me3 antibody used here was confirmed by peptide competition assay in the Diploma thesis of (Niedermair, 2010), performed at the Department of Radiation Oncology.

These results indicate that H3K9me3 is not significantly altered at damaged site. Some γ-H2AX foci were directly overlapping with H3K9me3 (Figure 2.11 A,B) which demonstrates that foci were formed also in regions designated with heterochromatic marks. In accordance with the literature, where no alterations of H3K9me3 were observed (Solovjeva et al., 2007; Ayoub et al., 2008; Luijsterburg et al., 2009), it can be assumed that H3K9me3 is randomly distributed and is not directly implicated in DSB repair.
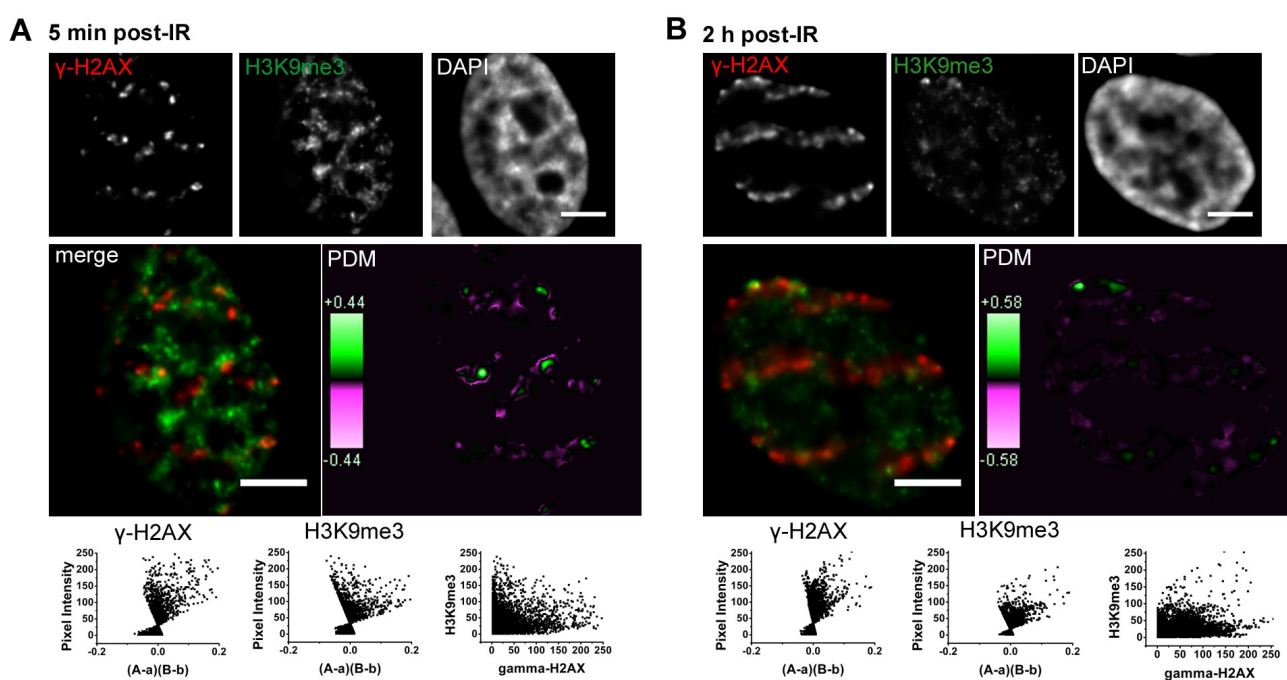
Figure 2.11: Distribution of H3K9me3 and γ-H2AX in HeLa cells following ion microirradiation at A) 5 min after IR and B) 2 h after IR. Microscopic images in the upper rows (A and B) show single slices of epifluorescence images with γ-H2AX (red), H3K9me3 (green) and chromatin stain with DAPI (blue). Mid rows shows red-green merges and PDM color-coded images. Pink color represents anti-correlation, green color represents co-localization. Bottom line shows PDM plots with PDM values and their corresponding intensities. Here, distribution of PDM values indicated random or mixed staining with negative and positive values skewing around the zero axis. Scatter plots in A) and B) bottom right, show distribution of intensities. Positive and negative correlations were observed. Scale is 5 μm.

Analysis of nucleus-wide alterations of H3K9me2/me3 following IR

During confocal image acquisition of H3K9me2 and H3K9me3 stained samples, it was observed that signal intensity was increased in samples shortly after irradiation compared to the intensities in unirradiated samples or in samples 2 h after IR, where the intensity was much lower. The increase of signal intensity was also observed in samples following α- and x-irradiation (Appendix B, and Figure 2.12, right column). Because of the increased intensity in samples 2 min and 15 min after IR, the gain of the confocal microscope was reduced to avoid overexposure of signals. This resulted in a few single bright spots of H3K9me2 staining in the nucleus, whereas other signals are close to background levels, as seen in samples 2 min and 15 min after IR (Figure 2.12). In contrast, in unirradiated samples and in samples 2 h after IR, signal intensity was lower and also more homogeneously distributed across the nucleus (Appendix B, and Figure 2.12, right column). This effect could hint to a radiation-induced translocation followed by an accumulation of histone H3 or H3K9me3/me2 at special sites of the cell nucleus which are independent from IRIF.

To test this hypothesis, the experiments were repeated after x-irradiation with subsequent pre-extraction of unbound proteins using an extraction buffer (Lukas et al., 2003). For this, cells were treated with a mild-detergent buffer containing 0.5% Triton-X-100 before fixation. Thereby, unbound proteins are removed from the nucleus before fixation and only bound or retained proteins are visualized by immunofluorescence. The pre-extraction buffer can be also used to reduce background in immunofluorescence samples (Lukas et al., 2003).

Figure 2.12 shows images of H3K9me2 and γ-H2AX staining in HeLa cells following x-irradiation for the indicated times either with extraction (Figure 2.12, left column) or without extraction (Figure 2.12, right column). In the samples denoted 2 and 15 min post-IR (second and third row of Figure 2.12), signal intensity of single H3K9me2-spots was clearly increased. In contrast, in unirradiated samples and samples 2 h after IR (first and last row of Figure 2.12), signal intensity of H3K9me2 shows a more homogenous distribution across the nucleus. This effect is clearly seen in images following the pre-extraction of unbound proteins (Figure 2.12, left column), but it is also also detectable in samples without pre-extraction (Figure 2.12, right column). Most probably, immunofluorescence staining itself is improved due to background reduction in pre-extracted samples which makes the staining more defined. Thus, the increase of signal intensity of H3K9me2 shortly after IR cannot only be explained by an accumulation of signal in a specific region of the cell nucleus. A possibility to verify changes in signal intensity

could be the simultaneous acquisition of two ion-irradiated fields on one objective slide fixed at different times after IR. I tried this by using the Mosaix option of a second epifluorescence microscope located in Großhadern. With Mosaix, larger areas in one objective slide can be acquired and then stitched to gain one large image. However, this attempt failed most probably due to the lack of sensitivity of the epifluorescence system. In addition, because cross talk of the filters of this microscope was observed, these data were omitted. Thus, the meaning of increased signal intensities of H3K9me2 shortly after IR remains an open question and needs further investigation.

In conclusion, the results described above show that methylation of H3K9 does not change neither locally at DSB sites nor any nucleus-wide alterations could be verified. This is in agreement with previous findings of others (Solovjeva et al., 2007; Ayoub et al., 2008; Luijsterburg et al., 2009). By contrast, (Falk et al., 2007) described a local decrease of H3K9me2. However, the quantitative analysis in the present work indicates a random distribution 15 min and 2 h after IR and no local decrease was observed for H3K9me2 15 min after IR. (Falk et al., 2007) observed also a local increase of H4K5Ac and conclude that the increase in acetylation is associated with chromatin decondensation. On the other hand, (O'Hagan et al., 2008) observed local hypoacetylation together with an enrichment of repressive marks at an enzyme-mediated DSB. Thus, I set out to investigate the local distribution of H4K5Ac.
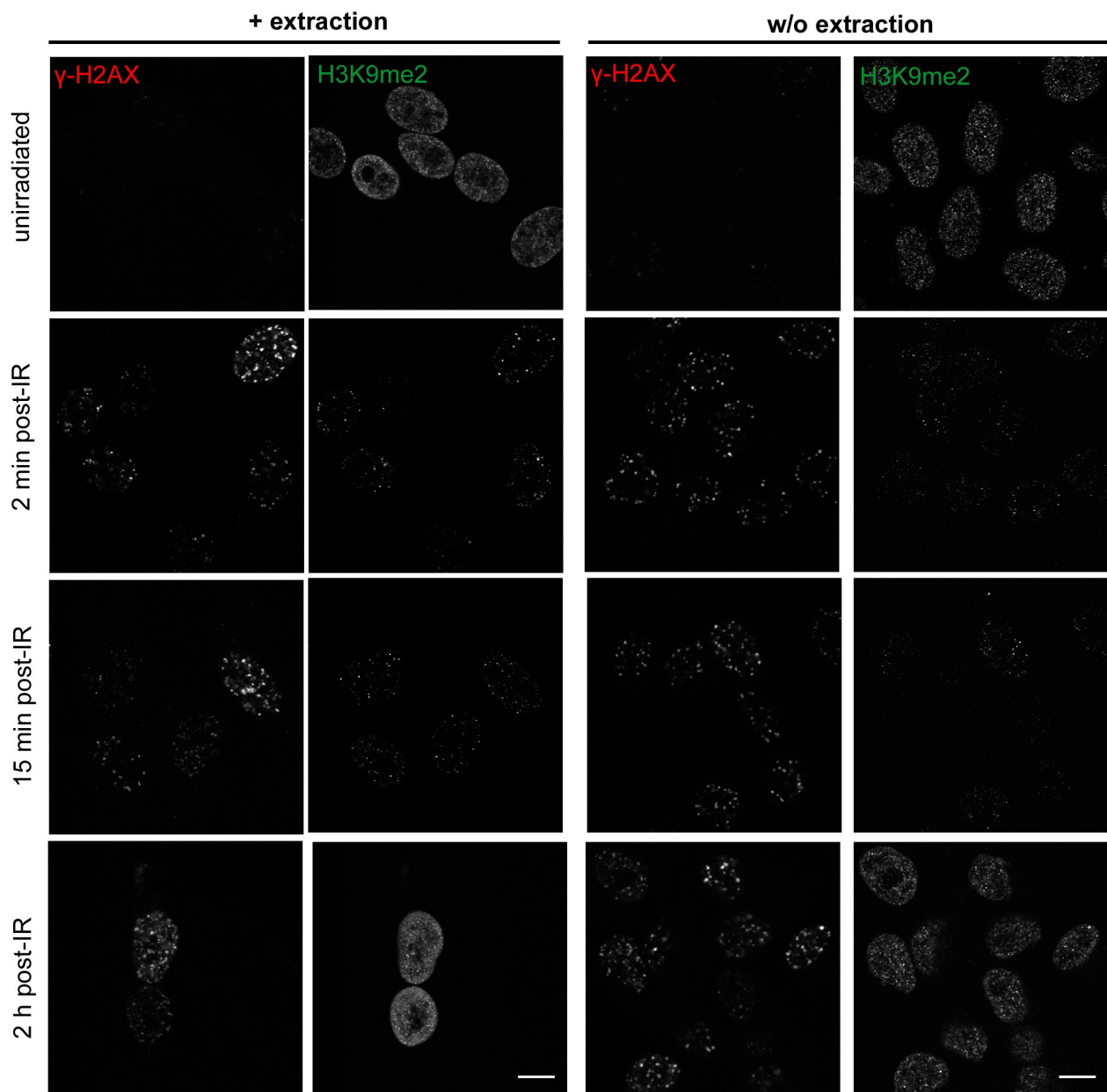
Figure 2.12: Distribution of H3K9me2 in HeLa cell nuclei at different times after X-irradiation with additional extraction of unbound proteins before fixation (left columns) or without (right columns). Times after irradiation are indicted on the left side of the images. Images are confocal single slices showing a number of cell nuclei for each point of time. IRIF are visualized with γ-H2AX (red) and the histone modification H3K9me2 (green). At 2 and 15 min after IR, signal intensity of the green channel was increased and gain of the confocal microscope was therefore decreased to avoid over-exposure. This results in only a few bright spots of high intensity in the green channel. In unirradiated samples and in samples 2 h after IR, the signal intensity was reduced and more homogenously distributed across the cell nucleus. The effect was observed after treatment with extraction buffer or without, respectively. Scale is 10 μm.

2.2.5 H4K5Ac is not increased at damaged sites

Because histone acetylation is associated with a decondensed chromatin status, staining of such acetylated histones is expected to mainly correlate with low intensities of chromatin stained with

DAPI. This was also observed for the histone modification H4K5Ac, the staining of which resulted in an inhomogeneous distribution of signals across the cell nucleus with only a few bright spots of high intensities. This is why only a small number of pixels were obtained in the green channel (H4K5Ac) and thus the quantitative analysis of H4K5Ac distribution and γ-H2AX foci was rather difficult. In Figure 2.13 A,B, brightness and contrast of the green channel were increased to enhance the visibility of the signals. Nevertheless, no local increase of H4K5Ac was observed at regions decorated with γ-H2AX neither at 15 min nor at 2 h after irradiation (Figure 2.13 A,B). By contrast, H4K5Ac appeared even under-represented at some γ-H2AX foci, despite some overlapping areas, at both times after IR (Figure 2.13 A,B). Distribution of PDM values was rather random with both negative and positive PDM values, as well as PDM values close to zero (Figure 2.13, plots in A and B). The PDM plots of PDM values obtained for the green channel (H4K5Ac) at 15 min after IR (Figure 2.13 A, middle plot in the lower row) clearly demonstrates the low number of pixels which were included in the analysis.

According to these data, the histone modification H4K5Ac appears not significantly increased at damaged sites in the times investigated, although the very inhomogeneous distribution hampered an accurate quantification. (O'Hagan et al., 2008) observed local hypoacetylation at an enzyme-mediated DSB analyzed by ChIP analysis. Local hypoacetylation of H4K16Ac was reported together with a local increase of repressive marks (O'Hagan et al., 2008), such as H3K27me3.
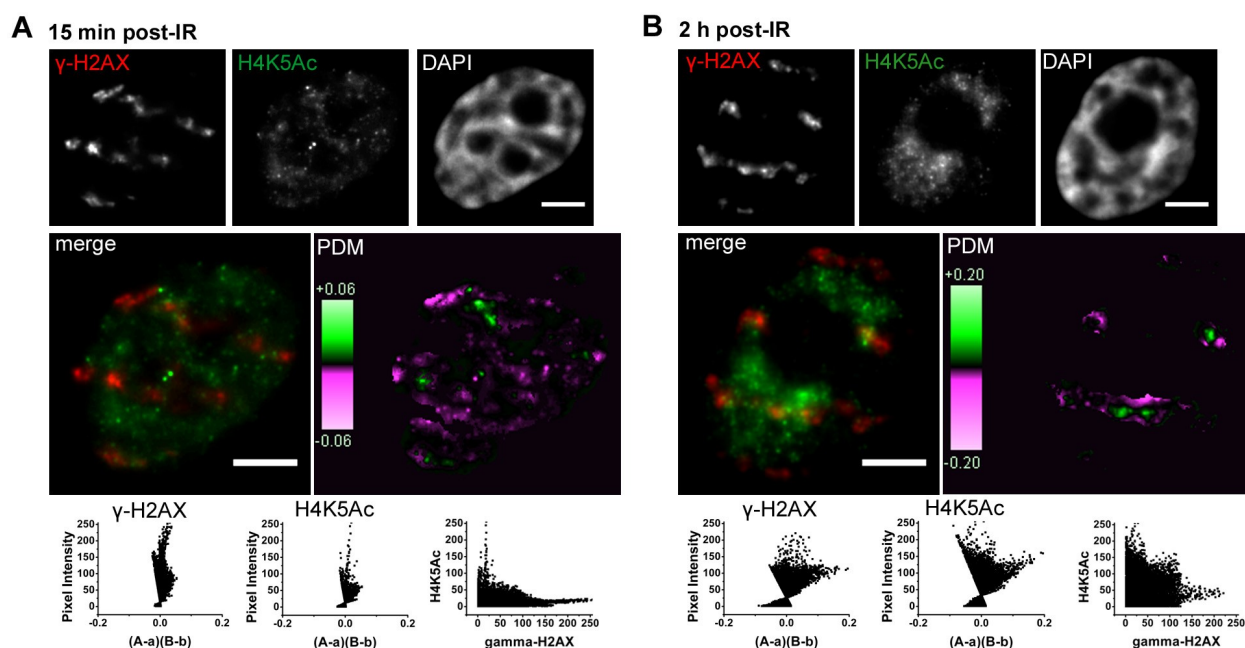
Figure 2.13: Distribution of H4K5Ac and γ-H2AX foci in HeLa cells following ion microirradiation. HeLa cells were fixed at either 15 min (A) or 2 h (B) following irradiation at the microbeam. Epifluorescence images show a representative mid-section of 3D image stacks. Cell were stained with antibodies against γ-H2AX (red channel), H4K5Ac (green channel) and chromatin was counter stained with DAPI (blue channel) (top rows in A and B). Mid rows show a red-green merge and a PDM color-coded image obtained by ICA. In the PDM images (A,B), pink color represents negative correlations, whereas green color represents positive correlations. PDM and and scatter plots (bottom rows) show the distribution of PDM values for each channel and a scatter plot of intensities of the red and the green channel (A,B). H4K5Ac showed an inhomogeneous distribution with a few bright spots with high intensities. H4K5Ac signal localized to regions of low DAPI intensities and were mainly under-represented at γ-H2AX foci with some small overlapping areas. Scale is 5 μm.

2.2.6 H3K27me3 is enriched at DSB sites

H3K27me3 is involved in polycomb-mediated silencing (Kirmizis et al., 2004; Pasini et al., 2008) established by the HMT EZH2 (Margueron et al., 2008). Interestingly, H3K27me3 and EZH2 were enriched at DSB sites (O'Hagan et al., 2008). Next, I tested the local distribution of H3K27me3 after ion microirradiation. Already shortly after irradiation, a slight accumulation of H3K27me3 at a number γ-H2AX foci was observed, which is represented by bright green staining in the color-coded PDM image and a number of positive values in the PDM- and scatter plots (Figure 2.14 A). 2 h after IR, accumulation of H3K27me3 was clearly evident and was confirmed using ICA, where co-localized areas are highlighted in green in the PDM image. Increased accumulation at 2 h after IR is also demonstrated by predominantly positive PDM values at high pixel intensities and by increased positive correlation of intensities shown in the PDM and scatter plots (Figure 2.14 B).
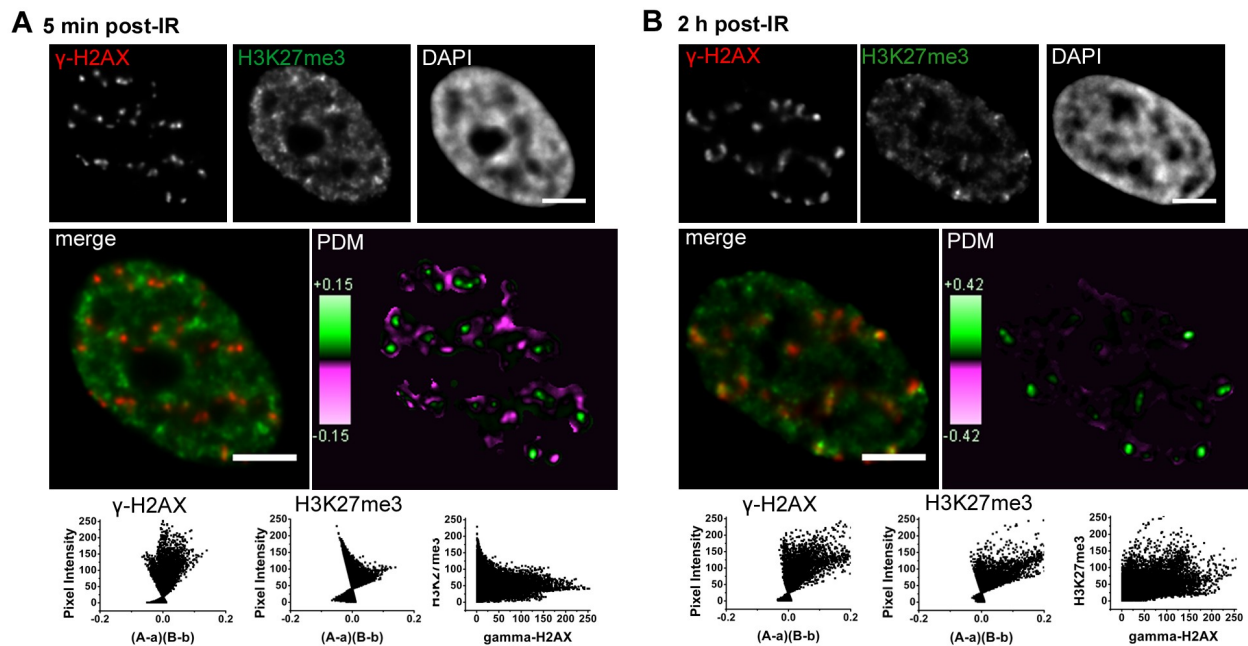
Figure 2.14: H3K27me3 is accumulating at DSB induced by ion microirradiation in HeLa cells. HeLa cells were irradiated at the ion microbeam and fixed either 5 min (A) or 2 h after irradiation (B). Fluorescence images in A) and B) show staining for γ-H2AX (red), H3K27me3 (green) and DAPI (blue) in the top row. Mid row shows red-green merges and the color-coded PDM images. Bright green staining represents co-localization, pink staining represents anti-correlation. At 5 min after IR (A), already slight accumulation of H3K27me3 at a number of γ-H2AX foci was evident (green in the PDM image). At 2 h after IR (B), clear accumulation of H3K27me3 was observed (green in the PDM image). This is also indicated by a large number of positive PDM values with high intensities skewing to the right more pronounced at 2 h after IR (B), and positive correlation is also represented by intensity distribution in the scatter plots (B). Scale is 5 μm.

In the meantime, H3K27me3 accumulation was also shown by others following laser microirradiation (Chou et al., 2010).

Taken together, this result and recent findings described in the literature (O'Hagan et al., 2008; Chou et al., 2010), corroborate the assumption that a repressive chromatin status is established at sites decorated with γ-H2AX. Quantitative analysis used in the present work showed a time-dependent accumulation of HP1β, which is most probably independent from H3K9me2/me3 interactions (Luijsterburg et al., 2009, own results), indicating that the heterochromatin pathway via H3K9 methylation and HP1 interactions might not be involved. Additionally, I also tested the distribution of H4K20me3 at DSB sites, an additional histone modification involved in heterochromatin formation (Schotta et al., 2004). However, the two H4K20me3 antibodies used did highly cross-react with other methyl states of H4K20 and also with other PTMs, as shown by peptide competition assay (Appendix A). Since H3K27me3 and enzymes, such as EZH2, involved in the polycomb pathway were found to accumulate at DNA damaged sites (O'Hagan et

al., 2008; Chou et al., 2010, own results), this hints to polycomb-mediated silencing at DSB sites rather than heterochromatin silencing.

Since Polycomb-mediated transcriptional silencing is generally accompanied by loss of active marks such as H3K4me3, it is tempting to speculate that this modification is altered at damage sites. Preliminary experiments already hinted at an under-representation of H3K4me3 at γ-H2AX foci (Ottmann, 2007). In the following, the distribution of H3K4me3 and further marks for transcriptional activation were analyzed for alterations at chromatin regions damaged by ionizing radiation.

2.2.7 H3K4me3 and γ-H2AX are mutually exclusive

Histone H3 tri-methylated at lysine 4 is associated with transcribed genes and transcriptionally active RNA Polymerase II (Barski et al., 2007). In immunofluorescence images, H3K4me3 staining yields a speckle-like pattern predominantly found in regions of low chromatin density (Zinner et al., 2006 and Figure 2.1 B). In the following, a role of H3K4me3 in DNA damage response was investigated.

Analysis of local distribution of H3K4me3 at DSB

To analyze the distribution of H3K4me3 and γ-H2AX foci in detail, cells were irradiated in a line pattern of 1 μm x 5 μm with the ion microbeam and fixed 2 and 5 h after IR (Appendix C). Specificity of the used H3K4me3 antibody was confirmed by peptide competition assay (Appendix A). By visual inspection of fluorescence images it seemed already apparent that γ-H2AX foci lie predominantly within regions where H3K4me3 is underrepresented (Appendix C). This effect could not be seen as clearly as the exclusion of RNA Pol II (chapter 2.2.2), probably due to the inhomogeneously distributed, speckle-like staining pattern of H3K4me3. Furthermore, this observation has not yet been reported in the literature. Thus it was necessary to exclude a chromatic error source, for example, that under-representation of one signal is caused by quenching effects of one fluorochrome by the other. To test this, secondary antibodies, which are labeled with fluorochromes, were flipped and combined with previously used primary antibodies (Appendix C). γ-H2AX was detected either with Cyanin 3, or with Alexa-488. Simultaneously, H3K4me3 was detected with either Alexa-488 or Cyanin 3. Under-representation of H3K4me3 at γ-H2AX foci was apparent in both cases (Appendix C). Thus artifacts by fluorochrome quenching could be excluded.

Exclusion of H3K4me3 and γ-H2AX was apparent in epifluorescence (Appendix C) and confocal images at different times after ion microirradiation. In confocal images, H3K4me3 staining pattern appeared more defined in comparison to epifluorescence images (Appendix C and Figure 2.15). γ-H2AX foci tracks induced by ion microirradiation almost never overlapped with H3K4me3 signal. This was confirmed using ICA for image evaluation, as represented in the mid rows of Figure 2.15 A, B, where PDM color-coded images show mainly pixels with negative PDM values highlighted in pink and almost no overlapping pixels which would be highlighted in green. Some exclusion was already evident at 5 min after IR and it was more pronounced at 2 h after IR, which is indicated by more negative PDM values at high intensities (PDM plots, Figure 2.15 B). Correlation analysis of epifluorescence images containing a large number of cell nuclei already hinted at a negative correlation which is more pronounced at later times after IR (for evaluation of epifluorescence images using Pearson´s coefficient and ICQ, see Appendix D).

A **5 min**

B **2 h**
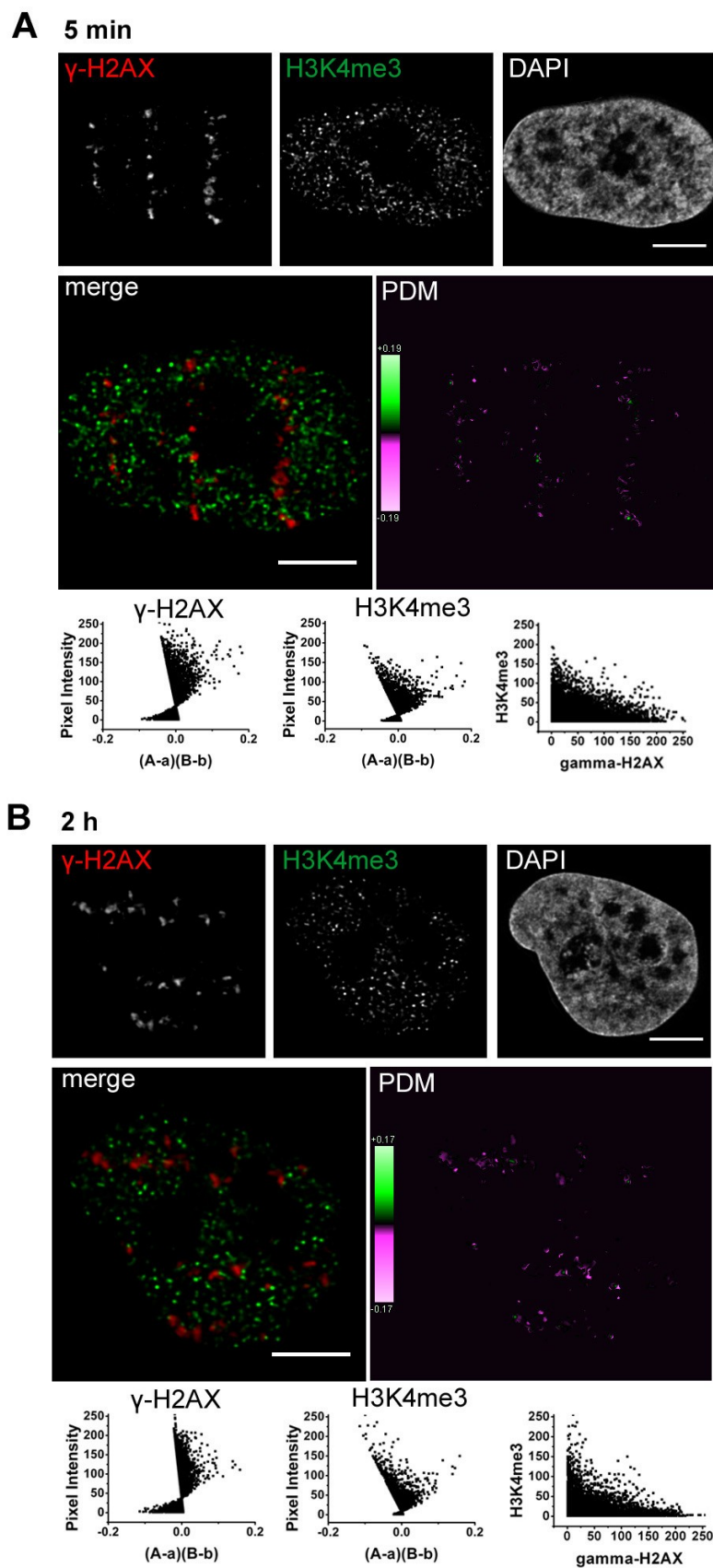
Figure 2.15: Distribution of H3K4me3 and γ-H2AX foci in HeLa cells following ion microirradiation fixed at A) 5min and B) 2 h after IR. Confocal images in A and B upper rows show single slices of mid-sections of a HeLa cell nucleus stained with γ-H2AX (red), H3K4me3 (green) and DAPI (blue). Mid rows show red-green merges and PDM color-coded images. Bottom rows show PDM plots with negative values skewing to the left and a scatter plot indicating distribution of intensities. Almost no overlapping pixels were detectable, demonstrated by the large proportion of negative PDM values. Scale is 5 μm.

Additionally, Spearman´s rank correlation coefficient was calculated for 19 - 20 cell nuclei of confocal image stacks at 5 min and 2 h after IR (Figure 2.16). Confocal images were chosen for statistical evaluation with Spearman´s coefficient, because these images are of higher quality than epifluorescence images. For 19 cell nuclei investigated at 2 h post-IR, all coefficients were negative. At 5 min after IR, most coefficients were slightly negative. Coefficients were ρ_{5min} = -0.019 ± 0.023 (SD) and ρ_{2h} = -0.061 ± 0.034 (SD), respectively (Figure 2.16). For both points of time the coefficients were significantly different from zero (P_0 = 0.015 at 5 min and P_0 = 7.63 x 10^{-6} at 2 h) and significantly different from each other (Mann-Whitney U test; P = 0.0003; *** in Figure 2.16). In addition to this, Spearman´s coefficient was also calculated for 10 cell nuclei 15
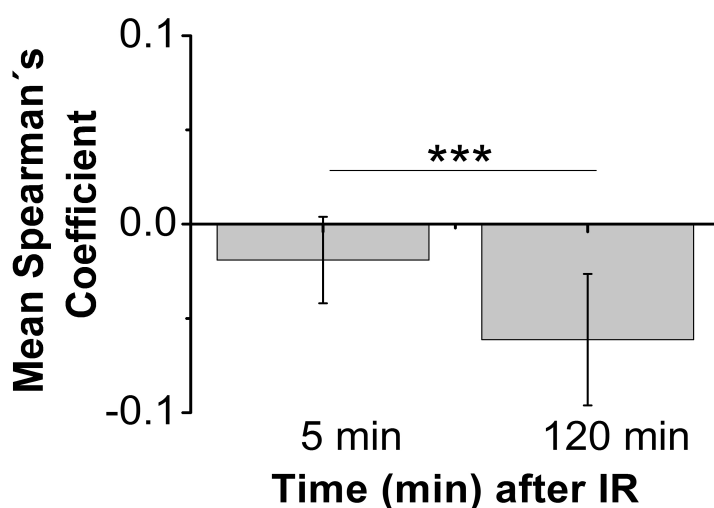
Figure 2.16: Mean Spearman´s rank correlation coefficient ρ for H3K4me3 and γ-H2AX in ion-irradiated HeLa cells. Indicated are mean and standard deviation (SD) of Spearman´s rank coefficients at 5 min (n = 15) and 2 h (n = 19; n = number of cell nuclei). Both coefficients are significantly different from each other (Mann-Whitney U test; ***P = 0.0003) and significantly different from zero (P_0 = 0.015 at 5 min; P_0 = 7.63 x 10^{-6} at 2 h).

min after IR obtained by epifluorescence microscopy (not shown). The coefficient ρ was also negative with ρ_{15min} = -0.059 ± 0.03 (SD), however, it was not significantly different from zero (P_0 = 0.064).

Distribution of H3K4me3 and γ-H2AX following ion microirradiation was also analyzed in BJ1 cells (hTERT-immortalized human fibroblast; Figure 2.17 A,B) and U2OS (human osteosarcoma; Figure 2.17 C,D). In both cell lines, exclusion of H3K4me3 and γ-H2AX was evident indicated by dominant pink color in the PDM color-coded images representing negative PDM values (microscopic images in middle rows of Figure 2.17 A-D). However, PDM values were only slightly negative as represented by PDM plots (bottom rows Figure 2.17 A-D) skewing slightly to the negative range, probably due to the large number of small intensities as discussed previously.
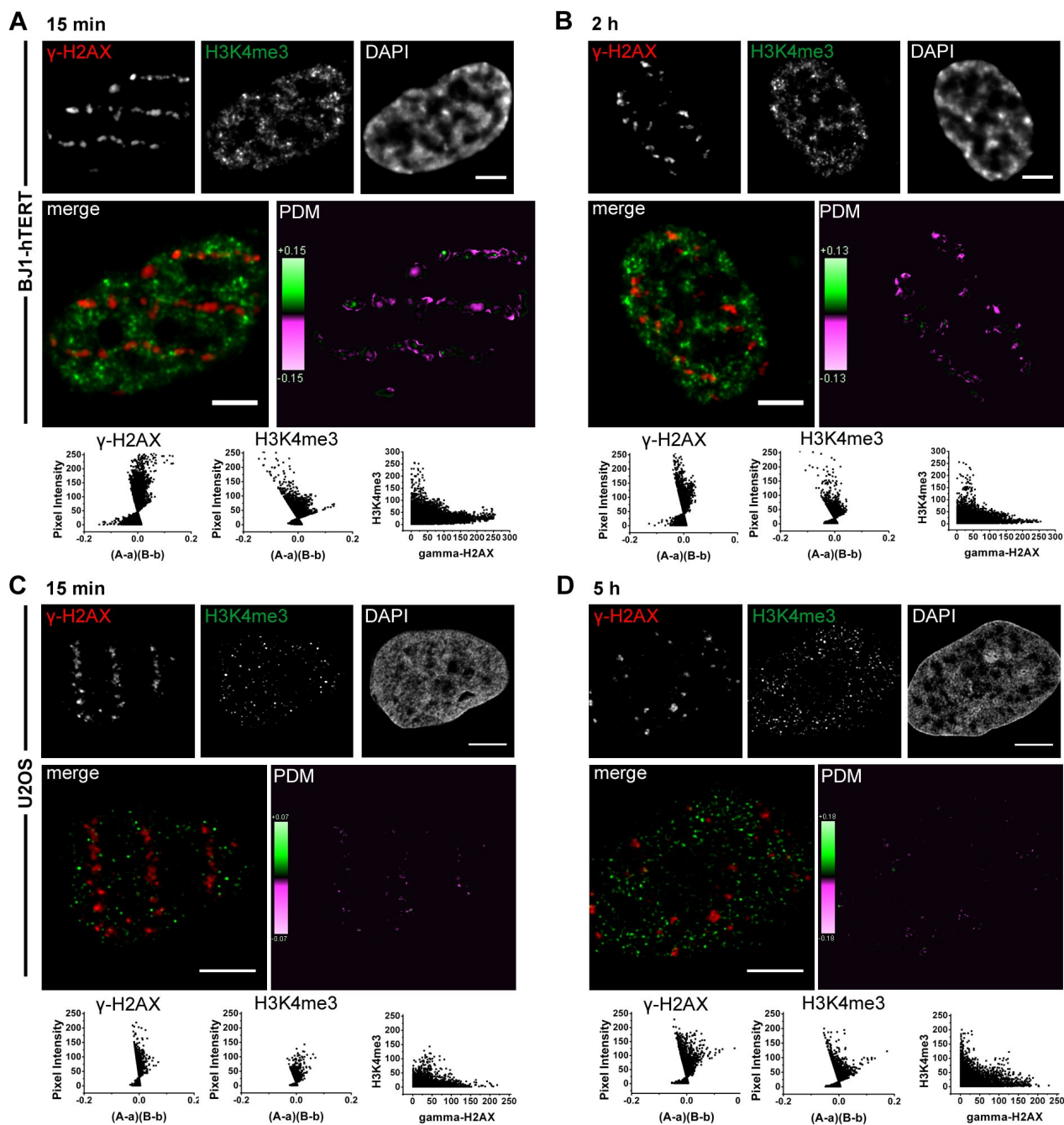
Figure 2.17: Under-representation of H3K4me3 at γ-H2AX foci in BJ1 and U2OS cells following ion microirradiation. Microscopic images show mid-sections of epifluorescence image stacks of BJ1 human fibroblasts 15 minutes (A) and 2 hours (B) after irradiation, and mid-sections of confocal image stacks of U2OS cells 15 min (C) and and 5 hours (D) after irradiation. Upper and mid rows of A-D) show γ-H2AX (red channel), H3K4me3 (green channel), DAPI (blue channel), red-green merges and PDM color-coded images. In the bottom rows in A-D), plots of γ-H2AX and H3K4me3 vs. PDM are shown, as well as the respective scatter plots. In both cell lines H3K4me3 was underrepresented at γ-H2AX foci as is evident from negative PDM values. Scale bars are 5 μm.

Additionally it was tested if this effect is also observable with a different type of ionizing radiation. Therefore, HeLa cells were irradiated with α-particles. Exclusion of H3K4me3 and γ-H2AX was also clearly evident (Figure 2.18). Almost no positive correlation was observed as indicated by dominant pink color in the color-coded PDM images and negative PDM values skewing to the left in the PDM plots (mid and bottom rows of Figure 2.18 A,B).
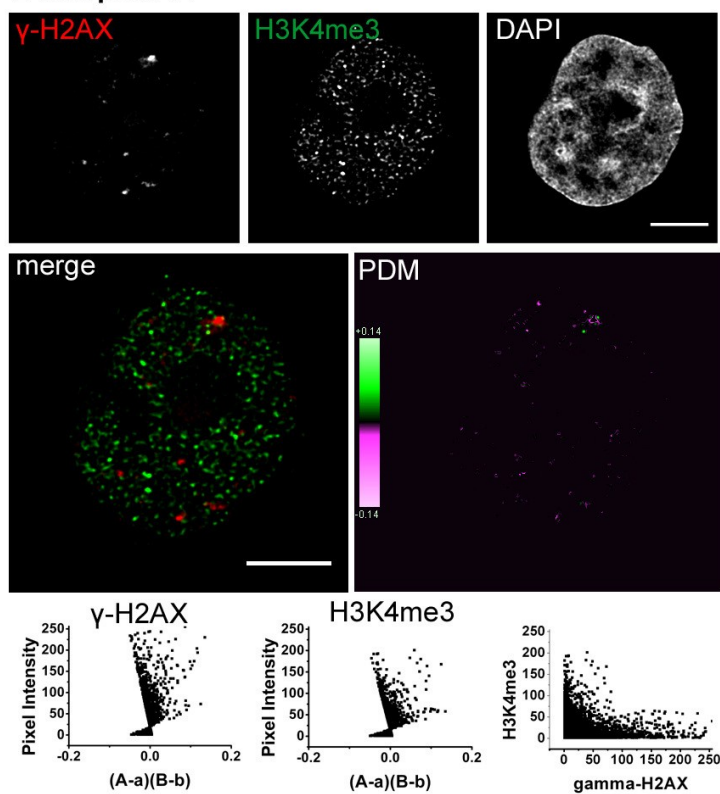
Figure 2.18: Distribution of H3K4me3 and γ-H2AX in HeLa cells after irradiation with α-particles. HeLa cells were irradiated and fixed either 5 min after IR (A) or 2 h after IR (B). Images show mid-sections of confocal image stacks with γ-H2AX in the red channel, H3K4me3 in the green channel, and DNA counter staining with DAPI in the blue channel. Red-green merges and PDM color-coded images are shown in the mid rows of A) and B). Bottom rows show PDM and scatter plots. H3K4me3 was mainly under-represented at γ-H2AX foci, which is demonstrated by pink staining in the PDM image and negative PDM values skewing to the left in the PDM plots. Scale is 5 μm.
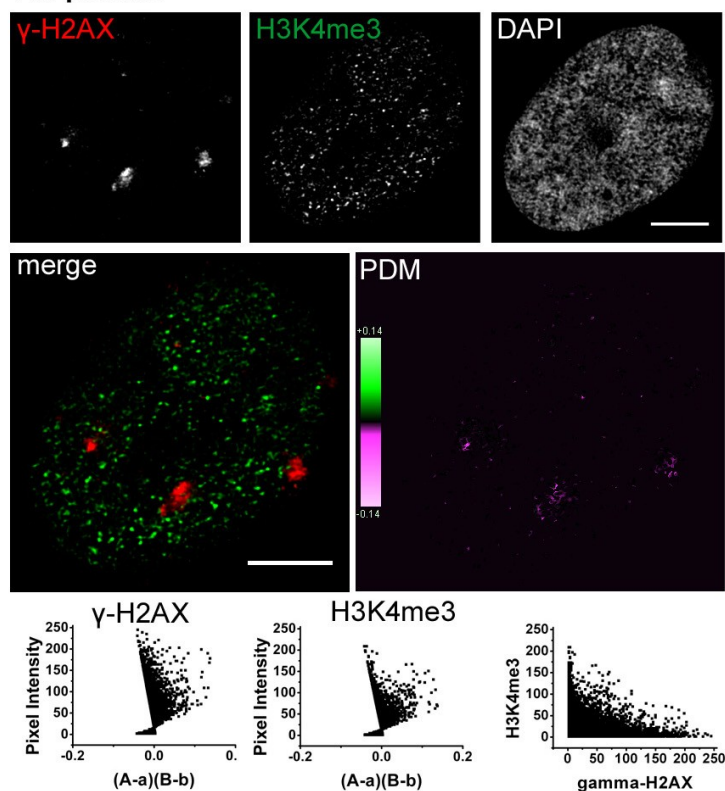
Distribution of H3K4me3 and γ-H2AX in 150-nm ultrathin sections

In ultrathin sections, the fluorescence signals are limited to 150 nm in the z-direction and out-off-focus light is abolished. To test the distribution of H3K4me3 and γ-H2AX also under those improved conditions, ICA was performed for cell nuclei following ultrathin sectioning and 2D confocal image acquisition. In Figure 2.19 an 150-nm ultrathin section of an irradiated HeLa cell nucleus is shown. Anti-correlation of γ-H2AX and H3K4me3 was clearly visible and was confirmed with image evaluation using ICA. Almost no overlapping pixels were detected, which is evident from the pink color in the PDM image (mid row of Figure 2.19) and negative PDM values in the PDM plots (bottom of Figure 2.19). Additionally, three serial sections of one nucleus stained for γ-H2AX and H3K4me3 were also obtained (Figure 2.20). It is demonstrated that H3K4me3 signals are found adjacent to γ-H2AX foci but were not found to directly overlap.

To summarize, the above described results show an exclusion of H3K4me3 and γ-H2AX foci in conventional microscopy and after ultrathin slicing. The mutual exclusion appears to increase with time after irradiation, as indicated by more negative Spearman´s correlation coefficients at 2 h after irradiation. To corroborate this finding, I investigated whether global levels of H3K4me3 are also reduced after irradiation using western analysis.
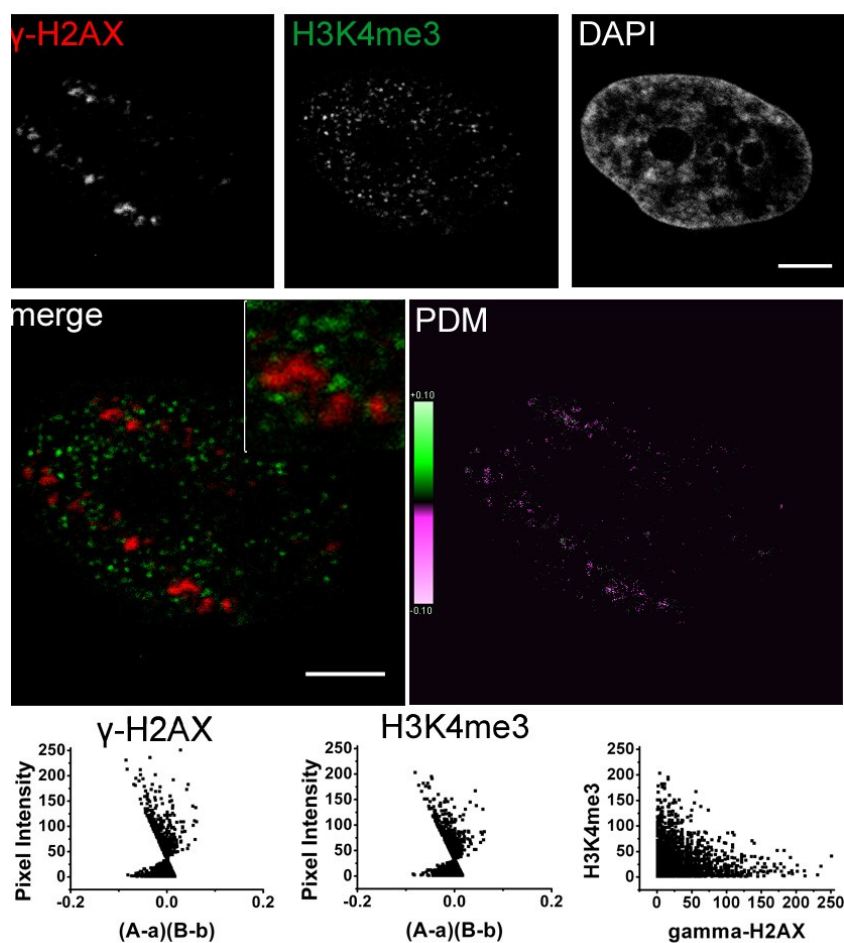
Figure 2.19: Under-representation of H3K4me3 and γ-H2AX in 150-nm ultrathin sections of a HeLa cell nucleus after ion irradiation. Microscopic images show raw confocal images of a HeLa cell nucleus. From these images only background noise was subtracted. Upper row shows γ-H2AX (red), H3K4me3 (green) and DAPI (blue). Mid row shows red-green merge and PDM color-coded image. ICA revealed anti-correlation of γ-H2AX and H3K4me3 in ultrathin sections with almost no overlapping pixels. This is represented by dominant pink staining in the PDM image, which represents negative PDM values. This is also demonstrated by negative PDM values skewing to the left in the PDM plot and anti-correlated signal intensities in the scatter plot (bottom row). Scale is 5 μm. Insert is 5 x 5 μm
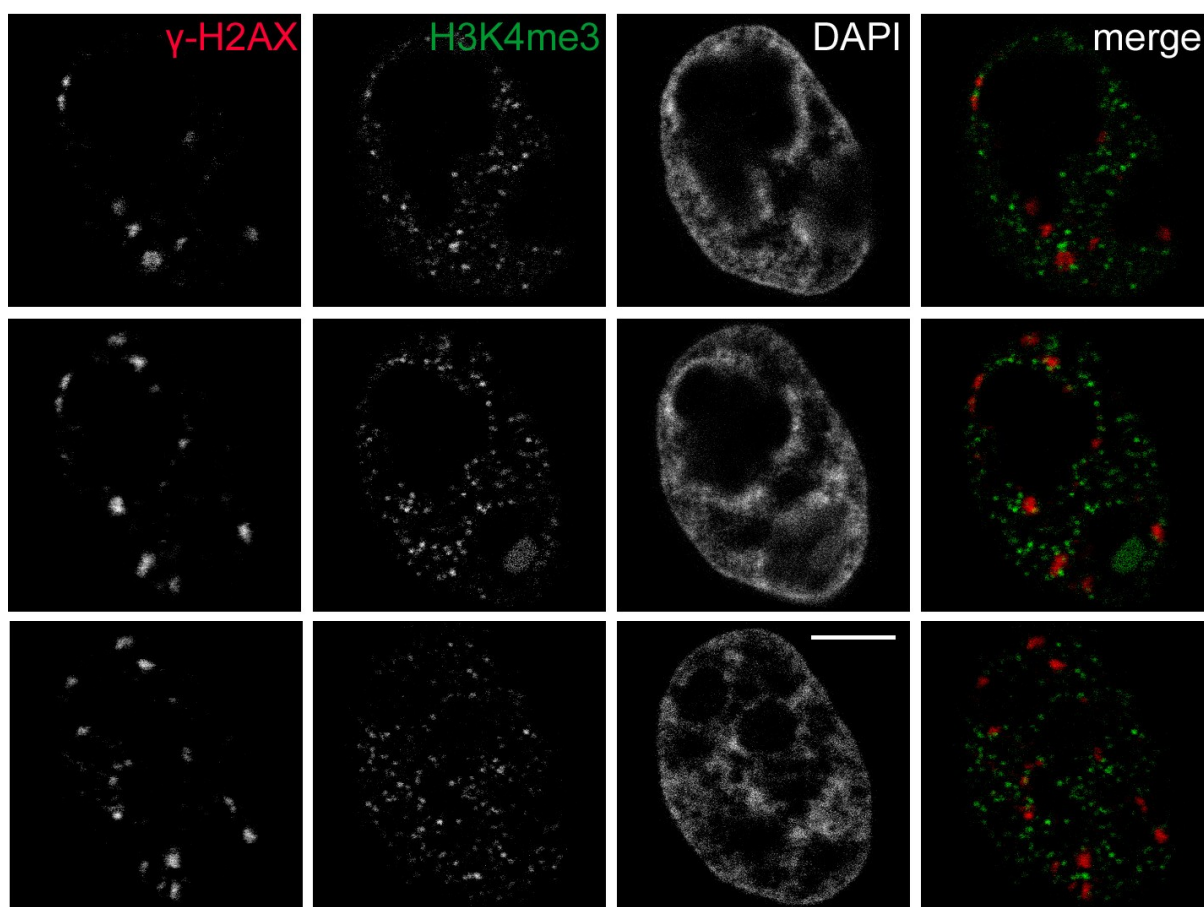
Figure 2.20: Serial 150-nm ultrathin sections of one irradiated HeLa cell nucleus. Shown are raw confocal images of 150-nm ultrathin serial sections (from top to bottom 150 nm each) of a cell nucleus which was stained before sectioning for γ-H2AX (red channel), H3K4me3 (green channel) and DAPI (blue channel). Right panel shows red-green merges. Almost no overlap of H3K4me3 and γ-H2AX foci was observed in serial ultrathin sections. Scale is 5 μm.

Global alterations of H3K4me3 level following irradiation

To detect slight alterations of protein amount in western analysis, quantification of chemiluminescence signal was performed using Bio1D software (peqlab). The amount of protein was then normalized to the loading control, Tubulin-α, and further normalized to the unirradiated control sample. By this, even small alterations can be detected which may not be noticed by visual inspection (B. Mazurek, personal communication).

Using this quantification procedure, I observed a slight reduction of H3K4me3 levels in HeLa whole cell extracts 24 h after x-irradiation with 2 and 10 Gy (Figure 2.21 A). Quantitative evaluation of protein amount of H3K4me3 is shown in Figure 2.22, by which a significant decrease of H3K4me3 24 h after irradiation with 0.5 and 2 Gy, respectively, could be confirmed. The graph shows the means of two independent experiments and standard deviations (SD) from

three blots of each experiment. Levels were normalized to the unirradiated control and to the loading control (Tubulin-α). At 1 and 3 h after IR no significant alteration in H3K4me3 levels was observed (Figure 2.22). The radiation-induced increase of γ-H2AX in these samples is demonstrated in Figure 2.21 B.

Although the time frames in which a decrease of global H3K4me3 levels was observed differed from the time frames of the local decrease of H3K4me3 at γ-H2AX foci, the data suggest that an active process is responsible for the under-representation of H3K4me3.
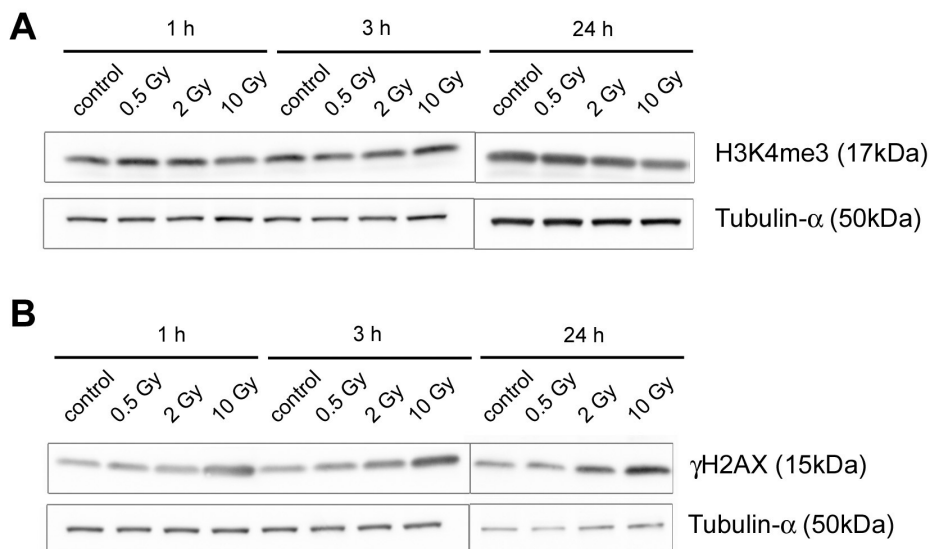
Figure 2.21: Western analysis of whole cell protein extracts from HeLa cells irradiated with different doses of X-ray and after different incubation times. Levels of A) H3K4me3 and whole H3, and B) γ-H2AX are shown at 1, 3 and 24 h after X-irradiation with 0.5, 2 and 10 Gy, respectively. H3K4me3 was slightly decreased 24 h after irradiation with 2 and 10 Gy, respectively (A). γ-H2AX levels increased in a dose-dependent manner and were still detectable at 24 h after IR (B). Tubulin-alpha served as loading control on the same blot as H3K4me3 was detected.
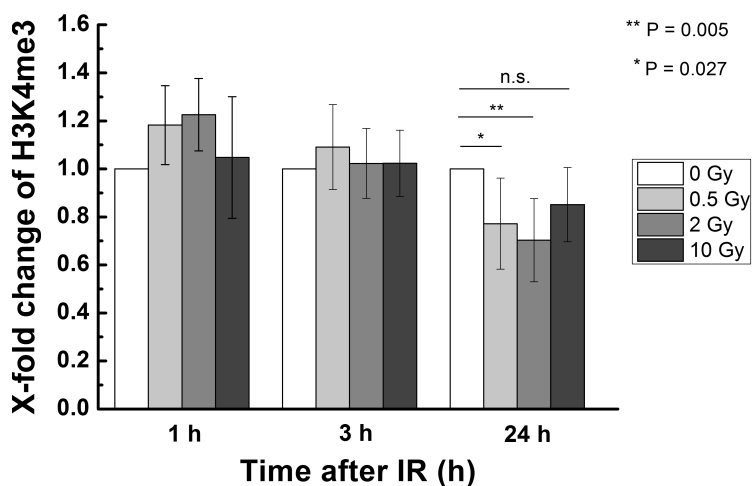
Figure 2.22: Quantification of H3K4me3 levels in western analysis. Western blots were analyzed for protein amount normalized to the loading control (Tubulin-alpha) and the unirradiated control. Shown are mean values and standard deviations (SD) of two independent experiments. Levels of H3K4me3 were significantly decreased in comparison to the respective unirradiated control at 24 h following irradiation with 2 Gy (students t-test).

2.2.8 H3K9Ac and γ-H2AX are mutually exclusive

Because most activated genes which are marked with H3K4me3 are also decorated with acetylation of H3, for example H3K9Ac, this mark was tested in the following for alteration at damaged sites. H3K9Ac also goes along with transcriptional activation. It was shown previously that the loss of H3K9Ac from promotor regions leads to repression of specific genes following DNA damage (Shimada et al., 2008), but no direct role for H3K9Ac at damaged DNA has been investigated so far. I tested if H3K9Ac is altered in the vicinity of DSB. ICA of HeLa cell nuclei following ion microirradiation suggested an under-representation of H3K9Ac at γ-H2AX foci already apparent 5 min post-IR (Figure 2.23 A). This effect was more pronounced at 2 h after IR as indicated by more negative PDM values (PDM plots in Figure 2.23 B), although a few overlapping pixels were observed. These results demonstrate under-representation of H3K9Ac at DSB in addition to loss of H3K4me3.
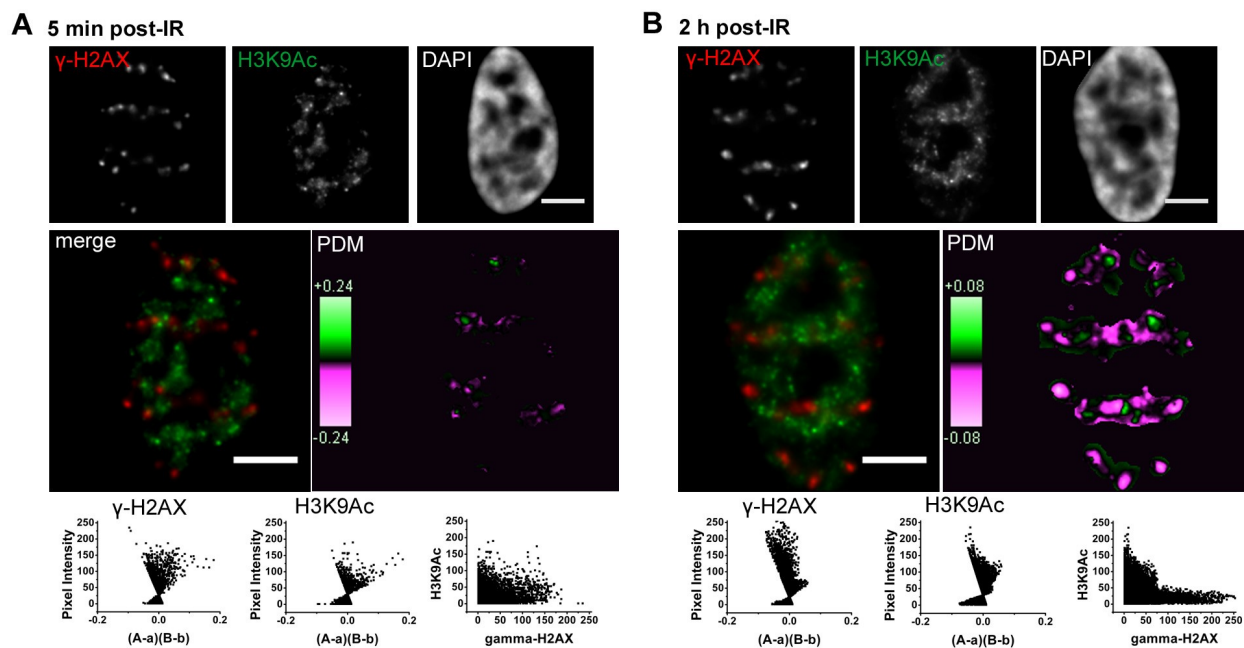
Figure 2.23: Distribution of H3K9Ac and γ-H2AX in HeLa cells after ion microirradiation fixed at A) 5 min and B) 2 h after IR. Microscopic images show single slices of epifluorescence image stacks after staining of cells with γ-H2AX (red), H3K9Ac (green) and DAPI (blue) (top rows). Mid rows show the red-green merges and the PDM color-coded images. Bottom row shows PDM and scatter plots. Mainly negative PDM values (pink in the PDM images and skewing to the left in the PDM plots) in A) and B) were obtained. Negative correlation of red and green signals was more pronounced at 2 h post-IR (B). Brightness/ contrast was enhanced for the green image, because otherwise only few bright signals would be visible. Scale is 5 μm.

2.2.9 Summary

The results described above demonstrate that loss of transcription (loss of initiating and elongating RNA polymerase II) from damaged sites is associated with loss of histone modifications which are known to mark active genes (H3K4me3, H3K9Ac). On the other hand, HP1β and repressive mark H3K27me3 were accumulating at DSB. By contrast, H3K9me3/me2 were not significantly altered at DSB. A statistical analysis suggested a time-dependent alteration of HP1β and H3K4me3 following DNA damage. In the case of H3K4me3, this suggests an active removal process occurring over time. Several mechanisms may be linked to such processes, like histone eviction and deposition of other histone variants or demethylation by the respective enzymes. In the following, several hypotheses are tested to analyze in more detail which processes might be involved in transcriptional repression at DSB sites.

2.3 Potential mechanisms for transcriptional repression at DSB

As discussed in two recent reviews, histone exchange and incorporation mediated by chromatin-remodeling complexes and histone chaperones might contribute to a specific chromatin pattern at DNA damage (Corpet and Almouzni, 2009; van Attikum and Gasser, 2009). In particular, nucleosomes are removed from damaged sites for chromatin opening and, after completion of repair, histones are incorporated to restore the previous pattern. Thus it can be hypothesized that loss of a respective pattern is either the result of active removal of the mark by enzymes or the result of a large-scale removal of the total histone or nucleosome carrying the respective marks from damaged site. In the following, several possible processes were investigated.

2.3.1 Incorporation of histone H3 variants

Incorporation of the histone variant H3.1 by CAF1 was observed at UV-damaged NER sites (Polo et al., 2006). Histone H3 variants are designated to have specific functions in chromatin architecture and function (Hake and Allis, 2006) and are associated with different modification patterns: H3.3 is largely associated with euchromatin and carries mainly modifications marking active genes (like H3K4me3), H3.2 is associated with facultative heterochromatin, and H3.1 with constitutive heterochromatin although in can be also decorated with activating marks (Hake et al., 2006). If loss of active marks went along with histone deposition, histones carrying active marks might be removed from the nucleosome.

Thus I tested if any of these variants is altered in relation to DSB induced by ionizing radiation. For this, HeLa cells expressing HA-tagged H3 variants (kind gift of S.B. Hake) were irradiated with the microbeam. Before, I tested whether the H3.3 variant overlaps with the H3K4me3 staining pattern by concomitant immunofluorescence of HA-tagged H3.3 and H3K4me3. Figure 2.24 shows that their staining patterns are overlapping to some extent, but are not completely similar.

In Figure 2.25, images and ICA for ion-irradiated HeLa cells expressing three different H3 variants, A) H3.3, B) H3.2, and C) H3.1, and cells containing an empty vector in D) are shown 2 h after IR. In D) a representative image of cells containing the empty-HA vector and stained with anti-HA is shown without ICA. Evaluation with ICA indicated that the H3.3, H3.2 and H3.1 variants are overlapping with γ-H2AX foci but are not enriched or absent from γ-H2AX foci. Negative and positive PDM values were obtained indicating a random distribution. Furthermore, areas with clear positive correlations for all three variants and γ-H2AX are present, as indicated

by bright green staining in the PDM color-coded images (Figure 2.25). In comparison to H3K9me2/me3, more overlapping areas are observed in these images. Because the pattern of the H3 variants is quite homogeneously distributed across the cell nucleus, this most probably explains the partial overlap of γ-H2AX and the respective H3 variant.

In conclusion, no significant loss or accumulation of the H3 variants was observed, which suggests that removal of histone H3 variants is not the process mainly responsible for the loss of active H3 modifications from regions decorated with γ-H2AX.
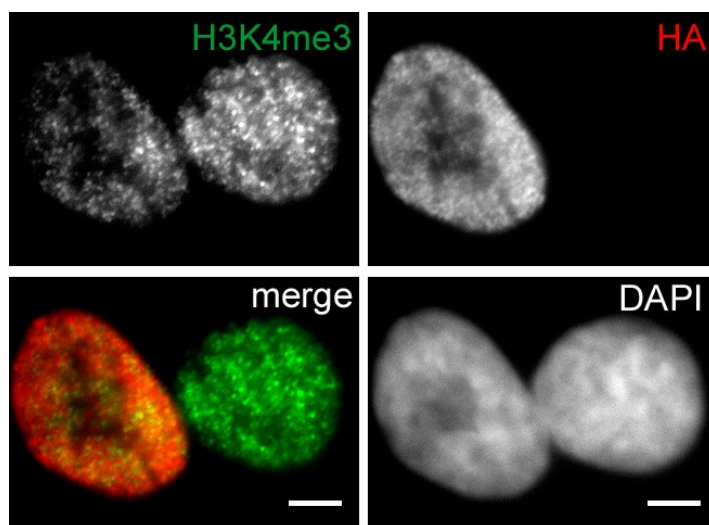
Figure 2.24: Distribution of H3.3 variant and H3K4me3 in HeLa cells stably expressing HA-tagged H3.3 variant. Images show in the upper row staining for H3K4me3 (green) and anti-HA (red), in the lower row red-green merge and chromatin stained with DAPI (blue). The left cell nuclei is positive for anti-HA, the right cell is negative (upper right image). Staining pattern of H3.3 (HA) and H3K4me3 was similar to some extent. They both coincide with regions of low chromatin density. However, the staining patterns were not completely overlapping. Scale bars are 5 μm.
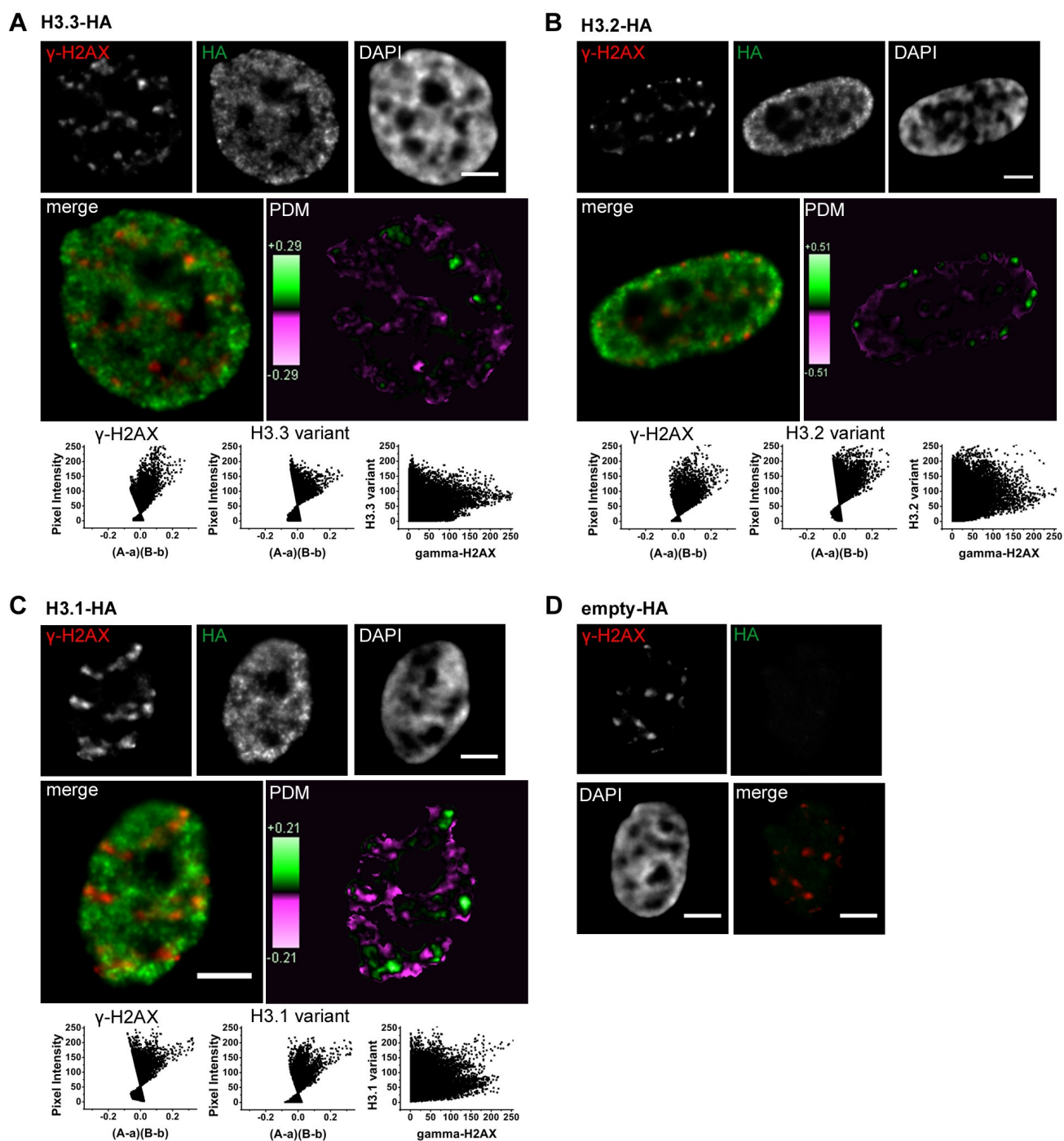
Figure 2.25: Distribution of Histone H3 variants and γ-H2AX foci in HeLa cells following ion microirradiation. Microscopic images show mid-sections of 3D epifluorescence microscopic images of HeLa cells stably expressing HA-tagged H3 variants. Shown are the H3 variants A) H3.3, B) H3.2, C) H.3.1, and in D) cells transfected with an empty HA-vector. Cells were labeled with anti-HA (green), co-stained with γ-H2AX foci (red) and DAPI (blue) (upper rows in A, C and upper and mid rows in D). Mid rows show a red-green merge and a PDM color-coded image in A-C). In D) only representative images are shown without ICA. Bottom rows in A-C) show PDM plots and a scatter plot. Positive and negative PDM values were obtained for high pixel intensities. Scale is 5µm.

2.3.2 Incorporation of new histones marked with H3K56Ac

Acetylation of H3K56 is a very recently detected modification in mammalian cells found on active and inactive gene promoters (Xie et al., 2009). H3K56Ac is located in the core unit of histone H3 and not on the N-terminal tail. Its role in mammalian cells in not clear yet and current findings are controversial (Corpet and Almouzni, 2009). (Das et al., 2009) suggest an increase following damage (γ-irradiation, UV and MMS treatment) and co-localization with γ-H2AX (seconds to minutes after γ-irradiation). Additionally, they suggest that histones are marked with H3K56Ac for incorporation by the chromatin-remodeler CAF1 following DNA damage (Das et al., 2009). On the other hand, (Tjeertes et al., 2009) report a global decrease of H3K56Ac after DNA damage, and, more recently the recruitment of histone deacetylases (HDAC1 and HDAC2) to DNA damage with a subsequent decrease of H3K56Ac was shown (Miller et al., 2010). In yeast, an involvement of H3K56Ac in the completion of repair was suggested (Chen et al., 2008), which might lead to an increase of this mark after completion of repair.

The situation for H3K56Ac at γ-H2AX foci induced with the ion microbeam was tested for HeLa cells (Figure 2.26 A,B) using an antibody which was previously used in the study of (Tjeertes et al., 2009) and tested for specificity in western analysis. Most pixel pairs of γ-H2AX and H3K56Ac were anti-correlated (pink in the PDM image, mid rows in Figure 2.26 A,B) and PDM values were slightly negative, skewing to the left in the PDM plots (diagrams in Figure 2.26 A,B). However, although some overlapping areas were observed (green in the PDM image and positive in the PDM and scatter plots in Figure 2.26 A,B), no significant accumulation of H3K56Ac could be observed at both times after irradiation (5 min and 2 h). Instead, H3K56Ac was rather under-represented at γ-H2AX foci. These findings are in agreement with (Tjeertes et al., 2009) and (Miller et al., 2010) who reported a decrease of H3K56Ac after DNA damage. Thus it can be concluded that H3 histones are not primarily marked with K56Ac at damaged sites at the times investigated.

Taken together, since histone H3 variants and also methylated H3K9 were not significantly altered in the vicinity of DSB and the histone mark H3K56Ac was not primarily enriched at DSB, this suggests that large-scale histone eviction is not the major mechanisms involved in the early response to DNA damage. Another possible mechanisms responsible for the under-representation of trimethylated H3K4 is the active demethylation of H3K4 at DSB. In the following I tried first, to find indications for a possible demethylase activity by investigating the

other methyl states of H3K4, and second, to point out a candidate demethylase among the five H3K4 demethylases known at present.
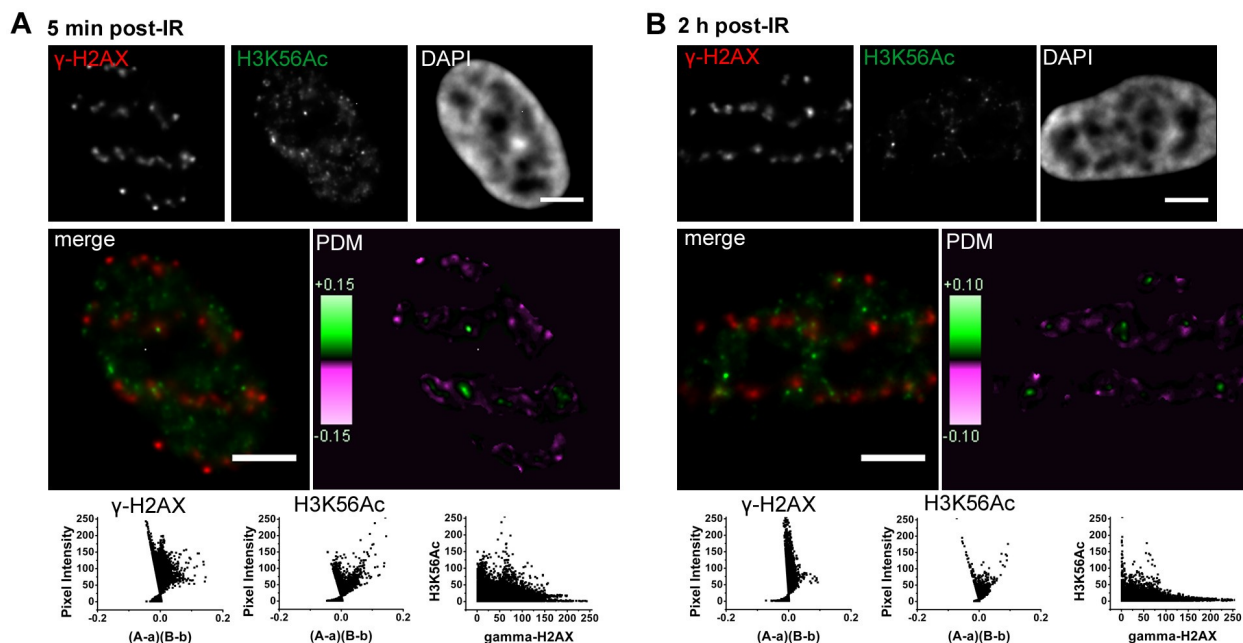
Figure 2.26: Distribution of H3K56Ac and γ-H2AX foci in ion-microirradiated HeLa cells. Cell were irradiated and fixed at A) 5 min post-IR, and B) 2 h post-IR. Microscopic images show mid-section of epifluorescence image stacks of cells stained with γ-H2AX (red), H3K56Ac (green) and DAPI (blue) in the upper row. Mid rows in A) and B) show a red-green merge and a PDM color-coded image. Pink color represents negative correlated pixel pairs of the red and the green channel, whereas green color represents positive correlation. PDM and scatter plots in bottom rows show the PDM values for red and green channel (left and mid panel) and distribution of intensities of both channels (right panel). Most pixels were anti-correlated despite a few co-localized pixels. Moreover, PDM values were only slightly negative in B). Intensities of the green channel were rather small despite a few bright spots which results in a small number of analyzed pixel pairs. Thus contrast was enhanced for better visualization. Scale is 5 μm.

2.3.3 Histone demethylation

Since the year 2007 five demethylases with the ability to demethylate H3K4me3 have been identified (reviewed in Cloos et al., 2008). Among these, the family of Jarid1 proteins specifically demethylates H3K4me3 and me2 (Christensen et al., 2007; Iwase et al., 2007; Klose et al., 2007; Yamane et al., 2007). Assuming that the under-representation of H3K4 at γ-H2AX foci is mediated by a demethylase, I tested the distribution of the lower methyl states of H3K4, H3K4me2 and H3K4me1, at γ-H2AX foci.

Under-representation of H3K4me2 at DSB hints to demethylase activity

To test if the different methyl states of histone H3 at lysine 4, H3K4me2 and H3K4me1, are enriched or are absent from DSB, HeLa cells were irradiated with the ion microbeam and images were analyzed with ICA (Figure 2.27). In Figure 2.27 B,C H3K4me2 and H3K4me1, respectively, are shown 5 h after irradiation. For comparison, under-representation of H3K4me3 is shown at 5 h after IR (Figure 2.27 A). The dimethylated form of H3K4 was also strongly anti-correlated, as represented by mainly pink colors in the PDM image and negative PDM values at high intensities, as shown in the plots (Figure 2.27 B). The monomethylated form of H3K4 was also anti-correlated. However, also some small overlapping areas were observed, demonstrated by slightly more positive PDM values in the PDM plots (Figure 2.27 C).

I conclude that these patterns are compatible with the action of a demethylating enzyme. At present, four demethylases of the JARID1 family are known to demethylate H3K4me3/me2 (Jarid1A-D). A fifth demethylase, FBXL10, was also shown to demethylate H3K4me3 but not H3K4me2 (Frescas et al., 2007). Since Jarid1A (also known as RBP2 or KDM5A) was implicated in the DNA damage response by others (Hayakawa et al., 2007) and since it acts in concert with the polycomb repressive complex 2 (PRC2) to establish a repressive chromatin status (Pasini et al., 2008), I investigated in the following if Jarid1A is accumulating at DSB sites.
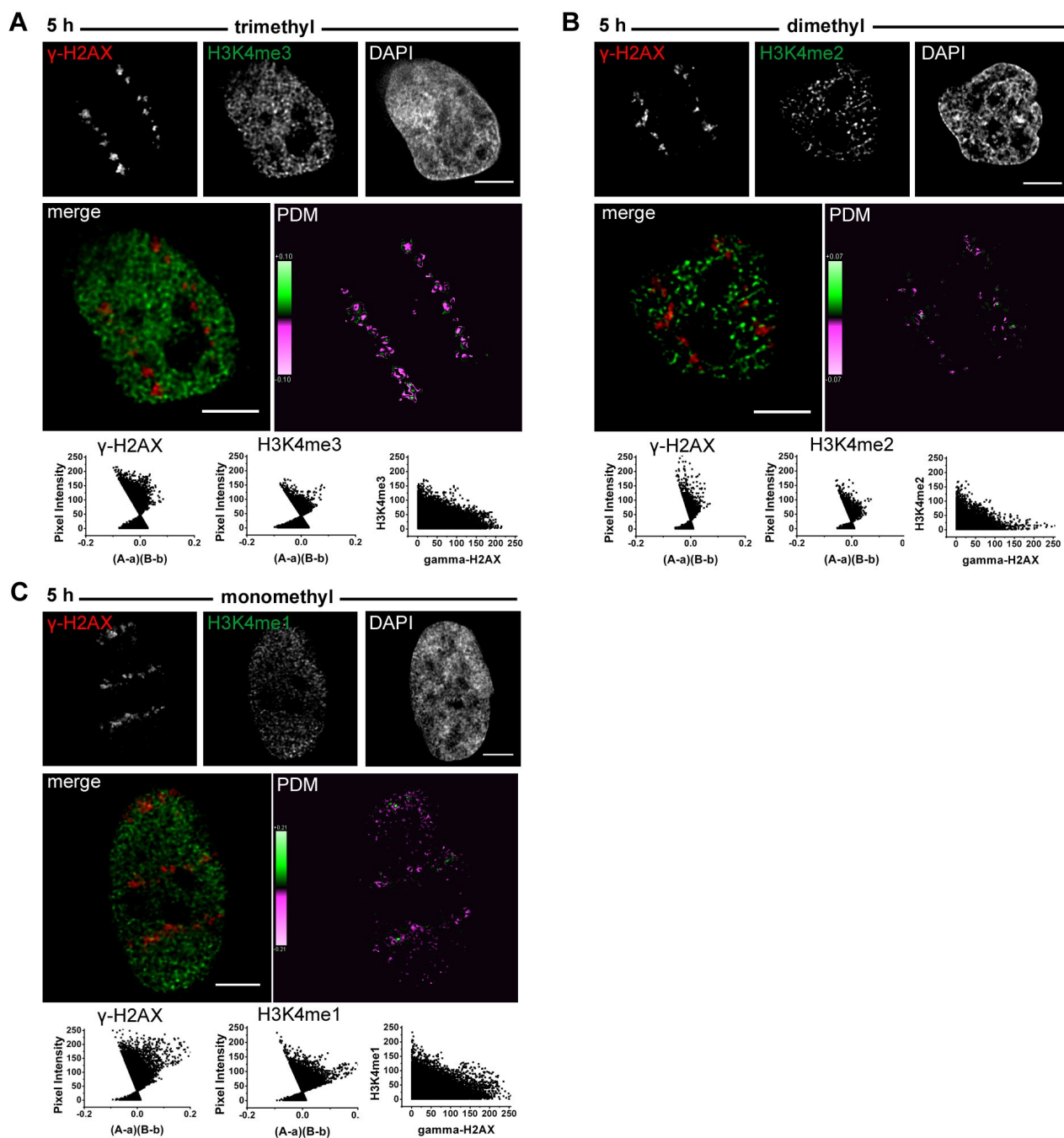
Figure 2.27: Under-representation of different H3K4 methyl states at γ-H2AX foci following ion microirradiation of HeLa cells. Correlation analysis shows distribution of H3K4me3 (A), H3K4me2 (B), and H3K4me1 (C) and γ-H2AX in HeLa cells at 5 h post irradiation. Microscopic images show single slices after 3D confocal microscopy with γ-H2AX (red channel), the respective H3K4 methyl state (green channel) and chromatin (DAPI; blue channel) in the upper rows, merges and PDM maps in the middle rows, and PDM plots of g-H2AX and the respective H3K4 methyl state, as well as the respective scatter plots in the bottom rows. All three methyl states were anti-correlated 5 h after ion microirradiation. The monomethylated form, H3K4me1, showed also some positive PDM values for pixels with high intensities. Scale bars are 5 μm.

Demethylation by specific demethylases

In 2008, Pasini and coworkers identified Jarid1A as a demethylase involved in Polycomb-mediated silencing during differentiation by interaction with PRC2 (Pasini et al., 2008). Components of PRC2 are the three PcG proteins, EZH2, EED, and SUZ12. EZH2 has lysine methyltransferase (KTM) activity and specifically trimethylates H3 at lysine27 (Sarma et al., 2008). Loss of transcriptional activity (decrease of H3K4me3) and development of a repressive status (increase of H3K27me3) at DNA damage, as shown in the present work, are similar to the observations made by (Pasini et al., 2008) for developmental genes. Moreover, a recent study by (Chou et al., 2010) also shows the recruitment of the PRC2 component EZH2, enrichment of H3K27me3 and recruitment of PARP to laser-induced damage. Further, as Jarid1A was implicated in DNA repair mechanisms due to interaction with the MRG15 complex which associates with TIP60 (Hayakawa et al., 2007), Jarid1A seemed to be a good candidate for actively removing tri- and dimethylation from H3K4 at DSB.

The histone demethylase Jarid1A accumulates at UV-laser-induced damage

Two isoforms of Jarid1A are known which can be distinguished by their length (Beshiri et al., 2010). Both isoforms contain a N-terminal and a central PHD (plant homeo) domain, which is able to interact with methylated H3K4 (Wang et al., 2009). In addition to this, the large isoform contains a C-terminal PHD domain which also binds H3K4me3/me2. The small isoform is lacking this C-terminal region. A draft of the large and the small Jarid1A isoform is shown in (Appendix E). To detect Jarid1A in immunofluorescence, two different antibodies were used which specifically recognize either the large Jarid1A isoform (Bethyl) or both isoforms (Cell Signaling – CST). The antibody obtained from Bethyl recognizes the large isoform of Jarid1A by binding a region between C-terminal amino acids 1640 – 1690 of Jarid1A (Appendix E). Staining pattern of Bethyl antibody results in a few small, but intense spots within the cell nucleus and a more moderate signal present in the nucleoli (Figure 2.28, and Benevolenskaya et al., 2005). The antibody obtained from Cell Signaling recognizes both isoform with a peptide specific for the region around Arg280 (communicated by Cell Signaling technical support) and results in an intense speckle-like pattern distributed across the nucleus with almost no signal in the nucleoli (Figure 2.29).

Various types of ionizing radiation were applied to HeLa cells to investigate if Jarid1A is recruited to DSB sites. Neither x-irradiation, nor α-irradiation nor ion microirradiation led to a detectable enrichment of Jarid1A large isoform to γ-H2AX foci at the times investigated (Figure 2.28). Additionally, recruitment of Jarid1A was tested with the second antibody recognizing both isoforms following α-irradiation (Figure 2.29, first and second row). However, no recruitment was observed using this antibody. Additionally, accumulation of EZH2 was tested, which is a component of the PRC2 complex and which was shown to accumulate at laser-induced damage (Chou et al., 2010), but EZH2 could not be detected following α-irradiation (Figure 2.29, third and bottom row).
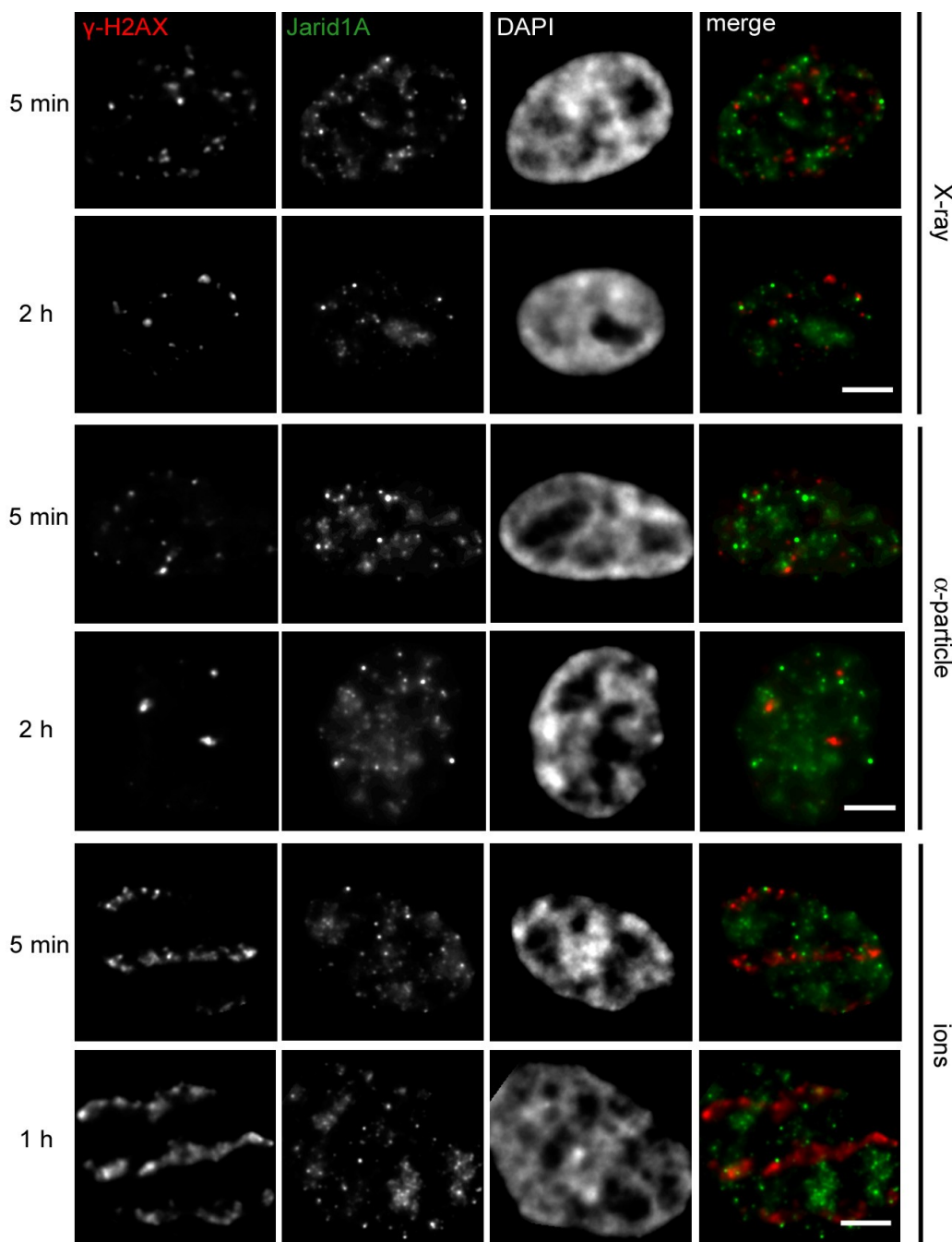
Figure 2.28: No recruitment of H3K4me3/me2 demethylase Jarid1A (Bethyl antibody) to γ-H2AX after different types ionizing radiation. Microscopic images show single slices after epifluorescence 3D microscopy with γ-H2AX (red channel), Jarid1A (green channel) and chromatin (DAPI, blue channel). HeLa cells were irradiated with different types of ionizing radiation (X-ray, α-particles, and ions) as indicated on the right site of the images. On the left side of the images, incubation time after IR is indicated. In most cells, Jarid1A showed a slight accumulation in nucleoli, but no enrichment at chromatin decorated with γ-H2AX. Scale bars are 5 μm.
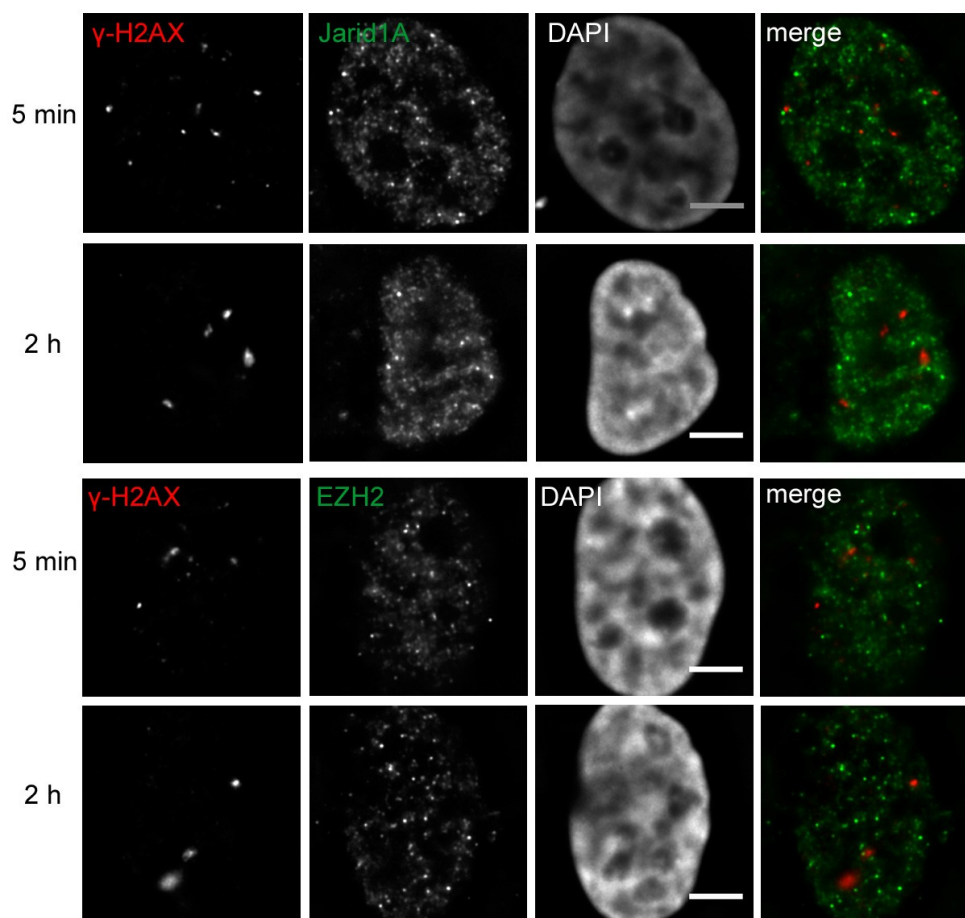
Figure 2.29: No recruitment of Jarid1A (CST antibody) or EZH2 to γ-H2AX foci after alpha-particle irradiation. Images show mid-sections of epifluorescence image stacks. Cells were stained with γ-H2AX (red channel), Jarid1A (green channel) (first and second rows) or EZH2 (third and last row), and chromatin (DAPI, blue channel). Cells were irradiated with α-particles and fixed at either 5 min or 2 h after IR (indicated on the left). Neither accumulation of Jarid1A nor of EZH2 at γ-H2AX foci was observed. Scale bars are 5 μm.

It is possible that the number of recruited proteins to single ionizing-radiation-induced DSBs is too small and cannot be detected with common immunofluorescence (Suzuki et al., 2011). Because laser-irradiation induces a large number of DSB to a restricted area and thus the density of DSB is high, accumulation of some proteins, which do not visibly accumulate after IR, can be detected following laser microirradiation. An example is the chromatin-remodeler ACF1, which was recruited to laser-induced damage but could not be observed at ion-induced damage (Sánchez-Molina et al., 2011, and S. Auer, personal communication). Thus, I tested if Jarid1A was accumulating following laser microirradiation. For this, living cells were irradiated at the spinning-disk microscope with an 405 nm laser with a spot size of 1 μm. One to two spots per cell nucleus were induced and accumulation of γ-H2AX was detectable at the sites of damage

induction (Figure 2.30). Foci formation of γ-H2AX indicates that DSB are also induced by that kind of damage induction. In addition to this, and in contrast to the situation after ionizing radiation, a slight accumulation of Jarid1A at laser damage sites was detectable with both antibodies 30 min following irradiation (Figure 2.30 A,B). Both antibodies were detectable at γ-H2AX foci. Overlap of γ-H2AX and single bright spots of Jarid1A detected by the Bethyl antibody, which recognizes the large isoform (Figure 2.30 B), suggests a recruitment of this Jarid1A-isoform to DSB. In addition, at spontaneously formed γ-H2AX foci also present in the same cell but of much less intensity (Figure 2.29 A), no accumulation of Jarid1A was observed.

To verify that loss of H3K4me3 at γ-H2AX foci is also evident after laser-induced damage, distribution of H3K4me3 was also tested after laser microirradiation (Figure 2.30 C). At the site of a large damaged-induced γ-H2AX focus (indicated by the white arrow) exclusion of H3K4me3 was clearly visible 30 min after radiation and was confirmed with correlation analysis (Figure 2.30 C).

Similarly, EZH2 was observed to slightly accumulate at UV-laser-induced damage 30 min after irradiation (Figure 2.30 D).

During the course of my work, a report by (Faucher and Wellinger, 2010) showed an increase of H3K4me3 at an enzyme-mediated DSB between 20 and 90 min after damage induction in yeast using ChIP analysis. Because H3K4me3 was also under-represented at 15 min after ion microirradiation (chapter 2.2.7) and 30 min after laser irradiation (Figure 2.30 C), I reason that these difference are due to the different organisms and methods used. However, to verify accumulation of Jarid1A between 20 and 90 min, I repeated the above described experiment using laser irradiation in a rectangle of 1 μm x 18 μm size (Figure 2.31 A-C). Jarid1A was recruited to laser-induced γ-H2AX sites at all times investigated (Figure 2.31 A-C). The antibody used for the detection of Jarid1A in this experiment recognizes only the large isoform (Appendix E, and Beshiri et al., 2010) and was kindly provided by E. Benevolenskaya. In Figure 2.31 B, sites of strong correlation of Jarid1A and γ-H2AX are seen, as well as areas of anti-correlation. In the anti-correlated area, the laser-irradiated line passes a nucleolus in which γ-H2AX signal was still detectable but not Jarid1A (Figure 2.31 B).

To summarize, following different types of ionizing radiation (x-ray, alpha-particle and ions), no recruitment or accumulation of Jarid1A or EZH2 was observed. By contrast, after laser microirradiation, accumulation of Jarid1A to γ-H2AX sites could be detected. Additionally, exclusion of H3K4me3 and γ-H2AX and slight accumulation of EZH2 at γ-H2AX foci could be

demonstrated after laser-spot irradiation. The accumulation of Jarid1A, including its large isoform, to γ-H2AX foci following laser irradiation suggests that Jarid1A is involved in the removal of H3K4me3/me2 from damaged sites.
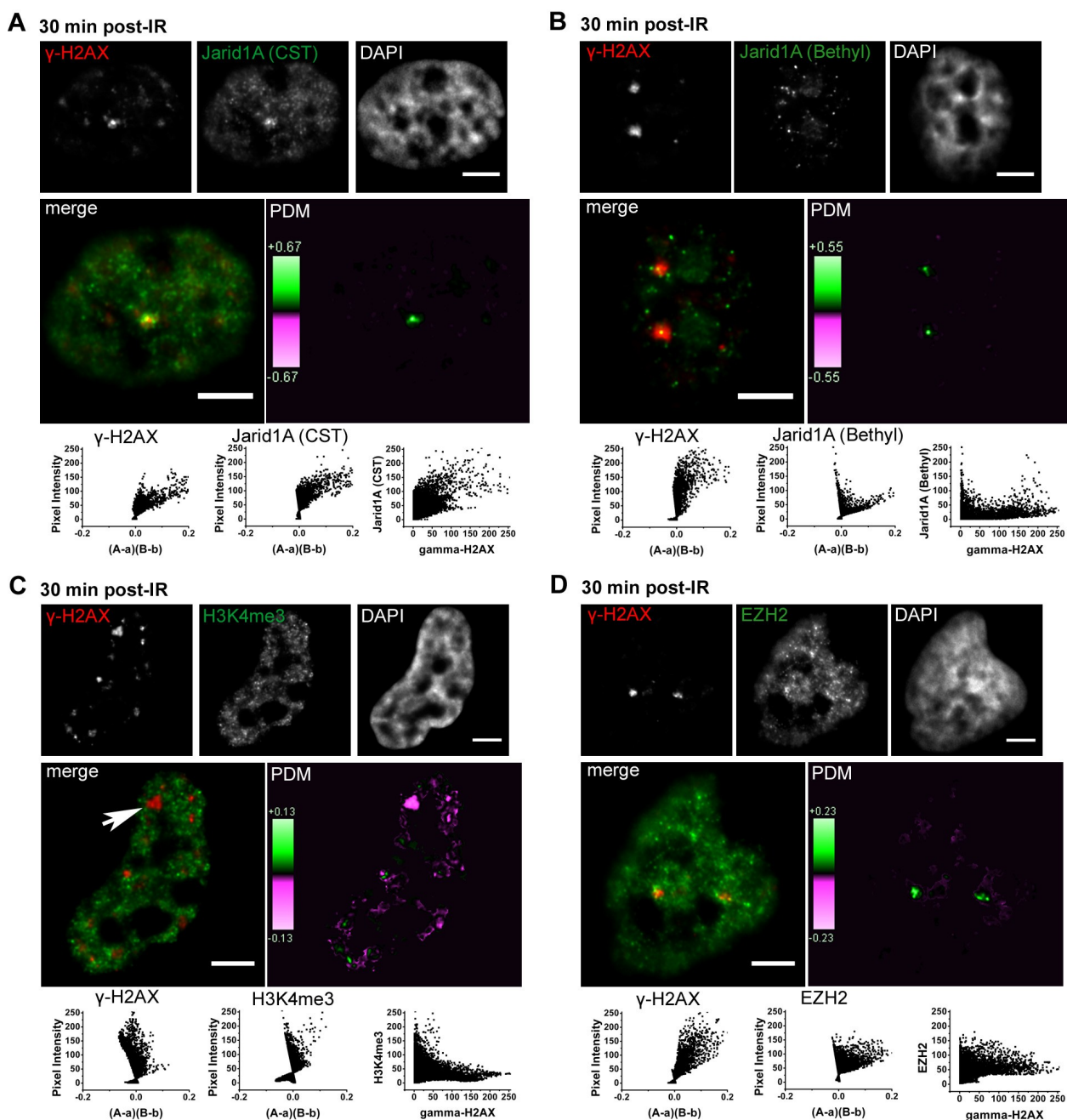
Figure 2.30: Slight accumulation of Jarid1A with both antibodies to laser-induced damage 30 min after laser microirradiation. HeLa cells were irradiated with a 405 nm laser with a spot size of 1 μm. 1-2 spots per cell nucleus were irradiated. In C) because other spontaneous foci are present in the same nucleus, IRIF is indicated by a white arrow. Cells were stained with γ-H2AX (red channel) and either A) Jarid1A (CST antibody, both isoforms), B) Jarid1A (Bethyl antibody, large isoform), C) H3K4me3 or D) EZH2 (green channels). DNA was counter stained with DAPI (blue). Upper rows in A-D) show a representative single slices from an image stack of each channel. Mid rows in A-D) show the respective red-green merge and the PDM color-coded image. Pink color represents anti-correlation, green color represents co-localization. PDM plots in A-D) show the value for each PDM and its respective intensity. Scatter plots show distribution of intensities. Positive PDM values skewing to the right and green color in the PDM image indicate positive correlation as is the case for Jarid1A in A) and B), and for EZH2 in D). Negative correlation of H3K4me3 and γ-H2AX is indicated by bright pink staining and negative PDM values skewing to the left (C). Scale is 5 μm.
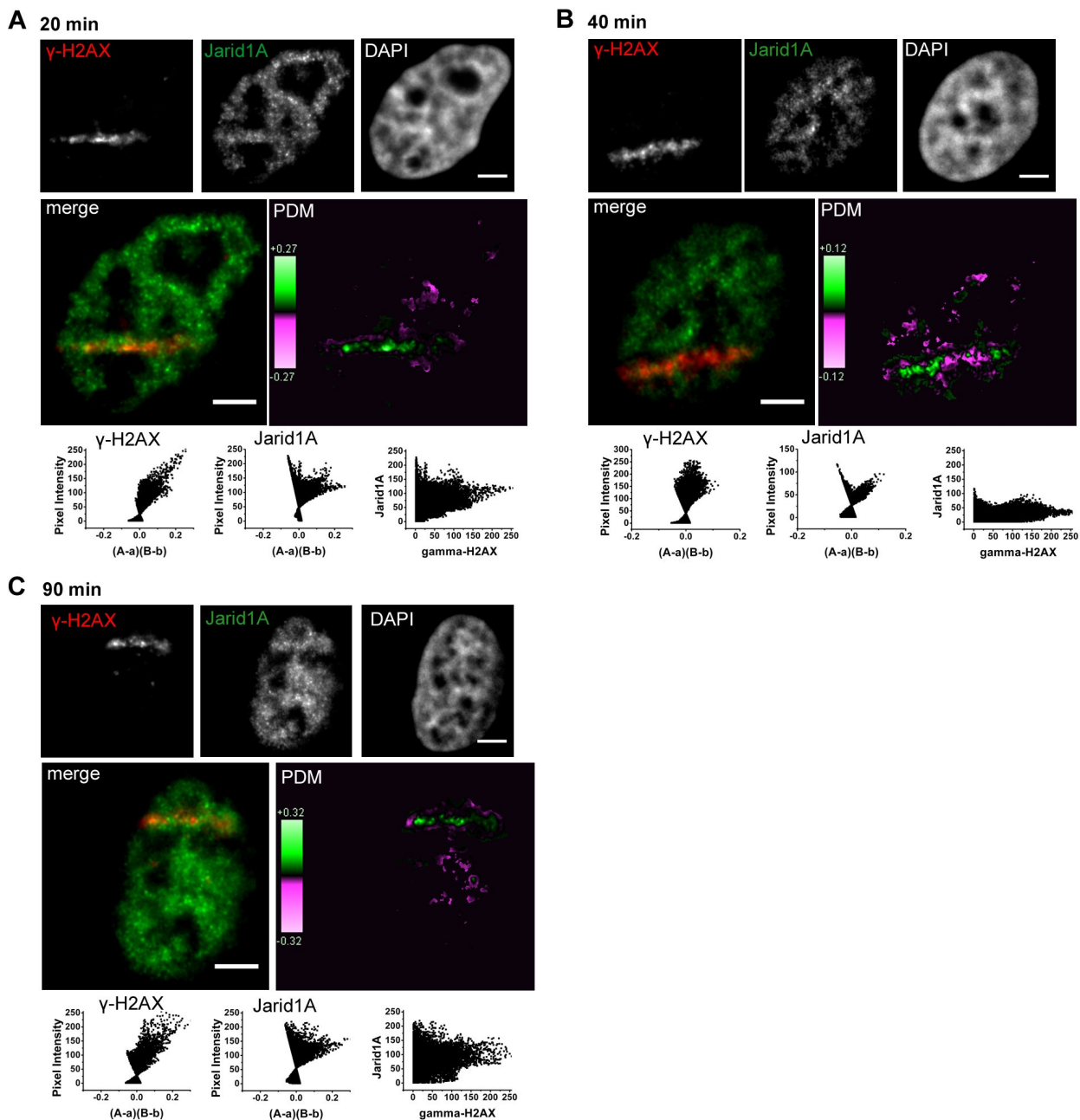
Figure 2.31: Accumulation of Jarid1A at laser-induced γ-H2AX sites after irradiation in a line pattern of 1 μm x 18 μm size at A) 20 min, B) 40 min, and C) 90 min following irradiation. Microscopic images show single slices after 3D epifluorescence microscopy with γ-H2AX (red channel), Jarid1A (green channel) and chromatin (DAPI; blue channel) in the upper rows, merges and PDM maps in the middle rows, and PDM plots of γ-H2AX and Jarid1a, respectively, as well as the respective scatter plots in the bottom rows. An antibody against Jarid1A was used which recognizes the large Jarid1A isoform (Beshiri et al., 2010). Jarid1A accumulates at laser-induced DNA damage at all times investigated. Evaluation with ICA confirms the positive correlation of Jarid1A and γ-H2AX as indicated by the pink color in the PDM map for positive correlation, as well as positive PDM values shown in the PDM plots. Note that in the cell shown in B), a region with apparent anti-correlation in the middle of the track is due to reduced Jarid1A signal in the nucleolus. Scale bars are 5 μm.

Knockdown of the demethylase Jarid1A

Since Jarid1A was recruited to laser-induced damage it can be speculated that this demethylase is involved in removing H3K4me3/me2 from damaged sites. To test this hypothesis, I tried to knockdown Jarid1A by treatment of cells with siRNA and to further analyze the effects of Jarid1A-depletion.

For down-regulation two different siRNA sequences were used which were previously described by (Benevolenskaya et al., 2005) and the sequence specificity of which was confirmed for both Jarid1A transcripts with the NCBI nucleotide blast (Appendix E).

After treatment with Jarid1A siRNA, some effects on cell morphology and on cell proliferation were observed which were also previously described (Benevolenskaya et al., 2005; Lopez-Bigas et al., 2008; Zeng et al., 2010). For example, after treatment of cells for a minimum of 48 h, a cell flattening and the formation of a 'scraggy' membrane was observed in several cells. Additionally, the total number of cells was significantly decreased as well as the proportion of Ki67-positive cells (a proliferation marker) after immunofluorescence staining. In western analysis, an induction of p21 was observed which may hint at a proliferation stop (data not shown). However, no decrease of Jarid1A protein levels could be observed. In Figure 2.32, Jarid1A protein levels in HeLa cells (Figure 2.32 A, B) and in SAOS cells (Figure 2.32 C) after knockdown are shown compared to untreated controls and controls treated with non-silencing siRNA. I tested different antibodies (Figure 2.32 A-C, left and right panels, respectively, and data not shown) and also another protein extraction procedure using high salt concentrations (Figure 2.32 B) as suggested by (Benevolenskaya et al., 2005). For a positive control of knockdown efficiency, cells were treated with WSTF siRNA. The knockdown of WSTF could be confirmed in western (Figure 2.32 A-C) and in real-time PCR analysis (Figure 2.33, right panel). However, real-time PCR of Jarid1A cDNA verified that Jarid1A was not efficiently targeted by siRNA treatment (Figure 2.33).

Thus Jarid1A knockdown in my hands was not efficient, in spite of thoroughly testing various knockdown conditions. For example, Jarid1A protein levels were analyzed after different incubation times after knockdown (48 – 120 h) and after application of various siRNA concentrations (50, 100, and 200 pmol). Further, the two siRNAs were tested alone and in combination. Two transfection procedures were applied to various cell lines: The transfection was performed in HeLa, U2OS and SAOS cells with either Dharmafect transfection reagent, which is routinely and successfully used in our laboratory, or with lipofectamin 2000, as

suggested by (Benevolenskaya et al., 2005). Last but not least, four different Jarid1A-antibodies were tested, including two antibodies kindly provided by E. Benevolenskaya (data not shown).

Because experiments on Jarid1A knockdown were performed during the final stages of my work, I could not perform further experiments. For future studies it would be useful to test siRNAs from companies which have already confirmed the knockdown efficiency, e.g. as used in (Stratmann and Haendler, 2011), for down-regulation of Jarid1A. Moreover, siRNAs labeled with a fluorophor such as Cyanin 3 could be helpful in identifying successfully transfected cells also in immunofluorescence images which then could be further analyzed with regard to the effect on H3K4me3 and γ-H2AX exclusion.

A

B

C
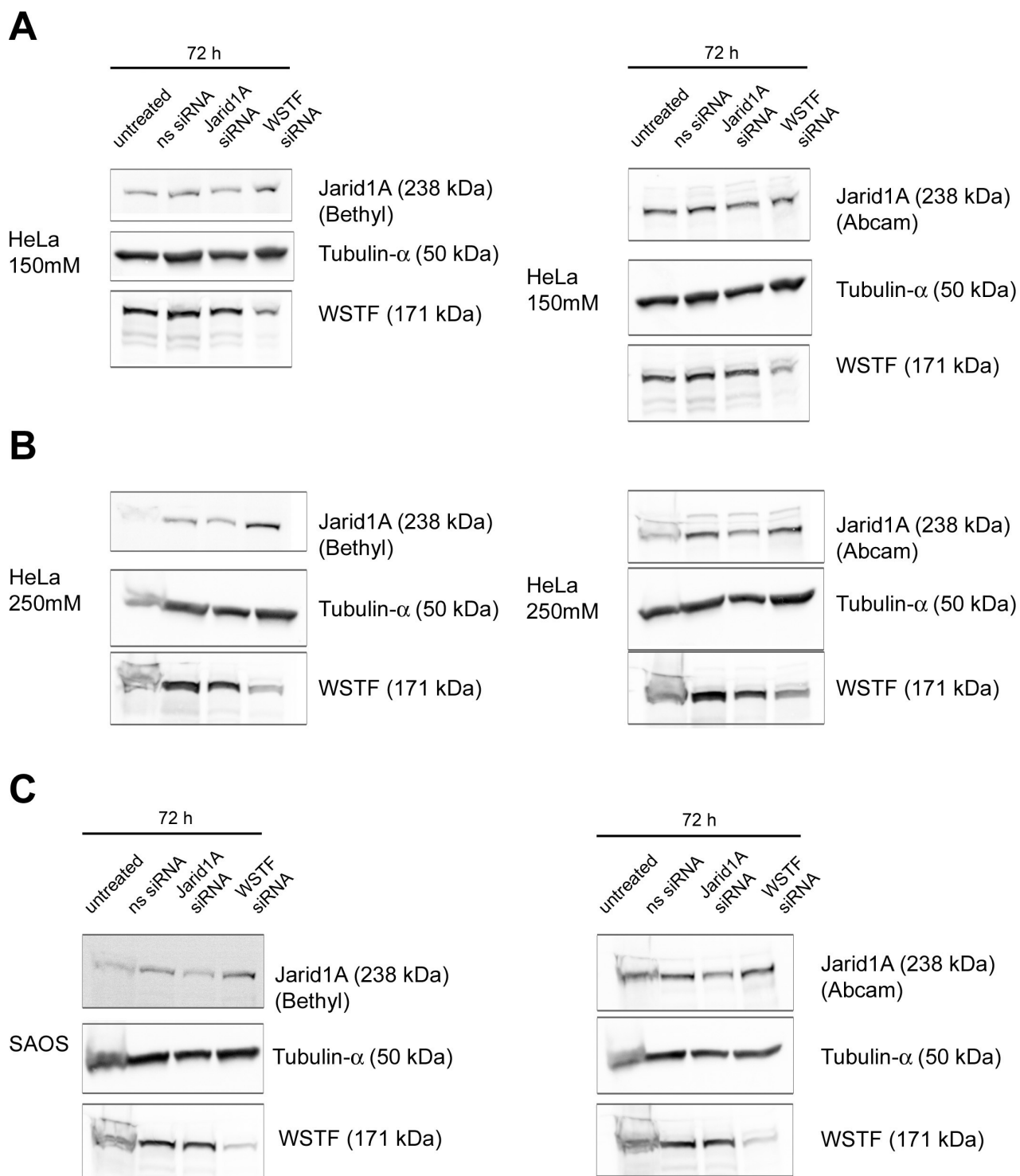
Figure 2.32: Western analysis of whole cell protein extracts from HeLa (A,B) or SAOS (C) cells, which were either untreated or treated with non-silencing siRNA (ns siRNA), Jarid1A siRNA (No. 2) or WSTF siRNA. A) Proteins were extracted from HeLa cells with 150 mM NaCl. Jarid1A was either detected with Bethyl antibody (left) or with Abcam´s antibody (right) in A). In B) proteins were extracted from HeLa cells with 250 mM, which was used to improve the extraction of Jarid1A. In C) proteins were extracted from SAOS cells with 150 mM. Jarid1A was detected with either Bethyl antibody (left) or Abcam´s antibody (right) and Jarid1A levels were slightly reduced after treatment with Jarid1A siRNA. Considering levels of Tubulin-alpha, unequal loading or proteins might have caused the decrease. WSTF was strongly reduced after treatment with WSTF siRNA.
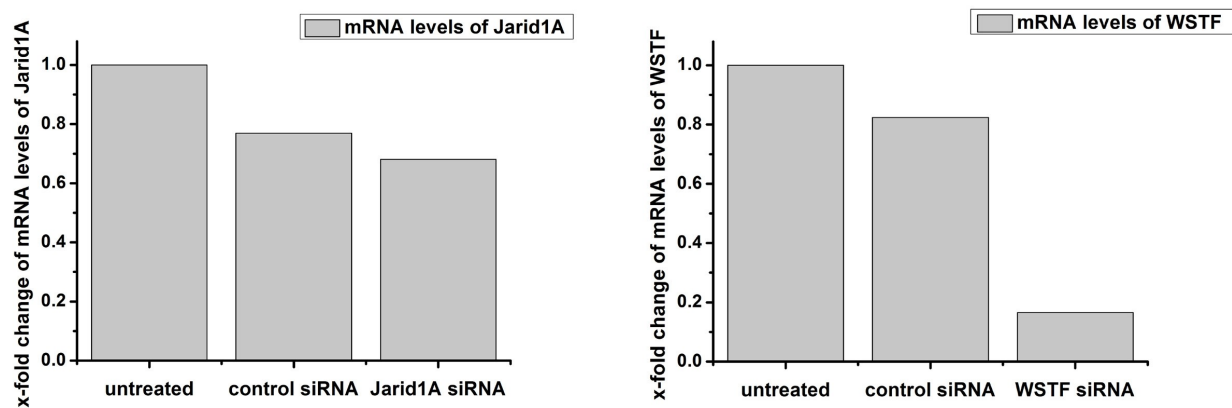
Figure 2.33: Expression levels of Jarid1A and WSTF after siRNA treatment using Lipofectamin 2000 for transfection. Respective cDNA was analyzed with quantitative real-time PCR. Left diagram shows mRNA levels of Jarid1A in untreated HeLa cells, or HeLa cells 72 h after treatment with either control (non-silencing) siRNA or after treatment with Jarid1A siRNA. Right diagram shows mRNA levels of WSTF in untreated HeLa cells, or HeLa cells 72 h after treatment with either control (non-silencing) siRNA or after treatment with WSTF siRNA. GAPDH was used as a reference gene. Amount of mRNA was normalized to the untreated control. mRNA levels of Jarid1A after siRNA treatment were only slightly reduced compared to untreated cells, but almost equal to the amount of mRNA in non-silencing siRNA treated cells. By contrast, WSTF mRNA levels were six-fold decreased compared to levels in non-silencing siRNA treated cells.

3 Discussion

3.1 Quantitative image analysis

In the present work, methods for quantitative image analysis were tested. For this, a plug-in for intensity correlation analysis (ICA) (Li et al., 2004) was used. With this plug-in also correlation coefficients such as Pearson´s and Manders´ coefficients are calculated. Additionally, it calculates the *Product of the Differences from the Mean* (PDM) of pixels pairs of two images. The PDM is calculated from (A-a)*(B-b), where A and B represent the intensity of one pixel in the channel A and B, respectively, and a and b are the respective mean values. This approach assumes that if two pixels co-localize, their intensity will vary in synchrony and thus they both will be either above or below the mean level. Consequently, their PDM value would be positive. In contrast, if two pixels are anti-correlated, this would result in a negative PDM value. The ICA plug-in generates a PDM color-coded map of the cell nucleus representing a PDM value in a respective color for each pixel. Additionally, PDM plots show the intensities of A and B plotted against the respective PDM value. A simple scatter plot represents the distribution of intensities of both channels.

ICA was evaluated by analyzing the correlation of chromatin and two known histone modifications which are predominantly found in regions of either low or high chromatin density. Dimethylation of H3 at lysine 9 (H3K9me2) is a histone modification associated with heterochromatin and thus was expected to co-localize with condensed chromatin which was stained with DAPI (Zinner et al., 2006). By contrast, trimethylation of H3 at lysine 4 (H3K4me3) is a marker of active genes and thus was expected to anti-correlate with high DAPI intensities, because active genes are correlated with decondensed chromatin (Misteli, 2007). By applying ICA on the two examples, the generated PDM images clearly demonstrated areas of co-localization and anti-correlation by either green or pink staining of different shade. However, for negative correlations only slightly negative PDM values were obtained as shown in the PDM plots.

A reason for the only slightly negative PDM values obtained for anti-correlation is the large proportion of pixels with small intensity. The small intensities lower the mean intensity and thus the chance to obtain strong negative PDM values for anti-correlation is diminished. Consequently, even for strong anti-correlations only slight negative PDM values are obtained.

Moreover, the ICQ proposed by (Li et al., 2004) is also strongly influenced by the large proportion of small intensities. For example, if two intensities in the channels A and B are only slightly above the threshold this results in a positive PDM values. The ICQ is calculated from the relation of positive PDM values to the total number of PDM values. Thus a large number of small, but still positive PDM values lower the chance to obtain strong negative values for the ICQ as well.

The large proportion of small intensities is a general problem in image analysis (Ronneberger et al., 2008). Small intensities can represent either true signals or represent unspecific background signals. Even though background correction can correct this bias to some extent, still a large number of small values remains that have impact on the analysis of correlations. For this reason, I concluded that PDM values of pixels with high intensity are the most important. PDM values in regard to intensities can easily be identified in the PDM plots, whereas correlations of high intensities can be considered using the scatter plots.

As mentioned above, small intensities are a major problem for the calculation of correlation coefficients (Ronneberger et al., 2008). The drawbacks of Pearson´s correlation coefficient and Manders´ coefficient are described in detail in the literature (Costes et al., 2004; Bolte and Cordelières, 2006; Ronneberger et al., 2008; Barlow et al., 2010) and were also faced in this study. In the above described example for chromatin and histone modifications, Pearson´s coefficient Rr, Manders´ overlap coefficient R and Manders´co-localization coefficients M1 and M2, and also the ICQ demonstrated co-localization for H3K9me2 and chromatin. Conversely, these coefficients and the ICQ were indicating a random distribution for the correlation of H3K4me3 and chromatin although pixels of high intensity were clearly anti-correlated.

To briefly discuss the reasons for this that are also discussed in detail in the literature and summarized in 1.4.2 (Costes et al., 2004; Bolte and Cordelières, 2006; French et al., 2008; Ronneberger et al., 2008), Manders´ overlap coefficient R and co-localization coefficients M1 and M2 do not consider the extent of intensities and thus are not suited for the question investigated in this work. Similarly, Pearson´s coefficient Rr is sensitive to small intensities. Moreover, Pearson´s Rr depends on a linear relation of signal intensities. This would assume that intensities are linearly increasing with the amount of macromolecules which is not necessarily the case in fluorescence images (French et al., 2008).

With regard to the main question investigated in the present work – the distribution of histone modifications at γ-H2AX foci - it can be further argued that the coefficients are mainly

influenced by the given distributions of signals in an image. In other words, correlation of the speckle-like pattern of the histone modification and γ-H2AX foci is determined by the chance to 'hit' a speckle with an ion. However, this chance is rather small. In contrast, if the histone modification pattern becomes more dense, then the possibility of co-localization increases. Thus, the random distribution of the two patterns would strongly affect the Pearson´s correlation coefficient and the ICQ, but no information about real correlations would be obtained (G. Dollinger, personal communication).

To circumvent the above described problems, Spearman´s rank correlation coefficient ρ was used in the cases where a quantification was needed. Using Spearman´s coefficient ρ, data are ranked in regard to their intensity. Thus, Spearman´s rank correlation coefficient ρ is both less sensitive to small intensities and also independent of the distribution of intensities (V.J. Schmid, personal communication). Additionally, V.J. Schmid proposed a correction of the ICQ by using a bootstrap technique as described in chapter 2.1.3. The results obtained for the corrected ICQ* compared to Spearman´s ρ were rather similar (Figure 2.2 in chapter 2.1.3). However, because Spearman´s coefficient was easier to compute, we relied on Spearman´s coefficient rather than on ICQ* for quantification.

In the present work, quantitative analysis with Spearman´s rank correlation coefficient ρ was successfully used to analyze alterations of correlations occurring over time, for example for HP1β and H3K4me3. Nevertheless, the obtained Spearman´s coefficients ρ were still small, in particular for the determination of anti-correlation. This was due to background signals or true signal with small intensities which still exist to a great extent, even if a suitable threshold was applied (V.J. Schmid, personal communication). The same problems are true for Pearson´s coefficient. These aspects are also discussed in a recent publication by (Barlow et al., 2010) in which they describe the difficulties of detecting anti-correlation. Additionally, it must be noted that a perfect correlation or anti-correlation can not be achieved in images of biological systems, because a perfect correlation would imply that pixels with the same intensity would coincide at any time.

In the present work, PDM images and plots were thus used for a quick and easy visualization of correlation in combination with Spearman´s rank coefficient for quantification. However, because calculation of Spearman´s coefficient was kindly provided by Prof. V.J. Schmid and could not be performed by myself, Spearman´s coefficient could not be calculated for every image shown in the present work. Instead, Spearman´s coefficient was only calculated for

images which were analyzed in detail and for which a large set of data was available for quantification and statistical comparison. These data were available for HP1β, H3K9me2, H3K4me3, and their correlation with γ-H2AX foci, respectively. For these marks, data sets of confocal images were collected during several beam times.

To summarize, the combination of PDM technique and quantitative measurements with Spearman´s rank correlation coefficient offers a proper tool to analyze fluorescence images. It was suitable for analyzing the complex pattern of histone modifications on the one hand, and the irradiation pattern of IRIF on the other hand. By using these methods, correlation of various histone modifications and candidate proteins at DSB could be analyzed. Certainly, these methods still face difficulties and drawbacks as discussed above, and improvement of such analyses is still of great interest (Barlow et al., 2010).

3.2 DNA double-strand break-induced silencing

3.2.1 Ion microirradiation with SNAKE

In general, ion microirradiation with the ion microbeam is a useful tool to induce DNA double-strand breaks to living cells. The damage thus-induced is well characterized and the dose can be precisely controlled (Hauptner et al., 2004; Greubel et al., 2008a; Hable et al., 2009). By applying the accelerated ions in a defined pattern, e.g. in the line pattern of 1 µm x 5 µm, the irradiation-induced foci can be precisely identified and they can be distinguished from spontaneously formed foci.

However, the organization and performance of experiments during the limited beam times also bears some difficulties. In addition to the logistical efforts and the time limitations of beam times, also cell culture conditions are challenging. For irradiation in a line pattern the cells are grown on a 6 µm mylar foil which is fixed to a steel container. The foil is pre-coated to ensure a proper adhesion of the cell monolayer during the perpendicular irradiation at the microbeam. However, handling of the containers bears risks of contamination of the sterile cell culture conditions. The fact that the containers have to be carried from the cell culture to the beam place for irradiation and back to the cell culture for post-irradiation incubation, increases contamination risks. Thus experiments which cover an extended incubation time after IR of up to 24 h or more are not easy to perform.

Due to the sophisticated devices needed for localized ion microirradiation, laser microirradiation is often used to induce DNA damage because it is easier to perform using laser scanning microscopes (Kruhlak et al., 2009). However, with laser irradiation, the kind of damage induced is difficult to determine, whereas microirradiation with heavy ions induces a defined number of breaks (Hauptner et al., 2006; Nagy and Soutoglou, 2009). Because laser microirradiation induces DNA damage of high density to a localized area, some proteins involved in the damage response are retained at these sites or a large number of molecules apparently accumulate, and thus their accumulation can be visualized in immunofluorescence. Hence, also proteins which are not foci forming in a sense like 53BP1 or MDC1, for example, can be visualized using laser irradiation. In contrast, the small number of molecules recruited to IR-induced damage is not always detectable and thus laser irradiation is a possibility to study protein accumulations at damaged sites (Suzuki et al., 2011). Recently, a detailed analysis of IR-induced vs. laser-induced damage was performed (Splinter et al., 2010). However, even high-resolution microscopy using a 4Pi microscope did not enable an exact dose estimation of UVA-laser-induced damage in the nuclear volume (Splinter et al., 2010). Thus, ion microbeams came even more into focus since targeted live cell irradiation is adapted for irradiation of nuclear structures, such as heterochromatin and euchromatin regions, respectively, or nucleoli (Hable et al., 2009), and since methods for irradiation of tissues and animal models were developed (Durante and Friedl, 2011).

3.2.2 Inhibition of transcription at DSB

When I started my work in the end of 2007, not much was known about alterations of histone modifications in the context of DNA damage response. To ensure an efficient DNA repair, the access – repair - restore model was proposed (Green and Almouzni, 2002). This model suggests that an 'open' chromatin status is necessary to allow repair and mediator proteins to recognize and bind to a DNA lesion. This model was underlined by subsequent studies which demonstrated a chromatin relaxation at damaged sites (Kruhlak et al., 2006; Ziv et al., 2006). Furthermore, it was shown that the relaxation of chromatin is mediated by hyperacetylation of histone H4 caused by Trrap-Tip60 (Murr et al., 2006; Stante et al., 2009). These studies gave first indications that histone modifications are critical in regulating the chromatin structure in the context of DNA repair.

However, histone modifications had not been investigated so far in detail with regard to their function as active or repressive marks. Observations of (Solovjeva et al., 2007) suggested an inhibition of transcription at damaged sites indicated by a loss of nascent RNA from sites marked with γ-H2AX. In the present work, using ion microirradiation and statistical evaluation of fluorescence images, I could show that initiating and elongating RNA polymerase II and γ-H2AX foci are mutually exclusive. These results suggest an inhibition of transcription at damaged sites. An inhibition of transcription has also been recently reported by others (Chou et al., 2010; Shanbhag et al., 2010). Consequently, this observation raised the question if inhibition of transcription is associated, first, with the loss of active chromatin marks, and second, if a repressive chromatin status is established at the sites of DSB which would resemble one of the known silencing pathways, e.g. heterochromatic silencing or polycomb-mediated silencing. Indeed, preliminary studies in our lab hinted at an under-representation of the active histone mark H3K4me3 (Ottmann, 2007), but lack of a robust quantification method hindered a proper evaluation. Using Intensity Correlation Analysis combined with Spearman´s rank correlation coefficient, I could show that H3K4me3 is lost from chromatin decorated with γ-H2AX and, even more, that the under-representation of H3K4me3 increases over time.

DSB-induced silencing is associated with loss of trimethylation at histone H3K4

After induction of DSB by IR, I observed an under-representation of H3K4me3 at damaged sites. To exclude that the under-representation was caused by microscopic artifacts, for example, fluorochrome quenching (S. Dietzel, H. Strickfaden, and T. Cremer, personal communication), I verified this effect after flipping the secondary antibodies (Cyanin 3 and Alexa-488, respectively).

The under-representation of H3K4me3 and γ-H2AX foci was observed in HeLa cells in confocal and epifluorescence images, as well as in 150-nm ultrathin sections. The mutual exclusion of H3K4me3 and γ-H2AX was also evident in cells at various points of time between 5 min and 5 h after ion-irradiation. Additionally, under-representation of H3K4me3 at γ-H2AX foci was observed and evaluated in U2OS osteosarcoma cells and in h-TERT-immortalized human fibroblasts (BJ1), and in HeLa cells also following α-particle irradiation. Furthermore, statistical analysis with Sperman´s rank correlation coefficient demonstrated the negative correlation of H3K4me3 and γ-H2AX foci. The under-representation was already evident at the earliest time amenable (~ 5 min) after ion microirradiation, as indicated by negative Spearman´s correlation

coefficients, and was more pronounced at 2 hours after IR. Similarly, I observed under-representation of acetylated H3K9 5 minutes and 2 hours after ion microirradiation, a mark which is associated with H3K4me3 in the context of transcription initiation.

These results show that the inhibition of transcription, indicated by the loss of initiating and elongating RNA polymerase II, is accompanied by alterations of histone modifications. The increase of the exclusion with time and the fact that loss of H3K4me3 can also be seen in whole cell extracts at 24 h after irradiation hint at an active removal process. However, it cannot be entirely excluded that γ-H2AX foci are already initially formed in chromatin regions where the active marks are under-represented. For example, Iacovoni and colleagues (2010) reported that the distribution of γ-H2AX foci around enzyme-mediated DSBs is influenced by gene transcription and that γ-H2AX is not propagating across regions that are decorated by RNA Pol II and H3K4me3 (Iacovoni et al., 2010). It has to be noted that (Iacovoni et al., 2010) used ChIP analysis to determine the distribution of γ-H2AX and H3K4me3 or RNA Pol II, respectively. They observed γ-H2AX 'holes' during the spreading of γ-H2AX around the DSB in which H3K4me3 and RNA Pol II were enriched. They were able to resolve the distribution of these patterns of up to ~ 10 bp large areas (Iacovoni et al., 2010). In contrast, (Nakamura et al., 2011) observed an increase of H3K4me3 near an enzyme-mediated DSB using ChIP analysis in mammalian cells. However, they did not analyze the distribution of γ-H2AX and H3K4me3 at these sites. The increase of H3K4me3 was dependent on the RNF20-mediated monoubiquitylation of H2BK120. During transcription, the monoubiquitylation of H2B precedes H3K4 and H3K79 methylation (Kim et al., 2009a). However, (Nakamura et al., 2011) suggest that the role of H2B monoubiquitylation in DSB repair is distinct from its function in transcription. More likely, H2B monoubiquitylation functions in chromatin-relaxation at DSB sites due to recruitment of SNF2h, a subunit of the ISWI chromatin-remodeling complex, which depended on H2BK120ub (Nakamura et al., 2011). Likewise, (Faucher and Wellinger, 2010) report an increase of H3K4me3 together with the occurrence of the yeast H3K4 methyltransferase Set1 at enzyme-mediated DSBs in yeast using ChIP analysis. Certainly, using immunofluorescence techniques, the resolution and accuracy of ChIP analysis can by far not be achieved. In contrast, the spreading of γ-H2AX over Mbp-large regions around the break and the amplification of signal by further γ-H2AX accumulation at these sites enables the visualization of γ-H2AX foci by immunofluorescence. The mutual exclusion of H3K4me3 and γ-H2AX foci observed in the present work thus assumes a large-scale exclusion of H3K4me3 and regions decorated with γ-H2AX around a break. This cannot exclude local alterations (Faucher and

Wellinger, 2010; Nakamura et al., 2011) or a per se exclusion (Iacovoni et al., 2010) at single nuclosome level detectable by ChIP.

Another caveat that must be considered is impaired immunodetection of H3K4me3 by epitope masking. Epitope masking means that binding of the H3K4me3 antibody to its epitope is impaired by e.g. other H3K4me3-binding proteins or modifications in the vicinity of lysine 4. Consequently, an additional peptide competition assay, for example with H3T3ph (S.B. Hake, personal communication) and H3R2 peptides (Guccione et al., 2007), respectively, two modifications which could interfere with the recognition of H3K4me3, could be useful. Still, the concomitant under-representation of H3K9Ac, the decrease of H3K4me3 in western analysis, and the accumulation of repressive marks at DSB on the other hand, argue against a simple epitope masking mechanisms responsible for the under-representation of H3K4me3. Furthermore, my results are in agreement with the observations of (O'Hagan et al., 2008) and (Chou et al., 2010) who also observed a loss of active marks and an accumulation of repressive marks at DSB. (O'Hagan et al., 2008) showed that hypoacetylation was dependent on the HDAC SIRT1 and a knockdown of SIRT1 reversed the effect of local hypoacetylation of H4K16 at DSB.

In summary, these results strongly suggest that the loss of active marks at DSB cannot solely be explained by the model of (Iacovoni et al., 2010). Certainly, it would be interesting to test how H3K4me3 is distributed on persisting γ-H2AX foci at later time points after irradiation and, additionally, if the restoration of chromatin after completion of repair leads to a restoration of the histone pattern. For example, (O'Hagan et al., 2008) observe an inheritance of the established silencing patterns from progenitor to daughter cells in which the DSB at the promoter CpG island persisted.

Repressive pattern at DSB resembles polycomb-mediated silencing

The loss of active marks raises the question if a general repressive pattern is established at DSB and if this pattern would resemble one of the known silencing pathways. Because the heterochromatin protein 1 β (HP1β) is involved in the formation and establishment of heterochromatin (Kwon and Workman, 2008), I investigated if HP1β is altered at DSB following ion microirradiation of HeLa cells. Interestingly, I observed accumulation of HP1β at 1 and 2 hours after irradiation. In contrast, at the earliest time amenable after irradiation (approximately 5 minutes) HP1β was not yet enriched at γ-H2AX foci. Statistical evaluation of pixel correlations

with Spearman´s rank correlation coefficient indicated an accumulation of HP1β with time with significantly positive coefficients at 1 and 2 hours after irradiation. Shortly after irradiation, the pixel pairs of HP1β and γ-H2AX were randomly distributed indicated by a mean coefficient not significantly different from zero.

The accumulation of HP1β at later points of time was also reported by others (Ayoub et al., 2009; Luijsterburg et al., 2009; Zarebski et al., 2009). Here, laser irradiation in combination with live cell imaging or subsequent immunofluorescence detection was used. (Luijsterburg et al., 2009) also showed the accumulation of the three HP1 isoforms (HP1α, -β, -γ) at γ-irradiation induced damage. By contrast, an earlier study of (Ayoub et al., 2008) suggested an active dispersal of HP1β from damaged sites quickly after targeted laser irradiation of heterochromatin (chromocenters) in mouse cells. Conversely, (Luijsterburg et al., 2009) did not observe a dispersal or loss of HP1β from damaged sites. My own results indicate that the accumulation was established at later times after irradiation and no accumulation was evident at the earliest point of time investigated. However, a mutual exclusion of HP1β and γ-H2AX foci shortly after irradiation could not be confirmed by statistical analysis.

Because HP1β interacts with the chromatin through binding of its chromodomain to H3K9me3/me2 (Bannister et al., 2001; Lachner et al., 2001), several studies investigated whether H3K9me3 is altered after DNA damage (Ayoub et al., 2008; Luijsterburg et al., 2009). However, neither global nor local changes were observed, although these authors did not rely on stringent quantification procedures of fluorescence images. Moreover (Luijsterburg et al., 2009) found that the recruitment of HP1β was independent from its chomodomain and rather depended on its chromoshadow domain. In contrast, (O'Hagan et al., 2008) observed a slight increase of H3K9me3 in the very close vicinity of an enzyme-mediated DSB analyzed by ChIP, and, more recently, the ultrastructural distribution of H3K9me3 and 53BP1 foci was investigated in ultrathin slices of gold-labeled cells using TEM (transmission electron microscopy) (Rübe et al., 2011). Their results suggest that 53BP1 is always co-localizing with H3K9me3, but not with H3K9Ac. This observation is, however, also in contrast to others who suggest that γ-H2AX foci preferentially form in regions devoid of H3K9me3 and HP1 (Cowell et al., 2007; Goodarzi et al., 2009). Although I did not quantify the distribution of H3K9me3 and γ-H2AX using Spearman´s coefficient due to the lack of data, ICA indicated a random distribution of the two patterns. Thus, also overlap of H3K9me3 with γ-H2AX foci was observed, but no significant enrichment of H3K9me3 was indicated using ICA.

In addition to this, I investigated the distribution of dimethylated H3K9, which is also bound by HP1β, albeit to a lesser extent (Nielsen et al., 2002; Fischle et al., 2003). Previously, dimethylated H3K9 was reported to decrease at DNA damage sites induced by γ-irradiation, while the acetylation of H4K5 increased (Falk et al., 2007). The authors conclude that this hints at chromatin decondensation at damaged sites. However, (Falk et al., 2007) did also not rely on quantification of correlations. Thus, I investigated the distribution of H3K9me2 at γ-H2AX foci in detail at 15 min and 2 h after ion microirradiation. H3K9me2 signals were partially overlapping with γ-H2AX foci or located also to the borders of γ-H2AX foci. Similarly, statistical image evaluation with Spearman´s coefficient indicated a random distribution of H3K9me2 and γ-H2AX at both times investigated. No significant alterations could be observed neither in confocal images nor after ultrathin sectioning of cells. Ultrathin sections, however, also showed that some γ-H2AX foci were devoid of any H3K9me2 signal. Thus the alterations described by (Falk et al., 2007) could not be verified at the times investigated.

Besides analysis of local H3K9me2 distribution at DSB, I observed an increase of signal intensities of H3K9me3 and H3K9me2 in confocal images shortly after irradiation (2 and 15 min), whereas the intensity of H3K9me3/me2 in unirradiated cells and in cells 2 h after irradiation was rather similar and homogeneously distributed. The increase of signal intensities shortly after IR resulted in a few signals of H3K9me of high intensities which were independent from γ-H2AX foci. This could be the result of an accumulation of these molecules at specific sites in the nucleus. However, pre-extraction of unbound proteins from the nucleus before fixation of cells did not abrogate this effect. Attempts to verify this effect by using Mosaix, a 'large-scale image acquistion' mode of the epifluorescence microscope, failed, most probably due to the lack of sensitivity of this system. Moreover, another microscope containing the Mosaix mode had to be used, in which the bleed-through of the filters was not accurately controlled. Thus, the data obtained with Mosaix could not be used for further analysis and the meaning of this observation remains elusive. However, the observation hints at an involvement of these modification in structural chromatin changes induced by irradiation.

An additional histone mark involved in heterochromatin formation is the trimethylation of H4K20. Because both antibodies used in the present work for the detection of H4K20me3 were cross-reacting with other methyl marks, as shown by peptide competition assay (see Appendix A), I had to omit these data and could not analyze the distribution of H4K20me3 at γ-H2AX foci.

In conclusion, my results suggest in agreement with findings of (Luijsterburg et al., 2009), that recruitment and/or binding of HP1 to chromatin in the context of the DNA damage response differs from its binding to chromatin in the context of heterochromatin formation. Diverse functions of HP1β are also discussed in a review of (Billur et al., 2009). Indeed, various subgroups of HP1β with different mobility in the cell nucleus exist that might have diverse functions (Schmiedeberg et al., 2004; Müller et al., 2009). Moreover, HP1β can be released from chromatin without any changes of H3K9me3 (Fischle et al., 2005). It remains to be elucidated, if subgroups of HP1β are involved in the damage response and how they can be distinguished, for example if they are differentially modified (Lomberk et al., 2006). In addition to this, a very recent report shows that HP1α is acting in the DDR via mechanisms which occur independent from H3K9me2/me3 binding and from its function in heterochromatin formation (Baldeyron et al., 2011). Thus, a comparable action might be also true for the HP1β isoform.

Another repressive histone modification is H3K27me3, which was implicated in polycomb-mediated silencing (Kirmizis et al., 2004). I observed an accumulation of the repressive mark H3K27me3 at DSB induced by ion microirradiation. The accumulation was already apparent at 5 min after irradiation but was more pronounced at 2 hours after irradiation. This indicates an installation of the methyl mark at DSB with time. During the course of my work, the installation of repressive marks at DSB was also shown by others (O'Hagan et al., 2008; Chou et al., 2010). (O'Hagan et al., 2008) demonstrate by ChIP analysis an increase of the polycomb-associated repressive histone mark H3K27me3 and a local hypoacetylation of H4K16Ac at an enzyme-mediated DSB. Accumulation of H3K27me3 was accompanied by accumulation of proteins mediating repression, such as EZH2 and SIRT1 (O'Hagan et al., 2008). EZH2 is a component of the polycomb-repressive complex 2 (PRC2) and has histone methyltransferase activity (Margueron et al., 2008; Sarma et al., 2008). SIRT1, the human homologue of the drosophila Sir2 that deacetylates H3K9 and H4K16, is probably responsible for the hypoacetylation of H4K16 at DSB, whereas EZH2 probably methylates H3K27 at DSB (O'Hagan et al., 2008). Furthermore, a recent study of (Chou et al., 2010) show a local increase of H3K27me3 also at laser-induced damage. Additionally, they observe recruitment of EZH2 and components of the NuRD chromatin remodeling complex to damaged sites. Moreover, the recruitment of the polycomb-associated proteins was dependent on PARP1 (Chou et al., 2010).

Taken together, inhibition of transcription at DSB associated with loss of H3K4me3 and H3K9Ac, together with the installation of repressive marks at DSB, such as H3K27me3 and

components of the PRC2 complex (O'Hagan et al., 2008; Chou et al., 2010), resembles polycomb-mediated silencing, as it was described for example, for the regulation of developmental genes (Pasini et al., 2008).

3.2.3 Potential mechanisms responsible for the loss of trimethylation at H3K4

The time-dependent accumulation of repressive marks and loss of active marks hints to active processes. The loss of trimethylation from H3K4 could be mediated by histone eviction and incorporation of new histones or by removal of the methyl groups by a specific demethlyase. In regard to the two possible mechanisms, I considered several histone marks or proteins that could point to either one of the mechanisms.

The acetylation of the histone H3 core at lysine 56 is a recently discovered and highly discussed modification (Corpet and Almouzni, 2009; Das et al., 2009; Tjeertes et al., 2009; Miller et al., 2010). Because (Das et al., 2009) suggested that histones are marked with H3K56Ac for incorporation by the histone chaperone CAF1 at DNA damaged sites, I investigated the distribution of H3K56Ac after ion microirradiation to test if H3K56Ac is enriched at DSB and thus marks newly incorporated histones. Despite a few overlapping signals, H3K56Ac was mainly under-represented at γ-H2AX foci at 5 min and 2 h after irradiation. My results suggest that histones at damaged chromatin are not preferentially marked with H3K56Ac, at least not at the times investigated. In contrast, my data rather suggest that H3K56Ac is under-represented at DSB, which is in agreement with (Tjeertes et al., 2009) who show a global decrease of this modification after DNA damage. Furthermore, (Miller et al., 2010) demonstrate that the histone deacetylases HDAC1 and HDAC2 are recruited to DNA damage and that they specifically deacetylate H3K56Ac in response to DNA damage.

Taken together, the observations in regard to H3K56Ac in the context of DNA repair are controversial (Das et al., 2009; Tjeertes et al., 2009; Miller et al., 2010; Vempati et al., 2010). In addition, studies in yeast hint at an involvement of H3K56Ac in the completion of repair (Chen et al., 2008; Costelloe and Lowndes, 2010). The controversies in the literature together with my results might, of course, also be an outcome of different cell types and antibodies used, as well as different incubation times, use of different damaging agents and different cell passages as discussed by (Corpet and Almouzni, 2009), and last but not least, of different imaging acquisition and analyzing techniques. For example, (Miller et al., 2010) found that the antibodies used for the detection of γ-H2AX and H3K56Ac by (Das et al., 2009) were both raised in rabbit,

which may result in a detection of both primary antibodies with the same fluorochrome. Similarly, (Vempati et al., 2010) report a co-localization of H3K56Ac and γ-H2AX, but the conspicuously perfect co-localization may also hint at experimental artifacts. In addition, they describe Chk2 and p53 foci following damage, which have not been described by others.

I also tested the distribution of H4K5Ac at γ-H2AX-decorated chromatin, but this turned out to be difficult to analyze. H4K5Ac coincided with regions of low chromatin density as expected, but its staining pattern was very inhomogeneous. A small number of single, bright spots was detectable and thus the number of analyzed pixels was very low and a statistical evaluation was not reasonable. Nonetheless, evaluation with ICA could not confirm an increase of H4K5Ac at damaged sites at 15 min after irradiation, as had been reported by (Falk et al., 2007). In contrast, H4K5Ac appeared to be mainly under-represented. Moreover, (Khobta et al., 2010) show an hypoacetylation of H4 at a proximal promoter region after oxidative damage. The treatment of cells with a HDAC inhibitor led to a partial restoration of expression of the damaged gene (Khobta et al., 2010). Also (O'Hagan et al., 2008) observed hypoacetylation of H4K16 at DSB sites.

Due to the mainly controversial findings, I propose that alterations of histone acetylations at DSB may be short-time and highly-dynamic events that are difficult to detect with immunofluorescence approaches, even more since it was also reported that initial hyperacetylation is followed by hypoacetylation (Falk et al., 2007; O'Hagan et al., 2008).

Although I did not observe accumulation of the histone mark H3K56Ac, histone eviction may still be a potential mechanisms responsible for the loss of active marks at DSB. Because histone H3 variants were previously shown to play a role at UV-damage NER sites (Polo et al., 2006), I tested the distribution of different H3 variants at γ-H2AX foci induced by ion microirradiation, using HeLa cells expressing HA-tagged histone H3 variants (a kind gift of S.B. Hake). The tail of the histone H3.3 variant is predominantly decorated with active marks such as H3K4me3, whereas the histone H3.2 variant is connected to silenced chromatin bearing H3K27me3 marks (Hake et al., 2006). The H3.1 variant is found in active and silenced regions and is decorated with various PTMs (Hake et al., 2006). After ion microirradiation of the HA-tagged cells, no significant alteration in the pattern of any of the variants was detected. The regions decorated with the respective variant were overlapping with γ-H2AX, but they were not significantly enriched or absent from γ-H2AX foci.

Because overlapping areas of H3 variants, as well as H3K9me2/me3 and unmethylated H3 (not shown) with γ-H2AX foci were generally observed, this suggests that the loss of H3K4me3 can not be explained by large-scale H3 eviction from the damaged sites. Of course, the eviction of single nucleosomes from damaged sites, as for example occurring directly at the damaged DNA ends, cannot be detected by immunofluorescence techniques. However, such single nucleosome eviction can also not explain the large-scale loss of H3K4me3 from γ-H2AX-decorated chromatin. Another mechanism involved in the removal of H3K4me3 could be the activation of a H3K4 demethylase. A demethylase of the Jumonji C domain protein family is able to remove one methyl group after the other (reviewed in Cloos et al., 2008) and since dimethylation of H3K4 is also found at sites of active transcription (Barski et al., 2007), it would be reasonable that the dimethylation mark would be removed from damaged sites as well. Thus I tested the distribution of the other methyl states, H3K4me2 and H3K4me1, at DSB. H3K4me2/me1 were also under-represented at γ-H2AX foci following ion microirradiation and at least the distribution of H3K4me2 was comparable to the under-representation of H3K4me3. For the monomethylated form, however, also some overlapping areas were observed. This pattern could be compatible with demethylation at H3K4.

Among five known H3K4me3 demethylases, Jarid1A (RBP2/KDM5A), which is able to demethylate H3K4me3/me2 (Christensen et al., 2007; Klose et al., 2007), was implied in DNA repair due to its interaction with the MRG15 complex (Hayakawa et al., 2007). Moreover, Jarid1A was shown to transiently interact with the PRC2 complex for demethylation of H3K4me3 in polycomb-mediated silencing at developmental genes in ES cells (Pasini et al., 2008). Thus I investigated the recruitment of Jarid1A after ion microirradiation, alpha-particle irradiation and x-irradiation of HeLa cells, but no accumulation at DSB was detectable.

As discussed before (chapter 3.2.1), the number and the density of DSB induced by IR is smaller than in the case of laser damage (Nagy and Soutoglou, 2009). In contrast to foci forming proteins, such as 53BP1, MDC1, Rad51 which are readily detectable at ion damaged sites, proteins which are recruited to the damage in lower amounts may be visible after laser irradiation, but not after ion irradiation using microscopic methods. This was for example recently reported for TRF2 (Splinter et al., 2010) and for the histone remodeler ACF1 (Sánchez-Molina et al., 2011, and S. Auer, personal communication). For this reason, laser microirradiation is often used to study accumulations of proteins at DNA damage. Thus, I tested accumulation of Jarid1A after laser microirradiation. After irradiation of cell nuclei in 1 μm² spots, accumulation

of the DSB-marker γ-H2AX was detectable. At these sites, also slight accumulation of Jarid1A was observed using two different antibodies. One of the antibodies did only detect the large isoform of Jarid1A and showed slight but intense signals overlapping with γ-H2AX. I repeated this experiment using laser irradiation in a line pattern of 1 μm x 18 μm. In these images, the large isoform of Jarid1A was detected at laser-induced γ-H2AX sites between 20 and 90 min after irradiation using a specific antibody (Beshiri et al., 2010). The enrichment of Jarid1A at γ-H2AX foci after laser-damage suggests that Jarid1A, and that its large isoform, is present at γ-H2AX foci.

To verify a role for Jarid1A in the DNA damage response by demethylation of H3K4, I tried to knockdown Jarid1A with two different siRNA sequences that have previously been successfully used (Benevolenskaya et al., 2005). After treatment of cells with siRNA, I observed some effects which were previously connected to the down-regulation of Jarid1A, such as induction of p21 and a decrease of cell proliferation indicated by a reduced cell number and a decrease of Ki67-positive cells (not shown) (Benevolenskaya et al., 2005; Lopez-Bigas et al., 2008; Zeng et al., 2010). However, levels of Jarid1A were not efficiently reduced neither on protein levels nor on mRNA levels. Various conditions for transfection were thoroughly tested, e.g. different incubation times after transfection, different concentrations of siRNAs, application of both siRNAs and each siRNA alone, transfection of different cell lines and the use of four different antibodies for Jarid1A-immunodetection, one of which was kindly provided by Dr. E. Benevolenskaya and which is described in (Beshiri et al., 2010). Additionally, I carefully verified that the siRNA sequences matched Jarid1A mRNA using the NCBI nucleotide blast and I further determined the amino acids which are supposed to be encoded in the targeted mRNA sequences (see Appendix E).

Reasons for the inefficiency of the knockdown might be that the sequences were already inaccurately provided or that they were digested by RNases due to improper handling. Consequently, for further studies different siRNAs should be used. In addition, the transfection of siRNA into the cells may still have been inefficient. Although transfection of other siRNAs can be successful using the same approach and reagents, as shown for the WSTF siRNA, the transfection of a different siRNA directed against another protein can be still unsuccessful. This shows the importance for optimization of conditions for transfection for each siRNA.

Furthermore, in addition to positive control siRNAs which are labeled with fluorophores, the use of siRNAs which have impact on cell morphology, such as siRNAs directed against lamins,

could be used for comparison with the knockdown of Jarid1A, which also induces a cell flatening after several days of transfection (E. Benevolenskaya, personal communication). On the other hand, a successful knockdown of Jarid1A on protein level can be still tricky, because some enzymatic activity might still remain. Another possibility for inactivation of Jarid1A could be the use of inhibitors (Lin et al., 2011), but to date non are available. Without an efficient deactivation of Jarid1A, a definite role for Jarid1A in the removal of H3K4 methylation could not be verified.

While the role of Jarid1A in DNA damage response remains to be elucidated, the involvement of other H3K4 demethylases is also possible. For example, it was shown recently that the loss of Jarid1A can be compensated by Jarid1B (KDM5B) (Islam et al., 2011). Furthermore, (Chou et al., 2010) observed that the recruitment of polycomb proteins to laser damage was dependent on PARP1. Interestingly, PARP1 was recently shown to regulate chromatin-structure in a KDM5B-dependent manner (Krishnakumar and Kraus, 2010). Thus, Jarid1B is also a good candidate for the removal of trimethylation at H3K4. For future studies, it would be reasonable to knockdown Jarid1A and Jarid1B, both alone and simultaneously, and to analyze the effect of the knockdowns on the mutual exclusion of H3K4me3 and γ-H2AX. Furthermore, it will be interesting to determine the effects of the knockdowns on the inhibition of transcription and on the efficiency of repair.

In general, because Jarid1A and Jarid1B are also up-regulated in specific cancer cells (Xiang et al., 2007; Zeng et al., 2010), they might have important roles in tumor development. Recently, Jarid1A was implicated in a drug-tolerance state of cancer cells (Sharma et al., 2010b). Thus targeted demethylase inhibition, however, not yet available, might be a promising sensitizer for anti-cancer therapy (Sharma et al., 2010a). The potential involvement of these demethylases in DSB repair certainly contributes to the understanding of epigenetic mechanisms involved in tumor development. It remains to be elucidated how the demethylase are involved in these processes in detail.

3.2.4 Conclusions and outlook

At the beginning of my PhD thesis, histone modifications were mostly connected to chromatin status such as heterochromatin and euchromatin and a large effort was undertaken to reveal DNA repair mechanisms with regard to chromatin compaction (Goodarzi et al., 2008; Goodarzi et al., 2009). It was assumed that heterochromatin regions are rather devoid of γ-H2AX foci and that

the repair machinery locates to EC (Cowell et al., 2007), whereas the repair in HC is more time-consuming and requires the protein kinase ATM (Goodarzi et al., 2008). A recent study provided more insights into the movement of γ-H2AX foci to the periphery of HC regions during repair (Jakob et al., 2011). In addition to this, the establishment of silencing patterns at DSB gained more attention (O'Hagan et al., 2008) and especially, the ubiquitylation of the histone H2A came into focus (Shanbhag et al., 2010).

Previously, ubiquitylation of H2A and H2AX at lysine 63 at damaged sites was shown to be responsible for the recruitment of e.g. 53BP1 and BRCA1 (Huyen et al., 2004; Mailand et al., 2007). An additional ubiquitylation mark at the histone H2A at lysine 119 (H2Aub119), which is connected to silencing (Nakagawa et al., 2008), was shown to contribute to the silencing at DSB (Shanbhag et al., 2010). Nakagawa and colleagues showed that H2Aub119 represses the di- and trimethlation of H3K4 and that transcriptional initiation is repressed by the inhibition of H3K4 methylation (Nakagawa et al., 2008). This links the initiation of transcription, as indicated by RNA Pol II phospho-Ser5 and H3K4me3, and H2Aub119 to the DNA damage response, because these marks are lost or enriched, respectively, at damaged sites (own results, Chagraoui et al., 2011; Ginjala et al., 2011).

(Ginjala et al., 2011) and (Chagraoui et al., 2011) connect the establishment of H2Aub119 to PRC1 (BMI) at damaged sites and, interestingly, the deubiquitylation of H2A119 was previously shown to directly antagonize Polycomb-mediated silencing (Zhao et al., 2008). Furthermore, the silencing observed by (Shanbhag et al., 2010) was dependent on ATM which prevented a transcription-associated decondensation of chromatin (Shanbhag et al., 2010). Thus it would be interesting to test if an inhibition of ATM would influence the loss of transcriptional marks at damaged sites and thus impair recruitment of PRC1 or PRC2.

Considering my own results and the data of the recent literature (e.g. reviewed in Gieni et al., 2011, and Greenberg, 2011) the DSB-induced silencing resembles polycomb-mediated silencing, suggesting the establishment of facultative heterochromatin at DSB. Thus the loss of H3K4me3 from DSB sites could be important for the inhibition of transcription itself by inhibiting the binding of transcription factors (Vermeulen et al., 2007), or be necessary to allow the binding of repressive proteins such as PRC2 at DSB, because active marks impair the binding of PRC2 (Schmitges et al., 2011). The binding of PRC2 could then be responsible for the loss of further active marks such as histone acetylations mediated by HDACs (Miller et al., 2010) and the establishement of repressive marks such as H3K27me3 by the methyltransferase EZH2 (O'Hagan

et al., 2008; Chou et al., 2010). This silencing mechanism is comparable to the polycomb-mediated silencing at developmental genes (Pasini et al., 2008) (summarized in Cloos et al., 2008).

Due to the findings in the literature that deacetylases and methyltransferases act in concert e.g. in the polycomb-mediated silencing, it is tempting to speculate that histone demethylases are also a part of this concerted action. Additionally, (Klose et al., 2007) suggest an interaction of Jarid1A with a histone deacetylase and deacetylases were shown to remove histone acetylations from DSB sites (Miller et al., 2010).

However, it is also possible that the loss of H3K4 is connected to the binding of the chromatin remodeler NuRD and its component CHD4 (Chou et al., 2010), because the PHD domain of CHD4 preferentially binds unmethylated H3K4 (Mansfield et al., 2011) and CHD4 was recently connected to the DNA damage response (Larsen et al., 2010; Smeenk et al., 2010).

Since the elongating form of RNA Pol II phosphorylated at Ser2 was also under-represented at DSB (own results, and Chou et al., 2010), it can be further hypothesized that the silencing at DSB is also accompanied by the loss of histone marks of transcriptional elongation, such as H3K36me3. Moreover, the ubiquitylation of H2B at lysine 120 (H2Bub120) is associated with transcription and it precedes and stimulates the methylation of H3K4 in transcription initiation (Kim et al., 2009a). Thus a connection between H2Bub120 deubiquitylation and the loss of H3K4me3 at damaged sites is possible. It remains to be elucidated in how far the DSB-mediated silencing resembles the known pathways in detail, and how various transcription factors, methyltransferases, demetyhlases, deacetylases, and last but not least deubiquitylases act in concert to prevent a transcription of the damaged DNA.

On the other hand, the role of HP1 proteins at damaged sites could be more related to constitutive heterochromatin (HC) formation. Silenced regions decorated with H3K9me3, but not H3K27me3, harbor, for example, KAP1, that promotes the binding of H3K9me methyltransferases (KTM1E) and recruits the NuRD deacetylase complex and HP1 (reviewed in Campos and Reinberg, 2009). Since KAP1, NuRD (Ziv et al., 2006; Noon et al., 2010; Smeenk et al., 2010) and HP1 were observed at damaged sites (Ayoub et al., 2009; Luijsterburg et al., 2009; Chou et al., 2010), own results), the role or, more presumably, the interaction or crosstalk of these silencing factors in the DNA damage response is possible. However, recent observation suggest other mechanisms for the involvement of HP1 in the DDR (Luijsterburg et al., 2009; Baldeyron et al., 2011).

All of the described alterations of histone modifications and mechanisms can be considered as epigenetic alterations. Nevertheless, it is noteworthy that an epigenetic alteration is regarded to be preserved and independent from a causative signaling event (reviewed by Campos and Reinberg, 2009). In this extensive review, it is also discussed if such single, local alterations of histone marks which occur in the context of for example, DNA repair can be considered as real alterations of epigenetic information (Campos and Reinberg, 2009). Thus the hypothesis of a histone code for the DNA damage response has to be reconsidered carefully. It remains an open question if single alterations at a DNA break are coding for the DNA damage response and are essential for the repair machinery, or if they are an outcome of the chromatin environment, or a combination thereof.

4 Methods

4.1 Cell culture

4.1.1 Cultivation of cells

HeLa (human cervix carcinoma), U2OS (human osteosarcoma) cells were grown in medium size cell culture flasks (T75) in RPMI supplemented with 10% FCS, 100 U/ml penicillin, 50 µg streptomycin, and L-Glutamin. BJ1 h-TERT human fibroblasts were cultivated in large cell culture flasks (T100) in DMEM and 199 medium (4:1) supplemented with 10% FCS, 100 U/ml penicillin and 50 µg streptomycin. HeLa cells containing different HA-tagged histone H3 variants were cultivated in DMEM, 10% FCS, 100 U/ml penicillin, 50 µg streptomycin and 400 µg G418. SAOS cells were kept in McCoys medium supplemented with 15% FCS, 100 U/ml penicillin, 50 µg streptomycin. All cell lines were kept in 5% CO_2 at 37°C. For optimal growth conditions, cells were split after they have reached confluence (every three to four days for HeLa, U2OS and SAOS, and every seven to twelve days for BJ1). The old medium was removed and cell layer was washed with 5 – 10 ml PBS. 1 ml Trypsin/ EDTA was added and distributed across the cell layer. After 3 – 5 min, the cells were detached from the flask bottom due to the enzymatic activity of trypsin. Detaching was enhanced by knocking laterally against the flask. Cell were re-suspended in 9 ml RPMI, which stops the enzymatic reaction, and about one tenth of the cell suspension was transferred to a new flask and filled up to 10 ml with fresh medium and cultivated further at 37°C, 5% CO_2.

4.1.2 Freezing and thawing of cells

Adherent cells were removed from the flask bottom by trypsination (see below). A cell number of about 10^{10} cells can be stored in one 2.0 ml cryo tube. Thus cells can be either pooled or split depending on cell number. Cells from one flask were re-suspended in 9 ml medium and centrifuged for 5 min at 500 x g. Medium was removed and the cell pellet was re-suspended in 1.5 ml FCS 10% DMSO and transferred to a 2.0 ml cryo tube. The tube was placed into a freezing box (Nunc), which contains a 2-propanol layer. The box is placed at – 80°C. The 2-propanol layer leads to a gentle cooling of 1°C per minute. After three days, the cryo tubes with cells were transferred from – 80°C into liquid nitrogen.

Cells were stored in liquid nitrogen diluted in FCS containing 10% DMSO in 2.0 ml cryo tubes. DMSO prevents crystallization during freezing, but at room temperature it is toxic for the cells. For cell thawing, frozen cells are thawed for ~ 2 min at RT and quickly re-suspended with their respective growth medium supplemented with FCS and transferred from the cryo tube to a 15 ml falcon tube. After a centrifugation step for 5 min at 500 x g, the medium was removed and pellet was re-suspended in 10 ml growth medium and disseminated into cell culture flasks. Between eight to twelve hours after seeding, the medium was replaced by fresh medium to remove remaining DMSO.

4.1.3 Determination of cell number

Cell number was determined with Buerker or Neubauer counter chambers. Adherent cells were removed from the flask bottom by trypsination and re-suspended in 9 ml of medium. For counting, 10 µl of the well mixed cell suspension were pipetted onto the chamber under the prearranged cover slip. For some experiments, it was necessary to exclude dead cells from counting. In this case, 10 µl cell suspension were mixed with 10 µl of Trypan blue, which stains dead cells. The cell number was counted with the help of the standardized rectangles of the chambers. The mean cell number which was counted in two to three of the squares was multiplied with 10^4 which gives the mean cell number per milliliter.

4.1.4 Seeding of cells in steel containers for ion microirradiation in a line pattern
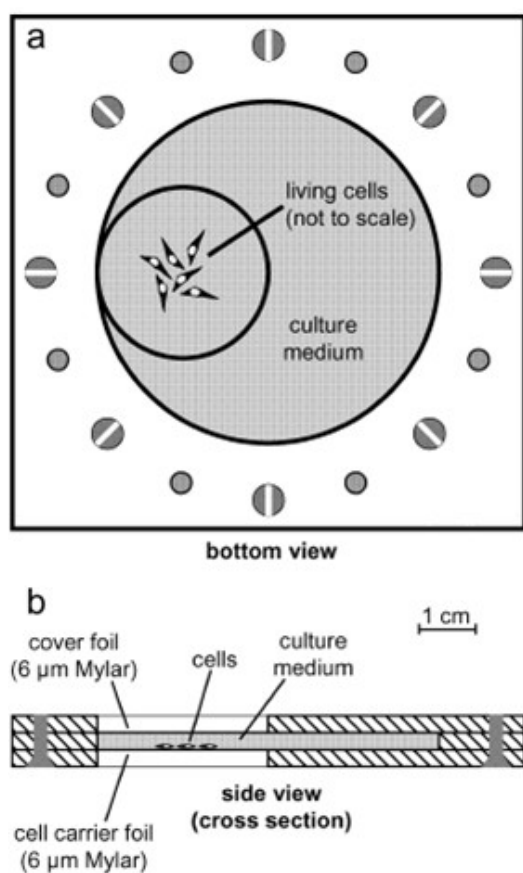
Figure 4.1: Draft of a stainless steel cell container for ion-irradiation in a line pattern. A) Bottom view of the container. Cells were seeded on 6 µm Mylar foil in the irradiation window and covered with medium. B) Side view of the cell container closed with the lid for irradiation (adapted from Hauptner et al. 2004).

For ion microirradiation, cells were seeded on a 6 µm Mylar foil, because the ions have to pass through the thin foil and would be decelerated by a glass or plastic bottom. The foil used for perpendicular ion microirradiation contains a grid with 300 x 300 µm coordinates to relocate the irradiated cells. The foil is fixed on to a stainless steel container (Figure 4.1), with the grid placed in the middle of the irradiation window. The area of the foil located at the irradiation window was pre-coated with Cell-TAK (BD Bioscience) to ensure proper cell attachment during irradiation (see 4.4.1). Approximately 24 h before irradiation, 3.0×10^5 cells in 1 ml were seeded directly on the grid. Containers were placed into an 10 mm petri dish to ensure sterile handling. The cells were incubated at 37°C, 5% CO_2 for 1 h to allow attachment and the containers were then filled with 7 ml medium. After incubation at 37°C, 5% CO_2 over night, cells were irradiated at the microbeam as described in (Hauptner et al., 2004) and in 4.4.1.

4.1.5 Seeding of cells in steel rings for alpha- and X-irradiation with subsequent immunofluorescence detection

For alpha irradiation, cells were seeded on a 6 µm Mylar foil fixed in a stainless steel ring of 2 cm diameter (Figure 4.2), because alpha particles would be blocked by a thick plastic or glass bottom. In general, cells were seeded in rings for immunofluorescence staining, where at the last step of the staining procedure, the foil with the stained cells is transferred to an objective slide and mounted for microscopy (described in 4.5). 3.0×10^5 cells were seeded in 2 ml medium in a

ring. The ring was placed into a 5 cm petri dish to ensure sterile handling. The cells were incubated at 37°C, 5% CO_2 over night and either irradiated or directly fixed and stained for immunofluorescence detection (4.5).
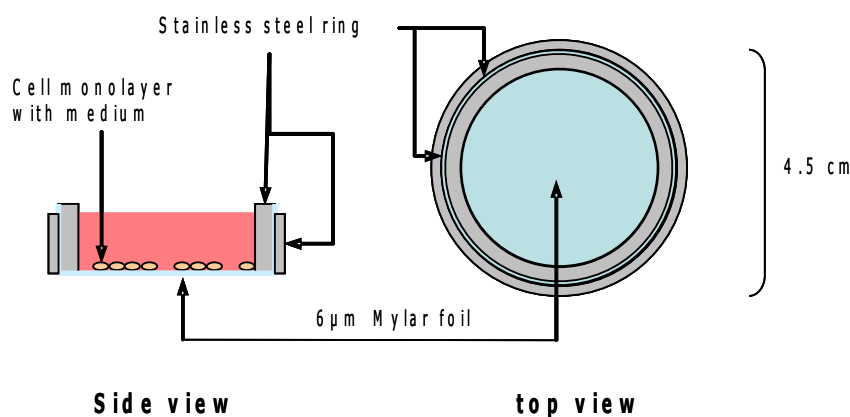
Figure 4.2: Draft of a stainless steel ring used for alpha-irradiation and immunofluorescence of cells. Cells are seeded directly on the 6 μm Mylar foil in 2 ml medium. Following immunofluorescence staining of fixed cells, an area of the foil was cut out and transferred to an objective slide, covered with a cover slip and mounted for microscopy (draft adapted from the dissertation of S. Auer 2011, modified).

4.2 Transfection of cells with siRNA

4.2.1 Knockdown of Jarid1A with Dharmafect

For transfection of cells with siRNA (silencing RNA), 200.000 cells were seeded in a 6-well (2 cm diameter) or a steel ring 24 h before transfection. For transfection performed in cell containers with subsequent ion microirradiation, cells were seeded in specially constructed steel zylinders with a diameter of 1.7 cm which are placed on the mylar foil. The number of cells was calculated according to the diameter of the surface and resulted in 120.000 cells. For down-regulation of Jarid1A/RBP2 the following siRNAs were used which were previously shown to down-regulate Jarid1A/RBP2 (Benevolenskaya et al., 2005); Table 4.1):

siRNA sequences

RBP2 No. 2	5' GCCAAGAACAUUCCAGCCUdTdT 3'
RBP2 No. 4	5' CUUGAGGCAAUGACCAGAGdTdT 3'
Non-silencing siRNA	5' UUCUCCGAACGUGUCACGUdTdT 3'

Table 4.1: siRNA sequences of RBP2 siRNAs No. 2 and No.4 (Benevolenskaya et al. 2005) and sequence of the non-silencing siRNA (Qiagen).

siRNAs were delivered in single-strands as a lyophilized powder. Before transfection, the powder was diluted to a concentration of 100 µM with RNAse free water. Single strands were annealed with their respective complementary strands by mixing and diluting them in annealing buffer to a final concentration of 20 µM. Single strands were annealed as described in the manufacturer´s protocol (Metabion). For transfection of HeLa and U2OS cells with Dharmafect, the volumes were calculated for one well of a six-well plate (2 cm diameter) according to the protocol provided by Dharmacon. 2.5 µl of the annealed double-stranded siRNA (either No. 2 or No. 4, 20 µM each) were diluted in 197.5 µl of serum-free RPMI medium (without antibiotics) and incubated for 5 min at RT. Meanwhile, 4 µl of Dharmafect reagent were diluted in 196.0 µl of serum-free RPMI medium (w/o antibiotics) and incubated for 5 min at RT. Both solutions were combined, mixed carefully and incubated for 20 min at RT. Subsequently, 1600 µl of RPMI medium supplemented with 10% FCS (w/o antibiotics) were added to the Dharmafect/siRNA mixture. Old medium was removed from the cells and Dharmafect/siRNA mixture was added to the cells.

4.2.2 Knockdown of Jarid1A with Lipofectamin 2000

For transfection of SAOS cells with Lipofectamin 2000, volumes were calculated for one well of a six-well plate (2 cm diameter) according to Invitrogen´s Lipofectamin 2000 protocol. Here, 5 µl of siRNA pool (2.5 µl from siRNA No. 2 and 2.5 µl of siRNA No.4; 20 µM each) were diluted in 250 µl of serum-free OptiMEM (Invitrogen) and incubated for 5 min at RT. Meanwhile, 5 µl of Lipofectamin 2000 were mixed and diluted in 250 µl of OptiMEM and incubated for 5 min at RT. Afterwards, both solutions were combined, carefully mixed and incubated for another 20 min at RT. OptiMEM is recommended by the supplier for lipofection, because it is serum-free and purified. After incubation, solutions were mixed with McCoys medium supplemented with 15% FCS (w/o antibiotics) and added to the cells after old medium has been removed.

Cells were incubated for 48 – 120 h. Whole cell protein extracts were produced with RIPA buffer as described in 4.12.1. 48 h after transfection of SAOS cells with Lipofectamin 2000 and

Jarid1A siRNA or control siRNA, medium was exchanged because many dead cells were observed. Effect on protein amount was tested with western analysis. For control, untreated cells and cells treated with non-silencing siRNA (Quiagen) were used. Cells seeded and transfected in rings were used for subsequent immunofluorescence staining (4.5). For subsequent ion microirradiation, cells were seeded and transfected in cell containers (4.1.4). For transfection in cell containers, the volume of siRNA was adapted to a final volume of 8 ml medium. For this, the volume of siRNA was multiplied by 4 using the Dharmafect protocol and Invitrogen´s protocol, respectively.

4.2.3 Transfection of cells according to Benevolenskaya´s protocol

The protocol can be found on the website of E. Benevolenskaya (http://www.uic.edu/com/bcmg/Lisa/Projects/Protocols.HMTl). Cells were split 2 days before transfection and kept in regular growth medium without antibiotics in a 10 cm dish. 1 h before transfection, medium was replaced with fresh medium. For transfection, 10 µl Lipofectamin 2000 (Invitrogen) were diluted in 1 ml OptiMEM (Gibco) and incubated for 5 min at RT. Meanwhile, 10 µl of siRNA stock (20 µM) or 5 µl of siRNA No. 2 and No.4, respectively, were diluted in 1 ml OptiMEM and incubated for 5 min at RT. Subsequently, both dilutions were mixed and incubated for additional 20 – 30 min at RT. After ~15 min of incubation, medium from cells was exchanged with 3 ml of OptiMEM. This was done quickly to avoid unnecessary stress for the cells. After the incubation, the mixture of Lipofectamin 2000 and siRNA was dropped onto the cells and solution was gently dispensed across the cell layer. Cells were incubated for 5 h at 5% CO_2, 37°C. Following transfection, OptiMEM was removed and changed on regular growth medium. Further treatment of cells, e.g. irradiation or whole cell protein extraction was performed within 48 to 96 h after transfection.

4.3 Analysis of mRNA levels with real-time PCR

4.3.1 RNA extraction

Total RNA was isolated from HeLa and SAOS cells using the Mirvana total-RNA isolation kit (Ambion). Cells were harvested and counted as described above. The amount of the extraction buffer was adjusted according to the cell number ($2*10^5$ of SAOS, and $1*10^7$ of HeLa) used. Isolation of RNA was performed according to the manufacturer´s protocol. RNA concentration

was determined with a Nanodrop spectrophotometer (Peqlab) at A_{260nm} and compared to the amount of proteins in the sample by measuring the absorbance at A_{280nm}. RNA was subsequently reversely transcribed into cDNA to enhance stability of the sample. Remaining amounts of RNA were stored at -80°C.

4.3.2 cDNA synthesis using reverse transcriptase

Subsequent to extraction, RNA was reversely transcribed into cDNA by reverse transcription (RevT). Depending on the number of cells from which RNA was extracted, the concentration of RNA was rather high or low. For highly concentrated samples ($\sim 10^7$ cells), cDNA was synthesized with Superscript reverse transcriptase (Invitrogen) according to manufacturer´s instructions using 5 µg of RNA template. For low amounts of RNA, 50 ng of RNA was used for cDNA synthesis with Sensiscript reverse transcriptase (Quiagen). To control for contamination with genomic DNA, samples without reverse transcriptase (No-RevT) were used in parallel. Mixtures for reverse transcription were prepared as described below (Table 4.2). cDNA was stored at -20°C, No-RevT samples were stored at -80°C.

Mastermix for RevT with Sensiscript	Mastermix for RevT with Superscript
2 µl 10x RT buffer	2 µl dNTP Mix (5 µM)
2 µl dNTP Mix (5mM of each dNTP)	1 µl Oligo-d(T) Primer (10 µM; 10 pmol/µl)
2 µl Oligo-d(T) Primer (10 µM; 10 pmol/µl)	X µl RNA template (5 µg)
1 µl RNA Inhibitor (RNaseOut; 10 units/µl)	X µl Nuclease-free water
X µl RNA template (50 ng)	Total: 12 µl
X µl Nuclease-free water	4 µl 5x First Strand buffer
1 µl Sensiscript Reverse Transcriptase	2 µl 0.1 M DTT
Total: 20 µl	1 µl RNA Inhibitor (RNaseOut; 40 units/µl)
	1 µl Superscript Reverse Transcriptase

Table 4.2: Mastermixes prepared for reverse transcription with either Sensiscript (left column) or Superscript (right column).

4.3.3 Quantitative real-time PCR

With quantitative real-time polymerase chain reaction (QRT-PCR), the targeted DNA is amplified and quantified in "real-time" during the reaction process. To analyze mRNA levels of a gene of interest in comparison to a stably expressed housekeeping gene, QRT-PCR was performed on a LightCycler 480 II from Roche Diagnostics equipped with a 96-well plate. A fluorescent dye (SYBR Green I) which intercalates with double-stranded DNA is used to detect

the amplified PCR products at the end of each elongation. For calculation of relative amounts of mRNA, the Ct (cycle-threshold) value is used, which indicates the crossing point where fluorescence intensity is higher than the background fluorescence value. Ideally, the amplification rate of cDNA is doubled in each cycle. For each transcript to be analyzed a standard curve was used to calculate the efficiency of amplification of the used primer combinations. They are listed in Table 4.3. Primer sequences were confirmed to target the gene of interest with NCBI nucleotide blast.

Name	Sequence	Source
GAPDH for*	5'-GAAGGTGAAGGTCGGAGTC-3'	Universal ProbeLibrary Roche
GAPDH rev*	5'-GAAGATGGTGATGGGATTTC-3'	Universal ProbeLibrary Roche
RBP2_1 for	5'-GCTGCTGCAGCCAAAGTTG-3'	(Benevolenskaya et al., 2005)
RBP2_1 rev	5'-AGCATCTGCTAACTGGTCTC-3'	(Benevolenskaya et al., 2005)
RBP2_2 for	5'-CCGGCATCTGCAAATTC-3'	Universal ProbeLibrary Roche
RBP2_2 rev	5'-ACGAAAGCTTTTTACTTCACAGG-3'	Universal ProbeLibrary Roche
WSTF for	5'-TGGGAGAAGAGTGTGACTTCG-3'	Universal ProbeLibrary Roche
WSTF rev	5'-TCCAAAGGATGAATCTTCACAAT-3'	Universal ProbeLibrary Roche

Table 4.3: Primers used for quantitative real-time PCR. All primers were obtained from Metabion and were a kind gift of B. Kempkes. (*for = forward; *rev = reverse)

The standard curve was produced from a dilution series of 10 µl from a previously obtained PCR product of the gene of interest (dilution series was: 10^{-2}, 10^{-4}, 10^{-6}, 10^{-8}, 10^{-10}). From this dilution series the efficiency of amplification can be calculated. For relative quantification, the 10^{-6}-diluted sample was further used for calibration. The housekeeping gene GAPDH was used as a reference. Nuclease-free water was used to control contamination and additionally, No-RevT samples were used to control contamination with genomic DNA. 8 µl of the SYPBR Green I master mix containing 1 µl each of the respective forward and reverse primer (0.5 µM), 5 µl of SYBR Green I and 1 µl of nuclease-free water, were pipetted into the wells of the 96-well plate. Subsequently, 2 µl of cDNA template (either undiluted or diluted 1:2 in nuclease-free water) were added to each well. The plate was sealed with an adhesive foil, centrifuged shortly at 3000 x g and QRT-PCR was performed as described in Table 4.4.

Analysis mode	Cycle	Segment	Temp. (°C)	Time	Acquisition mode
none	1	Preincubation	95	10 min	none
Quantification	45	Denaturation	95	2 s	none
		Annealing	63	10 s	none
		Extension	72	20 s	single
Melting curves	1	Denaturation	95	5 s	none
		Annealing	65	1 min	none
		Melting	97 (0.11°C/ s)	0 s	continuous
none	1	Cooling	40	30 s	none

Table 4.4: Program used for quantitative real-time PCR. (s = seconds; min = minutes)

4.4 Irradiation of cells

To induce DNA damage to living cells, they were irradiated with different types of ionizing radiation or with an UV-laser. For irradiation at different sources, varying conditions and devices were required as described in the following:

4.4.1 Ion microirradiation with SNAKE
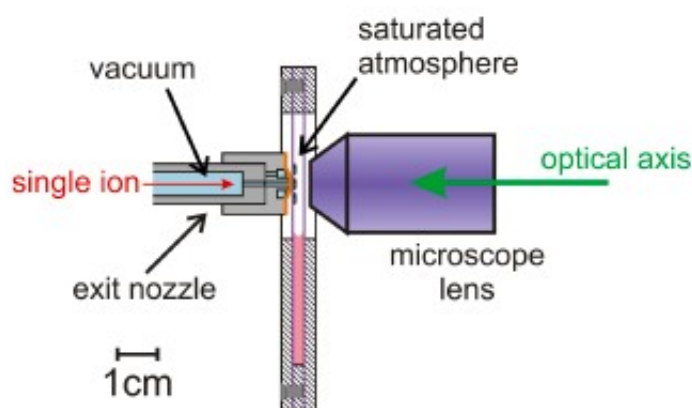
Figure 4.3: Set-up of the cell container at the ion microbeam SNAKE for ion microirradiation of live cells in a line pattern. Irradiation was performed with the cell container in an upright position. Accelerated single ions exit the vacuum through the exit nozzle and pass the cell layer in a perpendicular angle. During irradiation, the microscope objective was exchanged with a particle detector (taken from Hauptner et al. 2006a).

Ion microirradiation was performed with the ion microbeam SNAKE - Superconducting Nanoprobe for Applied Nuclear (Kern-) Physics Experiments - located at the Munich 14 MV tandem accelerator facility at the Maier-Leibnitz-Laboratorium. Because the tandem accelerator is used by a broad range of scientists, beam times are limited to approximately five weeks per year and the number of experiments is limited. In the present work, experiments were conducted within eight beam time periods and chances for repeating experiments were thus

limited. 24 h before irradiation 3.0×10^5 cells were seeded in stainless steel cell containers in the irradiation window as described above.

Irradiation was performed at room temperature and the cell container was placed in an upright position on the stage of an Axiovert 200 M microscope which was installed in a horizontal angle (Figure 4.3). With the aid of the microscope, the cell layer was focused on the focal plane of the exit nozzle from which the accelerated ions exit. The microscope can be used for live cell irradiation as well (Hable et al., 2009). For irradiation, the cell container was filled with a total volume of 6 ml medium and closed with a lid (Figure 4.3). In the upright position, the cells are not covered by medium, because this would decelerate the ions, instead they are kept in an H_2O-saturated atmosphere. Subsequently, cells were irradiated with accelerated 55 MeV carbon ions in a perpendicular angle. Thus irradiation-induced foci (IRIF), which were subsequently visualized by immunofluorescence (4.5), represent the ion hits through the cell nucleus. Ions were applied either in a line pattern of 1 μm x 5 μm or in a matrix pattern of 5 μm x 5 μm. The former pattern results in an average dose of 12 Gy, the latter in 2.4 Gy (Hauptner et al., 2004). The final size of the irradiated field is approx. 300 μm^2.

4.4.2 X-irradiation

X-irradiation was performed with a Philips MCN-X-ray tube with 250 kV at 13 mA or with 300 kV at 10 mA (2.5 + 4.0 mm Al and 1.0 mm Cu filtration) at a dose rate of 0.56 Gy/ min or 2 Gy/ min, respectively. For irradiation and subsequent protein extraction (4.12.1), cells were seeded in cell culture flasks (T75) and grown to confluency at time of irradiation. For irradiation with subsequent immunofluorescence staining (4.5), cells were grown on 6 μm mylar foil in stainless steel rings (4.1.5) to a confluent layer at time of irradiation. Irradiation was performed at room temperature. Unirradiated control samples were placed at room temperature for the irradiation duration. Following irradiation, the cells were incubated for indicated times at 37°C, 5% CO_2 and were either used for protein extraction or fixed for immunofluorescence staining.

4.4.3 α-particle irradiation

α-particle irradiation was performed with an [241]Americium source located at the Institute of Radiation Biology of the Helmholtz Center Munich. For irradiation, cells were grown on 6 μm mylar foil in rings as described above. Each sample was irradiated for 4 min at 37°C, which results in dose of 0.4 Gy and on average about four particle passages per cell nucleus. After

irradiation, cells were incubated for indicated times at 37°C, 5% CO_2 and fixed for immunofluorescence staining (4.5).

4.4.4 UV-laser irradiation

UV-laser irradiation at Leica SP5 LSM

Cells were seeded in a 5 mm µ-Dish (ibidi, Germany) or in Matek chambers (Nunc, USA) containing a grid for relocation of irradiated cells. UV-laser microirradiation was performed with a confocal laser scanning microscope (SP5 DMI 6000 CS, Leica, Germany) equipped with a UV-transmitting HCX PL 63x/1.4 oil objective at room temperature. Preselected spots of ~1 µm diameter were microirradiated with a 405 nm diode laser for 1s at 100% laser power, using the FRAP mode. After irradiation, the cells were incubated for 30 min at 37°C and 5% CO_2 before fixation.

UV-laser irradiation at Ultra View VoX spinning disk microscope

Cells were seeded in 5 mm MaTek chambers containing a grid for relocation of irradiated cells. Before irradiation, the growth medium was exchanged with live cell medium (DMEM without phenol red, 10% FCS and 25 mM HEPES). Cells were irradiated with a Perkin Elmer ultraView Vox spinning disc unit attached to an Axio Observer D1 microscope (Zeiss) equipped with a Plan-Apochromat 63x/1.4 oil objective using Volocity software at 37°C, 5% CO_2. For irradiation, the FRAP preview mode was used with repeatedly scanning (3000 iterations) of 1µm spots with 40-100% laser power of the 405 nm diode laser. Following irradiation, the cells were incubated for 15 min at 37°C, 5% CO_2 before fixation.

4.5 Immunofluorescence staining

Dependent on the device used for cell growth, either 3 ml (for cell containers used for ion microirradiation) or 2 ml (for rings of 2 cm diameter for all other immunofluorescence samples) of the respective solution were used to cover the complete cell layer. Before fixation, medium was removed and cell layer was quickly washed with PBS or where indicated, unbound proteins were extracted with a mild-detergent extraction buffer (25 mM HEPES pH 7.5, 50 mM NaCl, 1 mM EDTA, 3 mM $MgCl_2$, 300 mM sucrose and 0.5% Triton-X-100) for 5 min at 4°C (Lukas et al., 2003). Cells were fixed with freshly prepared 2% para-formaldehyde in PBS for 15 min at

RT, followed by a quick washing step with PBS. For permeabilization, the cell layer was incubated with PBS containing 0.1% Triton-X-100 three times for 5 min each. For blocking, cells were incubated with PBS containing 1% BSA, 0,15% glycine, three times for 10 min each. Before adding primary antibody solution, the liquid was removed completely from the cell layer. Primary antibodies were diluted in 75 µl blocking solution (PBS, 1% BSA, 0.15% glycine) and added to the cell layer. Incubation with primary antibodies was either 1 h at RT or over night at 4°C in a humidified chamber. Afterward, the samples were washed three times with PBS containing 0.1% Triton-X-100 for 5 min each, followed by incubation with blocking solution three times for 10 min each. Appropriate secondary antibodies were diluted in 75 µl blocking solution, added to the cell layer and the samples were incubated for a minimum of 45 min at RT in a humidified chamber. Before DNA counter staining with DAPI, secondary antibodies were removed by washing steps with PBS for 1 x 10 min and 2 x 5 min. DAPI stock solution (1mg/ml) was diluted in PBS (1:10000) and 2 or 3 ml, respectively, were added to the cell layer and incubated for 90 s followed by two washing steps with PBS for 2 min each. Subsequently, all liquid was removed, the cell layer was mounted with Vectashield and covered with a cover glass of 20 or 22 mm diameter. The foil with attached cells covered by the cover glass was cut out by using a heated element and fixed to an objective slide with nail polisher. To view details of primary and secondary antibodies used in the present work, see Table 5.2 and Table 5.3 in chapter 5.7.

4.6 Peptide Competition Assay

The present work mainly relies on immunodetection of different histone methyl states with commercially obtained antibodies (listed in Table 5.2 of chapter 5.7.1). To test these antibodies for their specificity, a peptide competition assay was performed. The primary antibody was incubated with a peptide which´s epitope is specifically recognized the antibody. The antibody was additionally incubated with various other peptides which are analogs of different methyl states at the same lysine or of other lysines to test cross reactivity of the antibody (listed in Table 5.4 of chapter 5.7.3). As previously described by (Zinner et al., 2006), the primary antibody was incubated in its respective working dilution in PBS containing 1% BSA and 0.15% glycine for 1 h at 37°C with an 100-fold-molar excess of peptide (15 amino acids length; information provided by the supplier). Cells were treated as done for immunofluorescence detection (4.5). The pre-incubated primary antibodies were added to the cells and incubated for about 12 h at 4°C. The

primary antibodies were detected with the appropriate secondary antibodies. H3K4me3 and H4K20me3 antibodies were also tested with their competing peptides in western immunoblotting. For this, the primary antibody was pre-incubated in its working dilution with 1 µg of peptide in 5% BSA for 1 h at 37°C or for 2 h at RT, as recommended by the antibody´s supplier. The pre-incubated antibody was added to the blotting membrane and the membrane was developed as described in chapter 4.13.3.

4.7 Ultrathin sectioning of stained cells

Ultra thin sectioning is commonly used for preparation of unstained cell samples and subsequent electron microscopy (Rouquette et al., 2009; Solimando et al., 2009). In the present work, ultra thin sectioning was established for immunolabeled cells combined with 2D confocal microscopy. By ultra thin sectioning of irradiated and stained cells using an ultra microtome (Leica UltraCUT), physical cell sections of 150 nm thickness were obtained.

4.7.1 Preparation of samples for embedding in liquid resin

Following immunofluorescence and DNA counter staining with DAPI as described in 4.5, the cell monolayer attached to mylar foil was prepared for ultra thin sectioning. Cells were dehydrated as follows: 30% EtOH 2 x 5 min, 50% EtOH 2 x 5 min, 70% EtOH 2 x 10 min, 90% EtOH 2 x 10 min, 100% EtOH 3 x 10 min. Because 100% EtOH is evaporating quickly, the volume was not aspirated completely to avoid drying of the cells. Subsequently, 100% EtOH was exchanged with liquid resin (LR White, London Resin Company, Berkshire, England), pre-warmed to RT, and incubated for 30 min at RT. Subsequently, resin was replaced with fresh resin and incubated over night at 4°C to prepare the cells for resin-embedding and subsequent polymerization.

4.7.2 Relocation and embedding of irradiated cells

To apply this method to cells which had been irradiated at the ion microbeam within an irradiated field of 300 x 300 nm, the challenge was to relocate the irradiated cells on the polymerized resin. The mylar foil used for ion microirradiation contains a grid for relocating the irradiated area (see chapter 4.4.1). To relocate this area with cells on the polymerized resin, the known coordinates of the irradiated area were marked by small holes introduced to the mylar foil with a small needle. The grid was cut out from the foil fixed to the container and the marked area was placed

in the center of a resin-filled capsule. The foil and the capsule were turned up-side down and incubated for 48 h at 60°C to allow polymerization. Before sectioning, the marked area was relocated on the polymerized surface and the foil was removed.

4.7.3 Preparation of the sectioned area

For sectioning, the area containing the irradiated cells had to be prepared as a "pyramid" with rectangular edges and an even surface with a size of about 200 μm^2. The size of the sectioned area is limited by the size of the knife. Preparation of the pyramid is done manually by using a razor blade. The resin block with the cells on the surface was fastened on the device of the microtome (Figure 4.4 A,B) and preparation of the pyramid was performed under the microscope of the ultra microtome. The ocular of the microtome contains an optical grid which was used for precise adjustment of the razor blade on the surface. At first, the surface surrounding the area to be sectioned had to be removed by raw cutting with a conventional razor blade. For final adjustment of the rectangular angles, extra sharp and fine razor blades with very thin and sharp blades were used. After preparation of the pyramid, the resin block is removed from the holder of the microtome (Figure 4.4 A) and fixed on to the arm of the microtome in a vertical position (Figure 4.4 C).
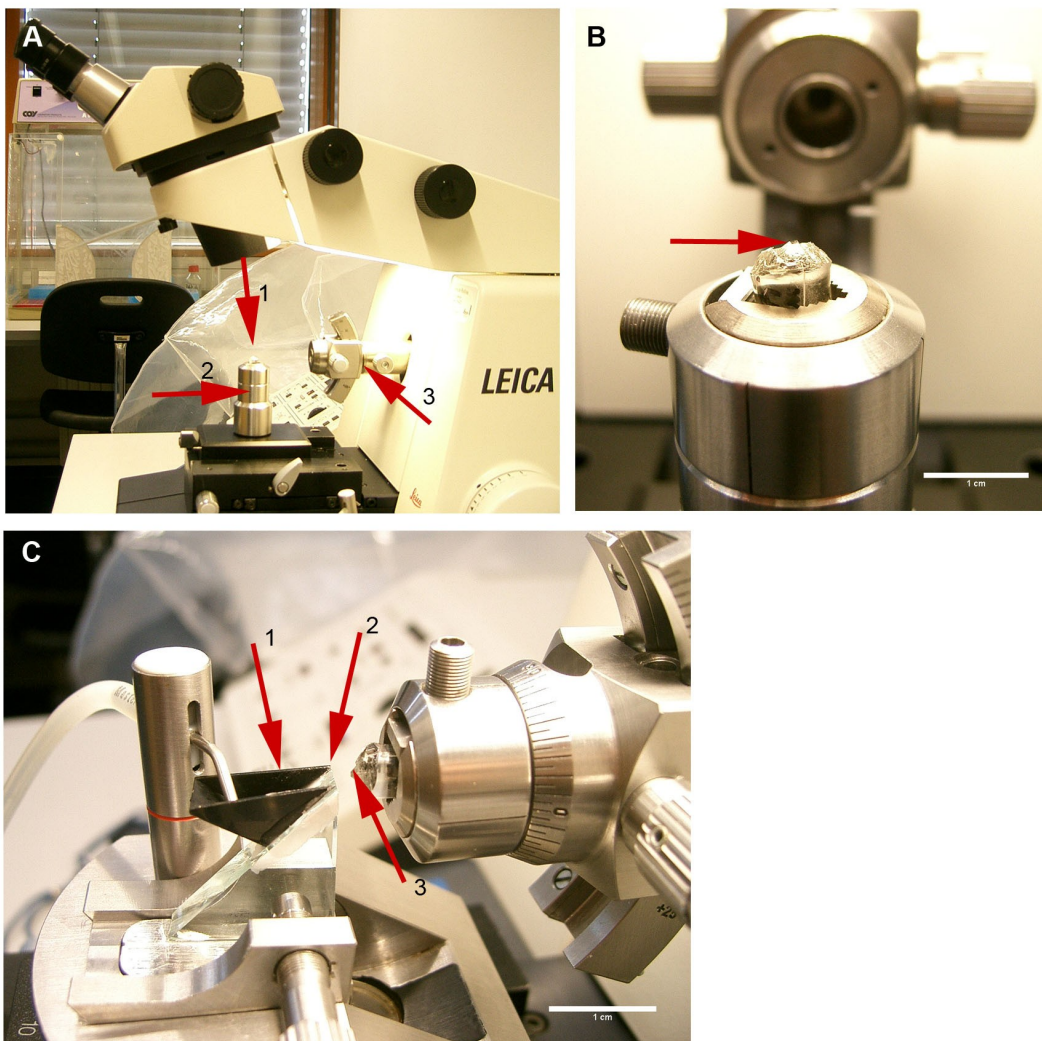
Figure 4.4: Illustration of the ultra microtome (Leica Ultracut) which was used for physical sectioning of immunolabeled cells. A) shows the ultra microtome with the holder (arrow 2) in the center of the optical focus (arrow 1) of the microscope where the polymerized resin block was fixed for manual cutting of the pyramid. Arrow 3 indicates the "arm" of the microtome where the block was finally fixed for sectioning. For sectioning, the holder was replaced by the set-up as shown in C. B) Front view of the holder with the resin block in an upright position. Arrow points to the pyramid, which was cut out manually from the surface by using razor blades. The arrowhead points directly to the head of the pyramid, which is a square of approx. 200 x 200 nm containing irradiated and stained cells. C) Set-up of the water reservoir (arrow 1), the glass knife (arrow 2) and the block fixed in the arm of the microtome in a vertical position (arrow 3). For sectioning, the reservoir was filled with Aqua dd. and the small tap on the left was used to adjust water level. Arrow 2 points directly to the blade of the glass knife. The head of the pyramid and the blade were adjusted precisely in all dimensions. Sections were collected on the water surface. The navigator of the microtome (not shown) was used for automated approaching and sectioning. Scale bar is 1 cm.

4.7.4 Sectioning

For sectioning, a glass knife with a clean and sharp blade was selected (Figure 4.4 C, arrow 2). The water reservoir (Figure 4.4 C, arrow 1) had to be fixed to the glass triangle with wax and/ or stripes. By heating the wax carefully, the hot wax was applied to the reservoir. It was important not to put too much wax close to the blade, because of its hydrophobic effect. When a diamond knife was used, it was already equipped with a water reservoir ready for use. The reservoir was cleaned by washing with distilled and filtered water. Then, the knife with the reservoir was fixed on the ultra microtome device (Figure 4.4 C). The reservoir was filled with ultra pure water in a way that the blade was coated with water but the water surface was still concave to preserve the block from getting wet. The small water-tap shown in Figure 4.4 C included with the ultra microtome was used to adjust the water level. to sectioning, the heater was set to 70° C. Objective slides and cover slips were cleaned with 80% Ethanol and placed on the heater.

Before sectioning, the following adjustments had to be performed at the microtome. First, the resin block with the pyramid was fixed in the holder of the arm of the microtome with the edges in vertical position to the table (Figure 4.4 C, arrow 3). With the help of the microscope of the ultra microtome, a clean and sharp area of the blade was selected and brought into a position parallel to the edges of the pyramid. During adjustment of the optimal position for sectioning, the water level was constantly checked to ensure that the blade was covered with water. When the water surface needed adjustment, then the block was placed into the "end position" (below the knife) to prevent the block from getting wet.

The knife and the block were slowly approached by using the small wheel of the navigator in steps of 0.5 μm. Meanwhile, the arm of the microtome with the block was moved up and down manually to permanently check the position and the angle of the block. While approaching, the edges of the block and the blade were precisely adjusted into a parallel position. In addition, the vertical distance of the block and the blade was corrected. The aim was to arrange all edges of the block in parallel to the blade (horizontally and vertically) and in the same distance to the blade.

On the navigator, the *begin and end* point for the arm was set by moving the arm closely above the blade (begin) and closely below the blade (end). In the range of *begin and end* point, the arm is moving very slow. This is the range, were the block was sectioned. It was important not to set the begin and end point too short, in case that adjustments during the sectioning had to be

performed. To ensure a parallel and precise adjustment of the block and the blade, the shadow of the blade on the block surface was used.

Now, the block was approached by using the button "step" on the navigator. First, a step size of 0.5 μm was used and further decreased up to 0.1 μm. Meanwhile, the positions of the block, the blade and the water level were controlled. When the first edges of the block were touched by the blade, the arm movement was set automatically. When using glass knifes, it was useful not to stop the sectioning procedure once started to keep the sections even. If it was necessary to stop the movement, the arm was stopped in the end position.

Approximately 40 μm of the pyramid (which means of the cell layer in Z) were sectioned. The color of the section indicates the thickness of the section (see table below). The sections were collected on the water surface. Here, sections of approximately 150 nm thickness appearing in a violet color were picked with a loop from the surface and transferred to a preheated cover slip. The heat evaporates the water and thereby the section could be evenly placed on the glass. At maximum nine sections in rows of three to three sections were placed on one cover slip. Finally, the cover slip with the sections was mounted with Vectashield and fixed on an objective slide with nail polish.

Color of ultrathin section	estimated thickness of section in nm
silver	80 – 90
gold	100
violet	150
blue	200

Table 4.5: Color and corresponding thickness of physical cell sections obtained by ultrathin slicing with an ultra microtome. Cells were embedded and polymerized in resin. Cell layer was cut with an ultra microtome into sections of approximately 150 nm. Sections were collected on a water surface where they appear in a specific color which corresponds to their thickness.

4.8 Image Acquisition

In the present work, the main approaches rely on microscopic images. Therefore, all settings and e.g. choice of fluorochromes, were done carefully and to best knowledge.

One critical event to consider for localization analysis is bleed-through. Here, signal of one channel would also be visible in the other channel and thus co-localization would be measured by mistake. Bleed-through can be avoided by choice of fluorochromes, by sequential acquisition of the channels and by narrow band emission filters. In Table 4.6 an overview of used

fluorochromes and their respective absorption and emission maxima and excitation wavelength is given.

Fluorochrome	Absorption maximum (nm)	Emission maximum (nm)	Excitation wavelength (nm)
Alexa Fluor 488	493	520	488
Cyanin 3	549	562	561
DAPI	358	463	405

Table 4.6: Spectral properties of fluorochromes used for fluorescence microscopy (adapted from Zeiss MicroImaging GmbH. www.zeiss.de/micro).

4.8.1 Confocal laser scanning microscopy

A confocal laser scanning microscope (SP5 DMI 6000 CS, Leica, Germany) equipped with a 63x/1.4 Plan-Apochromat oil objective and the software Leica Application Suite 1.7.0 was used. A 405 nm diode laser for DAPI, a DPSS diode laser (561 nm) for Cy3 and an argon laser (488 nm) for Alexa488/GFP fluorochromes were used. An Acousto Optical Beam Splitter (AOBS) was used. The SP5 was located at the LMU Biocenter in Martinsried (Munich) and access was kindly provided by Prof. T. Cremer. When starting the scanning, laser power was set to 10% and was later increased to 15 – 20% if necessary. An image format of 512 x 512 pixels was used. The zoom factor to scan single cell nuclei was set to 9.6, which results in a x,y-pixel size of 50 nm x 50 nm. The axial distance between the optical sections was 200 nm. Scanning of optical section was performed sequentially for the different fluorochromes. Images of ultrathin sections were collected with an x,y-pixel size of 50 nm x 50 nm. In the control panel of the system, personal settings were loaded to allocate functions to the control panel. Here, common settings were used such as gain offset, smart gain, zoom factor and adjustment of the z-position. In the live mode underexposed pixels were adjusted with the gain offset and overexposed pixels were adjusted with the smart gain function. This was carefully done for each scanned nucleus, because overexposed pixels in the acquired image would result in loss of information. On the other hand, underexposed pixels can be normalized afterwards without difficulty, as long as they are not similar to background signals. Filter setting of fluorochromes was performed in the filter histogram mode. They were 493 – 550 nm for 488 Argon laser and 565 – 602 for DPSS diode 561 nm laser.

Chromatic shift measurements

Chromatic shift measurements were kindly provided by Dr. Irina Solovei. Shift measurement was done for a voxel size of 50 x 50 x 100 or 120 nm. In most measurements, which were performed approx. every 2 – 3 months, z shift was < 160 nm between red and green channel. When the shift was larger than 180 nm, a shift correction was performed as described previously (Walter et al., 2006). In brief, settings were done according to measurements provided and were loaded into the ImageJ plug-in *StackGroom*. The plug-in automatically subtracts a suggested number of z slices (which is usually about 1 – 2 slices at the beginning or at the end of the stack) from the respective image stack to correct for chromatic shift.

4.8.2 Epifluorescence widefield microscopy

An inverse epifluorescence microscope (Zeiss AxioObserver Z1, Germany) using a Zeiss Plan-Neofluar 63x/1.3 glycerin objective, AxioVision 4.6 software and an AxioCamMr3 camera (Zeiss) was used for image acquisition. This microscope was located at the Maier-Leibnitz-Laboratoy in Garching. Mosaix images were acquired with an AxioObserver Z1 (Zeiss) using a Zeiss Plan-Neofluar 63x/1.3 glycerin objective, AxioVision 4.6 software and an AxioCamMr3 camera (Zeiss) located at the Department of Radiotherapy and Radiation Oncology in Großhadern (Munich). The axial distance between optical sections was 250 nm. Acquisition was performed sequentially for all channels. Filters used were 01 (BP 365/12) for DAPI, 38HE (BP 470/40 (HE) for GFP or A488, respectively, and filter 20 (BP 546/12) for Cy3, all obtained from Zeiss.

Chromatic shift measurements

For measurement of the chromatic shift, fluorescent labeled beads of 0.17 μm (TetraSpeck from Invitrogen) were dropped on an objective slide, dried and mounted according to manufacturers protocol. Beads were once mounted with Vectashield and once with Glycerin, 5% PBS, and for mounting a cover slip with a common thickness of 0.17 mm was used. Shift measurements were performed with help of Dr. Andreas Bolzer from Zeiss. For A488 and Cy3 z shift was < 250 nm. For DAPI and Cy3 the shift was < 500 nm and for DAPI and A488 < 250 nm. Hence, shift correction is necessary for analysis of signals in DAPI and signals in the red channel.

Bleed-through

The filters of the Zeiss AxioObserver Z1 in Garching were checked for bleed-through. Bleed-through of fluorochromes means that emission of one fluorochrome would overlap with the emission spectrum of the other fluorochrome and therefore signals might be detected in both channels. To test for bleed-through, two single stained samples (either A488 or Cy3) were generated and acquired in the respective channels. In this case, only a bleed-through of A488 into the Cy3 channel would be possible due to the emission of A488 which is close to the spectrum of Cy3. Respective images are shown in Figure 4.5. The upper row shows HeLa cells, which had been irradiated with alpha-particles and stained with γ-H2AX and DAPI. The respective secondary antibody to detect γ-H2AX was Cy3. Additionally, an image was acquired in the A488 channel to check if any signal resulting from the Cy3 fluorochrome was detected in the green channel (A488). The bottom row shows labeling of H3K4me3 primary antibody with A488-coupled secondary antibody, DAPI and additional image in the Cy3 (red) channel. In both cases, signal observed in the unlabeled channel was similar to background levels at high exposure times and showed slight auto-fluorescence of cell nuclei.
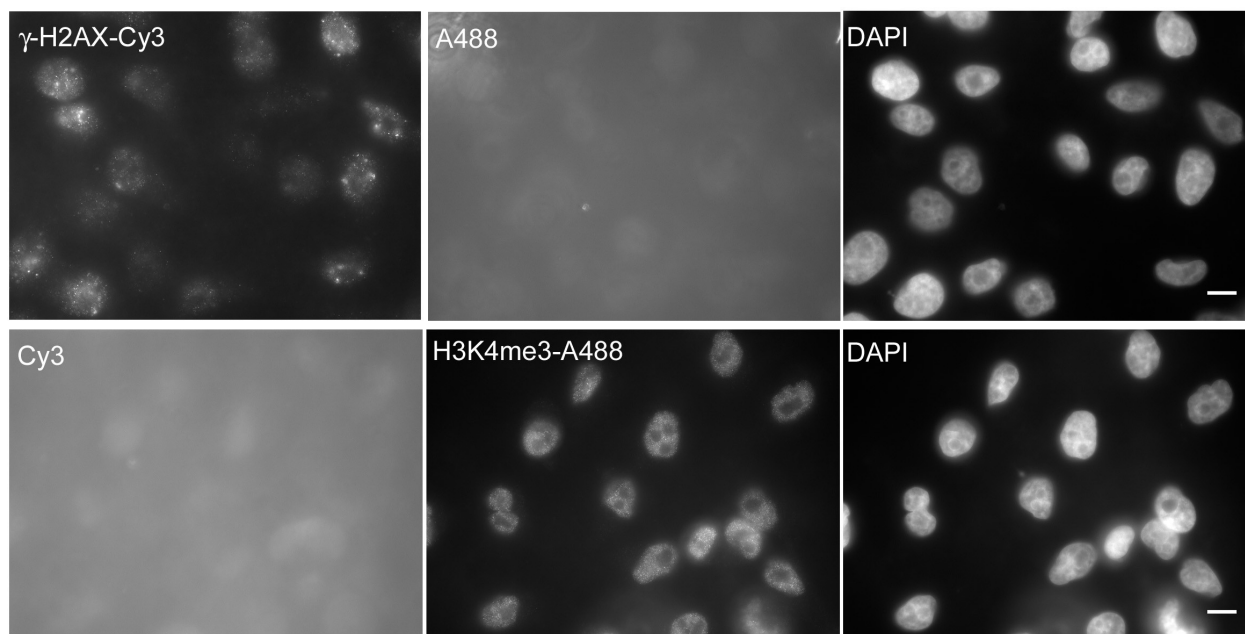
Figure 4.5: Immunofluorescence images showing single stained samples in the red (Cy3) and the green (A488) channel to check filters for bleed-through. Raw single slices of samples stained either with γ-H2AX-Cy3 (upper row), or H3K4me3 -A488 (bottom row) and DAPI (DNA) are shown. Signals of the unstained channel were similar to background and only slight auto-fluorescence of cell nuclei at high exposure times was observed.

4.9 Image processing

All z-stack images were deconvolved with Huygens deconvolution software (Scientific Volume Imaging) using the cmle (classical maximum likelihood estimation) algorithm with a maximum of 40 iterations and a 'quality criterion'' of 0.01 if not stated otherwise. For image processing the public domain software ImageJ 1.37c bundle downloaded from the website of the Wright Cell Imaging Facility (WCIF) (www.uhnresearch.ca/wcif) was used. In 3D confocal images Z-shift was measured and corrected as described in Walter et al. (2006). 2D images of ultrathin sections were not deconvolved. In images which were further used for correlation analysis, the segmented cell nucleus was cut out from the whole image and about three to seven mid-sections of the z-stack with clear staining were selected. Gray values in each channel were normalized to 8bit using the plug-in *Eightbit converter* written by C. Greubel. The *Eightbit Converter* takes the maximum gray value in an image, which is usually acquired as an 12 or 16bit image. Thus the maximum gray value in the image is set to 255 which is the maximum value of 8bit images. All other gray values are then normalized to this maximum. Normalization of images into 8bit means loss of information. However, it is useful for comparison of different images or different cells within an image, because signal intensities of two samples or of two areas in one sample, can significantly vary due to background, dirt, or density of cells.

Correction of background was necessary in most images because high background would distort localization analysis. For background subtraction, background was measured in the nucleoli or outside of the nucleus, where no true signal was expected for the detected protein, and the mean intensity of background signal plus $1 - 3$-fold standard deviation across the measured area was subtracted from the whole image (plug-in *ROI, background subtraction from ROI*). After background subtraction and before correlation analysis, gray values were again normalized to 8 bit. Intensity correlation analysis (ICA) was performed for pixel pairs of two channels for all selected optical sections. Usually these were three to seven mid-sections with defined staining (for details please see the following chapter 4.10). From each channel, a single representative slice was selected from mid-sections for illustration. Brightness and contrast were enhanced for the whole image where necessary. Images were assembled with Adobe Photoshop 7.0.1. Values for PDM- and intensity plots were obtained from intensity correlation analysis. Plots and diagrams were generated with Origin 7.5 or OriginPro 8.5 software.

4.10 Intensity Correlation Analysis
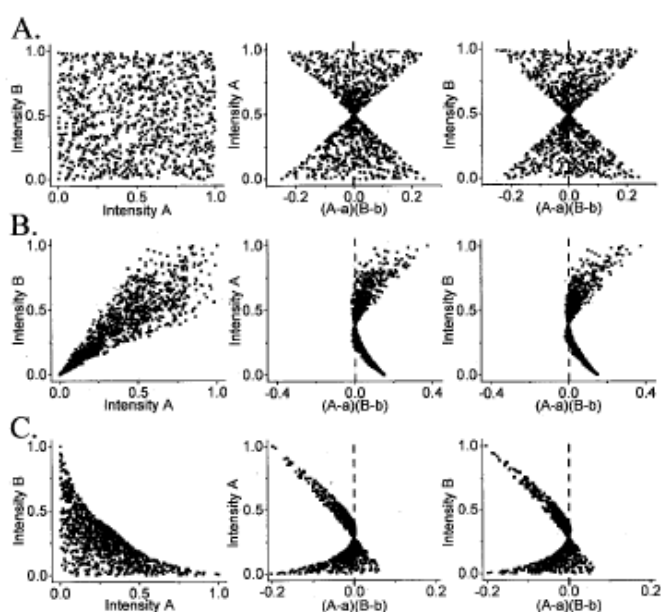
4.10.1 Background

Figure 4.6: Intensity correlation analysis for three simulated situations: A) random distribution, B) co-localization and C) anti-correlation. Intensity correlation analysis calculates the product of the differences from the mean (PDM = $(A_i$-a)*$(B_i$-b) for pixel pairs of two channels. Scatter plots in the left panel show the over all distribution of pixels and their respective intensity. PDM plots (mid and right panel) show the PDM value for each pixel and the corresponding intensity. The waistline of the hour glass shape represents the mean intensities (taken from Li et al., 2004).

(Li et al., 2004) described intensity correlation analysis (ICA) to determine correlation of pixel pairs between two channels in a quantitative and qualitative manner. ICA was performed with an automated graphic plug-in for the public imaging software ImageJ 1.37c (included with the WCIF bundle downloaded from the WCIF website). In the present work, ICA was used to determine correlation between pixel pairs of two channels, which correspond to irradiation-induced foci (IRIF) in one channel and the respective histone modification in the other channel. ICA calculates the *Product of the Differences from the Mean* (PDM) for pixel pairs of the two channels. The PDM is calculated from $(A_i - a)$*$(B_i - b)$, where A_i and B_i represent the respective pixel pair intensity in the two channels and *a* and *b* are the respective mean values of pixel intensity for both images. It is assumed that if two fluorochromes co-localize, the pixel pair intensities will vary in synchrony and the PDM value will be positive (Figure 4.6 B). On the other hand, if fluorochromes are randomly distributed the PDM value will be close to zero (Figure 4.6 A) and in the case of contra-localization (anti-correlation) the PDM value will be negative (Figure 4.6 C). By using the ICA plug-in, a PDM plot is generated for each channel and represents the distribution of pixel intensities and the respective PDM value (Figure 4.6 middle and right columns). Further a simple scatter plot is generated where pixel intensities of channel 1 and channel 2 are plotted against each other (Figure 4.6 left columns). Thus it can be

distinguished between high and low intensities and their correlation. Additionally, the ICA plug-in enables a color coded PDM mapping for the analyzed image, where the negative PDM values are represented in pink and positive values are green, whereas values close to zero are black. A color scale included with the PDM image indicates the values and their respective color (see Results section, chapter 2.1). For a quantitative measure of correlation of pixel pairs, the *Intensity Correlation Quotient – ICQ* and other correlation coefficients are calculated by the plug-in (Figure 4.6 in chapter 4.10.3). To compare images obtained at different point of times following irradiation, an additional Spearman´s rank correlation coefficient was calculated (4.11). Comparison of different coefficients and their advantages and disadvantages are further discussed in the Introduction (1.4.2) and in Results and Discussion chapters (2 and 3).

4.10.2 Performance

ICA was performed for three to seven mid-sections of a segmented cell nucleus. Beside a few changes described in the following, ICA was performed according to the instructions in (Khanna et al., 2006). Two channels (red and green) of the cell nucleus were opened with ImageJ 1.37c (WCIF bundle). Mid-sections of the image stack with clear staining were selected and upper and lower stacks were removed using the plug-in *Stack remover*. The cell nucleus was selected as ROI (r*egion of interest*) and any signal at the outside of the ROI was cleared. Images were converted to eight bit using the *Eightbit converter* (described in 4.9) and changes were applied to the image with the *Image adjust – adjust color balance* tool. Subsequently, using the *ROI – background subtraction from ROI* tool, background was measured in an area of the cell nucleus where no specific staining of the antibody was expected which is e.g. the nucleolus. Background was subtracted (mean background value plus 1 – 3-fold of standard deviation in the measured area) and gray values were normalized to eight bit. The *Intensity correlation analysis* tool was opened (*plug-ins – Colocalization analysis*) and images to be analyzed were selected in the window as channel 1 and channel 2. The settings for *Intensity correlation analysis* were as shown in Figure 4.6. The PDM image was saved as an 8bit image.

Figure 4.6: Settings for Intensity Correlation Analysis performed with ImageJ. The window shows the selection for channel 1 and channel 2 and the channel combination. *Use threshold* was selected, whereby pixels with a value of zero are excluded from the analysis and the analysis starts with pixels from value 1 except a different threshold has not been defined by the user. With further selections, a RGB merge of the two channels is generated, as well as PDM- and scatter plots. With cross hair size, the size of the plots can be adjusted. The PDM image is displayed and the PDM values are listed as a text file.

The ICA plug-in provides a *Lookup table* (LUT) for the color-code of PDM images by which PDM maps are shown in blue (anti-correlation) and yellow (co-localization). Because dark blue colors are difficult to observe on a black background, the LUT was changed to the color-
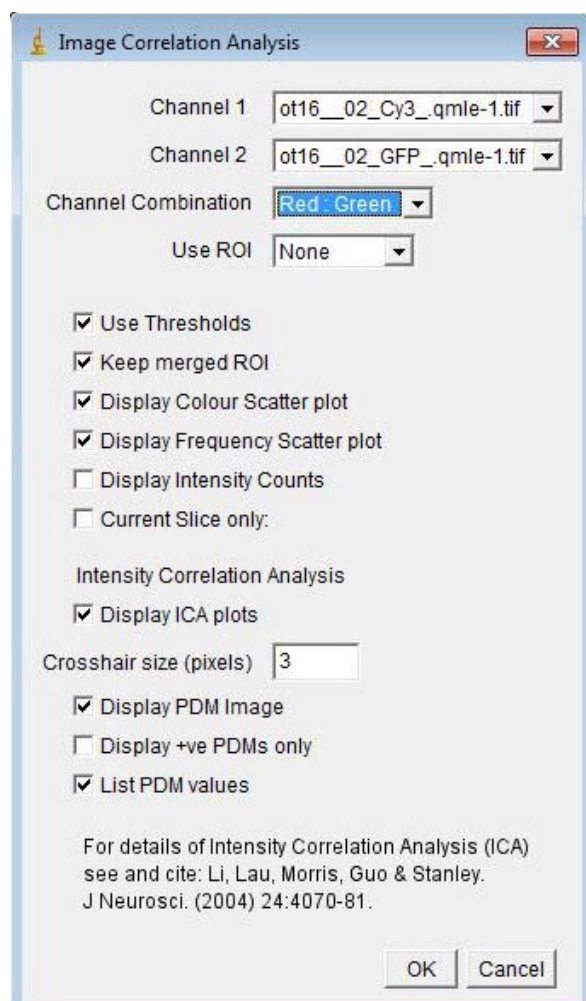
combination pink and green instead of blue and yellow. Values were not altered. The new LUT (ICA_red_green_LUT) was loaded to the image using the LUT panel (*plug-ins – LUT – LUT panel*). Images and plots were saved as TIFF. PDM and results tables were saved as text files. More details for individual applications are described on the WCIF website (http://www.uhnresearch.ca/facilities/wcif/imagej/colour_analysis.HMT#coloc_ica).

4.10.3 Correlation coefficients calculated with ICA

One possibility to quantify the number of positively or negatively correlated pixels is the Intensity Correlation Quotient (ICQ) proposed by (Li et al., 2004). Here, the ratio of the number of positive pixels to the total number of pixels was calculated and should reflect the degree of dependency (Li et al., 2004). From this value 0.5 was subtracted to generate the ICQ which results in a value for the ICQ in the range of +0.5 (perfect co-localization) to -0.5 (perfect contra-localization). Values close to zero should represent random distribution. Results table in Figure 4.6 shows the different coefficients which are additionally generated by the ICA plug-in. These are Pearson´s correlation coefficient Rr, Manders´ overlap coefficient R and Manders´ colocalization coefficients M1 and M2. Ch1:ch2 represents the red-green pixel ratio of channel 1 and channel 2. N+ve shows the number of pixels with positive PDM value, and Ntotal the total number of pixels. These two values are used to calculate the ICQ. For detailed description of the different coefficients see the Introduction 1.4.2.

Figure 4.6: Results window showing different correlation coefficients generated with the ICA plug-in for ImageJ. Top row shows the name of the two images. Below their weight and height in pixels is shown. In the table below the different coefficients are shown: (Rr) Pearson Correlation Coefficient, (R) Manders Overlap Coefficient, ch1:ch2 the pixel ratio of the two images, M1 and M2 the Manders Colocalization Coefficients, the number of positive pixels (N+ve) and the total number of pixels (Ntotal) by which the ICQ is calculated. Further, thresholds for channel 1 and channel 2 are shown which adopt values from 1 to 255 gray values (8bit) in this example.

4.11 Statistical evaluation of pixel correlation using Spearman´s rank correlation coefficient

Statistical analysis concerning Spearman´s coerrelation coefficient of pixel pairs and statistical tests were performed and written by Volker J. Schmid, Institute of Statistics, LMU Munich. Data

obtained by ICA, which are the PDM values and the corresponding intensities, were used to calculate Spearman´s rank correlation coefficient additionally to the obtained Pearson´s correlation coefficient, Manders´ overlap coefficient and the Intensity Correlation Quotient (ICQ) which was compared with Spearman´s correlation coefficient. Here, the intensities of each channel are ranked. Spearman´s coefficient is defined as $\rho = 1 - 6\ \Sigma d_i^2/(n(n^2-1))$, where d_i is the difference of the ranks of both channels in voxel i and n is the number of foreground pixel.

4.12 Protein extraction for Western immunoblotting

4.12.1 Whole cell protein extraction from cells grown in culture flasks

Cell culture flasks were placed on ice and washed twice with ice-cold PBS. 600 - 1000 µl of RIPA-buffer (150 mM NaCl, 1% NP-40, 10 mM MDOC, 0.1% SDS, 50 mM Tris-HCl pH 8.0) containing protease and phosphatase inhibitors (Roche´s miniComplete and PhosphoStop) were added to the cells and evenly distributed. After $3 - 5$ min incubation on ice, the cell layer was scratched off the bottom of the flask and lysed cell suspension was transferred to a 1,5 ml tube. Subsequently, samples were heated for 10 min at 104°C and then stored at -20°C.

4.12.2 Whole cell protein extraction from cell pellets

Cells were removed from the surface by trypsination as described in 4.1.1 and collected in 10 ml medium. Cells were counted as described previously (4.1.3) and centrifuged for 5 min, 500 x g at 4°C. Supernatant was removed and cells were washed for twice with ice cold PBS and transferred to a 1,5 ml tube. Cell pellet was either stored at -80°C or subsequent whole cell protein extraction was performed by adding RIPA buffer containing protease and phosphatase inhibitors (Roche´s miniComplete and PhosphoStop) to the cell pellet. The volume of RIPA buffer used was 20 µl for 1 x 10^4 cells. The pellet was mixed carefully, heated to 104°C for 10 min and extracts were stored at -20°C until usage.

4.13 Gel electrophoresis and Western immunoblotting

4.13.1 Protein separation

For Western Blot analysis, samples were partially thawed such that the core of the sample was still frozen. Samples were centrifuged for 1.5 min with 10000 x g. The DNA could be removed after this step, as it was not completely thawed and was pelleted. Samples were mixed with 4x Laemmli loading dye, heated to 95°C for 8 min and separated by gel electrophoresis. Proteins were separated on 12% Bis-Tris pre-cast gels from BioRad or for proteins larger than 100 kDa, either NuPage 3-8% Tris-Acetate gels from Invitrogen or 7,5% Tris-glycine gels from BioRad were used. Gels were run for 1.5 – 2 h at 100 Volt until proteins of interest in their respective size were passing the last third of the gel.

4.13.2 Electrotransfer

For blotting, the gel was removed from the box and placed on a nitrocellulose membrane, which was pre-equilibrated in transfer buffer (NuPAGE Invitrogen). The gel and the membrane were covered top down with three blotting papers pre-equilibrated in transfer buffer. Air bubbles were removed and gel and membrane were placed into the blotting chamber such, that proteins are transferred from the gel onto the membrane by electrotransfer from the positively charged cathode to the negatively charged anode. As proteins are covered with SDS which gives the proteins a negative charge, they move towards the positively charged cathode. After immunoblotting, membranes were stained with Ponceau Red 10% TCA for 5 min to detect and fix transferred proteins and protein standard on the membrane. To check for complete transfer, gels were stained in Coemassie brillant blue 50% methanol 10% acetic acid for 1 h and de-stained with 50% methanol 10% acetic acid for approx. 2 h. In the meantime, membrane was incubated in blocking solution for 1 h at RT. The blocking solution used was dependent on the suggestions of the antibody´s manufacturer. Either a commercially available block solution (Roti-Block, Pierce) was used or membranes were blocked with 5% milk TBS 0.1% tween. Primary antibody was diluted in 2 ml of the appropriate blocking solution in a 50 ml tube or in 5% BSA TBS-0.1% Tween as suggested by the manufacturer. The membrane was incubated with the primary antibody solution for either 1 - 2 h at RT or over night at 4°C on a rotating device. Following three washing steps of the membrane with washing buffer (PBS-Tween 0.3% or TBS-Tween 0.1% pH 7.5) for 5 min, the membrane was incubated in secondary antibody solution (0.35 µl mouse-HRP or 0.25 µl rabbit-HRP obtained from Santa Cruz, respectively, added to 20

ml of blocking solution) for 45 min at RT. Subsequently, the membrane was washed three times with washing buffer and once with PBS to remove Tween.

4.13.3 Detection and quantification of chemiluminescent signal

Immunodetection of the antibody was performed with Amersham™ ECL™ Advance developer (GE Healthcare). Solution A and B were mixed in a 1 : 1 ratio and the membrane was incubated in the solution for 5 min at RT. Chemiluminescence images were acquired with a CHEMISMART documentation system (peqlab, Vilber Lourmat) and the Chemi-Capt 5000 software. Images were acquired in full resolution mode and with 16 bit gray values. Quantitative analysis was realized with the Bio-1D software (Vilber Lourmat).

5 Material

5.1 Equipment

Device	Manufacturer
MCN-X-ray tube	Philips, USA
Alpha-particle ^{241}Americium source	Helmholtz Center Munich
Axiovert Z1	Zeiss, Germany
Camera AxioCam Mrm	Zeiss, Germany
Confocal laser scanning microscope SP5 (DMI 6000 CS)	Leica, Germany
Ultra View VoX spinning disk confocal unit	Perkin Elmer, USA
Axio Observer D1	Zeiss, Germany
Chemismart documentation system	PeqLab, Germany

5.2 Cells and media

Cell line	Origin	Media
HeLa	human cervix carcinoma	RPMI 1640 (PAA Laboratories GmbH), 10% FCS, 2 mM L-Glutamin, 1% Penicillin/Streptamycin
U2OS	Human osteosarcoma	RPMI 1640 (PAA Laboratories GmbH), 10% FCS, 2 mM L-Glutamin, 1% Penicillin/Streptamycin
BJ1 hTERT	hTERT immortalized human fibroblasts	DMEM (Sigma GmbH) and 199 medium (Sigma GmbH) 4:1, 10% FCS, 1% Penicillin/Streptamycin
HeLa H3-HA	Human cervix carcinoma	DMEM (Sigma GmbH), 10% FCS, 1% Penicillin/Streptamycin, 400μg G418 (kind gift of S.B. Hake, see Wiedemann et al. 2010 for details)
SAOS	human osteogenic sarcoma ("Sarcoma osteogenic")	McKoys with L-Glutamin (Sigma GmbH), 15% FCS, 1% Penicillin/Streptamycin

5.3 Solutions and reagents for cell culture

Product	Manufacturer
Dimethylsulfoxid (DMSO)	Merck
Fetal calf serum (FCS)	PAA Laboratories GmbH
L-Glutamin	Sigma

Product	Manufacturer
Phosphate buffered saline (PBS)	Dulbecco
Penicillin/Streptamycin	Sigma
Trypsin/EDTA	Biochrom AG
DharmaFECT Transfection Reagent (1 & 3)	Dharmacon Inc.
Lipofectamin 2000	Invitrogen
OptiMEM transfection medium	Invitrogen
SiRNA annealing buffer	Metabion
Non-silencing (negative) siRNA	Quiagen
MirVANA RNA isolation	Ambion
Reverse transcription Sensiscript	Stratagene
Reverse transcription SuperScript	Invitrogen

5.4 Consumables for cell culture and irradiation

Product	Manufacturer
Ibidi μ-Dish	Ibidi GmbH
MaTek chambers	Nunc
Six-wells	Nunc
Culture flasks	Schott
Steel rings	SBI*
Steel containers	SBI
Mylar foil	SBI

* former radiobiological institute, LMU

5.5 Reagents and buffers for immunofluorescence and western blotting

Reagent	Compounds	Application
Fixing solution	2% para-formaldehyde diluted in 100 ml PBS at 72°C	IF*
Permeabilization buffer	PBS 0.15% Triton-X-100	IF
Lukas buffer for extraction of unbound proteins	25 mM HEPES pH 7.5, 50 mM NaCl, 1 mM EDTA, 3 mM MgCl2, 300 mM Sucrose and 0.5% Triton-X-100	IF
Blocking solution	1% BSA, 0.15% Glycine in PBS	IF
DAPI stock solution	DAPI 1:10000 in PBS	IF

Reagent	Compounds	Application
Washing buffer I	PBS, 0.3% Tween 20	WB*
Wasching buffer II	TBS pH 8.0, 0.1% Tween 20	WB
Blocking solution I	Roti-®Block (Pierce) 1:10 in Aqua dest.	WB
Blocking solution II	5% milk in TBS-Tween 20 0.1%	WB
Blocking solution III	5% BSA in TBS-Tween 20 0.1%	WB
Ponceau-Red	5% Trichlor acetic acid, 0.2% Ponceau-S in Aqua dest.	WB
Re-Blot Plus Strong Stripping buffer (Pierce)	Stock diluted 1:10 in Aqua dest.	WB
ECL advanced developer (Amersham Bioscience)	Solution A and B mixed 1:1	WB
Coemassie brillant blue staining solution	10% acetic acid, 30% methanol, 0.1% Coemassie brillant blue	WB
Coemassie de-stain	10% acetic acid, 30% methanol	WB
RIPA buffer	150 mM NaCl, 1% NP-40, 10 mM Desoxcholinic acid, 0.1% SDS, 50 mM Tris pH 8.0 in aqua dest., supplemented with protease and phosphatase inhibitors (10x stock solutions Roche Applied Science)	WB
Running buffer I	20 x NuPAGE SDS Running buffer (Invitrogen) 1:20 in aqua dest.	WB
Running buffer II	10 x Tris/Glycine Running buffer (BioRad) 1:10 in aqua dest.	WB
Transfer buffer	20 x NuPAGE Transfer buffer (Invitrogen), 15% methanol in aqua dest.	WB

Table 5.1: Reagents and buffers for IF and WB. *IF: Immunofluorescence; *WB: Western Blot

5.6 Chemicals

Chemical	Manufacturer
Bovine serum albumin	Sigma Aldrich GmbH
Cell-TAK Tissue Adhesive	BD Bioscience
DAPI	Sigma Aldrich GmbH
DMSO	Merck
Ethanol p.a.	Merck
Ethanol 80%	Merck
Glycine	Sigma Aldrich GmbH
HCl 32%	Merck
LR white liquid resin	Merck

Chemical	Manufacturer
Methanol 100%	Merck
NaCl	Merck
Nonidet® P 40 Substitute	Fluka
Penicillin/Streptomycin	Sigma Aldrich GmbH
Para-formaldehyde	Sigma Aldrich GmbH
Ponceau S	Sigma Aldrich GmbH
Triton-X-100	Merck
Trypsin/EDTA	Biochrom AG
Tween 20	Merck
Vectashield w/o DAPI	Vector Laboratories

5.7 Antibodies and peptides

5.7.1 Primary antibodies

Antibody	Source; Cat.No.	Dilution	Application
Mouse α-H3 (unmod. Lys4)	Millipore; 05-1341	1:500	IF*
Rabbit α-H3 (whole)	CST*; 4499	1:200	WB*
Rabbit α-H3K4me1	Abcam; ab3825	1:500	IF
Rabbit α-H3K4me2	Abcam; ab7766	1:500	IF
Rabbit α-H3K4me3	Abcam; ab8580	1:500 1:1000	IF
Rabbit α-H3K4me3	CST; 9751	1:400 1:1000	IF WB
Mouse α-H3K4me3	Abcam; ab12209	1:500 1:1000	IF WB
Rabbit α-H3K9me2	Millipore; 04-768	1:200	IF
Rabbit α-H3K9me3	Abcam	1:500	IF
Rabbit α-H3K9me3	Millipore; 07-442	1:200	IF
Rabbit α-H3K9me1	Millipore; 07-450	1:500	IF
Rabbit α-γ-H2AX	Abcam; ab81299	1:200 1:10000	IF WB
Mouse α-γ-H2AX	Millipore; 05-636	1:350	IF
Rabbit α-53BP1	Novus; NB100-305	1:500	IF
Mouse α-CAF1 p150	Abcam; ab7655	1:500	IF
Rabbit α-HP1β	Abcam; ab10478	1:200	IF
Rat α-HP1β	Abcam; ab10811	1:50	IF

Antibody	Source; Cat.No.	Dilution	Application
Rabbit α-Jarid1A/RBP2	Bethyl; A300-897A-1	1:500 1:1000	IF WB
Rabbit α-Jarid1A/RBP2	CST; 3876	1:200 1:1000	IF WB
Rabbit α-Jarid1A/RBP2	Abcam; ab65769	1:500 1:1000	IF WB
Rabbit α-Jarid1A/RBP2L	Gift of E. Benevolenskaya	1:5000 1:500	WB IF
Rabbit α-H3K27me3	Millipore; 07-449	1:200	IF
Rabbit α-H3K56Ac	Millipore; 07-677	1:500	IF
Rabbit α-H3K9Ac	Millipore; 06-942	1:500	IF
Rabbit α-H4K5Ac	Millipore 06-759-MN	1:200	IF
Rabbit α-H4K20me3	Abcam; ab9053	1:200	IF
Rat α-Polymerase II Ser5 IgG2a	Gift of D. Eick	1:10	IF
Rat α-Polymerase II Ser2 IgG2a	Gift of D. Eick	1:10	IF
Rabbit α-Tubulin-α	Labvision; MS-581-P0	1:6000	WB
Rabbit α-SMC1	Abcam; ab21583	1:2000	WB
Rabbit α-p21	CST; 2947	1:1000	WB
Rabbit α-TIP60	Millipore; 07-038	1:200	IF
Mouse α-HA	CST; 2367	1:100	IF
Rabbit α-Ki67	Labvision; RM-9106-S0	1:500	IF
Rabbit α-CENP-F	Novus; NB500-101	1:500	IF
Rabbit α-EZH2	Sigma; E6906	1:500	IF
Mouse α-Nucleolin	Abcam; 13541	1:100	IF

Table 5.2: Primary antibodies. *IF: Immunofluorescence; *WB: Western Blot; *CST: Cell Signaling Technologies

5.7.2 Secondary antibodies

Antibody	Source; Cat.No.	Dilution	Application
Alexa Fluor 488 Goat α-rabbit IgG	Molecular Probes; A-11034	1:200	IF*
Alexa Fluor 488 Goat α-mouse IgG	Invitrogen; A11029	1:200	IF
Cyanin 3 Goat α-mouse F(ab)2	Jackson Immunoresearch; 115-165-072	1:500	IF
Cyanin 3 Goat α-rabbit IgG	Amersham; PA43004	1:500	IF
Peroxidase	Santa Cruz; sc2005	0.3 µl/	WB*

Antibody	Source; Cat.No.	Dilution	Application
Goat α-mouse		20ml	
Peroxidase Goat α-rabbit	Santa Cruz; sc2004	0.25 µl/ 20ml	WB
Cyanin 3 goat α-rat	Jackson Immunoresearch	1:200	IF

Table 5.3: Secondary antibodies. *IF: Immunofluorescence; *WB: Western Blot.

5.7.3 Peptides

Peptide	Source; CatNo.
H3K4me1	Abcam 1340
H3K4me2	Abcam 7768
H3K4me3	Abcam 1342
H3K9me1	Abcam 1771
H3K9me2	Abcam 1772
H3K9me3	Abcam 1773
H3K27me3	Abcam 1782
H3 unmodified	Abcam 2903
H4K20me1	Abcam 17043
H4K20me2	Abcam 14964
H4K20me3	Abcam 17567

Table 5.4: Peptides

6 References

Allahverdi, A., Yang, R., Korolev, N., Fan, Y., Davey, C.A., Liu, C.-F., and Nordenskiold, L. (2011). The effects of histone H4 tail acetylations on cation-induced chromatin folding and self-association. Nucleic Acids Res *39*, 1680-1691.

Allis, C.D., Jenuwein, T., and Reinberg, D. (2007). Epigenetics (Cold Spring Harbor, N.Y: Cold Spring Harbor Laboratory Press).

Alvarez, F., Muñoz, F., Schilcher, P., Imhof, A., Almouzni, G., and Loyola, A. (2011). Sequential establishment of marks on soluble histones H3 and H4. J. Biol. Chem *286*, 17714-17721.

Ayoub, N., Jeyasekharan, A.D., Bernal, J.A., and Venkitaraman, A.R. (2008). HP1-beta mobilization promotes chromatin changes that initiate the DNA damage response. Nature *453*, 682-686.

Ayoub, N., Jeyasekharan, A.D., Bernal, J.A., and Venkitaraman, A.R. (2009). Paving the way for H2AX phosphorylation: chromatin changes in the DNA damage response. Cell Cycle *8*, 1494-1500.

Bakkenist, C.J., and Kastan, M.B. (2003). DNA damage activates ATM through intermolecular autophosphorylation and dimer dissociation. Nature *421*, 499-506.

Baldeyron, C., Soria, G., Roche, D., Cook, A.J.L., and Almouzni, G. (2011). HP1 recruitment to DNA damage by p150CAF-1 promotes homologous recombination repair. The Journal of Cell Biology *193*, 81-95.

Bannister, A.J., Zegerman, P., Partridge, J.F., Miska, E.A., Thomas, J.O., Allshire, R.C., and Kouzarides, T. (2001). Selective recognition of methylated lysine 9 on histone H3 by the HP1 chromo domain. Nature *410*, 120-124.

Barcellos-Hoff, M.H., and Nguyen, D.H. (2009). Radiation carcinogenesis in context: how do irradiated tissues become tumors? Health Phys *97*, 446-457.

Barlow, A.L., MacLeod, A., Noppen, S., Sanderson, J., and Guérin, C.J. (2010). Colocalization Analysis in Fluorescence Micrographs: Verification of a More Accurate Calculation of Pearson's Correlation Coefficient. Microsc Microanal *16*, 710-724.

Barski, A., Cuddapah, S., Cui, K., Roh, T.-Y., Schones, D.E., Wang, Z., Wei, G., Chepelev, I., and Zhao, K. (2007). High-resolution profiling of histone methylations in the human genome. Cell *129*, 823-837.

Baylin, S.B., and Ohm, J.E. (2006). Epigenetic gene silencing in cancer - a mechanism for early oncogenic pathway addiction? Nat. Rev. Cancer *6*, 107-116.

Beisel, C., and Paro, R. (2011). Silencing chromatin: comparing modes and mechanisms. Nat. Rev. Genet *12*, 123-135.

Bekker-Jensen, S., Lukas, C., Melander, F., Bartek, J., and Lukas, J. (2005). Dynamic assembly and sustained retention of 53BP1 at the sites of DNA damage are controlled by Mdc1/NFBD1. J Cell Biol *170*, 201-211.

Benevolenskaya, E.V., Murray, H.L., Branton, P., Young, R.A., and Kaelin, W.G. (2005). Binding of pRB to the PHD protein RBP2 promotes cellular differentiation. Mol. Cell *18*, 623-635.

Berdasco, M., and Esteller, M. (2010). Aberrant epigenetic landscape in cancer: how cellular identity goes awry. Dev. Cell *19*, 698-711.

Berger, S., Kouzarides, T., Shiekhattar, R., and Shilatifard, A. (2009). An operational definition of epigenetics. Genes Dev *23*, 781-783.

Bernstein, B.E., Meissner, A., and Lander, E.S. (2007). The mammalian epigenome. Cell *128*, 669-681.

Beshiri, M.L., Islam, A., Dewaal, D.C., Richter, W.F., Love, J., Lopez-Bigas, N., and Benevolenskaya, E.V. (2010). Genome-wide analysis using ChIP to identify isoform-specific gene targets. J Vis Exp. *41*. http://www.jove.com/details.php?id=2101

Billur, M., Bartunik, H.D., and Singh, P.B. (2009). The essential function of HP1beta: a case of the tail wagging the dog? Trends Biochem. Sci. *2*, 115-123

Bolte, S., and Cordelières, F.P. (2006). A guided tour into subcellular colocalization analysis in light microscopy. J Microsc *224*, 213-232.

Botuyan, M.V., Lee, J., Ward, I.M., Kim, J.-E., Thompson, J.R., Chen, J., and Mer, G. (2006). Structural basis for the methylation state-specific recognition of histone H4-K20 by 53BP1 and Crb2 in DNA repair. Cell *127*, 1361-1373.

Campos, E.I., and Reinberg, D. (2009). Histones: annotating chromatin. Annu. Rev. Genet. *43*, 559-599.

Chagraoui, J., Hébert, J., Girard, S., and Sauvageau, G. (2011). An anticlastogenic function for the Polycomb Group gene Bmi1. Proc. Natl. Acad. Sci. U.S.A *108*, 5284-5289.

Chen, C.-C., Carson, J.J., Feser, J., Tamburini, B., Zabaronick, S., Linger, J., and Tyler, J.K. (2008). Acetylated lysine 56 on histone H3 drives chromatin assembly after repair and signals for the completion of repair. Cell *134*, 231-243.

Chou, D.M., Adamson, B., Dephoure, N.E., Tan, X., Nottke, A.C., Hurov, K.E., Gygi, S.P., Colaiácovo, M.P., and Elledge, S.J. (2010). A chromatin localization screen reveals poly (ADP ribose)-regulated recruitment of the repressive polycomb and NuRD complexes to sites of DNA damage. Proc. Natl. Acad. Sci. U.S.A. *107*, 18475-18480.

Christensen, J., Agger, K., Cloos, P.A.C., Pasini, D., Rose, S., Sennels, L., Rappsilber, J., Hansen, K.H., Salcini, A.E., and Helin, K. (2007). RBP2 belongs to a family of demethylases, specific for tri-and dimethylated lysine 4 on histone 3. Cell *128*, 1063-1076.

Cloos, P.A.C., Christensen, J., Agger, K., and Helin, K. (2008). Erasing the methyl mark: histone demethylases at the center of cellular differentiation and disease. Genes Dev. *22*, 1115-1140.

Conchello, J.-A., and Lichtman, J.W. (2005). Optical sectioning microscopy. Nat. Methods *2*, 920-931.

Corpet, A., and Almouzni, G. (2009). A histone code for the DNA damage response in mammalian cells? EMBO J *28*, 1828-1830.

Costelloe, T., and Lowndes, N. (2010). Chromatin assembly and signalling the end of DNA repair requires acetylation of histone H3 on lysine 56. Subcell Biochem *50*, 43-54.

Costes, S.V., Daelemans, D., Cho, E.H., Dobbin, Z., Pavlakis, G., and Lockett, S. (2004). Automatic and quantitative measurement of protein-protein colocalization in live cells. Biophys. J *86*, 3993-4003.

Costes, S.V., Ponomarev, A., Chen, J.L., Nguyen, D., Cucinotta, F.A., and Barcellos-Hoff, M.H. (2007). Image-based modeling reveals dynamic redistribution of DNA damage into nuclear sub-domains. PLoS Comput. Biol *3*, e155.

Cowell, I.G., Sunter, N.J., Singh, P.B., Austin, C.A., Durkacz, B.W., and Tilby, M.J. (2007). gammaH2AX foci form preferentially in euchromatin after ionising-radiation. PLoS ONE *2*, e1057.

Cremer, T., and Cremer, M. (2010). Chromosome territories. Cold Spring Harb Perspect Biol *2*, a003889.

Cremer, T., Cremer, M., Dietzel, S., Müller, S., Solovei, I., and Fakan, S. (2006). Chromosome territories--a functional nuclear landscape. Curr. Opin. Cell Biol *18*, 307-316.

Das, C., Lucia, M.S., Hansen, K.C., and Tyler, J.K. (2009). CBP/p300-mediated acetylation of histone H3 on lysine 56. Nature *459*, 113-117.

Dunleavy, E.M., Almouzni, G., and Karpen, G.H. (2011). H3.3 is deposited at centromeres in S phase as a placeholder for newly assembled CENP-A in G(1) phase. Nucleus *2*, 146-157.

Durante, M., and Friedl, A.A. (2011). New challenges in radiobiology research with microbeams. Radiation and environmental biophysics *3*, 335-338

Efron, B., and Tibshirani, R. (1993). An introduction to the bootstrap (New York: Chapman & Hall).

Elsaesser, S.J., and Allis, C.D. (2010). HIRA and Daxx constitute two independent histone H3.3-containing predeposition complexes. Cold Spring Harb Symp Quant Biol *75*, 27-34.

Falk, M., Lukasova, E., Gabrielova, B., Ondrej, V., and Kozubek, S. (2007). Chromatin dynamics during DSB repair. Biochim. Biophys. Acta *1773*, 1534-1545.

Faucher, D., and Wellinger, R.J. (2010). Methylated H3K4, a Transcription-Associated Histone Modification, Is Involved in the DNA Damage Response Pathway. PLoS Genet *6*, e1001082.

Feinberg, A.P., Ohlsson, R., and Henikoff, S. (2006). The epigenetic progenitor origin of human cancer. Nat. Rev. Genet *7*, 21-33.

Felsenfeld, G., and Groudine, M. (2003). Controlling the double helix. Nature *421*, 448-453.

Fernández-Suárez, M., and Ting, A.Y. (2008). Fluorescent probes for super-resolution imaging in living cells. Nat. Rev. Mol. Cell Biol *9*, 929-943.

Fischle, W., Tseng, B.S., Dormann, H.L., Ueberheide, B.M., Garcia, B.A., Shabanowitz, J., Hunt, D.F., Funabiki, H., and Allis, C.D. (2005). Regulation of HP1-chromatin binding by histone H3 methylation and phosphorylation. Nature *438*, 1116-1122.

Fischle, W., Wang, Y., Jacobs, S.A., Kim, Y., Allis, C.D., and Khorasanizadeh, S. (2003). Molecular basis for the discrimination of repressive methyl-lysine marks in histone H3 by Polycomb and HP1 chromodomains. Genes Dev *17*, 1870-1881.

FitzGerald, J., Moureau, S., Drogaris, P., O'Connell, E., Abshiru, N., Verreault, A., Thibault, P., Grenon, M., and Lowndes, N.F. (2011). Regulation of the DNA damage response and gene expression by the Dot1L histone methyltransferase and the 53Bp1 tumour suppressor. PLoS ONE *6*, e14714.

Fraga, M.F., Ballestar, E., Villar-Garea, A., Boix-Chornet, M., Espada, J., Schotta, G., Bonaldi, T., Haydon, C., Ropero, S., and Petrie, K., et al. (2005). Loss of acetylation at Lys16 and trimethylation at Lys20 of histone H4 is a common hallmark of human cancer. Nat. Genet *37*, 391-400.

French, A.P., Mills, S., Swarup, R., Bennett, M.J., and Pridmore, T.P. (2008). Colocalization of fluorescent markers in confocal microscope images of plant cells. Nat Protoc *3*, 619-628.

Frescas, D., Guardavaccaro, D., Bassermann, F., Koyama-Nasu, R., and Pagano, M. (2007). JHDM1B/FBXL10 is a nucleolar protein that represses transcription of ribosomal RNA genes. Nature *450*, 309-313.

Gardner, K.E., Allis, C.D., and Strahl, B.D. (2011). Operating on chromatin, a colorful language where context matters. J. Mol. Biol *409*, 36-46.

Gieni, R.S., Ismail, I.H., Campbell, S., and Hendzel, M.J. (2011). Polycomb group proteins in the DNA damage response: A link between radiation resistance and "stemness". Cell Cycle *10*, 883-894.

Ginjala, V., Nacerddine, K., Kulkarni, A., Oza, J., Hill, S.J., Yao, M., Citterio, E., van Lohuizen, M., and Ganesan, S. (2011). BMI1 is recruited to DNA breaks and contributes to DNA damage-induced H2A ubiquitination and repair. Mol. Cell. Biol *31*, 1972-1982.

Goldberg, A.D., Banaszynski, L.A., Noh, K.-M., Lewis, P.W., Elsaesser, S.J., Stadler, S., Dewell, S., Law, M., Guo, X., and Li, X., et al. (2010). Distinct factors control histone variant H3.3 localization at specific genomic regions. Cell *140*, 678-691.

Goodarzi, A.A., Noon, A.T., and Jeggo, P.A. (2009). The impact of heterochromatin on DSB repair. Biochem. Soc. Trans *37*, 569-576.

Goodarzi, A.A., Noon, A.T., Deckbar, D., Ziv, Y., Shiloh, Y., Löbrich, M., and Jeggo, P.A. (2008). ATM signaling facilitates repair of DNA double-strand breaks associated with heterochromatin. Mol. Cell *31*, 167-177.

Green, C.M., and Almouzni, G. (2002). When repair meets chromatin. First in series on chromatin dynamics. EMBO Rep *3*, 28-33.

Green, C.M., and Almouzni, G. (2003). Local action of the chromatin assembly factor CAF-1 at sites of nucleotide excision repair in vivo. EMBO J *22*, 5163-5174.

Greenberg, R.A. (2011). Histone tails: Directing the chromatin response to DNA damage. FEBS Letters.

Greubel, C., Hable, V., Drexler, G.A., Hauptner, A., Dietzel, S., Strickfaden, H., Baur, I., Krücken, R., Cremer, T., and Dollinger, G., et al. (2008a). Competition effect in DNA damage response. Radiation and environmental biophysics *47*, 423-429.

Greubel, C., Hable, V., Drexler, G.A., Hauptner, A., Dietzel, S., Strickfaden, H., Baur, I., Krücken, R., Cremer, T., and Friedl, A.A., et al. (2008b). Quantitative analysis of DNA-damage response factors after sequential ion microirradiation. Radiation and environmental biophysics *47*, 415-422.

Guccione, E., Bassi, C., Casadio, F., Martinato, F., Cesaroni, M., Schuchlautz, H., Lüscher, B., and Amati, B. (2007). Methylation of histone H3R2 by PRMT6 and H3K4 by an MLL complex are mutually exclusive. Nature *449*, 933-937.

Hable, V., Greubel, C., Bergmaier, A., and Reichart, P. (2009). The live cell irradiation and observation setup at SNAKE. Nuclear Instruments and Methods in Physics B, 2090-2097.

Hake, S.B., and Allis, C.D. (2006). Histone H3 variants and their potential role in indexing mammalian genomes: the "H3 barcode hypothesis". Proc. Natl. Acad. Sci. U.S.A *103*, 6428-6435.

Hake, S.B., Garcia, B.A., Duncan, E.M., Kauer, M., Dellaire, G., Shabanowitz, J., Bazett-Jones, D.P., Allis, C.D., and Hunt, D.F. (2006). Expression patterns and post-translational modifications associated with mammalian histone H3 variants. J. Biol. Chem *281*, 559-568.

Hauptner, A., Dietzel, S., Drexler, G.A., Reichart, P., Krücken, R., Cremer, T., Friedl, A.A., and Dollinger, G. (2004). Microirradiation of cells with energetic heavy ions. Radiation and environmental biophysics *42*, 237-245.

Hauptner, A., Krücken, R., Greubel, C., Hable, V., Dollinger, G., Drexler, G.A., Deutsch, M., Löwe, R., Friedl, A.A., and Dietzel, S., et al. (2006). DNA-repair protein distribution along the tracks of energetic ions. Radiation protection dosimetry *122*, 147-149.

Hayakawa, T., Ohtani, Y., Hayakawa, N., Shinmyozu, K., Saito, M., Ishikawa, F., and Nakayama, J.-i. (2007). RBP2 is an MRG15 complex component and down-regulates intragenic histone H3 lysine 4 methylation. Genes Cells *12*, 811-826.

Heintzman, N., Stuart, R., Hon, G., Fu, Y., Ching, C., Hawkins, R., Barrera, L., Van, C., Qu, C., and Ching, K., et al. (2007). Distinct and predictive chromatin signatures of transcriptional promoters and enhancers in the human genome. Nat Genet *39*, 311-318.

Hublitz, P., Albert, M., and Peters, A.H.F.M. (2009). Mechanisms of transcriptional repression by histone lysine methylation. Int. J. Dev. Biol *53*, 335-354.

Huen, M., Grant, R., Manke, I., Minn, K., Yu, X., Yaffe, M., and Chen, J. (2007). RNF8 transduces the DNA-damage signal via histone ubiquitylation and checkpoint protein assembly. Cell *131*, 901-914.

Huyen, Y., Zgheib, O., Ditullio, R.A., Gorgoulis, V.G., Zacharatos, P., Petty, T.J., Sheston, E.A., Mellert, H.S., Stavridi, E.S., and Halazonetis, T.D. (2004). Methylated lysine 79 of histone H3 targets 53BP1 to DNA double-strand breaks. Nature *432*, 406-411.

Iacovoni, J.S., Caron, P., Lassadi, I., Nicolas, E., Massip, L., Trouche, D., and Legube, G. (2010). High-resolution profiling of gammaH2AX around DNA double strand breaks in the mammalian genome. EMBO J. *29*, 1446-1457.

Islam, A.B.M.M.K., Richter, W.F., Lopez-Bigas, N., and Benevolenskaya, E.V. (2011). Selective targeting of histone methylation. Cell Cycle *10*, 413-424.

Iwase, S., Lan, F., Bayliss, P., La Torre-Ubieta, L. de, Huarte, M., Qi, H.H., Whetstine, J.R., Bonni, A., Roberts, T.M., and Shi, Y. (2007). The X-linked mental retardation gene SMCX/JARID1C defines a family of histone H3 lysine 4 demethylases. Cell *128*, 1077-1088.

Iwase, S., Xiang, B., Ghosh, S., Ren, T., Lewis, P.W., Cochrane, J.C., Allis, C.D., Picketts, D.J., Patel, D.J., and Li, H., et al. (2011). ATRX ADD domain links an atypical histone methylation recognition mechanism to human mental-retardation syndrome. Nat. Struct. Mol. Biol *18*, 769-776.

Jackson, S.P., and Bartek, J. (2009). The DNA-damage response in human biology and disease. Nature *461*, 1071-1078.

Jakob, B., Splinter, J., Conrad, S., Voss, K.-O., Zink, D., Durante, M., Lobrich, M., and Taucher-Scholz, G. (2011). DNA double-strand breaks in heterochromatin elicit fast repair protein recruitment, histone H2AX phosphorylation and relocation to euchromatin. Nucleic Acids Res *15*,6489-6499

Jenuwein, T., and Allis, C.D. (2001). Translating the histone code. Science *293*, 1074-1080.

Jones, P.A., and Baylin, S.B. (2007). The epigenomics of cancer. Cell *128*, 683-692.

Karagiannis, T.C., Harikrishnan, K.N., Kn, H., and El-Osta, A. (2007). Disparity of histone deacetylase inhibition on repair of radiation-induced DNA damage on euchromatin and constitutive heterochromatin compartments. Oncogene *26*, 3963-3971.

Kastan, M.B., and Bartek, J. (2004). Cell-cycle checkpoints and cancer. Nature *432*, 316-323.

Khanna, R., Li, Q., Sun, L., Collins, T.J., and Stanley, E.F. (2006). N type Ca2+ channels and RIM scaffold protein covary at the presynaptic transmitter release face but are components of independent protein complexes. Neuroscience *140*, 1201-1208.

Khobta, A., Anderhub, S., Kitsera, N., and Epe, B. (2010). Gene silencing induced by oxidative DNA base damage: association with local decrease of histone H4 acetylation in the promoter region. Nucleic Acids Res *38*, 4285-4295.

Kim, J., Guermah, M., McGinty, R.K., Lee, J.-S., Tang, Z., Milne, T.A., Shilatifard, A., Muir, T.W., and Roeder, R.G. (2009a). RAD6-Mediated transcription-coupled H2B ubiquitylation directly stimulates H3K4 methylation in human cells. Cell *137*, 459-471.

Kim, Y.-C., Gerlitz, G., Furusawa, T., Catez, F., Nussenzweig, A., Oh, K.-S., Kraemer, K.H., Shiloh, Y., and Bustin, M. (2009b). Activation of ATM depends on chromatin interactions occurring before induction of DNA damage. Nat. Cell Biol. *11*, 92-96.

Kinner, A., Wu, W., Staudt, C., and Iliakis, G. (2008). Gamma-H2AX in recognition and signaling of DNA double-strand breaks in the context of chromatin. Nucleic Acids Res *36*, 5678-5694.

Kirmizis, A., Bartley, S.M., Kuzmichev, A., Margueron, R., Reinberg, D., Green, R., and Farnham, P.J. (2004). Silencing of human polycomb target genes is associated with methylation of histone H3 Lys 27. Genes Dev *18*, 1592-1605.

Klose, R.J., Yan, Q., Tothova, Z., Yamane, K., Erdjument-Bromage, H., Tempst, P., Gilliland, D.G., Zhang, Y., and Kaelin, W.G. (2007). The Retinoblastoma Binding Protein RBP2 Is an H3K4 Demethylase. Cell *128*, 889-900.

Koturbash, I., Baker, M., Loree, J., Kutanzi, K., Hudson, D., Pogribny, I., Sedelnikova, O., Bonner, W., and Kovalchuk, O. (2006). Epigenetic dysregulation underlies radiation-induced transgenerational genome instability in vivo. Int. J. Radiat. Oncol. Biol. Phys *66*, 327-330.

Koturbash, I., Pogribny, I., and Kovalchuk, O. (2005). Stable loss of global DNA methylation in the radiation-target tissue--a possible mechanism contributing to radiation carcinogenesis? Biochem. Biophys. Res. Commun *337*, 526-533.

Kouzarides, T. (2007). Chromatin Modifications and Their Function. Cell *128*, 693-705.

Kovalchuk, O., and Baulch, J.E. (2008). Epigenetic changes and nontargeted radiation effects--is there a link? Environ. Mol. Mutagen. *49*, 16-25.

Krishnakumar, R., and Kraus, W.L. (2010). PARP-1 regulates chromatin structure and transcription through a KDM5B-dependent pathway. Mol. Cell *39*, 736-749.

Kruhlak, M.J., Celeste, A., and Nussenzweig, A. (2009). Monitoring DNA breaks in optically highlighted chromatin in living cells by laser scanning confocal microscopy. Methods Mol. Biol *523*, 125-140.

Kruhlak, M.J., Celeste, A., Dellaire, G., Fernandez-Capetillo, O., Müller, W.G., McNally, J.G., Bazett-Jones, D.P., and Nussenzweig, A. (2006). Changes in chromatin structure and mobility in living cells at sites of DNA double-strand breaks. J. Cell Biol. *172*, 823-834.

Kwon, S.H., and Workman, J.L. (2008). The heterochromatin protein 1 (HP1) family: put away a bias toward HP1. Mol Cells *26*, 217-227.

Lachner, M., O'Carroll, D., Rea, S., Mechtler, K., and Jenuwein, T. (2001). Methylation of histone H3 lysine 9 creates a binding site for HP1 proteins. Nature *410*, 116-120.

Larsen, D.H., Poinsignon, C., Gudjonsson, T., Dinant, C., Payne, M.R., Hari, F.J., Danielsen, J.M.R., Menard, P., Sand, J.C., and Stucki, M., et al. (2010). The chromatin-remodeling factor CHD4 coordinates signaling and repair after DNA damage. J. Cell Biol *190*, 731-740.

Li, Q., Lau, A., Morris, T.J., Guo, L., Fordyce, C.B., and Stanley, E.F. (2004). A syntaxin 1, Galpha(o), and N-type calcium channel complex at a presynaptic nerve terminal: analysis by quantitative immunocolocalization. J. Neurosci. *24*, 4070-4081.

Lieber, M.R. (2008). The mechanism of human nonhomologous DNA end joining. J. Biol. Chem *283*, 1-5.

Lin, W., Cao, J., Liu, J., Beshiri, M.L., Fujiwara, Y., Francis, J., Cherniack, A.D., Geisen, C., Blair, L.P., and Zou, M.R., et al. (2011). Inaugural Article: Loss of the retinoblastoma binding protein 2 (RBP2) histone demethylase suppresses tumorigenesis in mice lacking Rb1 or Men1. Proc. Natl. Acad. Sci. *108*, 13379-13386.

Linger, J., and Tyler, J.K. (2005). The yeast histone chaperone chromatin assembly factor 1 protects against double-strand DNA-damaging agents. Genetics *171*, 1513-1522.

Lomberk, G., Bensi, D., Fernandez-Zapico, M.E., and Urrutia, R. (2006). Evidence for the existence of an HP1-mediated subcode within the histone code. Nat. Cell Biol *8*, 407-415.

Lopez-Bigas, N., Kisiel, T.A., Dewaal, D.C., Holmes, K.B., Volkert, T.L., Gupta, S., Love, J., Murray, H.L., Young, R.A., and Benevolenskaya, E.V. (2008). Genome-wide analysis of the H3K4 histone demethylase RBP2 reveals a transcriptional program controlling differentiation. Mol. Cell *31*, 520-530.

Lopez-Serra, P., and Esteller, M. (2011). DNA methylation-associated silencing of tumor-suppressor microRNAs in cancer. Oncogene, 1-14

Loree, J., Koturbash, I., Kutanzi, K., Baker, M., Pogribny, I., and Kovalchuk, O. (2006). Radiation-induced molecular changes in rat mammary tissue: possible implications for radiation-induced carcinogenesis. Int. J. Radiat. Biol. *82*, 805-815.

Loyola, A., Bonaldi, T., Roche, D., Imhof, A., and Almouzni, G. (2006). PTMs on H3 variants before chromatin assembly potentiate their final epigenetic state. Mol. Cell *24*, 309-316.

Luebben, W.R., Sharma, N., and Nyborg, J.K. (2010). Nucleosome eviction and activated transcription require p300 acetylation of histone H3 lysine 14. Proc. Natl. Acad. Sci. *107*, 19254-19259.

Luger, K., Mäder, A.W., Richmond, R.K., Sargent, D.F., and Richmond, T.J. (1997). Crystal structure of the nucleosome core particle at 2.8 A resolution. Nature *389*, 251-260.

Luijsterburg, M.S., Dinant, C., Lans, H., Stap, J., Wiernasz, E., Lagerwerf, S., Warmerdam, D.O., Lindh, M., Brink, M.C., and Dobrucki, J.W., et al. (2009). Heterochromatin protein 1 is recruited to various types of DNA damage. J. Cell Biol. *185*, 577-586.

Lukas, C., Falck, J., Bartkova, J., Bartek, J., and Lukas, J. (2003). Distinct spatiotemporal dynamics of mammalian checkpoint regulators induced by DNA damage. Nat Cell Biol *5*, 255-260.

Maeshima, K., Hihara, S., and Eltsov, M. (2010). Chromatin structure: does the 30-nm fibre exist in vivo? Current Opinion in Cell Biology *22*, 291-297.

Mailand, N., Bekker-Jensen, S., Faustrup, H., Melander, F., Bartek, J., Lukas, C., and Lukas, J. (2007). RNF8 ubiquitylates histones at DNA double-strand breaks and promotes assembly of repair proteins. Cell *131*, 887-900.

Manders, E., Verbeek, F., and Aten, J. (1993). Measurements of co-localization of objects in dual-color confocal images. Journal of Microscopy, 375-382.

Manders, E.M., Stap, J., Brakenhoff, G.J., van Driel, R., and Aten, J.A. (1992). Dynamics of three-dimensional replication patterns during the S-phase, analysed by double labelling of DNA and confocal microscopy. J. Cell. Sci *103 (Pt 3)*, 857-862.

Mansfield, R.E., Musselman, C.A., Kwan, A.H., Oliver, S.S., Garske, A.L., Davrazou, F., Denu, J.M., Kutateladze, T.G., and Mackay, J.P. (2011). Plant Homeodomain (PHD) Fingers of CHD4 Are Histone H3-binding Modules with Preference for Unmodified H3K4 and Methylated H3K9. J. Biol Chem *286*, 11779-11791.

Margueron, R., Li, G., Sarma, K., Blais, A., Zavadil, J., Woodcock, C.L., Dynlacht, B.D., and Reinberg, D. (2008). Ezh1 and Ezh2 Maintain Repressive Chromatin through Different Mechanisms. Mol. Cell *32*, 503-518.

Markaki, Y., Gunkel, M., Schermelleh, L., Beichmanis, S., Neumann, J., Heidemann, M., Leonhardt, H., Eick, D., Cremer, C., and Cremer, T. (2010). Functional nuclear organization of transcription and DNA replication: a topographical marriage between chromatin domains and the interchromatin compartment. Cold Spring Harb. Symp. Quant. Biol *75*, 475-492.

Matthews, A.G.W., Kuo, A.J., Ramón-Maiques, S., Han, S., Champagne, K.S., Ivanov, D., Gallardo, M., Carney, D., Cheung, P., and Ciccone, D.N., et al. (2007). RAG2 PHD finger couples histone H3 lysine 4 trimethylation with V(D)J recombination. Nature *450*, 1106-1110.

Miller, K.M., Tjeertes, J.V., Coates, J., Legube, G., Polo, S.E., Britton, S., and Jackson, S.P. (2010). Human HDAC1 and HDAC2 function in the DNA-damage response to promote DNA nonhomologous end-joining. Nat Struct Mol Biol *17*, 1144-1151.

Misteli, T. (2007). Beyond the sequence: cellular organization of genome function. Cell *128*, 787-800.

Misteli, T., and Soutoglou, E. (2009). The emerging role of nuclear architecture in DNA repair and genome maintenance. Nat. Rev. Mol. Cell Biol *10*, 243-254.

Mothersill, C., and Seymour, C. (2003). Radiation-induced bystander effects, carcinogenesis and models. Oncogene *22*, 7028-7033.

Müller, K.P., Erdel, F., Caudron-Herger, M., Marth, C., Fodor, B.D., Richter, M., Scaranaro, M., Beaudouin, J., Wachsmuth, M., and Rippe, K. (2009). Multiscale analysis of dynamics and interactions of heterochromatin protein 1 by fluorescence fluctuation microscopy. Biophys. J *97*, 2876-2885.

Murr, R., Loizou, J.I., Yang, Y.-G., Cuenin, C., Li, H., Wang, Z.-Q., and Herceg, Z. (2006). Histone acetylation by Trrap-Tip60 modulates loading of repair proteins and repair of DNA double-strand breaks. Nat. Cell Biol. *8*, 91-99.

Nagy, Z., and Soutoglou, E. (2009). DNA repair: easy to visualize, difficult to elucidate. Trends Cell Biol *19*, 617-629.

Nakagawa, T., Kajitani, T., Togo, S., Masuko, N., Ohdan, H., Hishikawa, Y., Koji, T., Matsuyama, T., Ikura, T., and Muramatsu, M., et al. (2008). Deubiquitylation of histone H2A

activates transcriptional initiation via trans-histone cross-talk with H3K4 di- and trimethylation. Genes Dev *22*, 37-49.

Nakamura, K., Kato, A., Kobayashi, J., Yanagihara, H., Sakamoto, S., Oliveira, D.V.N.P., Shimada, M., Tauchi, H., Suzuki, H., and Tashiro, S., et al. (2011). Regulation of homologous recombination by RNF20-dependent H2B ubiquitination. Mol. Cell *41*, 515-528.

Niedermair, T. (2010). DNA Reparatur in Heterochromatin und anderen Chromatinbereichen. Diploma thesis (Fakültät für Biologie: LMU).

Nielsen, P.R., Nietlispach, D., Mott, H.R., Callaghan, J., Bannister, A., Kouzarides, T., Murzin, A.G., Murzina, N.V., and Laue, E.D. (2002). Structure of the HP1 chromodomain bound to histone H3 methylated at lysine 9. Nature *416*, 103-107.

Noon, A.T., Shibata, A., Rief, N., Löbrich, M., Stewart, G.S., Jeggo, P.A., and Goodarzi, A.A. (2010). 53BP1-dependent robust localized KAP-1 phosphorylation is essential for heterochromatic DNA double-strand break repair. Nat. Cell Biol *12*, 177-184.

O'Hagan, H.M., Mohammad, H.P., and Baylin, S.B. (2008). Double strand breaks can initiate gene silencing and SIRT1-dependent onset of DNA methylation in an exogenous promoter CpG island. PLoS Genet. *4*, e1000155.

Ottmann, C. (2007). Etablierung und Anwendungen von Methoden zur Analyse von Veränderungen der Histon-Modifikationen an strahlengeschädigtem Chromatin. Diploma thesis (Fakültät für Biologie: LMU).

Pasini, D., Hansen, K.H., Christensen, J., Agger, K., Cloos, P.A.C., and Helin, K. (2008). Coordinated regulation of transcriptional repression by the RBP2 H3K4 demethylase and Polycomb-Repressive Complex 2. Genes Dev. *22*, 1345-1355.

Pinato, S., Scandiuzzi, C., Arnaudo, N., Citterio, E., Gaudino, G., and Penengo, L. (2009). RNF168, a new RING finger, MIU-containing protein that modifies chromatin by ubiquitination of histones H2A and H2AX. BMC Mol. Biol *10*, 55.

Pogribny, I., Koturbash, I., Tryndyak, V., Hudson, D., Stevenson, S.M.L., Sedelnikova, O., Bonner, W., and Kovalchuk, O. (2005). Fractionated low-dose radiation exposure leads to accumulation of DNA damage and profound alterations in DNA and histone methylation in the murine thymus. Mol. Cancer Res *3*, 553-561.

Polo, S.E., Roche, D., and Almouzni, G. (2006). New histone incorporation marks sites of UV repair in human cells. Cell *127*, 481-493.

Pouget, J.-P., and Mather, S.J. (2001). General aspects of the cellular response to low- and high-LET radiation. European Journal of Nuclear Medicine and Molecular Imaging *28*, 541-561.

Probst, A.V., and Almouzni, G. (2011). Heterochromatin establishment in the context of genome-wide epigenetic reprogramming. Trends Genet *27*, 177-185.

Probst, A.V., Dunleavy, E., and Almouzni, G. (2009). Epigenetic inheritance during the cell cycle. Nat. Rev. Mol. Cell Biol *10*, 192-206.

R Development Core Team (2010). R: A Language and Environment for Statistical Computing. http://www.r-project.org/. 31.08.2011.

Ramanathan, B., and Smerdon, M.J. (1986). Changes in nuclear protein acetylation in u.v.-damaged human cells. Carcinogenesis *7*, 1087-1094.

Riley, T., Sontag, E., Chen, P., and Levine, A. (2008). Transcriptional control of human p53-regulated genes. Nat. Rev. Mol. Cell Biol *9*, 402-412.

Robertson, K.D. (2005). DNA methylation and human disease. Nat. Rev. Genet *6*, 597-610.

Rodgers, J.L., and Nicewander, W.A. (1988). Thirteen Ways to Look at the Correlation Coefficient. The American Statistician, 59-66.

Rodríguez-Paredes, M., and Esteller, M. (2011). Cancer epigenetics reaches mainstream oncology. Nat Med, 330-339.

Rogakou, E.P., Pilch, D.R., Orr, A.H., Ivanova, V.S., and Bonner, W.M. (1998). DNA double-stranded breaks induce histone H2AX phosphorylation on serine 139. J. Biol. Chem *273*, 5858-5868.

Ronneberger, O., Baddeley, D., Scheipl, F., Verveer, P.J., Burkhardt, H., Cremer, C., Fahrmeir, L., Cremer, T., and Joffe, B. (2008). Spatial quantitative analysis of fluorescently labeled nuclear structures: problems, methods, pitfalls. Chromosome Res. *16*, 523-562.

Roth, S.Y., Denu, J.M., and Allis, C.D. (2001). Histone acetyltransferases. Annu. Rev. Biochem *70*, 81-120.

Rouquette, J., Cremer, C., Cremer, T., and Fakan, S. (2010). Functional nuclear architecture studied by microscopy: present and future. Int Rev Cell Mol Biol *282*, 1-90.

Rouquette, J., Genoud, C., Vazquez-Nin, G.H., Kraus, B., Cremer, T., and Fakan, S. (2009). Revealing the high-resolution three-dimensional network of chromatin and interchromatin space: A novel electron-microscopic approach to reconstructing nuclear architecture. Chromosome Res. *6*, 801-810

Rubbi, C., and Milner, J. (2003). p53 is a chromatin accessibility factor for nucleotide excision repair of DNA damage. EMBO J *22*, 975-986.

Rübe, C.E., Lorat, Y., Schuler, N., Schanz, S., Wennemuth, G., and Rübe, C. (2011). DNA repair in the context of chromatin: new molecular insights by the nanoscale detection of DNA repair complexes using transmission electron microscopy. DNA Repair (Amst.) *10*, 427-437.

Ruijter, A.J.M. de, van Gennip, A.H., Caron, H.N., Kemp, S., and van Kuilenburg, A.B.P. (2003). Histone deacetylases (HDACs): characterization of the classical HDAC family. Biochem. J *370*, 737-749.

San Filippo, J., Sung, P., and Klein, H. (2008). Mechanism of eukaryotic homologous recombination. Annu. Rev. Biochem *77*, 229-257.

Sánchez-Molina, S., Mortusewicz, O., Bieber, B., Auer, S., Eckey, M., Leonhardt, H., Friedl, A.A., and Becker, P.B. (2011). Role for hACF1 in the G2/M damage checkpoint. Nucleic acids res, Epub ahead of print.

Sarma, K., Margueron, R., Ivanov, A., Pirrotta, V., and Reinberg, D. (2008). Ezh2 Requires PHF1 To Efficiently Catalyze H3 Lysine 27 Trimethylation In Vivo. Molecular and Cellular Biology *28*, 2718-2731.

Schermelleh, L., Heintzmann, R., and Leonhardt, H. (2010). A guide to super-resolution fluorescence microscopy. J. Cell Biol *190*, 165-175.

Schmiedeberg, L., Weisshart, K., Diekmann, S., Meyer Hoerste, G. zu, and Hemmerich, P. (2004). High- and low-mobility populations of HP1 in heterochromatin of mammalian cells. Mol. Biol. Cell *15*, 2819-2833.

Schmitges, F.W., Prusty, A.B., Faty, M., Stützer, A., Lingaraju, G.M., Aiwazian, J., Sack, R., Hess, D., Li, L., and Zhou, S., et al. (2011). Histone methylation by PRC2 is inhibited by active chromatin marks. Mol. Cell *42*, 330-341.

Schotta, G., Lachner, M., Sarma, K., Ebert, A., Sengupta, R., Reuter, G., Reinberg, D., and Jenuwein, T. (2004). A silencing pathway to induce H3-K9 and H4-K20 trimethylation at constitutive heterochromatin. Genes Dev *18*, 1251-1262.

Shanbhag, N.M., Rafalska-Metcalf, I.U., Balane-Bolivar, C., Janicki, S.M., and Greenberg, R.A. (2010). ATM-dependent chromatin changes silence transcription in cis to DNA double-strand breaks. Cell *141*, 970-981.

Sharma, S., Kelly, T.K., and Jones, P.A. (2010a). Epigenetics in cancer. Carcinogenesis *31*, 27-36.

Sharma, S.V., Lee, D.Y., Li, B., Quinlan, M.P., Takahashi, F., Maheswaran, S., McDermott, U., Azizian, N., Zou, L., and Fischbach, M.A., et al. (2010b). A Chromatin-Mediated Reversible Drug-Tolerant State in Cancer Cell Subpopulations. Cell *141*, 69-80.

Shi, Y., Lan, F., Matson, C., Mulligan, P., Whetstine, J.R., Cole, P.A., Casero, R.A., and Shi, Y. (2004). Histone demethylation mediated by the nuclear amine oxidase homolog LSD1. Cell *119*, 941-953.

Shilatifard, A. (2008). Molecular implementation and physiological roles for histone H3 lysine 4 (H3K4) methylation. Curr. Opin. Cell Biol. *20*, 341-348.

Shimada, M., Niida, H., Zineldeen, D.H., Tagami, H., Tanaka, M., Saito, H., and Nakanishi, M. (2008). Chk1 is a histone H3 threonine 11 kinase that regulates DNA damage-induced transcriptional repression. Cell *132*, 221-232.

Shogren-Knaak, M., Ishii, H., Sun, J.-M., Pazin, M.J., Davie, J.R., and Peterson, C.L. (2006). Histone H4-K16 acetylation controls chromatin structure and protein interactions. Science *311*, 844-847.

Smeenk, G., Wiegant, W.W., Vrolijk, H., Solari, A.P., Pastink, A., and van Attikum, H. (2010). The NuRD chromatin-remodeling complex regulates signaling and repair of DNA damage. J. Cell Biol *190*, 741-749.

Solimando, L., Luijsterburg, M.S., Vecchio, L., Vermeulen, W., van Driel, R., and Fakan, S. (2009). Spatial organization of nucleotide excision repair proteins after UV-induced DNA damage in the human cell nucleus. J. Cell. Sci. *122*, 83-91.

Solovjeva, L.V., Svetlova, M.P., Chagin, V.O., and Tomilin, N.V. (2007). Inhibition of transcription at radiation-induced nuclear foci of phosphorylated histone H2AX in mammalian cells. Chromosome Res. *15*, 787-797.

Splinter, J., Jakob, B., Lang, M., Yano, K., Engelhardt, J., Hell, S.W., Chen, D.J., Durante, M., and Taucher-Scholz, G. (2010). Biological dose estimation of UVA laser microirradiation utilizing charged particle-induced protein foci. Mutagenesis *25*, 289-297.

Stante, M., Minopoli, G., Passaro, F., Raia, M., Vecchio, L.D., and Russo, T. (2009). Fe65 is required for Tip60-directed histone H4 acetylation at DNA strand breaks. Proc. Natl. Acad. Sci. U.S.A. *106*, 5093-5098.

Stewart, G.S., Wang, B., Bignell, C.R., Taylor, A.M.R., and Elledge, S.J. (2003). MDC1 is a mediator of the mammalian DNA damage checkpoint. Nature *421*, 961-966.

Strahl, B.D., and Allis, C.D. (2000). The language of covalent histone modifications. Nature *403*, 41-45.

Stratmann, A., and Haendler, B. (2011). The histone demethylase JARID1A regulates progesterone receptor expression. FEBS Journal *278*, 1458-1469.

Streffer, C. (2010). Strong association between cancer and genomic instability. Radiat Environ Biophys *49*, 125-131.

Stucki, M., Clapperton, J.A., Mohammad, D., Yaffe, M.B., Smerdon, S.J., and Jackson, S.P. (2005). MDC1 directly binds phosphorylated histone H2AX to regulate cellular responses to DNA double-strand breaks. Cell *123*, 1213-1226.

Sun, Y., Jiang, X., and Price, B.D. (2010). Tip60: Connecting chromatin to DNA damage signaling. Cell cycle (Georgetown, Tex.) *9*.

Sun, Y., Jiang, X., Chen, S., Fernandes, N., and Price, B.D. (2005). A role for the Tip60 histone acetyltransferase in the acetylation and activation of ATM. Proc. Natl. Acad. Sci. U.S.A. *102*, 13182-13187.

Sun, Y., Jiang, X., Xu, Y., Ayrapetov, M.K., Moreau, L.A., Whetstine, J.R., and Price, B.D. (2009). Histone H3 methylation links DNA damage detection to activation of the tumour suppressor Tip60. Nat. Cell Biol.

Suzuki, K., Yamauchi, M., Oka, Y., Suzuki, M., and Yamashita, S. (2011). Creating localized DNA double-strand breaks with microirradiation. Nat Protoc *6*, 134-139.

Tatum, D., and Li, S. (2011). Evidence that the histone methyltransferase Dot1 mediates global genomic repair by methylating histone H3 on lysine 79. J Biol Chem *286*, 17530-17535.

Taverna, S.D., Li, H., Ruthenburg, A.J., Allis, C.D., and Patel, D.J. (2007). How chromatin-binding modules interpret histone modifications: lessons from professional pocket pickers. Nat Struct Mol Biol *14*, 1025-1040.

Thiru, A., Nietlispach, D., Mott, H.R., Okuwaki, M., Lyon, D., Nielsen, P.R., Hirshberg, M., Verreault, A., Murzina, N.V., and Laue, E.D. (2004). Structural basis of HP1/PXVXL motif peptide interactions and HP1 localisation to heterochromatin. EMBO J *23*, 489-499.

Timinszky, G., Till, S., Hassa, P., Hothorn, M., Kustatscher, G., Nijmeijer, B., Colombelli, J., Altmeyer, M., Stelzer, E., and Scheffzek, K., et al. (2009). A macrodomain-containing histone rearranges chromatin upon sensing PARP1 activation. Nat Struct Mol Biol *16*, 923-929.

Tjeertes, J.V., Miller, K.M., and Jackson, S.P. (2009). Screen for DNA-damage-responsive histone modifications identifies H3K9Ac and H3K56Ac in human cells. EMBO J. *13*, 1878-1889

Tse, C., Sera, T., Wolffe, A.P., and Hansen, J.C. (1998). Disruption of higher-order folding by core histone acetylation dramatically enhances transcription of nucleosomal arrays by RNA polymerase III. Mol. Cell. Biol *18*, 4629-4638.

van Attikum, H., and Gasser, S.M. (2005). ATP-dependent chromatin remodeling and DNA double-strand break repair. Cell Cycle *4*, 1011-1014.

van Attikum, H., and Gasser, S.M. (2009). Crosstalk between histone modifications during the DNA damage response. Trends Cell Biol. *19*, 207-217.

van Steensel, B., van Binnendijk, E.P., Hornsby, C.D., van der Voort, H.T., Krozowski, Z.S., Kloet, E.R. de, and van Driel, R. (1996). Partial colocalization of glucocorticoid and

mineralocorticoid receptors in discrete compartments in nuclei of rat hippocampus neurons. J. Cell. Sci *109 (Pt 4)*, 787-792.

Vempati, R., Jayani, R., Notani, D., Sengupta, A., Galande, S., and Haldar, D. (2010). p300-mediated acetylation of histone H3 lysine 56 functions in DNA damage response in mammals. J Biol Chem *285*, 28553-28564.

Vermeulen, M., Mulder, K., Denissov, S., Pijnappel, W., van, S., Varier, R., Baltissen, M., Stunnenberg, H., Mann, M., and Timmers, H. (2007). Selective anchoring of TFIID to nucleosomes by trimethylation of histone H3 lysine 4. Cell *131*, 58-69.

Walter, J., Joffe, B., Bolzer, A., Albiez, H., Benedetti, P.A., Müller, S., Speicher, M.R., Cremer, T., Cremer, M., and Solovei, I. (2006). Towards many colors in FISH on 3D-preserved interphase nuclei. Cytogenet. Genome Res *114*, 367-378.

Wang, G.G., Song, J., Wang, Z., Dormann, H.L., Casadio, F., Li, H., Luo, J.-L., Patel, D.J., and Allis, C.D. (2009). Haematopoietic malignancies caused by dysregulation of a chromatin-binding PHD finger. Nature *459*, 847-851.

Wang, H., Zhai, L., Xu, J., Joo, H.-Y., Jackson, S., Erdjument-Bromage, H., Tempst, P., Xiong, Y., and Zhang, Y. (2006). Histone H3 and H4 Ubiquitylation by the CUL4-DDB-ROC1 Ubiquitin Ligase Facilitates Cellular Response to DNA Damage. Molecular Cell *22*, 383-394.

Wiedemann, S.M., Mildner, S.N., Bönisch, C., Israel, L., Maiser, A., Matheisl, S., Straub, T., Merkl, R., Leonhardt, H., and Kremmer, E., et al. (2010). Identification and characterization of two novel primate-specific histone H3 variants, H3.X and H3.Y. J. Cell Biol *190*, 777-791.

Williams, R.S., Williams, J.S., and Tainer, J.A. (2007). Mre11–Rad50–Nbs1 is a keystone complex connecting DNA repair machinery, double-strand break signaling, and the chromatin template. Biochem. Cell Biol *85*, 509-520.

Xiang, Y., Zhu, Z., Han, G., Ye, X., Xu, B., Peng, Z., Ma, Y., Yu, Y., Lin, H., and Chen, A.P., et al. (2007). JARID1B is a histone H3 lysine 4 demethylase up-regulated in prostate cancer. Proc. Natl. Acad. Sci. U.S.A *104*, 19226-19231.

Xie, W., Song, C., Young, N.L., Sperling, A.S., Xu, F., Sridharan, R., Conway, A.E., Garcia, B.A., Plath, K., and Clark, A.T., et al. (2009). Histone h3 lysine 56 acetylation is linked to the core transcriptional network in human embryonic stem cells. Mol. Cell *33*, 417-427.

Yamane, K., Tateishi, K., Klose, R.J., Fang, J., Fabrizio, L.A., Erdjument-Bromage, H., Taylor-Papadimitriou, J., Tempst, P., and Zhang, Y. (2007). PLU-1 Is an H3K4 Demethylase Involved in Transcriptional Repression and Breast Cancer Cell Proliferation. Mol. Cell *25*, 801-812.

Yuan, G., and Zhu, B. (2011). Histone variants and epigenetic inheritance. Biochimica et biophysica acta. Epub ahead of print.

Zaratiegui, M., Irvine, D.V., and Martienssen, R.A. (2007). Noncoding RNAs and Gene Silencing. Cell *128*, 763-776.

Zarebski, M., Wiernasz, E., and Dobrucki, J.W. (2009). Recruitment of heterochromatin protein 1 to DNA repair sites. Cytometry A *75*, 619-625.

Zeitlin, S.G., Baker, N.M., Chapados, B.R., Soutoglou, E., Wang, J.Y.J., Berns, M.W., and Cleveland, D.W. (2009). Double-strand DNA breaks recruit the centromeric histone CENP-A. Proc. Natl. Acad. Sci. U.S.A *106*, 15762-15767.

Zeng, J., Ge, Z., Wang, L., Li, Q., Wang, N., Björkholm, M., Jia, J., and Xu, D. (2010). The histone demethylase RBP2 Is overexpressed in gastric cancer and its inhibition triggers senescence of cancer cells. Gastroenterology *138*, 981-992.

Zhao, Y., Lang, G., Ito, S., Bonnet, J., Metzger, E., Sawatsubashi, S., Suzuki, E., Le Guezennec, X., Stunnenberg, H.G., and Krasnov, A., et al. (2008). A TFTC/STAGA module mediates histone H2A and H2B deubiquitination, coactivates nuclear receptors, and counteracts heterochromatin silencing. Mol. Cell *29*, 92-101.

Zinner, R., Albiez, H., Walter, J., Peters, A.H.F.M., Cremer, T., and Cremer, M. (2006). Histone lysine methylation patterns in human cell types are arranged in distinct three-dimensional nuclear zones. Histochem. Cell Biol. *125*, 3-19.

Ziv, Y., Bielopolski, D., Galanty, Y., Lukas, C., Taya, Y., Schultz, D.C., Lukas, J., Bekker-Jensen, S., Bartek, J., and Shiloh, Y. (2006). Chromatin relaxation in response to DNA double-strand breaks is modulated by a novel ATM- and KAP-1 dependent pathway. Nat. Cell Biol. *8*, 870-876.

7 Abbreviations

2D	two-dimensional
3D	three-dimensional
53BP1	p53-binding protein 1
A488	Alexa fluor 488
ATM	Ataxia telangiectesia mutated
ATR	Ataxia telangiectasia and Rad-related
BSA	bovine serum albumine
bp	Base pairs
BrdU	5-bromo-2'-deoxyuridine
CAF1	Chromatin assembly factor 1
CENP-A	Centromeric protein A
Cy3	Cyanin 3
DAPI	4',6-diamidino-2-phenylindole
DDR	DNA damage response
DMEM	Dulbecco´s modified eagle serum
DNA	Deoxyribo-nucleic acid
DSB	double-strand break(s)
DMEM	Dulbecco´s modified eagle serum
EC	Euchromatin
EDTA	Ethylendiamintetraacetat
EtOH	Ethanol
EZH2	Enhancer of Z(este) homologue 2
FCS	Fetal calf serum
γ-H2AX	Phosphorylated H2AX
h	Hour(s)
HAT	Histone acetyltransferase
HC	Heterochromatin
HDAC	Histone deacetylase
HDACi	Histone deacetylase inhibitor
HP1β	Heterochromatin protein 1 beta
HR	Homologous recombination
h-TERT	Human telomerase reverse transcriptase
HMT	Histone methyltransferase
ICA/ ICQ	Intensity correlation analysis / Intensity correlation quotient
IF	immunofluorescence

IR	Ionizing radiation
IRIF	Irradiation-induced foci
Jarid1A	Jumonji-ARID protein 1a (synonyms: RBP2 or KDM5A)
Jarid1B	Jumonji-ARID protein 1b (synonyms: PLU1 or KDM5B)
kDa	Kilo dalton
KDM	Lysine (K) demethylase
KMT	Lysine (K) methyltransferase
LSM	Laser scanning microscope
Mbp	Mega base pairs
MDC1	Mediator of DNA damage checkpoint 1
MeOh	Methanol
min	Minutes
MLL	Mixed lineage leukemia
MRN	Mre11-Rad50-Nbs1 complex
miRNA	microRNA
µm	Micrometer
NA	Numerical aperature
ncRNA	Non-coding RNA
NHEJ	Non-homologous end-joining
nm	Nanometer
ns	Non-silencing
NuRD	Nuclesome remodeling complex
PBS	Phosphate-buffered saline
PDM	Product of the differences from the mean
PFA	para-formaldehyde
PHD	Plant homeo domain
PRC1/2	Polycomb-represssive complex 1 /2
PSF	Point spread function
PTMs	Post-translational modifications
RBP2	Retinoblastom binding protein 2
RevT	Reverse transcription
RPMI	Cell culture medium from the roswell park memorial institute
rpm	Rounds per minute
RNA	Ribonucleic acid
RT	Room temperature
siRNA	Silencing RNA
TSS	Transcriptional start site

Appendix A

Peptide competition assay of histone methyl antibodies
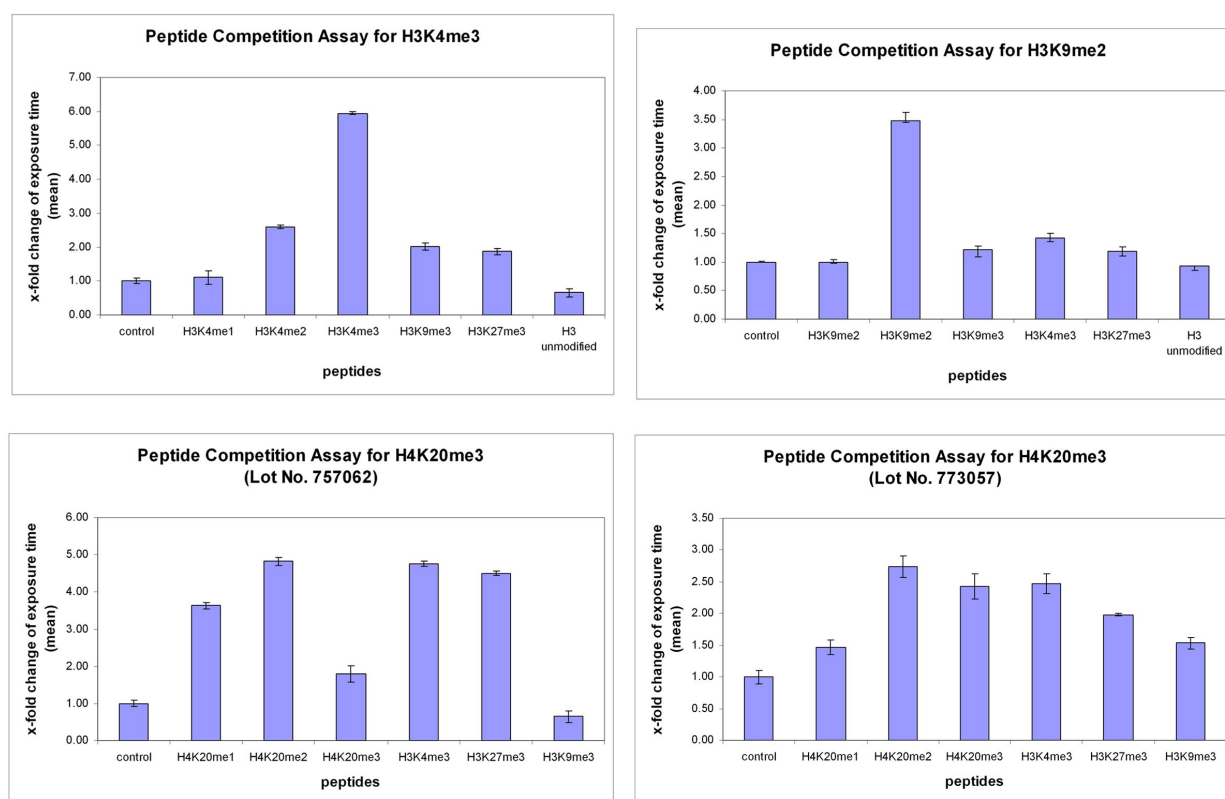
Figure A.1: X-fold change of mean exposure time in images, where primary antibody was incubated with various competing peptides. Primary antibody was incubated with a 100-fold molar excess of its specific peptide or various unspecific peptides as indicated. Exposure time was measured in five images of each condition and was than normalized to exposure time of the control. Shown are mean values and standard deviations (SD). After incubation of the primary antibody with its specific peptide, exposure time was significantly increased as shown for H3K4me3 (Abcam 8580) and H3K9me2 (Millipore 04-768). H3K4me3 did slightly cross react with the dimethylated peptide. Two antibodies for H4K20me3 (Abcam 9053) were tested. Both showed unspecific cross reactions and thus were not used further.
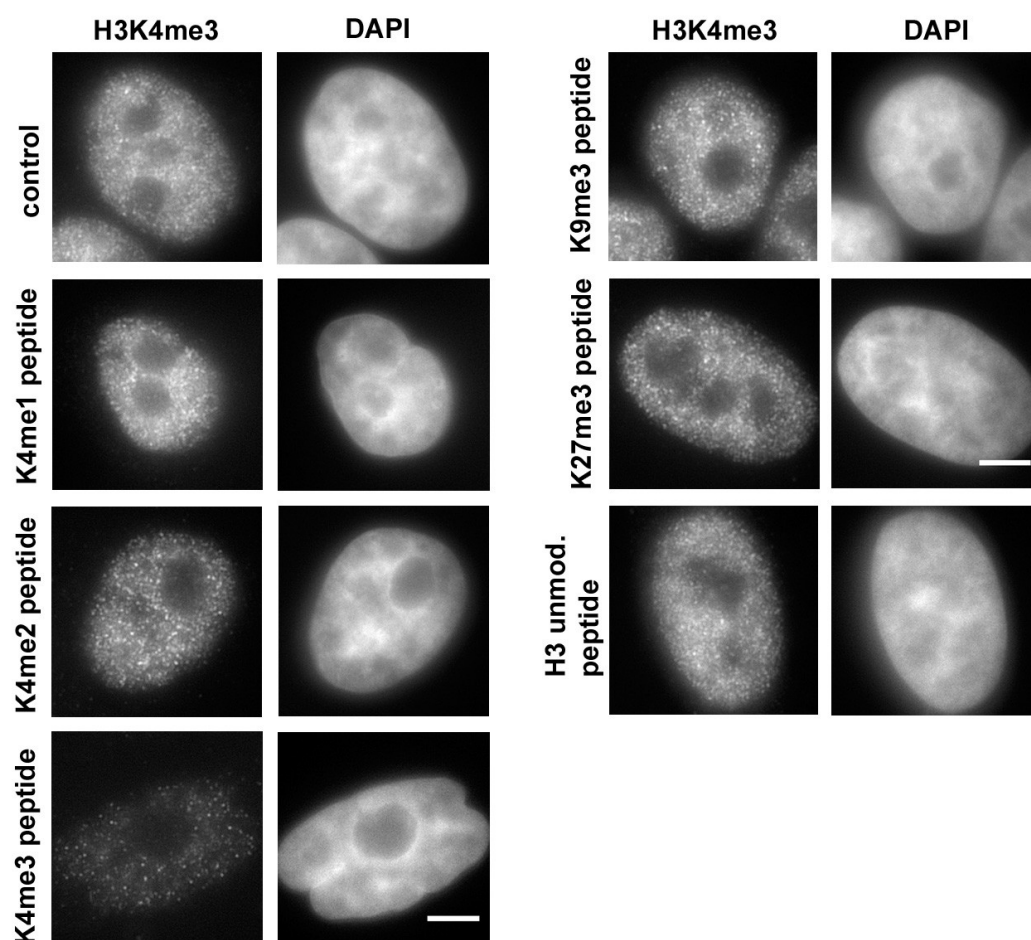
Figure A.2: Histone methyl antibodies were tested for their specificity with competing peptides. Shown are raw epifluorescence single slices of images of HeLa cells, which were stained with H3K4me3 (green channel) and DAPI (blue channel). Primary antibody was incubated with a 100-fold molar excess of its specific peptide (H3K4me3 peptide) or various unspecific peptides as indicated on the left site of the images. Automatic measurement of exposure times showed that incubation with the specific peptide led to an increase of exposure time. In the images shown, the exposure time was set manually to that of control images to show the differences in signal intensity. H3K4me3 antibody was specifically blocked by its corresponding peptides, whereas unspecific cross reactions were not observed. Scale bar is 5 µm.

Appendix B

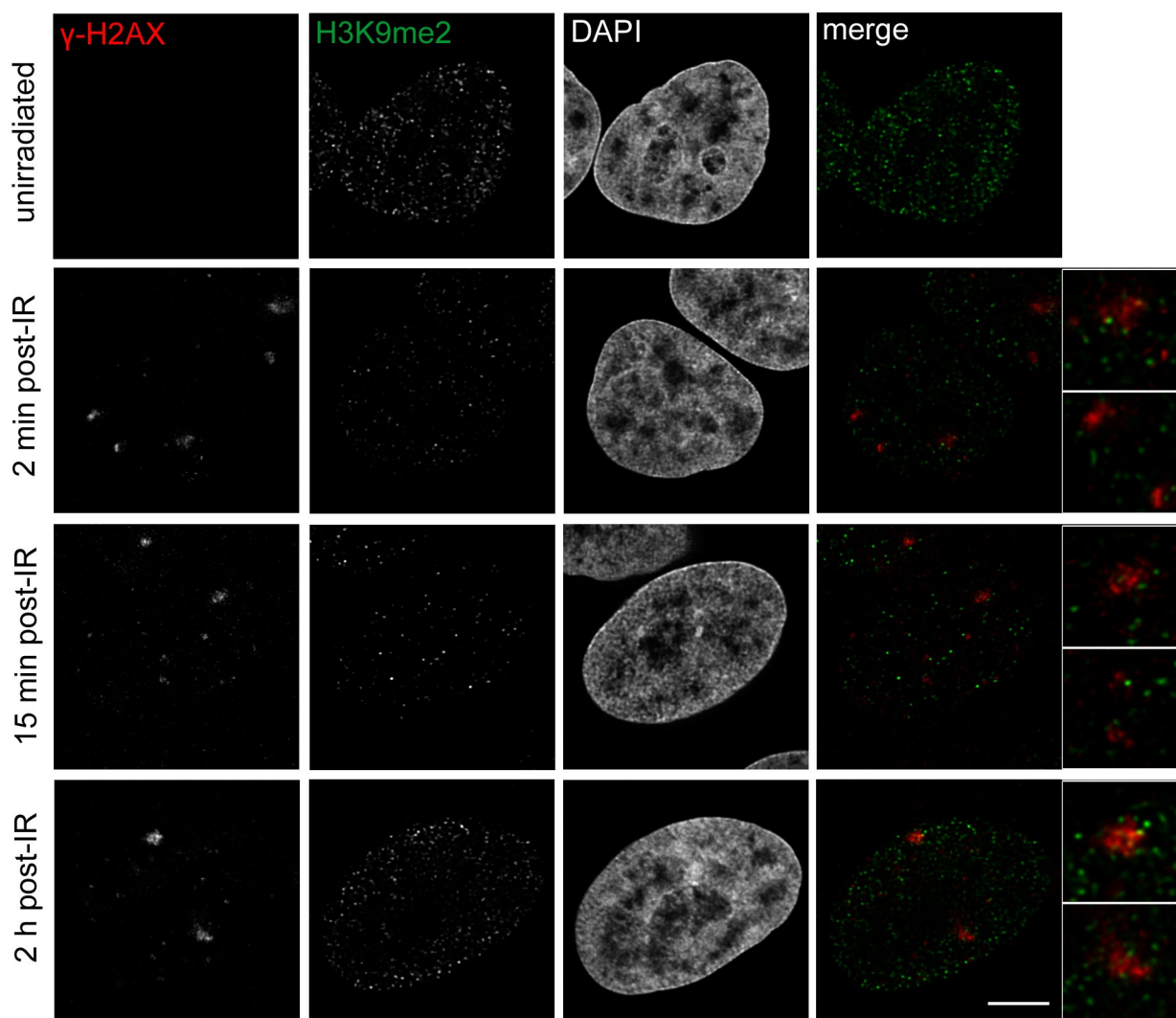## Distribution of H3K9me3/me2 in cell nuclei after α-irradiation
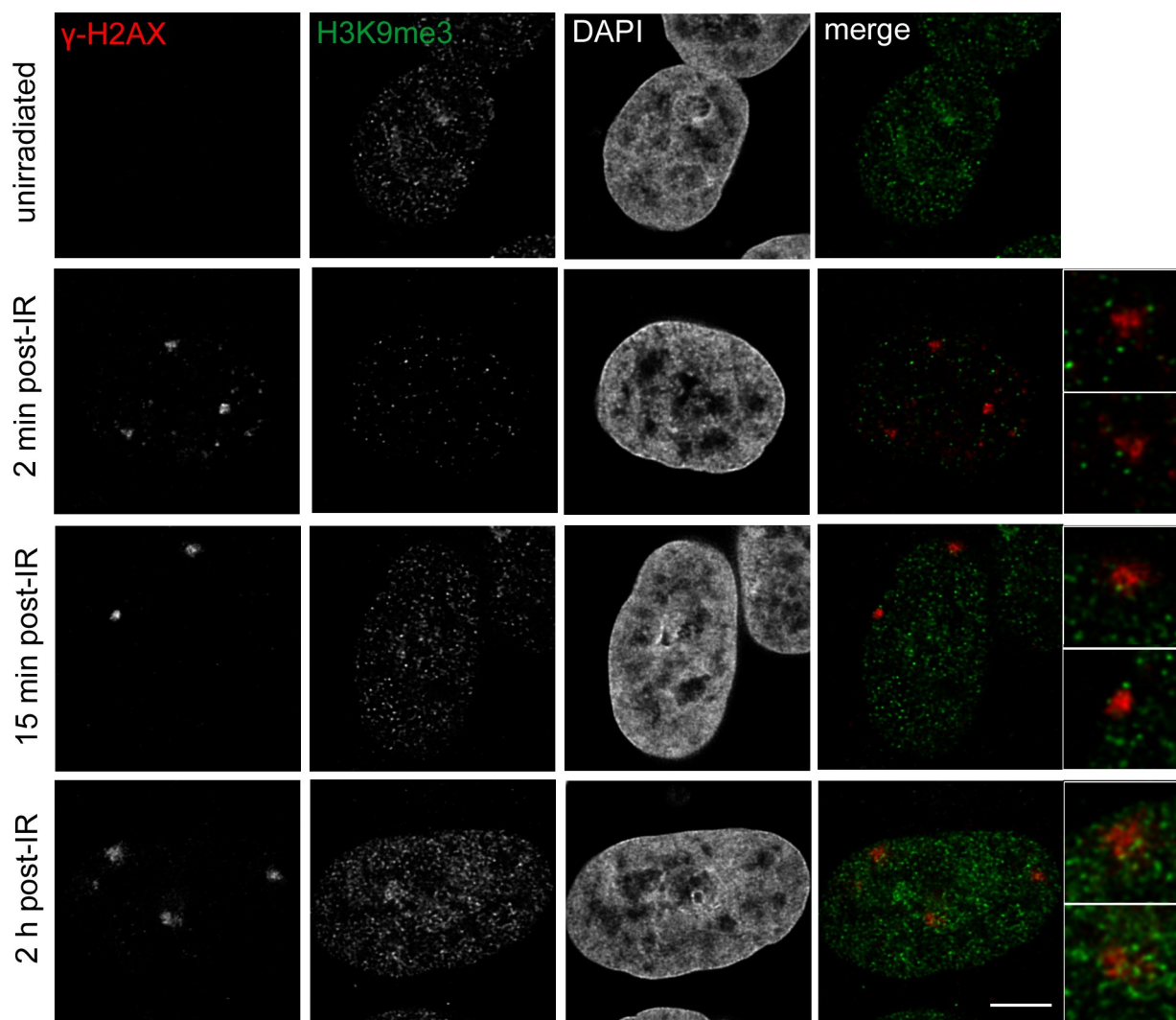
Figure B.1: Distribution of γ-H2AX and H3K9me3 in HeLa cell nuclei at different times following alpha-particle irradiation. Shown are microscopic single slices of mid-sections of confocal image stacks. Images show γ-H2AX (red), H3K9me3 (green), DNA counter stain with DAPI (blue) and red-green merges. Enlargements represent distribution of H3K9me3 at and around selected IRIF in a red-green merge. Enlargements are 5 x 5 μm. Scale is 5 μm. In unirradiated nuclei and 2 h after irradiation, H3K9me3 pattern was more homogeneously distributed across the nucleus, than at shorter times (2 min, and also 15 min) after IR. Here, the signal intensities of single H3K9me3 spots were increased

Figure B.2: Distribution of γ-H2AX and H3K9me2 in HeLa cell nuclei at different times following alpha-particle irradiation. Shown are microscopic single slices of mid-sections of confocal image stacks. Images show irradiation-induced foci (IRIF) visualized with γ-H2AX (red) and distribution of γ-H2AX foci with H3K9me2 (green), DNA counter stain with DAPI (blue) and red-green merges. Enlargements represent distribution of H3K9me2 at and around selected IRIF in a red-green merge. Enlargements are 5 x 5 µm. Scale is 5 µm. In unirradiated nuclei and 2 h after irradiation, H3K9me2 pattern was more homogeneously distributed across the nucleus, than at shorter times (2 min and 15 min) after IR. Here, the signal intensities of single H3K9me3 spots were increased

Appendix C

Distribution of H3K4me3 and γ-H2AX in epifluorescence images of HeLa cells after IR
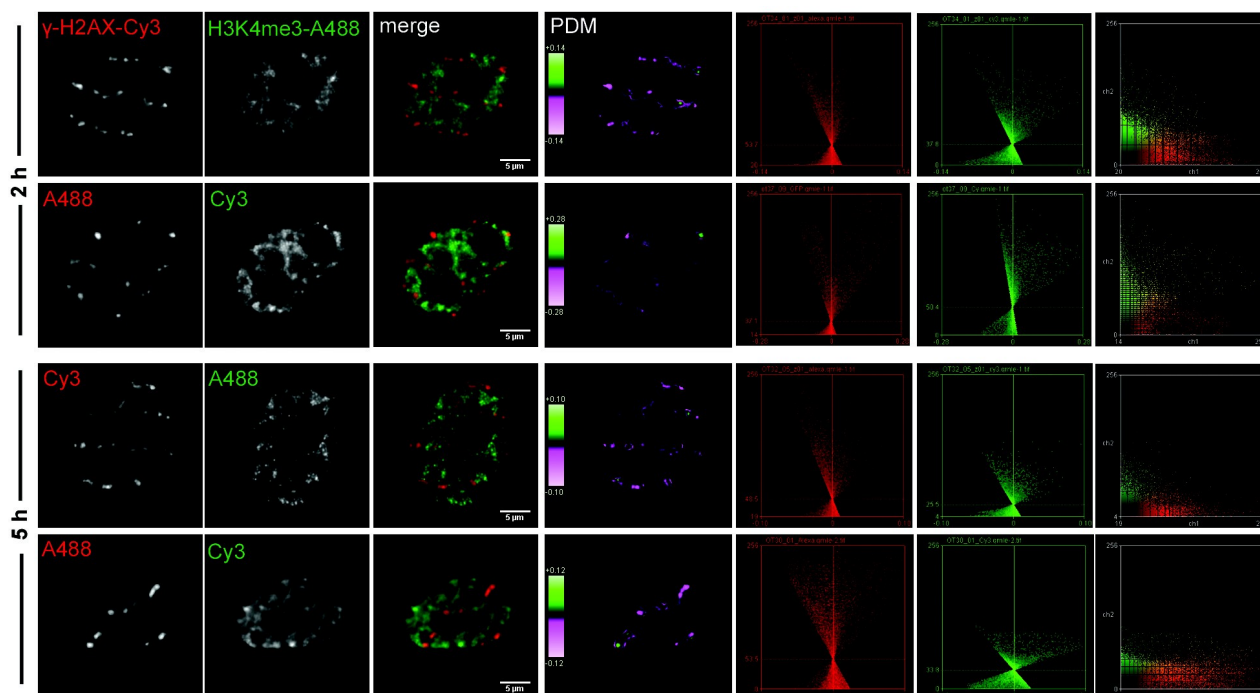
Figure C.1: Under-representation of H3K4me3 at γ-H2AX foci in ion-irradiated HeLa cells after flipping secondary antibodies. Epifluorescence images show γ-H2AX (red), H3K4me3 (green) and red-green merges. ICA was performed for a number of mid-sections of image stacks. PDM image represent localization of pixel pairs (pink = anti-correlation, green = correlation). ICA and scatter plots show PDM value and their corresponding intensities and intensity distribution of γ-H2AX (red) and H3K4me3 (green) channel. Secondary antibodies were exchanged to exclude fluorochrome quenching effects (indicated as Cy3 = Cyanin3 or A488 = Alexa Fluor 488, respectively). Scale is 5 μm.

Appendix D

Statistical evaluation of H3K4me3 distribution and γ-H2AX foci using Pearson´s correlation coefficient and ICQ
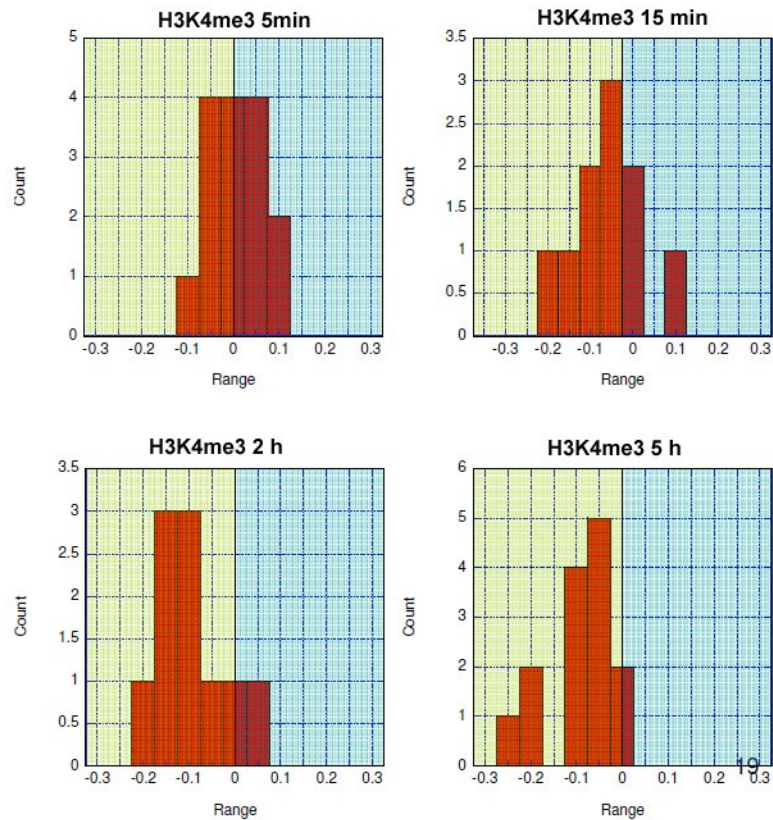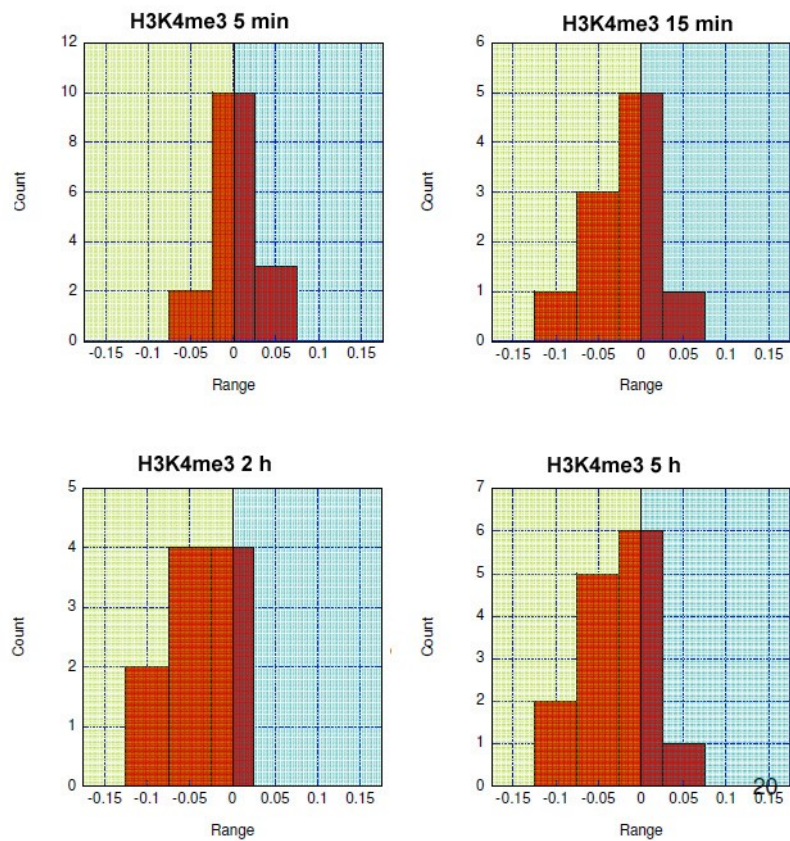

Figure D.1: Pearson´s coefficient determined for H3K4me3 and γ-H2AX in epifluorescence images of irradiated HeLa cells between 5 min and 5 h after IR. Histograms show the distribution of Pearson´s coefficient and the respective counts obtained for n = 10-15 cell nuclei evaluated with ICA. Pearson´s coefficient is distributed around zero at 5 min after IR and adopts more negative values between 15 min and 5 h after IR.

Figure D.2: ICQ determined for H3K4me3 and γ-H2AX in epifluorescence images of irradiated HeLa cells between 5 min and 5 h after IR. Histograms show the distribution of the ICQ and the respective counts obtained for n = 10-15 cell nuclei evaluated with ICA. ICQ adopts values close to zero 5 and 15 min after IR. 2 and 5 h after IR it adopts slightly negative values.
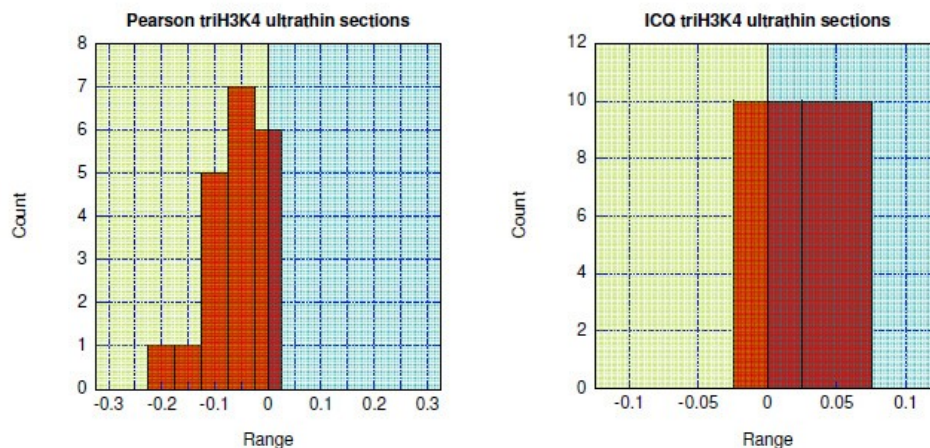
Figure D.3: Pearson´s coefficient and ICQ determined for H3K4me3 and γ-H2AX in ultrathin sections of HeLa cells 2 h after IR. Histograms show the distribution of Pearson´s correlation coefficient (left) and ICQ (right) and the respective counts obtained from ICA of n = 20 cell nuclei. Pearson´s coefficient indicates slight anti-correlation, whereas ICQ indicates random to positive correlations.

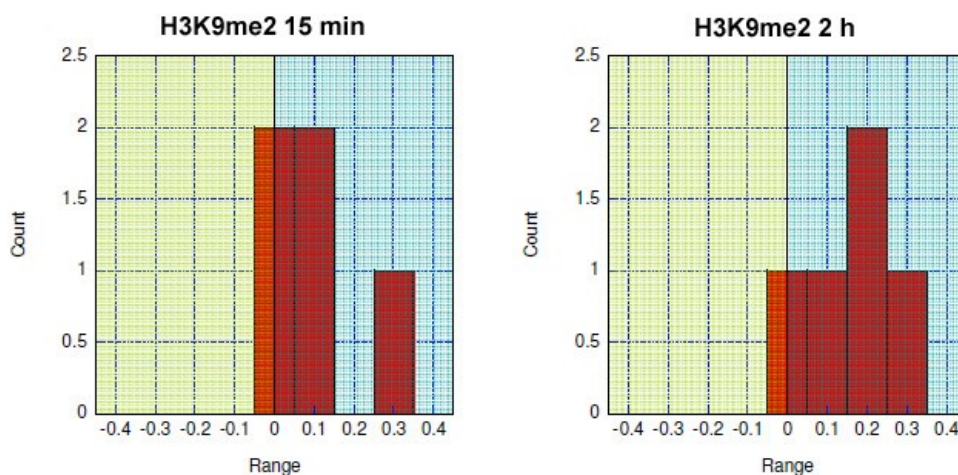# Statistical evaluation of H3K9me2 distribution and γ-H2AX using Pearson´s coefficient and ICQ

Figure D.4: Pearson´s correlation coefficient determined for H3K9me2 and γ-H2AX in epifluorescence images of HeLa cells 15 min and 2 h after IR. Histograms show distribution of Pearson´s coefficient and respective counts obtained for evaluation of n = 5 cell nuclei with ICA. Pearson´s coefficient adopts values close to zero 15 min after IR. 2H after IR the coefficient adopts more positive values.
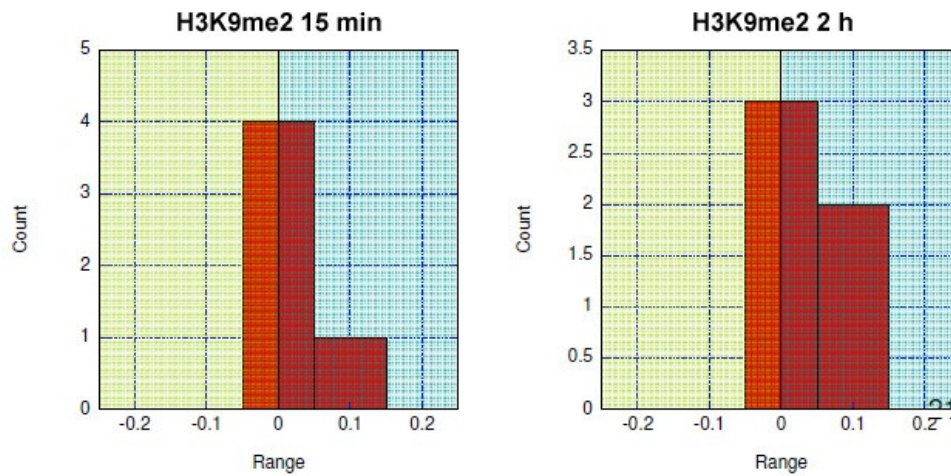
Figure D.5: ICQ determined for H3K9me2 and γ-H2AX in epifluorescence images of HeLa cells 15 min and 2 h after IR. Histograms show distribution of ICQ and respective counts obtained for evaluation of n = 5 cell nuclei with ICA. ICQ indicates random to slightly positive correlations.
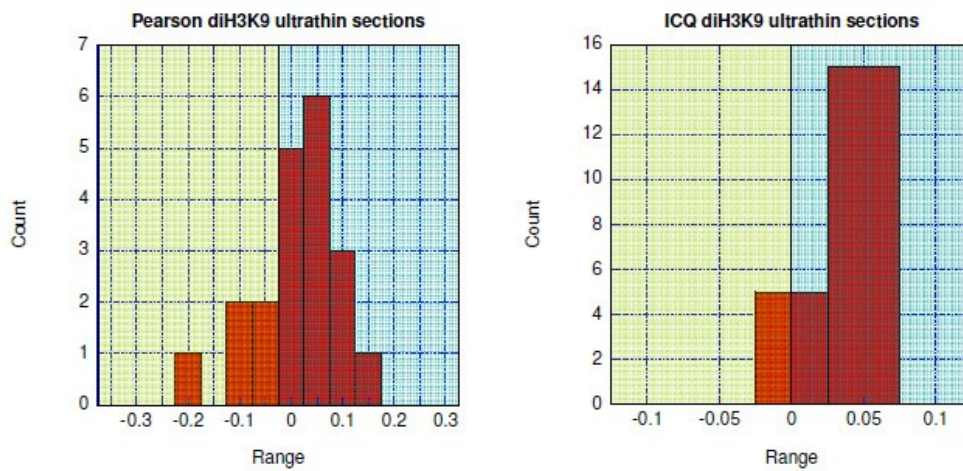

Figure D.6: Pearson´s coefficient and ICQ determined for H3K9me2 and γ-H2AX in ultrathin sections of HeLa cells 2 h after IR. Histograms show the distribution of Pearson´s correlation coefficient (left) and ICQ (right) for n = 20 cell nuclei. Pearson´s coefficient indicates random distribution with values close to zero. ICQ also indicates random to positive correlations.

Appendix E

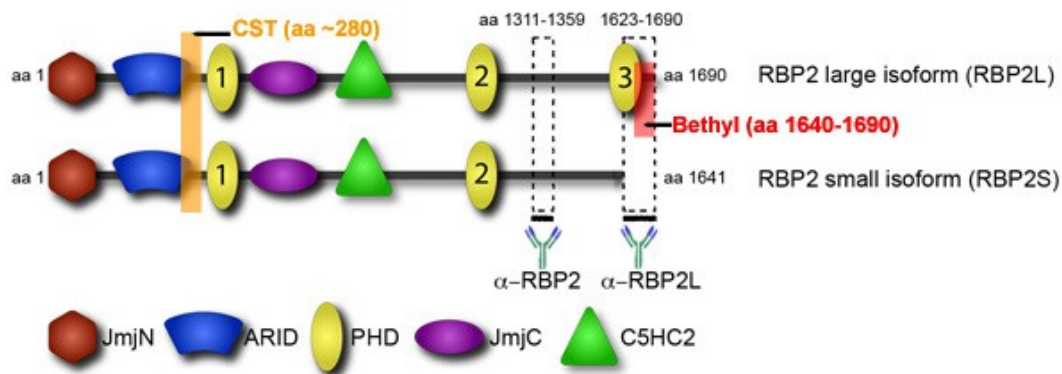## Draft of the large and the small Jarid1A (RBP2) isoform

Figure E.1: Draft of large and small isoforms of Jarid1A (RBP2). The large isoform (top) contains the C-terminal plant homeo domain (PHD3), which binds to H3K4me3/me2. The Jarid1A protein further contains a JmjN (red), a JmjC (pink), an ARID domain (blue) and a C5HC2 zinc finger domain (green). Four specific antibodies are indicated. Two antibodies described in (Beshiri et al, 2010) either bind the C-terminal region at amino acids 1623 – 1690 (-RBP2L) or to both isoforms by recognition of a more central region at amino acids 1311-1359 (-RBP2). Additionally, binding regions of two antibodies used in the present work are indicated, i.e. RBP2-antibody obtained from Cell Signaling technologies (CST; indicated in orange) binds around aa 280, whereas RBP2 antibody obtained from Bethyl (indicated in red) binds to aa 1640-1690 (Beshiri et al., 2010, modified).

Alignments of Jarid1A siRNAs with the primary sequence of Jarid1A large and small isoforms
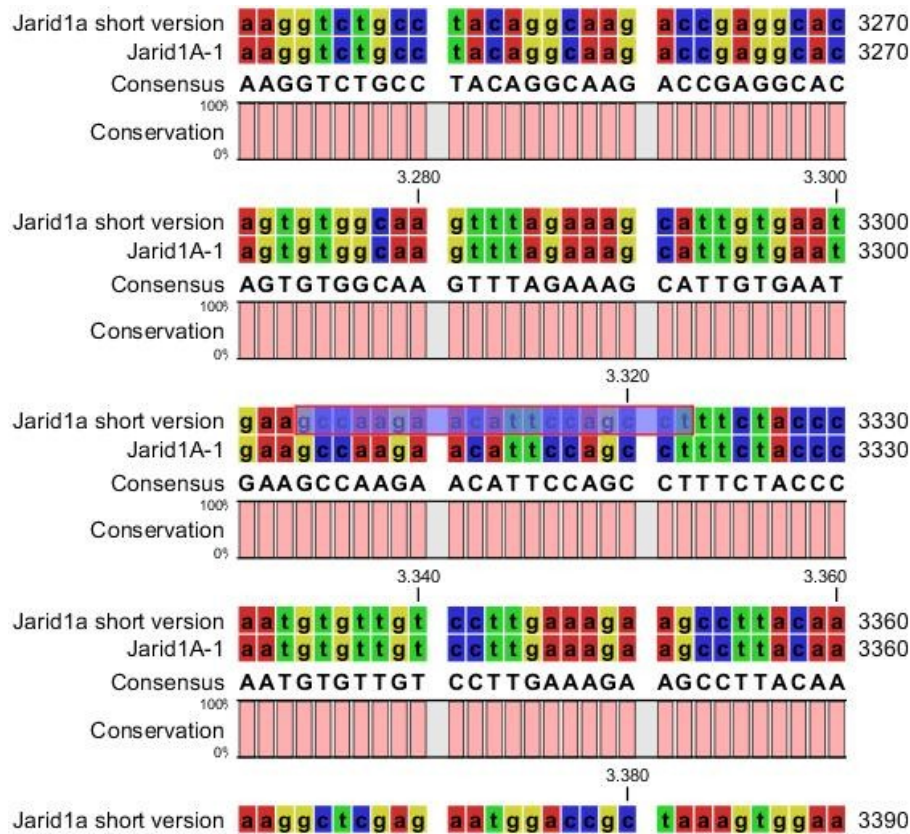

Figure E.2: Alignment of Jarid1A siRNA No.2 with the primary sequence of Jarid1A short and long isoforms. A detail of the primary sequence of Jarid1A short and large isoform (indicated as Jarid1A-1) is shown. The alignment with siRNA No. 2 is highlighted in violet and lies within the nucleotides of 3304-3322. This area encodes the aa 2941 – 2959.
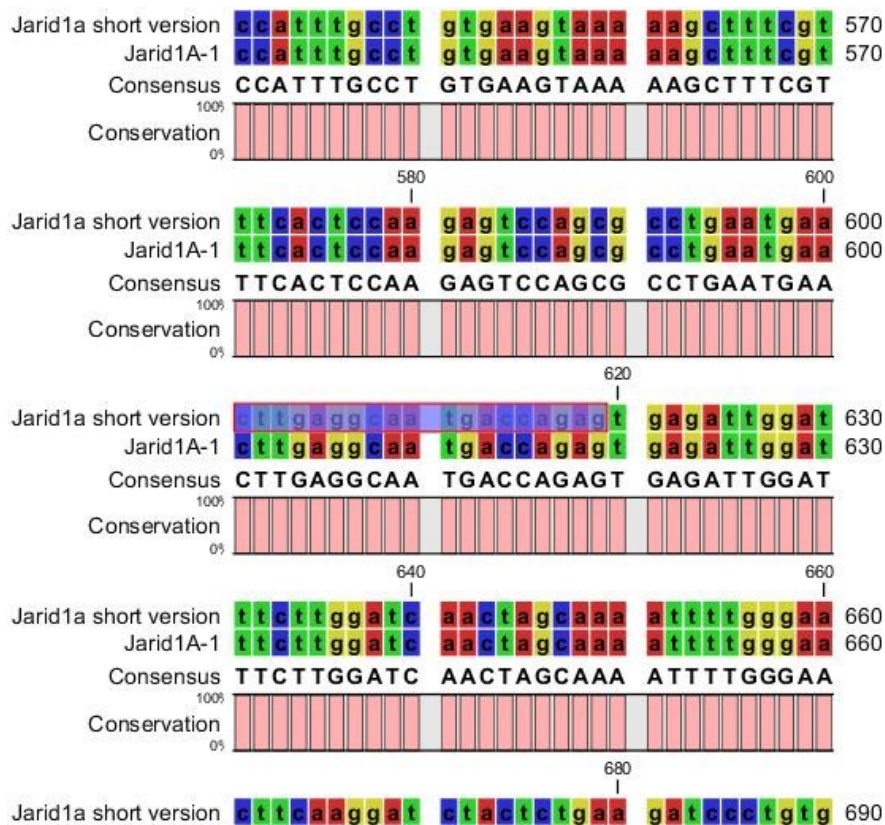
Figure E.3: Alignment of Jarid1A siRNA No.4 with the primary sequence of Jarid1A short and long isoforms. A detail of the primary sequence of Jarid1A short and large isoform (indicated as Jarid1A-1) is shown. The alignment with siRNA No. 4 is highlighted in violet and lies within the region of nucleotides 601 - 619. This area encodes the aa 238 – 256.

Ehrenwörtliche Versicherung

Ich versichere hiermit ehrenwörtlich, dass die vorgelegte Dissertation von mir selbständig und ohne unerlaubte Hilfe angefertigt ist.

München, den   Unterschrift

Acknowledgments

I would like to thank all the people who have supported and encouraged me during my PhD thesis.

At first, I would like to thank my supervisor PD Dr. Anna A. Friedl who gave me the opportunity to conduct my PhD in her lab. Thank you for your confidence, motivation, ideas, for listening and help at any time! Thank you for the Yogi attitude!

Next, I would like to thank my dear colleagues, in particular, Dr. Guido Drexler, Belinda Mazurek and Linda Kinzel who supported me at any time with their ideas or with just something eatable! Susanne Auer, Sophie Lindemaier, Markus Lauterbacher, Negi Moghaddam, Theresa Eiglsperger, and all diploma students and 'Hiwis' who worked here during that time, thank you for help and great time! I thank our technical assistance team Heike Hofmann, Diana Wieland, and Iris Bauer for help with experiments and support.

Further, I would like to thank Prof. Thomas Cremer for his second opinion on my thesis, for his advices and for giving me the opportunity to use and to learn about the great microscopes. Thanks to all the people of the Cremer lab, especially, Dr. Hilmar Strickfaden who helped me with microscopes and for initiating ultrathin sectioning, and Dr. Jacques Rouquette for teaching me sectioning. Thanks for technical help or reagents to Dr. Katrin Pfleghaar, Katrin Schneider, Corinna Hintermair, Dr. Sandra B. Hake, and Dr. Irinia Solovei.

I appreciate the work of Prof. Volker J. Schmid from the Institute of Statistics, LMU, for his support with statistical analyzes and his ideas.

I thank the staff of the Maier-Leibnitz-Laboratory for operating the accelerator, our physicists Christoph Greubel, Volker Hable and Prof. Günter Dollinger for performing irradiation at SNAKE and for fruitful discussions. Thanks to Dr. H. Ruhstorfer and Dr. M. Rosemann from the Institute of Radiation Biology at the Helmholtz Center Munich for access to the alpha-irradiation facility.

Finally, I would like to thank my mother for her support at any time, my family, my friends Klaus and Julia, and the 'Mädels'! Last but not least, Christian, you know that without you this work would not have come to being. Thank you so much.

Curriculum Vitae

Doris Mirjam Seiler

Date of birth: January 18th 1981
Place of birth: Munich, Germany

Education

2011 – present	Postdoctoral position, Technical University Munich, Clinical Cooperation Group Osteosarcoma, Group leader: PD Dr. Michaela Nathrath
2007 - 2011	PhD in Biology (Dr. rer. nat.), University Hospital of Munich, Department of Radiotherapy and Radiation Oncology Thesis title: Epigenetic Alterations at γ-H2AX-decorated Chromatin Regions after Ionizing Radiation Supervisor: PD Dr. Anna A. Friedl
2007	Diploma thesis, Helmholtz Center Munich (former GSF), Institute of Molecular Immunology Thesis title: Effect of Acidosis on the Effector Function of Cytotoxic T Cells Supervisor: Prof. Dr. Elfriede Noessner
2002 - 2007	Study in Biology, Technical University Munich Major subject: Biochemistry and cell biology Minor subjects: Human biology, immunology, animal ecology and behavior
1991 – 2000	A-level, Kurt-Huber-Gymnasium, Munich

Work Experience

2002 – 2006	Assistant to the sales department, ibidi integrated biodiagnostics GmbH, Munich
2001 - 2002	Assistant to the editorial office, FOCUS Magazin Verlag GmbH, Munich
2000 - 2001	Customer service, Camelot tele-communication-online-AG, Munich

Special Skills and Stays Abroad

2005	Internship, Helmholtz Center Munich (former GSF), Institute of Molecular Immunology Project: Detection of chemokine receptor CXCR1 on human blood lymphocytes Supervisor: Prof. Dr. Elfriede Noessner
2005	Stay abroad, Jagiellonian University Krakow, Faculty of Biotechnology, Poland. Funded by SOCRATES/ERASMUS exchange program.

Project: Isolation and characterization of an extracellular metallo protease of *Staphylococcus Intermedius*
Supervisor: Prof. Dr. Adam Dubin

2002   Internship, Max-Planck-Institute for Biochemistry, Munich, Department of Structure Research
Supervisors Prof. Dr. Robert Huber & Dr. Jens Kaiser

2001   Stay abroad, Australia, participation in Conservation Volunteers Australia (ATCV)

Language Skills

German: Native speaker
English: Fluent
French: Basics
Spanish: Basics
Polish: Basics

Publication

Seiler D.M., Rouquette J., Schmid V.J., Strickfaden H., Ottmann C., Drexler G.A., Mazurek B., Greubel C, Hable V., Dollinger G., Cremer T., and Friedl A.A. (2011) Double-strand break-induced transcriptional silencing is associated with loss of tri-methylation at H3K4. Chromosome Research *19,* 883-899.

Conferences

- 3rd SFB Transregio Symposium 2010 - „CHROMATIN - Assembly and Inheritance of Functional States", 2010, University of Munich. Poster: Do DNA Double-Strand Breaks Induce Changes in Epigenetic Information?

- GBS – Annual Meeting of German Society for Research on Radiobiology, 2010, University Hospital Hamburg. Poster: Do DNA Double-Strand Breaks Induce Changes in Epigenetic Information?

- Women in Radiation Sciences - A Century after Marie Curie, 2009, Helmholtz Center Munich. Poster: Analysis of Radiation-Induced Changes in Epigenetic Information.

- EMBO Conference Series on Chromatin and Epigenetics, 2009, EMBL Heidelberg. Poster: Analysis of Radiation-Induced Changes in Epigenetic Information.

- 10th Biennial Meeting of German Society for Research on DNA Repair, 2008, Charité Berlin. Poster: Chromatin Alterations in Cellular DNA Damage and Repair.

- 5th General Meeting of the International Proteolysis Society, 2007, University of Patras, Greece. Contribution to poster: A Novel Member of the Thermolysin Family. Cloning and Biochemical Properties of Unusually Expressed Metalloprotease from Staphylococcus pseudintermedius".

Courses

- Workshop "Scientific Writing in English", 2011, Graduate Center LMU, University of Munich

- Workshop "Karriere in der Wissenschaft – Scientific Career", 2010, Graduate Center LMU, University of Munich

- User workshop "AxioVision II: Fortgeschrittene – advanced training", 2010, Carl Zeiss MicroImaging GmbH, Munich

- Workshop "Presenting Professionally", 2009, Graduate Center LMU, University of Munich